ESMRMB
European Society for Magnetic Resonance in Medicine and Biology

ESMRMB 2019 Congress

October 3-5, Rotterdam/NL

Book of Abstracts

Friday

DOI: 10.1007/s10334-019-00754-2

www.esmrmb.org

I10 Teaching Session

08:00–09:00 *Room 1 - Willem Burger Zaal*

Machine Learning for Acquisition

I10.01

Artefact Reduction with Machine Learning

T. Kuestner
King's College London, London, UNITED KINGDOM

Learning Objectives: To provide an overview of state-of-the-art machine learning and deep learning methods for artefact reduction in MRI.

To demonstrate the application of learning methods for artefact localization, quantification, quality assurance and assessment, restoration and correction.

To illustrate future perspectives and integrations into clinical practice.

Body: Magnetic Resonance Imaging (MRI) is a very flexible imaging modality providing a variety of contrast mechanisms and applications to visualize anatomical structures and physiological functions. The immense and flexible sequence and reconstruction choice makes it on one hand tunable to specific needs and applications but demands on the other hand a profound technical knowledge. This flexibility and the complexity of the imaging process give rise to different kinds of artefacts[1, 2]. The artefacts can be grouped into patient-related (e.g. physiological motion), hardware-related (e.g. B0/B1 inhomogeneity) and signal-processing-related (e.g. aliasing) with each of the groups having different origins and implications on the final image. Whilst some artefacts can be mitigated or avoided by careful MR sequence and reconstruction selection, proper parametrization and/or optimal acquisition conditions, not all these objectives can be fulfilled simultaneously. Hence artefacts can still remain in the image degrading the diagnostic quality.

Usually a visual inspection is performed by a human MR specialist to ensure images of sufficient quality or to identify potential artefacts. This manual processing can be very time- and cost-intensive. Moreover, in the context of large epidemiological cohort studies[3, 4], the extent and complexity of acquired data make a manual analysis practically impossible. Automated analysis of the data by machine learning approaches can therefore support the human observer in ensuring sufficient image quality. Machine-learning based curation and correction methods can also help to improve the image quality or to speed up reconstruction and analysis tasks.

In this talk, we will provide an overview of machine and deep learning methods used for MR artefact identification, quantification and localization covering different artefacts and body regions. We demonstrate how these techniques can be utilized to ensure data quality and to provide a real-time feedback to the user. Extending on this, we will highlight approaches used for deep-learning based motion artifact correction and reconstruction of undersampled MR data. We conclude by discussing future directions and remaining challenges.

References:

1. Krupa Pol J Radiol 2015;80.
2. Morelli Radiographics 2011;31(3).
3. Ollier Pharmacogenomics 2005;6(6).
4. Bamberg Radiology 2015;277(1).

I10.02

A Short Review of Current Trends in Deep Learning for Magnetic Resonance Fingerprinting

A. Maier
Friedrich-Alexander-University Erlangen-Nuremberg, Computer Science, Erlangen, GERMANY

Learning Objectives: Magnetic Resonance Fingerprinting + Deep Learning.

Body: MR Fingerprinting (MRF) is an emerging technique for quantitative MR Imaging [1]. Recently, several groups proposed to improve the fingerprint matching procedure using methods of machine learning. One of the first approaches involved using convolutional neural networks for MRF [2] as it is fast in terms of execution time [3]. Approximately at the same time also, traditional fully connected neural networks were investigated for MRF [4], e.g. introducing a bottleneck layer to mimic dimensionality reduction techniques [5]. Generally, use of the complex signal was found to be better than using only the real part [6]. Building on these first successful observations, soon more advanced machine learning techniques were adopted to MRF. As in conventional fingerprinting, inclusion of spatiotemporal context was found to be successful [7]. Further research was able to successfully integrate advanced deep learning concepts [8].

For future research adaptation of advanced concepts of deep learning reconstruction seems interesting. For example, end-to-end training using variational networks [9] seems suitable. Also, as noise modelling in MRF is difficult, arbitrary noise augmentation methods [10] might be useful. Another useful perspective might be the integration of physical knowledge into deep nets [11] which was already applied successfully in other image reconstruction domains.

References:

[1] Ma D et al. Magnetic resonance fingerprinting. Nature 495(7440), 187–192 (2013).

[2] Hoppe E et al. Deep Learning for Magnetic Resonance Fingerprinting: A New Approach for Predicting Quantitative Parameter Values from Time Series. GMDS 243, 202–206. (2017).

[3] Hoppe E et al. 2018. Deep Learning for Magnetic Resonance Fingerprinting: Accelerating the Reconstruction of Quantitative Relaxation Maps. ISMRM.

[4] Cohen O et al.: MR fingerprinting Deep RecOnstruction NEtwork (DRONE). MRM 80(3), 885–894 (2018).

[5] Golbabaee M et al. (2019). Geometry of deep learning for magnetic resonance fingerprinting. ICASSP 2019 (7825–7829).

[6] Virtue P et al., Better than real: Complex-valued neural nets for mri fingerprinting, ICIP 2017. 3953–3957.

[7] Balsiger F et al. (2018). Magnetic resonance fingerprinting reconstruction via spatiotemporal convolutional neural networks. MLMIR (39–46).
[8] Fang Z et al. (2018). Deep learning for fast and spatially-constrained tissue quantification from highly-undersampled data in magnetic resonance fingerprinting (MRF). MLMI (398–405).
[9] Kobler E et al. (2017). Variational networks: connecting variational methods and deep learning. GCPR 2017 (281–293).
[10] Horger F et al. (2018). Towards Arbitrary Noise Augmentation—Deep Learning for Sampling from Arbitrary Probability Distributions. MLMIR (129–137).
[11] Maier A et al. (2018). Precision learning: towards use of known operators in neural networks. ICPR 2018 (183–188).

I11 Teaching Session

08:00–09:00 *Room 2 - Van Weelde Zaal*

Non-Gadolinium Based Contrast Agents

I11.01

An Overview of MRI-based Contrast Agents

D. Longo
National Research Council of Italy (CNR), Institute of Biostructures and Bioimaging (IBB), Turin, ITALY

Learning Objectives: The aim of this talk is to tackle the following learning objectives:
- To provide an overview of MRI contrast agents belonging to several classes, including Gadolinium-based, iron oxide nanoparticles, CEST agents, hyperpolarized molecules and magnetic particles.
- To explore contrast agents that can provide similar information to Gd-based agents.
- To consider new added information provided by novel contrast agents.
- To understand the potential clinical traslability of these contrast agents.

Body: In this lecture the basic concepts for different classes of MRI-based contrast agents will be provided, including mechanism of action and contrast efficiency. After introducing the main applications of clinical Gd-based contrast agents for tumor diagnosis and perfusion/vascularization assessment, some insights into the use of novel contrast agents for providing similar information will be covered. In addition, novel contrast agents that may provide additional information related to tumor microenvironment (tumor metabolism and acidosis) will be addressed, as well as potential translation to clinical applications.

References:

1. Wahsner J, Gale EM, Rodriguez–Rodriguez A, Caravan P (2018) Chemistry of MRI Contrast Agents: Current Challenges and New Frontiers. Chem Rev. https://doi.org/10.1021/acs.chemrev.8b00363.
2. Aime S, Botta M, Terreno E (2005) Gd(III)-based contrast agents for MRI. Advances in Inorganic Chemistry—Including Bioinorganic Studies, Vol 57 57:173–237. https://doi.org/10.1016/s0898-8838(05)57004-1.
3. Vinogradov E, Sherry AD, Lenkinski RE (2013) CEST: from basic principles to applications, challenges and opportunities. J Magn Reson 229:155–172. https://doi.org/10.1016/j.jmr.2012.11.024.
4. Anemone A, Consolino L, Arena F, Capozza M, Longo DL (2019) Imaging tumor acidosis: a survey of the available techniques for mapping in vivo tumor pH. Cancer Metastasis Rev. https://doi.org/10.1007/s10555-019-09782-9
5. Anemone A, Consolino L, Longo DL (2017) MRI-CEST assessment of tumour perfusion using X-ray iodinated agents: comparison with a conventional Gd-based agent. Eur Radiol 27 (5):2170–2179. https://doi.org/10.1007/s00330-016-4552-7
6. Liu F, Laurent S, Fattahi H, Vander Elst L, Muller RN (2011) Superparamagnetic nanosystems based on iron oxide nanoparticles for biomedical imaging. Nanomedicine (Lond) 6 (3):519–528. https://doi.org/10.2217/nnm.11.16 [doi]
7. Sinharay S, Pagel MD (2016) Advances in Magnetic Resonance Imaging Contrast Agents for Biomarker Detection. Annu Rev Anal Chem (Palo Alto Calif) 9 (1):95–115. https://doi.org/10.1146/annurev-anchem-071015-041514
8. Brindle KM (2015) Imaging metabolism with hyperpolarized (13)C-labeled cell substrates. J Am Chem Soc 137 (20):6418–6427. https://doi.org/10.1021/jacs.5b03300
9. Knopp T, Gdaniec N, Moddel M (2017) Magnetic particle imaging: from proof of principle to preclinical applications. Phys Med Biol 62 (14):R124–R178. https://doi.org/10.1088/1361-6560/aa6c99.

I11.02

Clinical Applications of SPIOs

A. Yilmaz
University Hospital Münster, Department of Cardiology I, Division of Cardiovascular Imaging, Münster, GERMANY

Learning Objectives: Acquire knowledge on biophysical properties and biodistribution of SPIOs.
- Get a general idea on preclinical application of SPIOs in cardiovascular diseases.
- Appreciate the value of first clinical studies with SPIOs in cardiovascular diseases.

Body: Cardiovascular magnetic resonance (CMR) is an integral part in the diagnostic work-up of various cardiovascular diseases. In this context, superparamagnetic iron oxide-based contrast agents (SPIOs) can provide additional diagnostic information regarding the assessment of e.g. myocardial infarction, myocarditis or aortic diseases.

After intravenous administration, these nanoparticles are taken up by activated monocytes and macrophages, which predominantly accumulate in regions associated with inflammation as was successfully shown in recent preclinical studies. Different formulations of SPIOs with diameters smaller than 20 nm have been widely used preclinically as contrast agents for molecular imaging. Because of their unique biophysical properties, and their different biodistribution and higher magnetic relaxation rates compared with gadolinium-based contrast agents, SPIOs were expected to expand the clinical field of contrast-enhanced magnetic resonance imaging. However, some clinically approved SPIOs were discontinued owing to harmful side effects or to limited reimbursement options. Today, ferumoxytol is the only available SPIO formulation for clinical use.

First clinical studies with ferumoxytol that was clinically approved for the treatment of iron deficiency anaemia recently demonstrated a superior diagnostic value of iron oxide nanoparticles compared to gadolinium-based compounds for imaging of myocardial inflammation in patients with acute myocardial infarction. Somewhat challenging results were obtained in case of human myocarditis.

References:

Yilmaz A. Contrastingly small iron oxides. Nat Biomed Eng. 2017 Aug;1(8):623–624. https://doi.org/10.1038/s41551-017-0124-7.
Bietenbeck M(1), Florian A(1), Faber C(2), Sechtem U(3), Yilmaz A(1). Remote magnetic targeting of iron oxide nanoparticles for cardiovascular diagnosis and therapeutic drug delivery: where are we now? Int J Nanomedicine. 2016 Jul 15;11:3191–203. https://doi.org/10.2147/ijn.s110542. eCollection 2016.
Bietenbeck M, Florian A, Sechtem U, Yilmaz A. The diagnostic value of iron oxide nanoparticles for imaging of myocardial inflammation–quo vadis? J Cardiovasc Magn Reson. 2015 Jul 8;17:54. https://doi.org/10.1186/s12968-015-0165-6.
Yilmaz A(1), Dengler MA, van der Kuip H, Yildiz H, Rösch S, Klumpp S, Klingel K,
Kandolf R, Helluy X, Hiller KH, Jakob PM, Sechtem U. Imaging of myocardial infarction using ultrasmall superparamagnetic iron oxide nanoparticles: a human study using a multi-parametric cardiovascular magnetic resonance imaging approach. Eur Heart J. 2013 Feb;34(6):462–75. https://doi.org/10.1093/eurheartj/ehs366. Epub 2012 Oct 26.

I12 Teaching Session

08:00–09:00 *Room 3 - Ruys & van Rijckevorsel Zaal*

Maximising the Value of MR: From Methods to Clinical Routine

I12.01

From Research Methodolgy to Clinical Product

G. Langs
Medical University of Vienna, Computational Imaging Research Lab, Vienna, AUSTRIA

Learning Objectives: Understand the steps necessary to develop machine learning methodology at the interface between computer science and radiology

- Understand the transition from a research project and corresponding methods and prototypes, to a process aiming at a product

Body: In this talk we will discuss the path from novel methodology, techniques and prototypes developed in an acamedic research project, towards a product that can be deployed and finds a stable user base. I will illustrate this with examples from research projects focussing on method development in the area of machine learning and image processing, and the transition towards further development in the frame of a spin-off. I will discuss learnings, insights, and surprises along that way.

References:

www.khresmoi.eu—EUproject KHRESMOI.
www.contextflow.com—contextflow.

I12.02

Value-based MRI

M. van Buchem
Leiden University Medical Center, Radiology, Leiden, NETHERLANDS

Learning Objectives: 1. to be familiar with the principles of value-based healthcare.
2. To be able to translate value-based healthcare principles in radiology.
3. To be able to translate value-based healthcare principles in MRI.

Body: Value-based healthcare (VBHC) has become a leading principle in organizing healthcare worldwide. In this presentation the principles of VBHC will be explained. In addition, we will discuss how these principles could be translated in the field of radiology. And finally, how MRI fits into this picture will be described.

I13 Plenary Session

09:15–10:30 *Room 1 - Willem Burger Zaal*

Machine Learning in MRI

I13.01

Current Role of Machine Learning in MRI

J. Schnabel
King's College London, UK, School of Biomedical Engineering and Imaging Sciences, London, UNITED KINGDOM

Learning Objectives: #To gain an overview of the current role of machine learning in MRI, with focus on deep learning
#To gain an understanding of how deep learning can be used along the entire MRI pipeline, from acqusition right through to clinical interpretation
#To understand that deep learning can operate in k-space or in the image domain
#To use cardiac MRI for illustrative applications of deep learning for sparse reconstruction, quality control, and segmentation
#To speculate on the future role of machine learning in MRI
Body: This talk will give an overview of the current role of machine learning in MRI [1, 2], with a focus on deep learning methods [3]. Traditionally, machine learning in this context has operated on individual components of the MR imaging pipeline, in order to accelerate or improve image acquisition or reconstruction, or to perform post-processing tasks such as denoising, image segmentation [4] or disease classification. Recently, methods that are operating either in k-space or in the spatial domain have been developed, that can be used for simultaneous tasks that are normally performed in a sequential manner. This includes, but is not limited to, performing image quality control directly in k-space, and learning improved image reconstructions and segmentations. To illustrate some of these approaches, I will draw from examples in cardiac magnetic resonance imaging to show how these approaches can be effectively combined to build potentially very powerful, and very fast, integrated MR imaging pipelines [5, 6]. It may be speculated that the future role of machine learning in MRI will be to extract clinically relevant informations at the time of image acquisition, almost obleviating the use of images in clinical practice.

References:

[1] Lundervold AS, Lundervold A. An overview of deep learning in medical imaging focusing on MRI. Zeitschrift für Medizinische Physik 29(2) pp 102–127 (2019)
[2] Litjens G, Kooi T, Ehteshami B, Arnaud B, Setio A, Ciompi F, Ghafoorian M, van der Laak J, van Ginneken B, Sánchez C. A survey on deep learning in medical image analysis. Med Image Anal 42:60–88 (2017)
[3] LeCun Y, Bengio Y, Hinton G. Deep learning. Nature vol. 521, pp.436–444 (2015)
[4] Ronneberger O, Fischer P, Brox T. UNet: Convolutional Networks for Biomedical Image Segmentation. Proc. MICCAI 2015, Springer LNCS 9351, pp. 234–241 (2015)
[5] Oksuz, I., Ruijsink, JB, Puyol Anton, E, Clough, JR, Lima da Cruz, GJ, Bustin, A, Prieto Vasquez, C, Botnar, RM, Rueckert, D, Schnabel, JA & King, A. P. Automatic CNN-based detection of cardiac MR motion artefacts using k-space data augmentation and curriculum learning. Med Image Anal 55:136–147 (2019).
[6] SmartHeart: Next-generation cardiovascular healthcare via integrated image acquisition, reconstruction, analysis and learning http://wp.doc.ic.ac.uk/smartheart/

I13.02

Collaboration of Academia and Industry in Machine Learning

F. Knoll
NYU, New York, UNITED STATES

Learning Objectives: Understand the challenges and opportunities of collaborations between academia and industry for Machine Learning in Radiology.
Understand possible collaboration models and boundary conditions than can lead to successful translational research.
Body: Medical imaging and radiology were identified as one of the predominant areas where artificial intelligence (AI) and Machine Learning (ML) are expected to play a major role in the future. In the past, the technological developments in this field were mainly driven by groups from academic research centers. However, during the last years, there has been a substantial increase of interest from industry in AI and ML. Countless startup companies are emerging in this field, fueled by enormous resources from venture capital and the global IT giants Google, Facebook, Apple, Amazon and Microsoft all have and continue to build up dedicated AI research departments now. In the field of radiology, this creates both unique challenges and opportunities. In order to perform successful translational ML research in radiology, company or industrial research lab requires a collaboration with a hospital or an academic medical center to have access to data, imaging science expert knowledge and a test platform to evaluate the performance of a method or a potential product. However, since the performed research is centered around patient data, in order for such a collaboration to be successful, it requires careful consideration of regulatory, legal and most important ethical principles.
In this talk, I will provide an overview of possible collaboration models and suggestions for boundary conditions that should be enforced. As an illustrative example, I will describe the ongoing collaboration between NYU Radiology and Facebook Artificial Intelligence Research (FAIR) in the field of accelerated MR data acquisition with Machine Learning [1, 2].

References:

1. Zbontar J, Knoll F, Sriram A, Muckley MJ, Bruno M, Defazio A, Parente M, Geras KJ, Katsnelson J, Chandarana H, Zhang Z, Drozdzal M, Romero A, Rabbat M, Vincent P, Pinkerton J, Wang D, Yakubova N, Owens E, Zitnick CL, Recht MP, Sodickson DK, Lui YW. fastMRI: a publicly available raw k-space and DICOM dataset for accelerated MR image reconstruction using machine learning. arXiv:1811.08839.
2. Knoll F, Muckley MJ, Zbontar J, Drozdzal M, Geras KJ, Yakubova N, Chandarana H, Lui YW, Sodickson DK, Zitnick CL, Recht MP. fastMRI: a publicly available raw k-space and DICOM dataset for accelerated MR image reconstruction using machine learning. Proceedings of the International Society for Magnetic Resonance in Medicine, p657 (2019).

I13.03

What is Needed to Get Machine Learning into Clinical Practice

M. Prokop

Radboudumc, Radiology and Nuclear Medicine, Nijmegen, The Netherlands

Learning Objectives: # To understand the current legal and regulatory issues of machine learning applications in radiology

To learn to which application areas of machine learning are ready for use and which require better integration into clinical workflow

To understand how performance issues of machine learning applications influence their integration into the clinical workflow

To learn how to chose which algorithms to use and when to wait for the next generation

Body: Machine learning is one of the technologies summarized under "artificial intelligence". It is a computer technology that is able to solve tasks without using explicit instructions. Applications can cover anything from automation of logistic tasks, image acquisition and reconstruction, image normalization, image segmentation, lesion detection and characterization and many more.

Implementation of machine learning techniques depends not only on the application area, the regulatory claim of the application and the performance of the algorithm but also on radiologist's acceptance, regulatory issues, workflow and payment issues.

Some applications such as machine-learning based image reconstruction for MR but also CT and other imaging techniques have already been implemented in many sites, often without knowing that the techniques are machine learning based. Applications that automate and streamline logistic tasks, such as hanging protocols for MR that are synchronized across scanners, or applications that prioritize exams for urgent reporting are starting to be used.

Image analysis applications, however, are more tricky: performance and workflow integration become the crucial issues. Radiologists are legally responsible, so they have to stay involved in the reporting and sign-off process but the ease with which output of the machine learning algorithms can be accepted, rejected or adapted will determine the success in practice. Loading times, processing times, speed and ease of interaction will determine user acceptance. Paying schemes are not yet sufficiently developed and depend on how much added value these systems provide in an environment where earning margins are under pressure and time is money.

Recent development such as deep learning have help to substantially improve performance of many applications, given large and diverse enough training data sets. Issues of how to judge performe as a user will be discussed.

References:

1: Mazurowski MA, et al. Deep learning in radiology: An overview of the concepts and a survey of the state of the art with focus on MRI. JMRI 2019;49(4):939–954.

2: Hyun CM, et al. Deep learning for undersampled MRI reconstruction. Phys Med Biol 2018;63(13):135007.

3: Liu F, et al. Deep Learning MR Imaging-based Attenuation Correction for PET/MR Imaging. Radiology 2018;286(2):676–684.

S09 Scientific Session

10:50–12:20 *Room 1 - Willem Burger Zaal*

Machine Learning in MRI

S09.02

In silico proof-of-principle for reproducible brain tumor predictions on individual NMR voxels based on endogenous microvascular susceptibility effects using support vector machine classification

A. Hahn[1], J. Bode[2], S. Schuhegger[3], V. J. F. Sturm[1], M. O. Breckwoldt[1], S. Heiland[1], C. H. Ziener[4], M. Bendszus[1], F. T. Kurz[1]

[1]*Heidelberg University Hospital, Department of Neuroradiology, Heidelberg, Germany,* [2]*German Cancer Research Center (DKFZ), Schaller Research Group, Molecular Mechanisms of Tumor Invasion, Heidelberg, Germany,* [3]*University of Heidelberg, Department of Physics and Astronomy, Heidelberg, Germany,* [4]*German Cancer Research Center (DKFZ), Department of Radiology E010, Heidelberg, Germany*

Purpose/Introduction: Malignant tumors like glioblastoma multiforme remodel microvasculature during growth. Changes to the magnetically susceptible vasculature collectively influence the T_2*-relaxation within NMR voxels [1]. By isolating the vascular susceptibility and diffusion hindering effects within virtual NMR voxels, we test the possibility of learning abstract classifying contrasts using statistical machine learning.

Subjects and Methods: We imaged the entire brain's microvasculature in n = 3 healthy NMRI nu/nu nude mice; n = 6 such mice with U87 glioblastoma xenografts, 3 weeks after tumor cell implantation; and n = 6 NOD Scid Gamma mice with GL261 glioblastoma, 4 weeks post implantation, using fluorescence light sheet microscopy (Ultramicroscope II, LaVision Biotec) after optical tissue clearing [2]. The vasculature was segmented in 3D using ilastik [3], noise filtered in Matlab (Mathworks), and used to determine local Larmor frequency distortions from the paramagnetic deoxyhemoglobin within the blood [4] (simplified with constant composition and oxygenation of 60% [5]). Cubic subvolumes with 100, 200, 300, and 400 µm side length were extracted from tumors and healthy brain tissue to simulate spin dephasing during FID with diffusion at D = 1 μm^2/ms with random walks in C ++11, at field strength B_0 = 3 Tesla in time steps of dt = 0.1 ms up to t = 1 s. The attenuation was parametrized with exponential fits, assuming linear (t), quadratic (t^2), and monomial (t^b) time dependence in the exponent; for the full decay, short-time signal ($t < 200$ ms), and long-time regime ($t > 200$ ms). Support vector machines were trained to predict the tissue type of a virtual voxel signal based on the fit variables using LibSVM [6]. We tested prediction accuracies on signals simulated exclusively from a mouse previously not used for training.

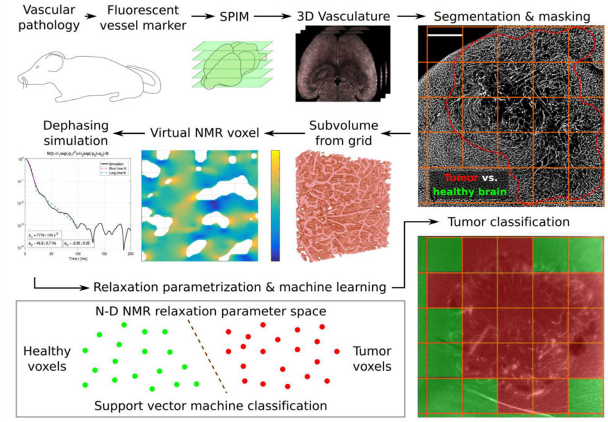

Workflow diagram, presenting the image acquisition using single plane illumination microscopy (SPIM) upon Lectin-FITC labeling of vessel lumen and tissue clearing. The segmented vessel data is partitioned to simulate spin dephasing during F

Results: U87 glioblastoma could be identified against healthy tissue from all brain regions with stable accuracies above 75% with as little as 20 training decays from each group, with rising trends for increasing training set sizes (Fig. 2). The more angiogenic GL261 tumors could be classified correctly with stable accuracies above 90% with 300 and 400 µm virtual voxels (Fig. 3). Our fully reproducible results with small training cohorts show that high prediction accuracies can be achieved with feasible training sizes, which presents a successful proof-of-concept.

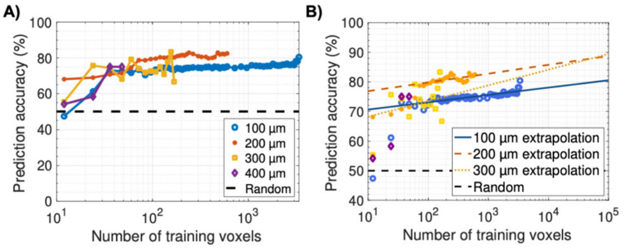

Prediction accuracy with different NMR voxel dimensions for healthy brain vs. U87 tumor classification, with A) original testing data, and B) extrapolations to the steady regime, assuming approximately y(x) = a*log(x)+b with x ≥ 72 training signals.

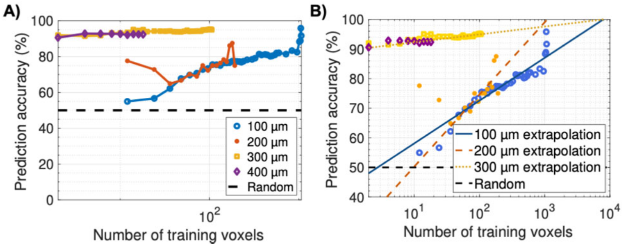

Prediction accuracies for healthy tissue vs. GL261 tumor classification. Panel A) shows original testing data and panel B) includes extrapolations with y(x) = a*log(x)+b and fitting with x ≥ 36 training signals.

Discussion/Conclusion: We affirm the feasibility of learning abstract contrast for brain tumor classification on single-voxel FID-signals based on endogenous, static BOLD effects. Our results motivate experimental analogies with tailored pulse sequences to sample relevant echo time regimes, which can be found with the toolset presented here.

References:

1. J Magn Reson 2001;151:107–117.
2. Front Neurosci 2019;12:1004.
3. IEEE Int Symp Biomed Imaging 2011.
4. Neuroimage 2008;40:1130–1143.
5. Magn Reson Med 2001;45:533–42.
6. ACM Trans Instell Technol 2011;2:27:1–27.

S09.03

Classification of Crohn’s disease in terminal ileum based on cine magnetic resonance enterography at 3T

B. Bayrambas[1], G. H. Hatay[1], E. Ozturk-Isik[1], O. Algin[2]
[1]Bogazici University/Biomedical Engineering Institute, Istanbul, TURKEY, [2]Bilkent University, National MR Research Center (UMRAM), Ankara, TURKEY

Purpose/Introduction: Crohn’s disease is an inflammatory bowel disease mostly affecting terminal ileum of small bowel. It has a lifelong negative impact on patients’ digestive tract. Generally, Crohn’s disease causes decrease in motility and increase in mural thickness in the affected segment. The purpose of this study is to classify the patients’ terminal ileum as healthy or diseased with machine learning algorithms based on magnetic resonance enterography (MRE) [1] and compare the results with the radiologist’s final decision.

Subjects and Methods: Dynamic cine MRI was acquired by a 2D coronal plane balanced-SSFP sequence (True-FISP/Siemens) using a standard body matrix coil at a 3T MR scanner (Siemens Skyra). An experienced radiologist marked terminal ileum as a region of interest in each dynamic MRI series. Cine MRE of 166 patients (101 male, 65 female, age: 15–63) were used for assessment. Terminal ileum of 79 of these patients were defined as diseased and 87 of them were defined as healthy by the radiologist. The motility of these ROIs were quantified in MATLAB (MathWorks, Inc., Natick, MA) with two different algorithms, which were optical flow analysis (OF) [2] and a gradient based analysis (GBA) (Fig. 1). OF algorithm calculates velocity vectors, whose magnitude gives OF motility metric, based on in-plane pixel brightness [3]. Mean gradients representing change in pixel intensities at each dynamic series were calculated as a measure of gradient based motility. The radiologists’ decision was taken as the gold standard.

The association between the motility metrics was assessed by using a Spearman rank correlation test. The dataset was randomly divided into two groups as training (130 patients) and test (36 patients) sets. OF and GBA motility metrics along with the mural thickness were used to train two separate classification models. A linear support vector machine (SVM) algorithm with 5 fold-cross validation was trained. The classification algorithm was run on different test sets 100 times and the mean performance measures were calculated.

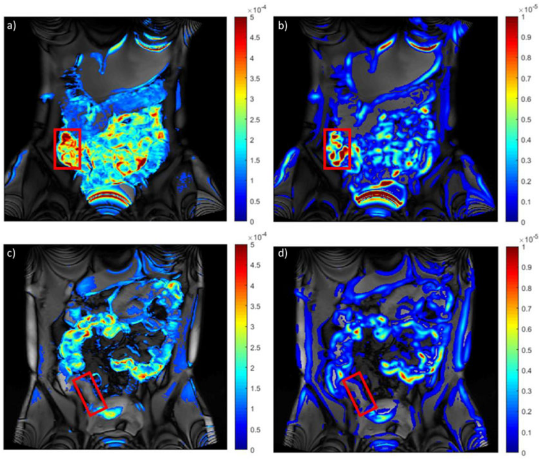

Figure 1: GBA (a,c) and OF (b,d) motility maps of a healthy (top) and a diseased (bottom) volunteer showing terminal ileum with marked ROIs.

Results: OF and GBA motility features were highly correlated ($r = 0.91$, $P < 0.001$). Crohn’s disease was classified with 92.8% (sens = 88.6%, spec = 95.5%) and 93.4% (sens = 89.5%, spec = 96.0%) accuracies based on OF and GBA motility metrics along with the mural thickness, respectively (Table 1). The specificity values were slightly higher due to data imbalance in test datasets.

Feature	Accuracy (%)	Sensitivity (%)	Specificity (%)
Mural thickness and OF motility	92.8 ±3.9 (83.3-100.0)	88.6 ± 6.6 (71.9-99.5)	95.5 ± 3.8 (81.9-99.6)
Mural thickness and GBA motility	93.4 ± 3.6 (83.3-100.0)	89.5 ± 6.9 (68.8-99.6)	96.0 ± 3.3 (86.9-99.6)

Table 1: Mean accuracy, sensitivity and specificity values of linear SVM algorithm according to test set predictions.

Discussion/Conclusion: Crohn’s disease was classified with a high accuracy based on OF or GBA motility metrics together with mural thickness. A semi-automated tool including supervised machine learning algorithms could be useful for assisting radiologists in Crohn’s disease assessment based on MRE.

References:

[1] Mantarro, et al. WJR, 2017. 2017. **9**(2): 46–54
[2] Hahnemann, et al. JMRI, 2015. **41**(2): 354–60
[3] Horn, et al. AI, 1981. **17**(1–3): 185–203

S09.04

Deep learning for 3D MR fingerprinting: a dual pathway parameter mapping and reconstruction approach

I. Horvath[1], C. M. Pirkl[1], G. Buonincontri[2], M. I. Menzel[3], P. A. Gómez[1], B. H. Menze[1]
[1]Technical University of Munich, Informatics, Garching, GERMANY, [2]IRCCS Fondazione Stella Maris, Pisa, ITALY, [3]GE Healthcare Global Research, Munich, GERMANY

Purpose/Introduction: The signature element of MR Fingerprinting (MRF), the matching of acquired signal evolutions to a precomputed dictionary, has proven to allow reliable and accurate parameter quantification. Its heavy memory and computational requirements, however, make it very inefficient. Compression algorithms[1] and deep learning approaches[2] have hence emerged to accelerate MRF reconstruction. Inspired by their success, we address the inherent limitation of MRF by proposing a hybrid neural network architecture which is capable of:

- Efficiently compressing the MRF data in the time domain.
- Reliably inferring T1 and T2 estimates.
- Recovering artefact-free MRF image time-series.

Subjects and Methods: With its dual pathway design (Fig. 1), the model recovers information from images corrupted by spatial aliasing to learn the non-linear relationship between the temporal evolution of the MRF signal as input, and the T1 and T2 output parameters, whilst also providing artifact-free signal time-series.

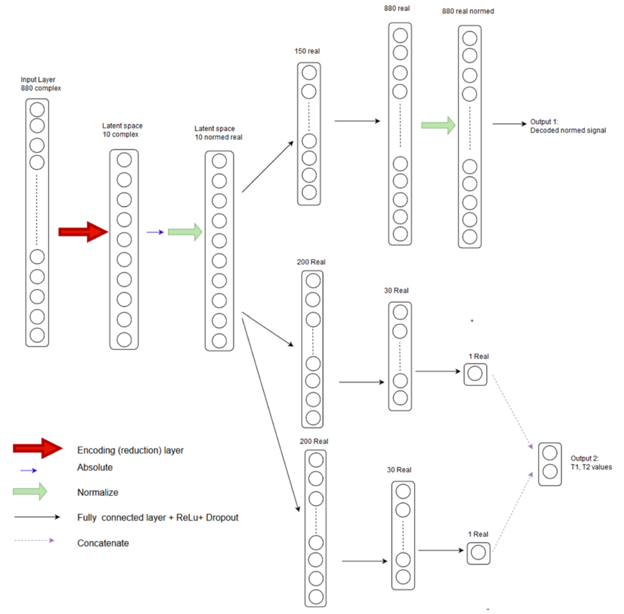

The network receives the complex MRF signal as input and outputs T1 and T2 estimates together with the artifact-free signal curve. It has a linear encoding layer followed by a dual pathway for simultaneous parameter prediction and signal recovery.

We created a dataset of synthetic MRF signals[3] for ranges of T1 = [100:20:4000]ms and T2 = [20:4:600]ms to train our network and to obtain a dictionary matching (DM) reference. The model was trained using ReLU activation and L1 loss for parameter estimation and L2 loss for the signal recovery pathway.

We validated our method on 3D MRF scans of a phantom and a healthy volunteer (f, 27 years), after obtaining informed consent in compliance with the German Act on Medical Devices.

The 3D MRF acquisition (3T MR750w system, GE Healthcare, 32-ch receive-only head RF coil) is based on the following schedule: after an initial, adiabatic inversion (TI = 18 ms), flip angles ($0.8° \leq$ FA $\leq 70°$) are applied in a ramp-up/down pattern with TR/TE = 12 ms/ 1.8 ms and 880 repetitions. Data was acquired using 3D spiral projection sampling[4] (55 in-plane, 880 through-plane rotations) with $19.2 \times 19.2 \times 19.2\ \text{cm}^3$ FOV and $0.96 \times 0.96 \times 0.96\ \text{mm}^3$ isotropic resolution.

As the network's first layer is a linear projection, we can apply the dimensionality reduction directly on the k-space data prior the (linear) Fourier transform to accelerate image reconstruction.

Results: For both phantom and in vivo scans, T1 and T2 network predictions agree well with conventional DM estimates (Fig. 2). For high relaxation times, predicted values are below the DM result. Also, the reconstructed image time-series correspond with the matched dictionary entries (Fig. 3).

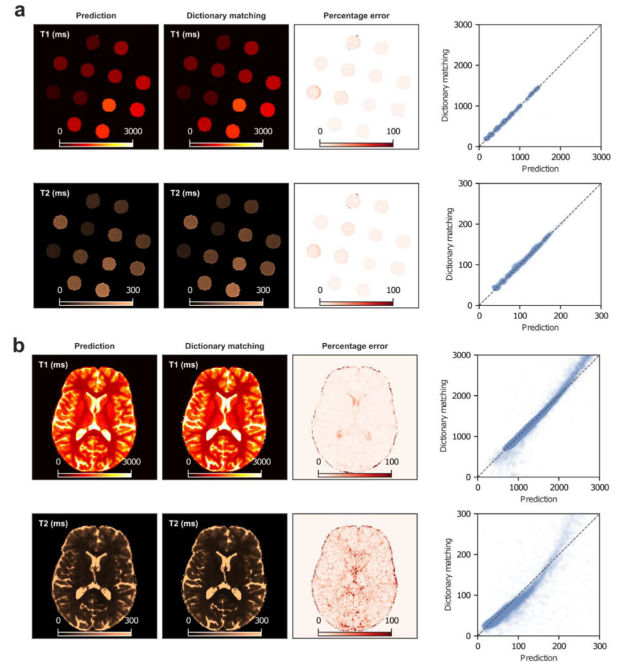

For phantom (a) and in-vivo (b) MRF acquisitions, our network achieves a prediction quality comparable to state-of-the-art DM. For high relaxation times in CSF, predicted T1 and T2 values are below the DM estimates.

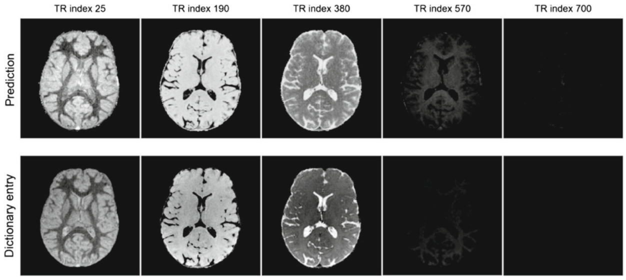

Representative MRF images along the acquisition train. Both network prediction and dictionary entry do not show visual artifacts, providing good image quality.

Discussion/Conclusion: We propose a flexible deep learning framework which synchronizes dimension reduction and parameter estimation to accelerate MRF in two ways: (1) We speed up MRF image reconstruction and (2) efficiently infer T1 and T2 parameters with significantly reduced computation times and resources compared to state-of-the-art DM.

References:

1. McGivney DF et al. *IEEE TMI*. 2014;33:2311–2322.
2. Cohen O et al. *Magn. Reson. Med.* 2018;80(3):885–894.
3. Weigel M. *J. Magn. Reson. Imaging JMRI*. 2015;41(2):266–295.
4. Cao X et al. *Magn Reson Med*. 2019;00:1–13.

S09.05

A deep learning approach to T1 mapping in quantitative MRI

E. Ribeiro Sabidussi[1], M. Nicastro[2], S. Bazrafkan[2], Q. Beirinckx[2], B. Jeurissen[2], A. J. den Dekker[2], S. Klein[1], D. H. J. Poot[1]
[1]Erasmus Medical Center, Biomedical Imaging Group Rotterdam, Department of Radiology and Medical Informatics, Rotterdam, NETHERLANDS, [2]University of Antwerp, imec, Visionlab, Department of Physics, Antwerp, BELGIUM

Purpose/Introduction: Quantitative MRI aims to measure biophysical tissue parameters through the analysis of the MR signal[1]. Conventional parameter estimation methods, which often rely on a voxel-wise mapping, ignores spatial redundancies. In this work, a deep learning method for *T1* mapping is proposed to overcome this limitation.

Subjects and Methods: In an Inversion Recovery (IR) experiment the observed signal intensity at each voxel is given by the parametric model:

$f_n\ (A, B, T1) = \mathrm{I}\ A + B\ \mathrm{e}(TI_n/T1)\ \mathrm{I},\ \mathrm{n} = 1, \ldots, \mathrm{N},$ (1)

where $[\mathrm{TI}_n]^{N}_{n=1}$ are the inversion times, *T1* the voxel-wise longitudinal relaxation and *A* and *B* are parameters linked to proton density (PD), inversion efficiency and other machine related constants[2].

We propose to use a ResNet[3] (Fig. 1) to directly predict *T1*, *A* and *B* maps given *N* T1-weighted (T1w) images from an IR experiment. To train and evaluate the network, 2600 pairs of ground-truth (GT) maps and *N* T1w images were created. Each GT map was built by assigning *T1* and PD values[4] to 2600 axial brain slices, extracted from 20 anatomical models (Brainweb database[5]). *A* and *B* maps were set to PD and $-(k)\cdot$PD, respectively, where $k \sim N(2.0, 0.04)$ encodes uncertainties of flip angles to each slice. Similarly, *T1* and PD values changed per slice according to their reported variability[4].

From each GT set, 10 IR T1w were generated via Eq.1, with 10 *TI* values logarithmically spaced, ranging from 50 ms to 8500 ms. Training, validation and testing subsets were created with 1300, 650 and 650 samples, respectively. At each training epoch, samples were corrupted by rotations (0.0 ± 1.0)°, translations (0.0 ± 1.5)px and Gaussian noise (SNR varying from 3 to 100).

The performance of the network was assessed via its RMSE and standard deviation (STD) levels through 20-fold repeated experiments for each noise level. Additionally, the error bias and STD of our results were compared to a voxel-wise iterative maximum likelihood (MLE) method on 100 noise realizations, SNR = 10, of a single slice.

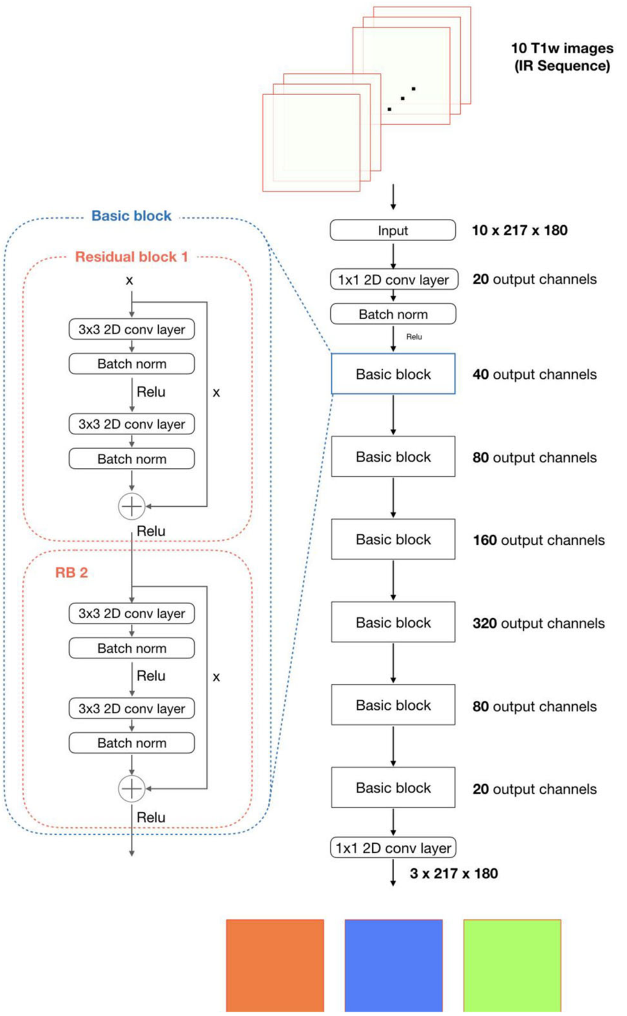

Results: Our estimator achieved low T1 RMSE even at SNR = 10(0.11 ± 0.011)s (Fig. 2.a). The high inference precision is demonstrated in Fig. 2.b, where low T1 STD values are reported for SNR > 10. Figure 3 shows that the ResNet presented outperforms a conventional *T1* mapping method in terms of bias and STD.

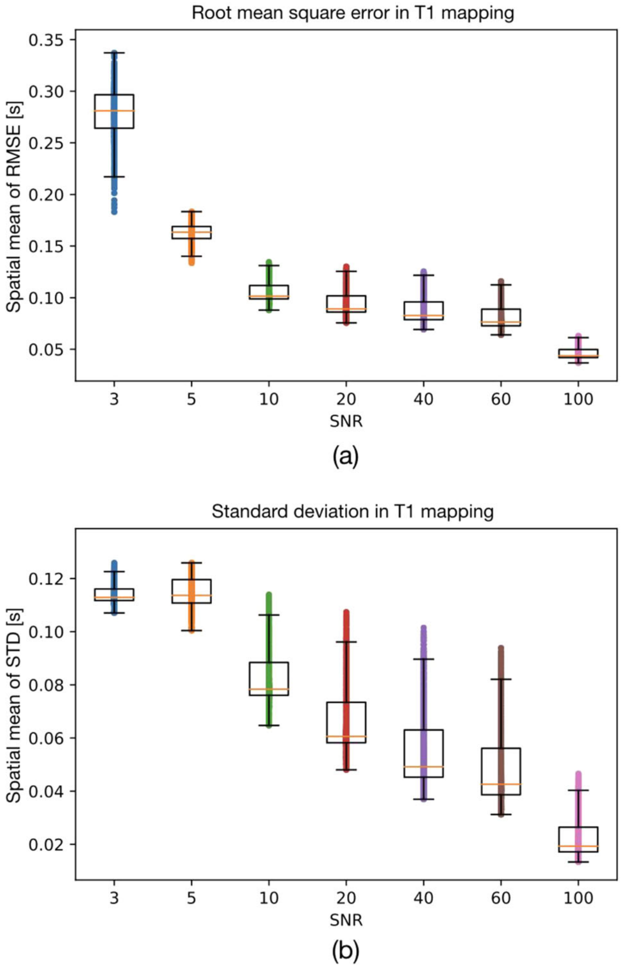

ResNet RMSE (a) and SD (b) for T1 mapping in testing subset. RMSE and SD were calculated via the spatial mean of a 20-fold repeated Monte Carlo simulation at each SNR level.

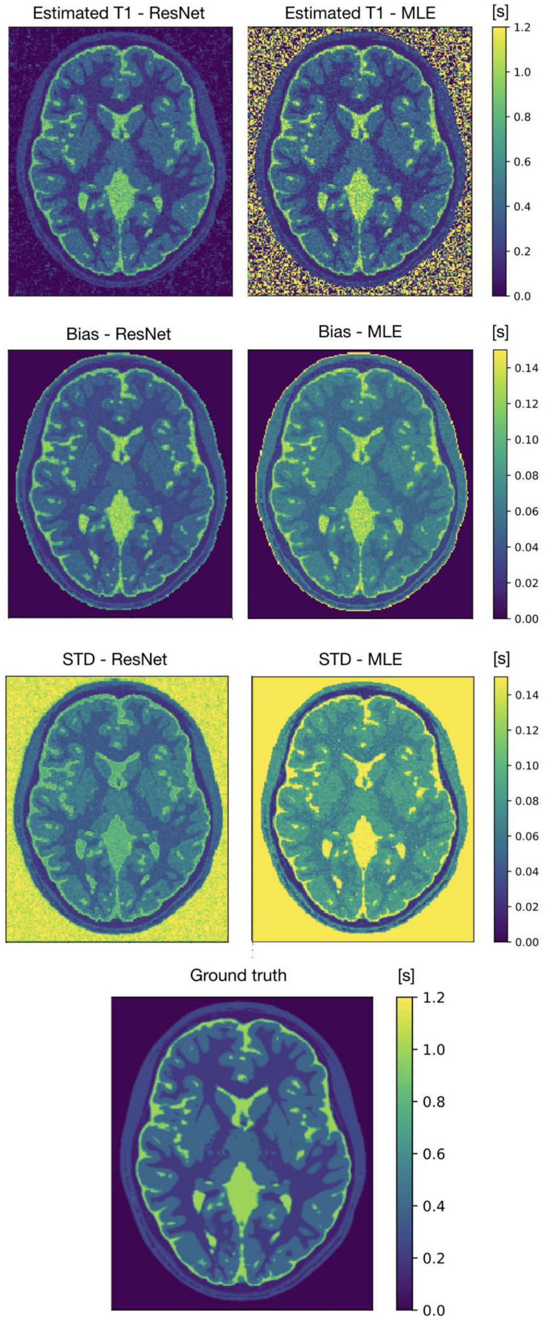

T1 Bias and standard deviation maps for the ResNet and MLE estimator. 100-fold repetition of a single slice. IR sequences were corrupted by Gaussian noise with SNR=10.

Discussion/Conclusion: In this work, we proposed a ResNet architecture for *T1* mapping and demonstrated its superior precision performance over a conventional method. The results indicate that our estimator is capable of predicting *T1* maps with high precision and low error, while taking only a small fraction of the inference time used by the MLE algorithm (0.7 s and 50 s per slice, respectively).

References:

1. P. Tofts, New York, NY, USA: Wiley, 2004.
2. J.K. Barral et al., MRM, 2010, 64:1057–1067.
3. H. Kaiming et al., IEEE CVPR, 2016, 770–778.
4. G.E. Gold et al., Am. J. Roentgenol., 2004, 183:343–351.
5. R.K.S. Kwan et al., IEEE TMI, 1999, 18:1085–97—https://mcgill.ca/bic.

S09.06

MRI zero: fully automated invention of MRI sequences using supervised learning

A. Loktyushin[1], K. Herz[2], F. Glang[2], B. Schölkopf[3], K. Scheffler[2], M. Zaiss[2]
[1]Max Planck Institute for Biological Cybernetics, High-field Magnetic Resonance, Tübingen, GERMANY, [2]Max Planck Institute for Biological Cybernetics, Tübingen, GERMANY, [3]Max Planck Institute for Intelligent Systems, Tübingen, GERMANY

Purpose/Introduction: We present a supervised learning approach to automatically generate MR sequences and corresponding reconstruction from scratch without providing sequence programming rules. New framework is tested in human brain measurement at 3T.

Subjects and Methods: The entire scanning and reconstruction process is simulated end-to-end as a fully differentiable concatenated sequence of tensor operations. Each tensor operation from the stack implements: RF events (RFE) (i.e. flip angles and phases), gradient moment events (GME) in x and y, delay times, and a weighting for an ADC, acting on the input model spin system (given in terms of PD, T1 and T2, and ΔB0). At the sequence learning step, we use Adam[1] optimizer to find the sequence parameters given the loss function specified with respect to data fidelity and SAR cost terms.

Task and target

We evaluate the proposed method on a simple task: match a target GRE-derived image by optimizing the gradients and flip angles and putting a penalty on SAR. Target sequence details: transient RF- and gradient-spoiled gradient echo readout with linear phase encoding, $24 \times 24/48 \times 48$, TR/TE/FA = 20 ms/3 ms/5°. Low FA decreases image blurring. As task sequences we used the same timing pattern and ADC as the target sequence, where for gradients and flip angles we approached four different tasks:

Task 1: clone target GME and RFE, optimize only RFE with SAR penalty

Task 2: clone target RFE, set GME to 0, optimize GME only

Task 3: set RFE and GME to 0, optimize both RFE and GME

Task 4: set RFE and GME to 0, optimize both RFE and GME with SAR penalty

Results: The result of task 1 displayed in Fig. 1a–e shows that the optimizer prefers to lower flip angles in the outer k-space lines to reduce SAR by 40% keeping a small image error. Figure 1f–j shows how spatial encoding is learned from scratch (Task 2). Figure 2a–c shows that when learning both RFE and GME, too high flip angles are chosen (Task 3). This can be mitigated by putting an additional penalty on SAR. Figure 3c–e shows the full potential of MRI zero: the invention of a complete MRI sequence (Task 4) that is applicable to image acquisition at a real system (3T Siemens, Prisma) in phantoms and in vivo (Fig. 3).

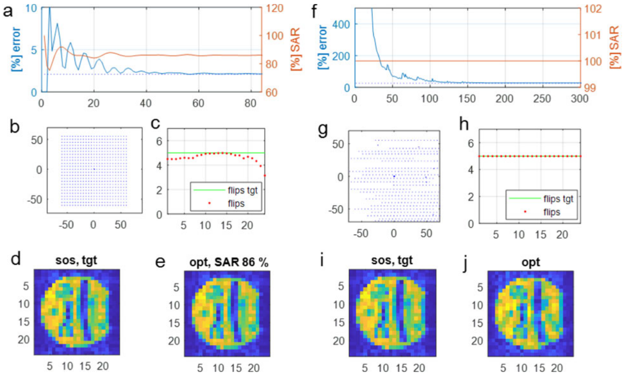

Fig1. Task 1, (f-j) Task 4. a,f: Training error curves and SAR over iterations. b,g: k-space sample locations at the last iteration. c,h: flip angles (red) compared to target flip angles (green). (d,i) target images, (e,j) invented sequence images.

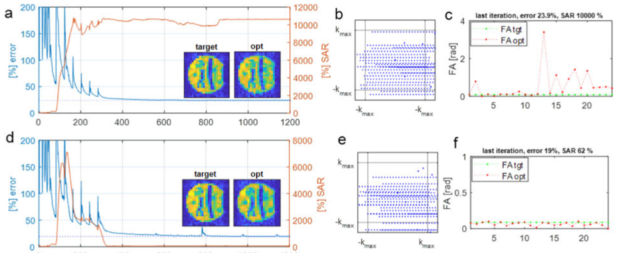

Fig2. First row: Task 3, second row: Task 4. a,d: Training error curves and SAR over iterations. b,e: k-space sampling at the last iteration. c,f: flip angles at the last iteration (red) compared to target flip angles (green).

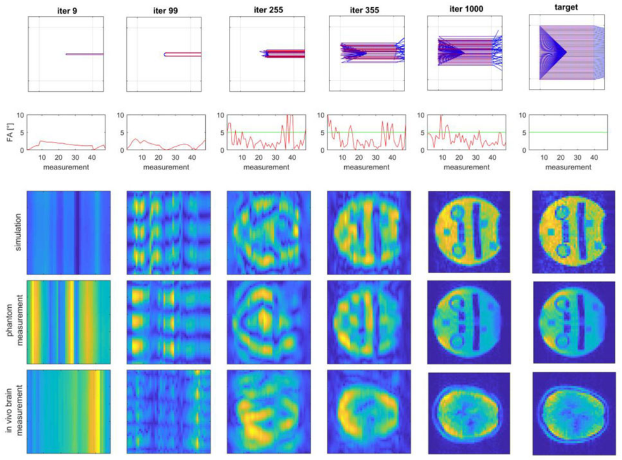

Fig3. Row 1: training error curve, Row 2: k-space sampling at different iterations, Row 3: flip angles over measurement repetitions. Row 4: simulation-based reconstruction. row 5: phantom scan, row 6: in vivo brain scan. GIF: tinyurl.com/y4z9qlhz

Discussion/Conclusion: We have developed a fully automated MRI sequence generator based on the Bloch equation simulations and supervised learning. While we focus on basic image generation herein, having such a tool at hand paves the way to a novel way of generating optimal MR sequence and reconstruction solely governed by the target provided, which could be a certain MR image, but the possibilities for targets are limitless, e.g. quantification, activation, segmentation or contrasts of other image modalities.

Acknowledgements: M. Zaitsev for PULSEQ codes (pulseq.github.io). MPG, DFG: ZA 814/2-1. EU Horizon 2020 (667510).

References:
[1] Kingma, Diederik P., and Jimmy Ba. "Adam: A method for stochastic optimization." arXiv:1412.6980 (2014).

S09.07

Efficient and robust reconstruction using the recurrent inference machine

D. Karkalousos[1], K. Lønning[2], S. O. Dumoulin[1], J.-J. Sonke[2], M. W. Caan[3]
[1]*Spinoze Centre for Neuroimaging, Amsterdam, NETHERLANDS,*
[2]*Netherlands Cancer Institute, Amsterdam, NETHERLANDS,*
[3]*Amsterdam UMC, Biomedical Engineering & Physics, Amsterdam, NETHERLANDS*

Purpose/Introduction: Deep-learning based image reconstruction accelerates both acquisition and reconstruction time beyond what is currently possible. Recurrent Inference Machines (RIMs) generalize to heterogeneous imaging conditions [1]. Here we propose to gain efficiency in the RIM using a more lenient network architecture in reconstructing images unseen during training. Furthermore we assess the robustness in reconstructing data with varying types of undersampling patterns.

Subjects and Methods: RIMs reconstruct iteratively, enabling the model to evaluate its own estimate of a prior distribution gradient with respect to this reconstruction state. The log-likelihood is known analytically from the MR-data acquisition process, and its gradient with respect to the current reconstruction is given explicitly as another input. Hereby, the model learns to find a reconstruction in agreement with the maximum a posteriori objective. The recurrent unit consists of three convolutional layers interleaved by two Recurrent Units. In addition to the Gated Recurrent Unit (GRU) [Cho] [3], the Minimally Gated Unit (MGU) [4] and Independently RNN (IndRNN) [5], were used as potentially more efficient units (Fig. 1). We used the l1-norm averaged over 8 recurrent steps as a loss function.

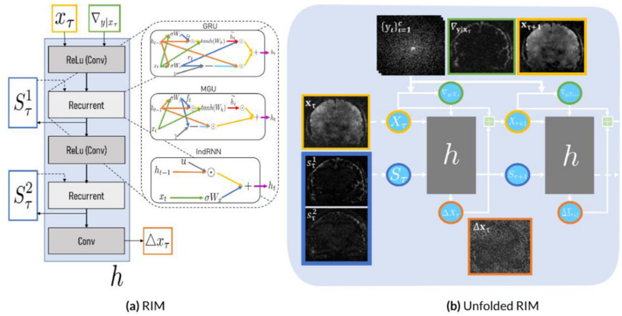

(a) RIM (b) Unfolded RIM

The Recurrent Inference Machine with different configurations, i.e. Gated Recurrent Unit (GRU), Minimally Gated Unit (MGU) and Independent Recurrent Neural Network (RNN)

Three types of multi-coil raw data of 12 subjects were used for training: 1.0 mm T1w brain scans at Philips 3T, 0.7 mm T2*w multi-echo brain scans at Philips 7T, and 0.6 mm T2w TSE knee scans [2]. For validation, a 12-times prospectively undersampled 1.0 mm T2w brain scan was acquired. Two subjects were used for validation and testing, and the remaining subjects for training.

We trained 4 RIMs on each modality separately, and on joint data with equal sampling from the three modalities. The models to evaluate were selected on the validation sets, and then cross-evaluated on the test set. The Structural Similarity (SSIM) was used as a metric. For training, random undersampling patterns were applied. To test for robustness of the RIM to variable types of patterns and texture not seen during training, an image with text superimposed on the tissue was synthesized and undersampling with random, period grid and pseudo-radial undersampling patterns.

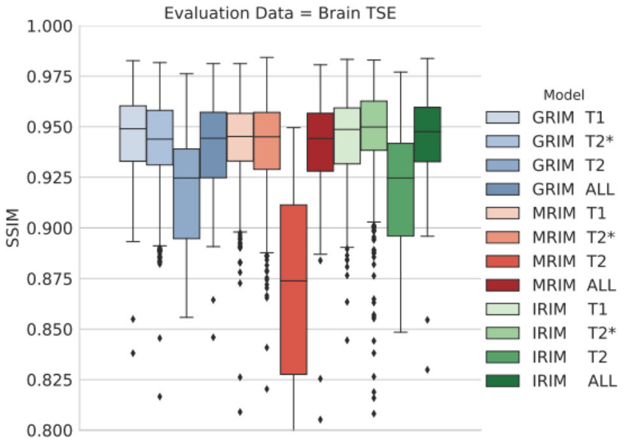

Structural Similarity of different network infrastructures, trained on separate and all data modalities, evaluated on 8-fold accelerated brain TSE.

Results: The MRIM performed worst, especially for T2w (Fig. 2). The model trained on T2*w had more negative outliers. Training on all data does not increase the SSIM compared to training on one modality. The RIM can successfully reconstruct textures unseen during training, and data undersampled in different manners than during training (Fig. 3). Randomly undersampled data results in minimal aliasing noise. Prospectively acquired T2w-data can be succesfully reconstructed.

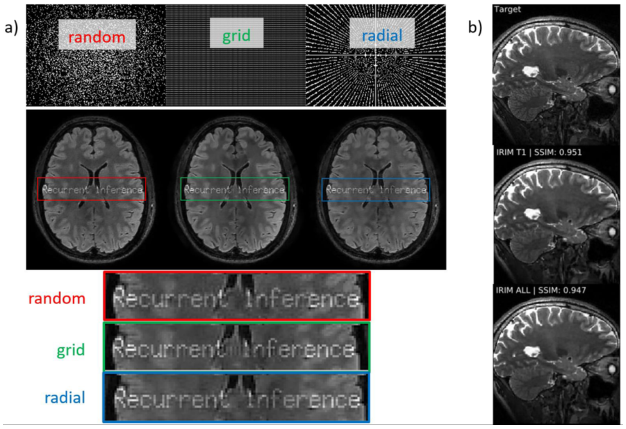

Left: varying sampling patterns, and reconstruction results of texture unseen during training. Right: reconstructed prospectively undersampled TSE (12x).

Discussion/Conclusion: The RIM with IndRNN recurrency enables efficient reconstruction, and is robust against varying texture, contrast and undersampling pattern.

References:
[1] Lonning, 2019
[2] Epperson, 2013
[3] Cho, 2014
[4] Zhou, 2016
[5] Li, 2018

S09.08

Can a Convolutional Neural Network reduce the Measurement Time for ^{23}Na Quantification?

A. Adlung[1], N. Paschke[1], A.-K. Schnurr[1], E. Neumaier Probst[2], S. Mohamed[2], M. Samartzi[3], M. Fatar[3], L. R. Schad[1]
[1]Computer Assisted Clinical Medicine, Medical Faculty Mannheim, Heidelberg University, Mannheim, GERMANY, [2]Department of Neuroradiology, University Medical Center and Medical Faculty Mannheim, Heidelberg University, Mannheim, GERMANY, [3]Department of Neurology, University Medical Center and Medical Faculty Mannheim, Heidelberg University, Mannheim, GERMANY

Purpose/Introduction: Quantitative ^{23}Na MRI is a biomarker for essential physiological processes such as ischemic stroke [1] but suffers from long measurement time. In this work, we used a Convolutional Neural Network (CNN) to generate quantifiable ^{23}Na MR images from strongly undersampled data.

Subjects and Methods: We included ^{23}Na MR brain acquisitions from 25 stroke patients (76.6 ± 10.3 years, 15 female) in this study. The images were acquired with a 3T MRI (MAGNETOM Trio, Siemens Healthineers, Erlangen, Germany) and a bird-cage dual-tuned ^{23}Na/^{1}H head coil (Rapid Biomedical, Rimpar, Germany) using a 3D radial density-weighted sequence [2] with a protocol described previously [1]. The measurement time of the quantitative ^{23}Na MRI amounted to 10 min per dataset.

Reconstruction was done in MATLAB (The MathWorks, Inc., Natticks, USA) with a convolution-based regridding algorithm (Kaiser Bessel, width = 4) and application of a Hanning filter in k-space. The full image (FI) included 6000 projections for the reconstruction and the undersampled image (UI) included 1500 projections. Images were reconstructed in 3D with a zero-filling factor of two, resulting in a 120 × 120 × 120voxel image (Fig. 1). UI estimates an image that could have been acquired with a recording time of 2.5 min.

A CNN with extended U-Net Architecture has been implemented in Python 3.5 using Tensorflow 1.10. The CNN was trained to predict FI with UI as input.

The configuration of the CNN was: Four encoding and four decoding stages, each stage consisting of 2 to 3 convolutional layers. The batch size was 8; the patch size was set to 64 × 64voxel. Training ran 20 epochs with a learning rate of 0.001 and the Adam optimizer (Fig. 2). We compared loss functions L1 (absolute difference) and L2 (mean squared error), generating the output images CNN L1 and CNN L2 (Fig. 1). Our data was split into 20 training and 5 test cases, from each case 50 slices were considered. We used the structural similarity index (SSIM) and the Signal-to-Noise Ratio (SNR) for evaluation.

Results: SSIM of CNN L1 and CNN L2 in reference to FI were similar to each other (both Ø = 0.9026) but higher than SSIM of UI (Ø = 0.8813). The SNR of UI was around 50% the SNR of FI, both CNNs gain SNR (Table 1). It proved an increased image quality for CNN generated images with both loss functions (Fig. 1a), and the line plot in Fig. 1b shows the development of the differences in signal intensity.

Discussion/Conclusion: SSIM and SNR values indicated increased image quality and structural similarity to FI for the CNN images. Both loss functions yielded similar good results and will thus be further investigated. Our CNNs were able to reduce the amount of necessary acquired data while preserving the sodium quantification.

	01	02	03	04	05
SSIM (UI,FI)	0.8859	0.8575	0.9071	0.8385	0.9174
SSIM(CNN L1, FI)	0.9112 (+2.9%)	0.8724 (+1.7%)	0.9250 (+2.0%)	0.8594 (2.5%)	0.9448 (+3.0%)
SSIM(CNN L2, FI)	0.9091 (+2.6%)	0.8765 (+2.2%)	0.9247 (+1.9%)	0.8597 (+2.5%)	0.9430 (+2.8%)
SNR FI	20.67	19.91	24.37	19.64	23.49
SNR UI	10.11	9.65	11.47	9.47	11.31
SNR CNN L1	27.68	33.51	34.11	30.01	35.06
SNR CNN L2	33.93	39.09	43.58	29.71	41.36

Table 1: Evaluation of the test images 01 to 05. Comparison of CNN L1 and CNN L2 to FI and UI by calculating SNR and SSIM to FI in absolute values as well as the relative change to UI.

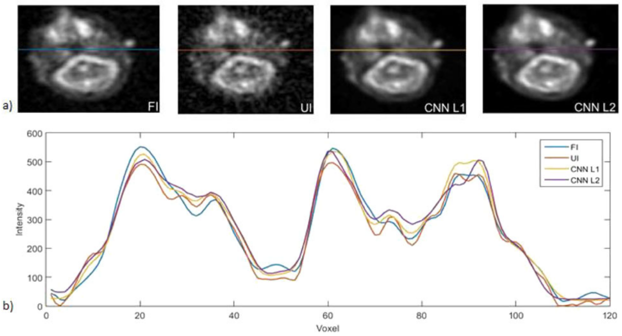

Fig.1: One slice of the four different versions of test image 02. a) Showing the different image qualities b) Line plot for the images in a) (location marked by colored line). Illustrating the signal intensity over the 120voxel length of the images.

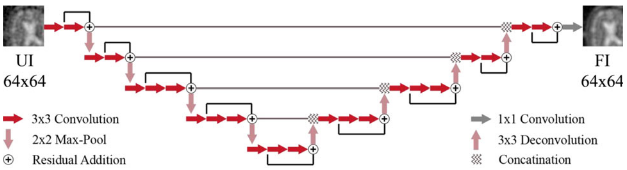

Fig.2: CNN with extended U-Net Architecture showing the Input (left) and the Label (right), as well as the different encoding and decoding stages of the network and their connections.

References:

The project was funded by Dietmar Hopp Stiftung GmbH "Na-MRI for acute stroke" 23014019.

[1] Neumaier-Probst, et al. (2015). Int J Stroke 10:56–61.
[2] Nagel, et al. (2009). *MRM* 62.6: 1565–1573.

S09.09

Adversarial inpainting of MR images using deep adversarial networks

K. Armanious[1], **T. Küstner**[2], B. Yang[1], S. Gatidis[3]
[1]University of Stuttgart, Institute of Signal Processing and System Theory, Stuttgart, GERMANY, [2]King's College London, Biomedical Engineering Department, London, UNITED KINGDOM, [3]University Hospital of Tübingen, Department of Radiology, Tübingen, GERMANY

Purpose/Introduction: Partial distortions is a common phenomenon in MR images due to various reasons such as localized perturbations resulting from metallic implants. In this work, we propose a new deep adversarial framework for the inpainting of partially deteriorated or in-complete MR images. The aim is to realistically inpaint missing information in MR scans to fit homogeneously in the given surrounding region. This is of interest for further image analysis tasks, such as PET/MRI attenuation correction.

Subjects and Methods: In this work, we propose a new framework based on adversarial networks for the inpainting of missing regions in MR images. The framework, referred to as ip-MedGAN, consists of three deep convolutional neural networks.

First, the CasNET generator, consisting of multiple U-nets, receives as input an MR image with randomly cropped out squared region of size 1/16 of the original image area. The generator is trained to inpaint the missing regions via two discriminator networks.

The global discriminator (GD) receives as inputs the inpainted output by the generator and the complete ground truth MR image. GD calculates the adversarial loss function and an additional non-adversarial perceptual loss to guide the generator to inpaint the missing regions in a globally homogeneous manner with respect to the given context information. The local discriminator (LD) only receives as inputs the inpainted region by the generator and the corresponding ground truth target region instead of the entire images. By focusing on smaller regions, the LD guides the generator to inpaint higher quality details.

To evaluate the performance of the proposed framework, an anonymized dataset of T2-weighted (FLAIR) MR scans from the head region was collected from 44 volunteers. MR data from 30 volunteers were used for training with the remaining 14 volunteers for validation. All scans were resampled to 1 × 1 × 1 mm^3 and normalized to a range of 0 to 1. Subsequently, 2-dimensional slices of matrix size 256 × 256 pixels were extracted.

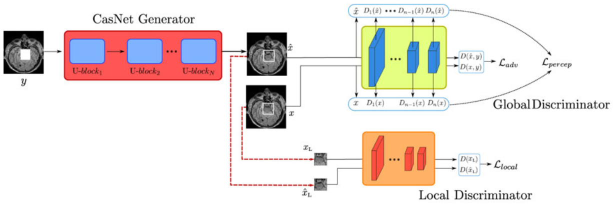

Fig.1: An overview of the ip-MedGAN for MR image inpainting. The CasNet generator progressively refines the inpainted results through stacked U-Net networks. The inpainting performance is guided by two networks, the global and local discriminator net

To evaluate the proposed framework, quantitative and qualitative comparisons were conducted between the proposed ip-MedGAN framework and other adversarial frameworks such as the GLCIC[1] and MedGAN[2].

Results: As evident by the results in Fig. 2 and Table1, the proposed ip-MedGAN provided the most realistic and homogeneously inpainted MR regions as indicated both qualitatively and quantitatively.

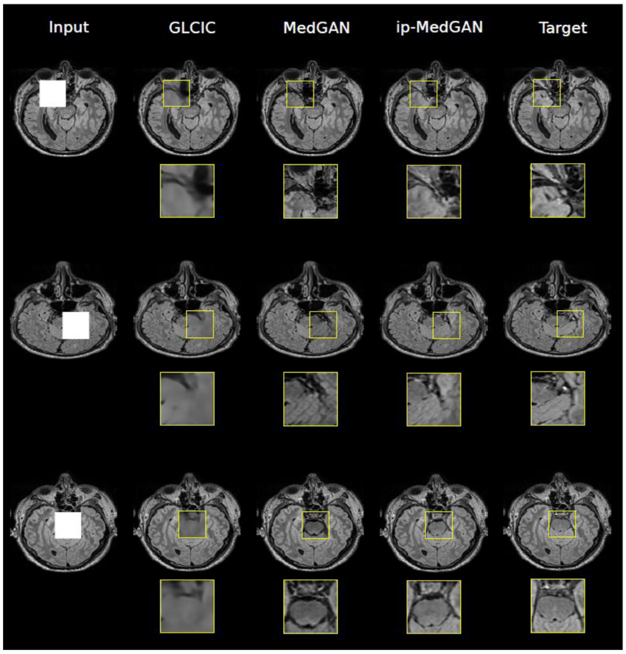

Fig.2: Qualitative comparison between different inpainting frameworks. The proposed ip-MedGAN framework results in the best performance with respect to similarity with the ground truth target MR images.

Model	SSIM	PSNR	UQI
GLCIC	0.2287	15.01	0.8229
MedGAN	0.3034	15.91	0.7830
ip-MedGAN	0.3818	18.32	0.9262

Tab.1: Qualitative performance of the different inpainting frameworks using SSIM, PSNR and UQI as evaluation metrics. The proposed ip-MedGAN surpasses the other frameworks with respect to all the utilized metrics.

Discussion/Conclusion: We propose the use of deep adversarial networks for the inpainting of incomplete or distorted MR images. The presented framework results in detailed and realistic inpainted regions. Future studies will investigate the in-painting of arbitrary shaped missing regions.

References:

1: S. Iizuka, et al., “Globally and Locally Consistent Image Completion”, ACM Transactions on Graphics, 2017.
2: K. Armanious, et al., “MedGAN: Medical image translation using GANs”, http://arxiv.org/abs/1806.06397, arXiv preprint, 2019.

S10 Scientific Session

10:50–11:50 *Room 2 - Van Weelde Zaal*

MR Spectroscopy Methods

S10.02

Quantification of ^{31}P MR spectra using deep learning

H. N. Dang, M. E. Ladd, P. Bachert, A. Korzowski
German Cancer Research Center (DKFZ), Division of Medical Physics in Radiology, Heidelberg, GERMANY

Purpose/Introduction: Phosphorus Magnetic Resonance Spectroscopic Imaging (^{31}P MRSI) provides information about the energy metabolism and pH in vivo, in the form of spectra. Current methods for quantification of ^{31}P metabolite signals, like AMARES [1], are non-linear fitting-tools, which are bound to long processing time and specification of starting values.

In this work, we demonstrate feasibility of a rapid method for spectral quantification with no user input, based on deep learning.

Subjects and Methods: A convolutional neural network (CNN) was implemented based on a resnet18 [2] architecture using the Pytorch framework (Fig. 1). For the estimation of amplitudes, damping factors and frequencies, separate networks were trained. Each network takes a complex-valued free inductive decay (FID) as input and outputs the values of the corresponding parameter for each metabolite separately.

Training datasets were generated by simulation of ^{31}P spectra based on the parametric model as used in [1]. ^{31}P spectra included all metabolites typically visible in human calf muscle, and parameter ranges for amplitude, damping and resonance frequency were carefully chosen for each metabolite to resemble the characteristics of realistic in vivo data. To each spectrum, Gaussian white noise was added with SNR level between 10 and 30. In total 80000 spectra were generated as a training set and 20000 spectra as a validation set.

An additional test set of 1000 spectra was generated to compare accuracy performance using mean absolute percentage error (MAPE) and computational time between the proposed method and the AMARES quantification implemented in jMRUI 5.2 [3].

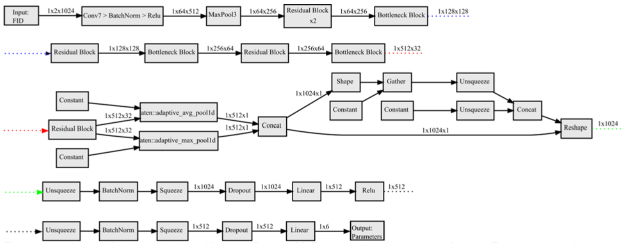

Figure 1: Architecture of the proposed model for quantification of 31P spectra, based on a resnet18 model. Training employed mean squared error as loss function and Adam solver as optimizer.

Results: Fitted spectra show, that the proposed method enables spectra quantification, even for peaks at the detection limit (Fig. 2). CNN outperforms AMARES by means of MAPE within the test dataset (Table 1), except for PCr. Evaluation of the test set on the CPU took 34.26 min for AMARES and only 5.1 s for the CNN.

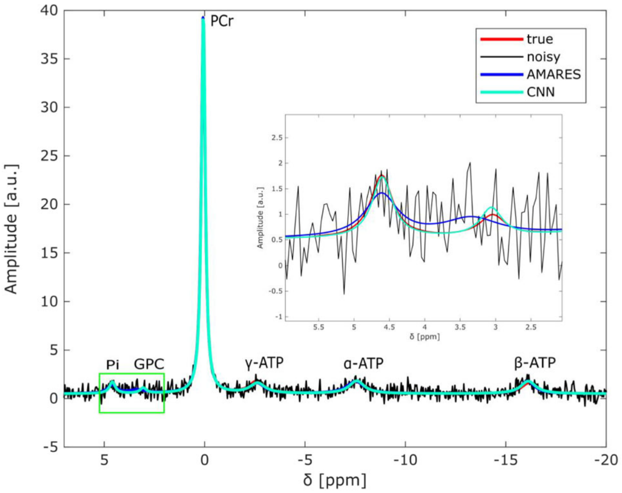

Figure 2: Fits of a simulated 31P spectrum using AMARES and CNN for parameter quantification.

Metabolite	Amplitude - CNN	Amplitude - AMARES	Frequency - CNN	Frequency - AMARES	Damping - CNN	Damping - AMARES
PCr	0.005	0.003	0.203	0.043	0.028	0.005
γ-ATP	0.049	0.086	0.008	0.153	0.051	0.189
α-ATP	0.047	0.097	0.002	2.828	0.051	4.468
β-ATP	0.048	0.121	0.001	0.022	0.051	0.930
Pi	0.082	0.148	0.003	0.112	0.110	5.686
GPC	0.126	0.356	0.008	1.345	0.138	14.121

Table 1: Mean absolute percentage error (MAPE) to ground truth for AMARES and CNN across the entire test set (SNR level between 10-30).

Discussion/Conclusion: The proposed deep learning approach could be considered as an alternative to well established quantification methods for ^{31}P MRSI in the future, due to comparable performances in accuracy. The major advantage of the method is a huge reduction of computational time. Future work has to incorporate artifacts and strong phase variations in the training dataset to adequate handle even more realistic conditions for in vivo ^{31}P spectra.

References:

1. Vanhamme L, et al. (1997), Improved method for accurate and efficient quantification of MRS data with use of prior knowledge. *Journal of magnetic resonance*, *129*(1), 35–43.
2. He K, et al. (2016), Deep residual learning for image recognition. In Proceedings of the IEEE conference on computer vision and pattern recognition (pp. 770–778).
3. Naressi A, et al. (2001), Java-based graphical user interface for the MRUI quantitation package. Magnetic Resonance Materials in Physics, Biology and Medicine, 12(2-3):141–152.

S10.03

Towards structure and metabolism of glycogen C_1-C_6 by localized ^{13}C MRS at 7T using broadband ^1H-decoupling and low-power NOE by means of bi-level WALTZ cycles

E. Serés Roig[1], R. Gruetter[2]

[1]Laboratory of Functional and Metabolic Imaging (LIFMET), Ecole Polytechnique Fédérale de Lausanne (EPFL), Lausanne, SWITZERLAND, [2]Laboratory of Functional and Metabolic Imaging (LIFMET), Centre d'Imagerie BioMédicale (CIBM), Ecole Polytechnique de Lausanne (EPFL), Lausanne, SWITZERLAND

Purpose/Introduction: Whilst in vivo ^{13}C-MRS of glycogen is typically performed via the C_1-carbon signal [1, 2], the ^{13}C-MR relaxation properties of the various C_1-C_6 signals may bring complementary information for investigating glycogen metabolism [3], at the expense of their low-sensitivity. Precisely, localized ^{13}C-MRS at 7T using bi-level broadband ^1H-decoupling benefits of an improved sensitivity and spectral-resolution, allowing distinct detection of glycogen C_2-C_6 [4]. The aim of this study was to further explore the advantage of localized ^{13}C-MRS at 7T using bi-level broadband ^1H-decoupling in terms of achievable-bandwidth and sensitivity-gain, while investigating its potential feasibility towards simultaneous detection of glycogen C_1–C_6 at 7T.

Subjects and Methods: Proton-decoupled ^{13}C-MRS was performed on a 7T human-scanner (Siemens Erlangen/Germany) using a home-built ^{13}C-linear/^1H-quadrature RF-surface-coil. A pulse-acquire sequence for localized ^{13}C-MRS using bi-level ^1H-decoupling was developed [4]. Bi-level ^1H-decoupling consisted of a series of WALTZ-cycles interleaved with 100 ms time delays during ^{13}C-relaxation for the generation of low-power NOE, and WALTZ-16 for broadband ^1H-decoupling during ^{13}C-acquisition. The duration of the main WALTZ-cycle 90°-pulse was fixed to 0.5 ms to cover the ~ 3 ppm of glycogen H_1-H_6 [5]. The decoupling-bandwidth was measured on 99%-^{13}C-enriched formic-acid bubble placed at the ^{13}C-coil centre. The performance of the sequence was evaluated in vitro on a phantom containing 800 mM natural-abundance of glycogen, and in vivo by measuring natural-abundance metabolites in the human calf and brain.

Results: Bi-level ^1H-decoupling resulted in a decoupling-bandwidth > 900 Hz at 7T (Fig. 1). An improved spectral-resolution and sensitivity was further implied from the ^{13}C-MRS spectra of glycogen C_1-C_6 in vitro at 7T (Fig. 2). In particular, the signal-enhancements of glycogen C_1-C_6 in vitro were $\geq 40\%$, higher than those in the literature [3]. Besides, the ^{13}C-T_1 of glycogen-C_6 in vitro was found to be ~ half of those of glycogen C_1-C_5, in agreement with [3], as attributed to the two-bonded protons of the C_6 versus one of the C_1-C_5. The signal-enhancement of glycogen-C_1 in the human calf using bi-level ^1H-decoupling was ~ 1.4, while high spectral-resolution and sensitivity was further implied from the detection of natural-abundance *myo*-Inositol C_1-C_6 as well as tentatively Glu, Gln, Cr + Cho, NAA and Asp in the human brain (Fig. 3).

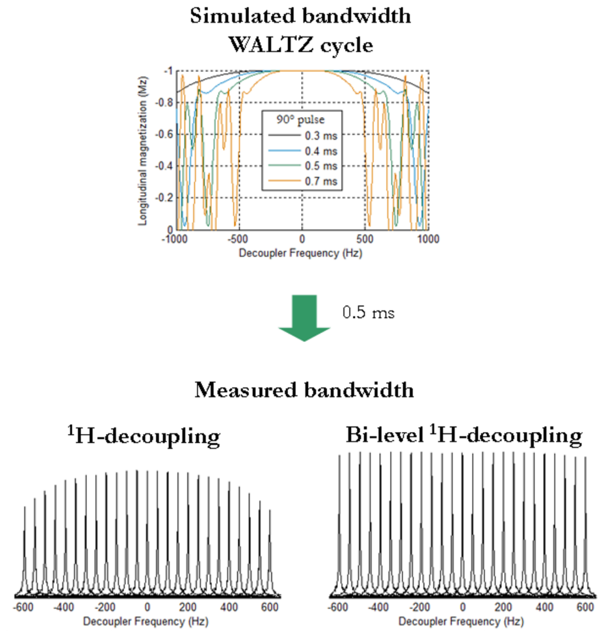

Simulated bandwidth of a WALTZ cycle (top). Measured bandwidth using WALTZ16 without and with NOE (bottom), using 90° pulse = 0.5ms. The two measured bandwidths are shown with the same vertical scale, but are not scaled with the simulation.

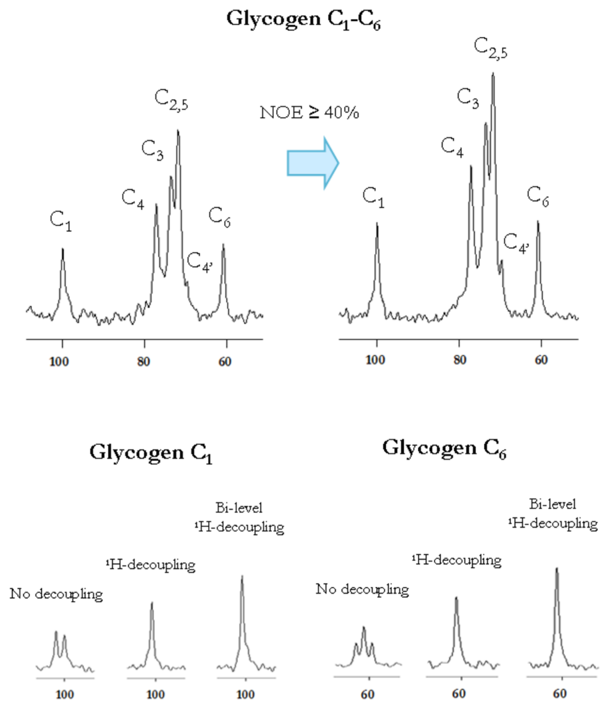

In vitro 1H-decoupled 13C MR spectra of glycogen C1-C6 without NOE (top left) and with NOE (top right), glycogen C1 (bottom left) and glycogen C6 (bottom right), using the centre of the 13C spectrum at ~80ppm, 100.5ppm and 61ppm, respectively.

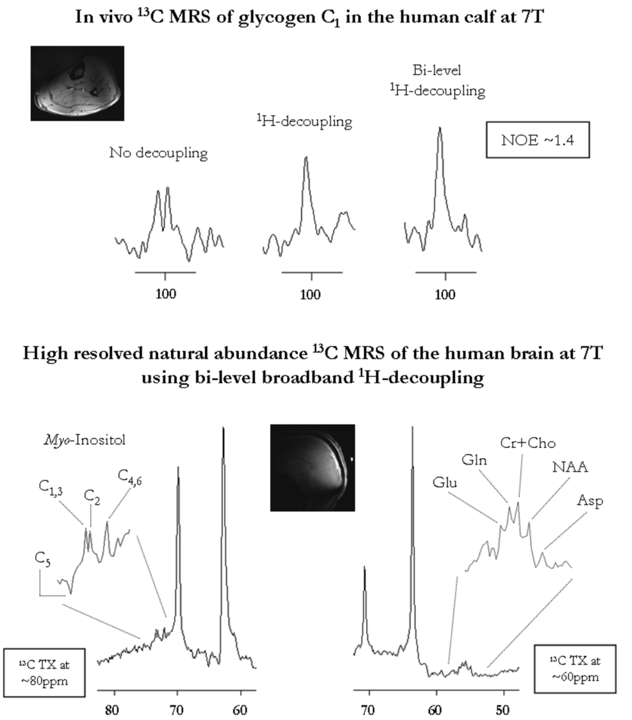

Detection of natural abundance glycogen C1 in the human calf (top) using few number of scans. The NOE enhancement of glycogen C1 in vivo was ~1.4. Detection of high resolved natural abundance metabolites in the human brain (bottom).

Discussion/Conclusion: We conclude that ^{13}C-MRS at 7T using bi-level broadband ^{1}H-decoupling improves both spectral-resolution and sensitivity of glycogen C_1-C_6 in vitro, as well as natural-abundance glycogen-C_1 in the human calf and high-concentrated metabolites in the human brain.

References:

[1] Gruetter R. JNR.2003;74(2):179–83
[2] Oz G. NInt.2003;43:323–9
[3] Sillerud LO. Bioch1983;22, 1087–1094
[4] Serés Roig E. MRS workshop.2018
[5] Chen W. Bioch.1993;32, 43

S10.04

CEST effect of agar: it's not a neutral baseline for realistic CEST-MRI parameter optimization

S. Mueller, R. Pohmann, K. Scheffler, M. Zaiss
Max Planck Institute for Biological Cybernetics, High-field Magnetic Resonance Center, Tuebingen, GERMANY

Purpose/Introduction: Ultra-high field (UHF) MRI in combination with specific saturation modules is a promising strategy to isolate CEST effects, e.g. of glutamate, or sugars. For in vitro optimization of sequence parameters, realistic T_1 and T_2 relaxation times are crucial [1]. Relaxation is often adjusted using agar, which was suspected previously to yield a CEST effect [2]. The CEST effect of agar is here characterized at various field strengths, concentrations and pH values. To avoid false positive results, the agar CEST effect must be taken into account when optimizing for CEST effects in realistic model solutions.

Subjects and Methods: Multiple agar model solutions were investigated under different conditions (pH 6–8, T = 25, 37 °C) at a Siemens whole body MR systems ($B_0 = 9.4$T and 3T) and 14T (Bruker). Different CEST saturation modules ($B_1 = 4$ to 7µT, 3 to 5 pulses, CW for $B_0 = 14$T; Gauss, Spinlock (SL), matched adiabatic SL[3]) were applied, before a 3D-gradient-echo readout ($T_E = 1.98$ ms, $T_R = 3.74$ ms). Post processing included B_1 [4] and B_0 correction based on WASABI[5] before evaluation of Z-spectrum asymmetry (MTR_{asym} [6]) at saturation offset Δω.

Results: The CEST effect of agar was detectable at all field strengths, increasing from < 1% MTR_{asym} at $B_0 = 3$T to 4% at 14T (Fig. 1). The effect of increased agar concentration (2% to 3%) seems to be counterbalanced by increased spillover due to shorter T_2, resulting in an almost unchanged MTR_{asym} at 9.4T (Fig. 2a). MTR_{asym} values were found to be anti-correlated to pH (Fig. 2b). The observed CEST effect of agar was pronounced for relatively short (0.5 to 0.8 s), but strong saturation ($B_1 = 5$–6 µT), indicating a faster exchange process (Fig. 3).

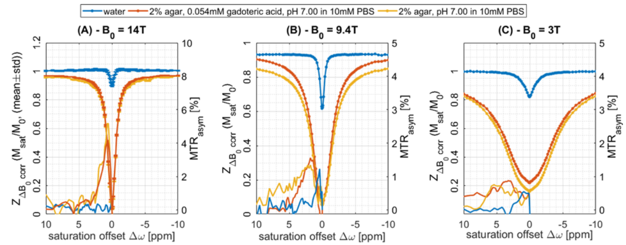

Fig.1: Z-spectra and MTRasym values at different field strengths, corrected for ΔB0(r) or ΔB0(r,t)[7] A smoothed before MTRasym calculation B Z-spectra corrected for B1 before MTRasym calculation C MTRasym is smoothed for better visualizati

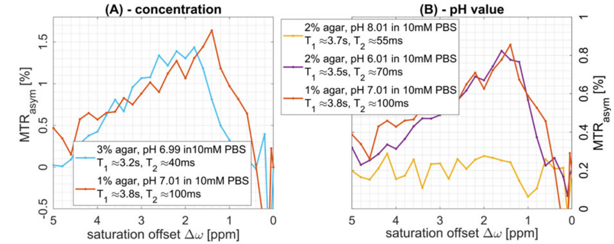

Fig.2: effect of concentration (A) and pH value (B) on MTRasym values of agar, measured at B0=9.4T, 37°C; data corrected for ΔB0(r,t)[7] and B1 before determining MTRasym; T2 from spin-echo measurements; T1 from SATREC measurement

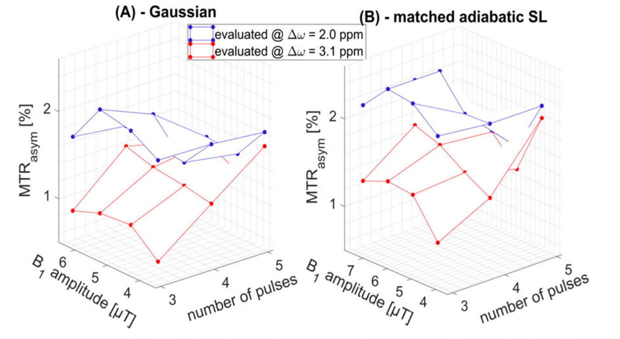

Fig.3: MTRasym for different saturation modules at B0=9.4T, 36°C; 100 ms pulses, DC=50%; data corrected for ΔB0(r); 2% agar + 0.054mM gadoteric acid, pH 6.98, T1=2131 ms, T2=55 ms; measured using Gaussian (A) or matched adiabatic SL[3] pulses (B)

Discussion/Conclusion: The agar CEST effect contributes to MTR_{asym} with up to 2% at 9.4T, the behavior hints to faster hydroxyl exchange processes of -OH groups apparent in agar. CEST effects of agar were smaller, but still not negligible at lower field strengths (Fig. 1).

Thus, agar is not a neutral baseline in model solutions for CEST characterization, and agar CEST effects could be mistaken for false positive CEST effects of metabolites studied in vitro. The agar CEST effect size depends on both, saturation and solution parameters, but can now be removed to enable realistic in vitro optimization of CEST-MRI.

References:

Financial support of the Max Planck Society, German Research Foundation (DFG, grant ZA 814/2-1), and European Union's Horizon 2020 research and innovation programme (Grant Agreement No. 667510) is gratefully acknowledged.

[1] Zaiss et al., NeuroImage 112 (2015)
[2] Li et al., Oncotarget 7 (2016)
[3] Herz et al., MRM 81 (2019)
[4] Windschuh et al., NMR Biomed. 28 (2015)
[5] Schuenke et al., MRM 77 (2017)
[6] Guivel-Scharen et al., J Magn Reson 133 (1998)
[7] Windschuh et al., MRM 81 (2019)

S10.05

Feasibility of functional spectroscopy on a clinical (3T) scanner

P. Bednarik[1], A. Svatkova[2], D. Deelchand[3], G. Silani[4], R. Lanzenberger[5], W. Bogner[1]
[1]Medical University of Vienna, Hgh Filed MR Center, Department of Biomedical Imaging and Image-guided Therapy, Vienna, AUSTRIA, [2]Medical University of Vienna, Department of Medicine III, Clinical Division of Endocrinology and Metabolism, Vienna, AUSTRIA, [3]University of Minnesota, Center for Magnetic Resonance Research, Department of Radiology, Vienna, AUSTRIA, [4]University of Vienna, Department of Applied Psychology: Health, Development, Enhancement and Intervention, Vienna, AUSTRIA, [5]Medical University of Vienna, Department of Psychiatry and Psychotherapy, Vienna, AUSTRIA

Purpose/Introduction: The functional spectroscopy (fMRS) is currently the sole non-invasive method for measurements of metabolite changes related to activation of brain energetic metabolism. Proton fMRS has been well established at 7T scanners and provided consistent results worldwide.[1, 2] As deficiency of energetic metabolism underlie pathophysiology of various neurological[3, 4]/psychiatric diseases, [5] reliable and reproducible fMRS method is essentially needed for clinical studies. To date, fMRS conducted at lower fields (e.g., 3T) mainly focused on lactate and showed substantial discrepancies.[6, 7] Thus, we test ability of fine-tuned semi-LASER MRS method[8] to provide sensitive fMRS measures on 3T.

Subjects and Methods: The fMRS/fMRI experiment was conducted on 3T Siemens Prisma scanner with 64-channel head-neck receive array coil. High-resolution MPRAGE images served to place fMRS voxel in the primary visual cortex. A FASTMAP technique minimized within-voxel B0 inhomogeneity. Spectra were acquired with sLASER localization sequence[8] (TE = 23 ms) from 10 healthy volunteers (29 ± 5 y.o.) during a fMRS paradigm with STIM (red-black checkerboard flickering at 8 Hz) and REST (black screen) periods. The first short REST (16 scans, TR = 5 s) was followed with 64 scans long STIM and REST (12 min. in total). The spectra from the end of STIM and second REST (2 × 48 scans) were postprocessed and summed in MRSpa (Fig. 1), quantified with LCmodel utilizing a basis set of 19 simulated metabolites and a spectrum of measured macromolecules. Concentrations were compared using paired *t* test. False discovery rate (FDR) reduced likelihood of false positives to 10%.

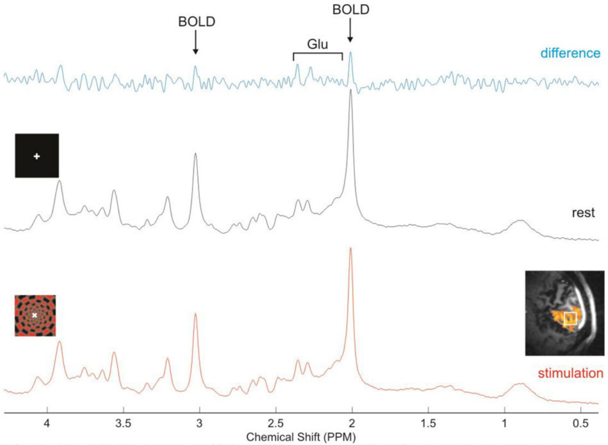

Fig.1. Sample spectra (NEX=48) acquired during STIM and REST in one volunteer. Their difference demonstrates changes related to concentration glutamate (Glu) change and linewidth difference caused by the BOLD effect.

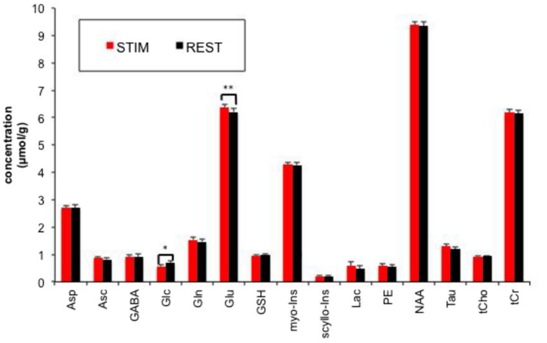

Fig.2. Neurochemical profiles quantifed during STIM and REST. Data are means. Error bars represent standard error of the mean.

Results: Significant increase of glutamate by 2.9% ± 1.9% (pFDR = 0.007) and decrease of glucose by 19.8% ± 17.5% (pFDR = 0.01) were observed in response to stimulus (Fig. 2). Lactate increase did not reach significance (pFDR = 0.03). Observed variance in glutamate responses (SD/mean = 68%) could be explained by variance in BOLD-fMRI fraction of activated voxels (SD/mean = 55%) within volume of interest. CRLB of glutamate were 4.4% ± 0.5%, i.e., in the order of expected changes (3–4%) and is lower than previously achieved values at 3T with PRESS.9 While changes of glutamate, glucose and lactate are consistent with our previous 7T studies, 10 we did not observe significant change in aspartate, likely due to lower SNR and CRLB of aspartate (10.8% ± 2.0%).

Discussion/Conclusion: Glutamate and glucose responses are consistent with previous 7T studies while the current study utilized shorter and clinically feasible paradigm. Our study proved ability of sLASER sequence to reliably quantify functional glutamate&glucose changes using clinical 3T scanner.

References:

1.Lin Y.JCBFM 2012.**2.**Schaller B.J Neurosci Res 2013.**3.**Iadecola C.Nat Rev Neursci 2004.**4.**Adanyeguh I.Neurology 2015.**5.**Taylor R.Neuroreport 2015.**6.**Prichard J.PNAS 1991.**7.**Sappey-Marinier D.JCBFM 1992.**8.**Deelchand D.MRM 2014.**9.**Stanley J.Neuroimage 2017.**10.**Bednarik P.JCBFM 2015&2018.

S10.06

Complex selection determine phases of ^{1}H and ^{19}F MR signals in SABRE-based hyperpolarization

R. Ringleb[1], F. Euchner[1], S. Hadjiali[2], U. Bommerich[1], C. Bruns[1], J. Bargon[3], G. Buntkowsky[2], J. Bernarding[1], **M. Plaumann**[1]
[1]Otto-von-Guericke University Magdeburg, Institute for Biometrics and Medical Informatics, Magdeburg, GERMANY, [2]Technical University Darmstadt, Institute of Physical Chemistry, Darmstadt, GERMANY, [3]University of Bonn, Institute of Physical and Theoretical Chemistry, Bonn, GERMANY

Purpose/Introduction: Signal Amplification By Reversible Exchange (SABRE) can be used to increase MR signals for molecular imaging.[1, 2] The mechanism of polarization transfer to heteronuclei is currently not fully understood.[3] Information concerning chemical shifts and more important scalar couplings are significant to estimate achievable signal enhancements and their signs. Here, we take a focus on a metal complex that is necessary for SABRE. In recent years, several Ir-based complexes were examined. Two of them are the Crabtree´s catalyst ([Ir(COD)(PCy$_3$)(py)]PF$_6$) and the [IrIMesCODCl] complex. The selection of the complex can lead to completely different phases of the detectable signals. This will be demonstrated here in different ^{1}H and ^{19}F spectra.

Subjects and Methods: Fluorinated compounds, such as 2-fluoropyridine, 3-fluoropyridine, fluorinated nicotinic acid, 2-amino-3, 5-difluoropyridine or 2-cyano-3, 5-difluoropyridine, were dissolved in CD$_3$OD or CD$_3$OD:D$_2$O mixtures. In presence of the Ir-complex (Crabtree's catalyst or [IrIMesCODCl]), the sample was degassed. Hyperpolarization was realized with about 50% enriched para-H$_2$ (6 bar, at 6 mT). The NMR spectra were detected by using a single pulse experiment on a Bruker WB-300 (7T) NMR spectrometer.

Results: Positive signal enhancements are detectable in ^{1}H NMR spectra when using Crabree's catalyst.

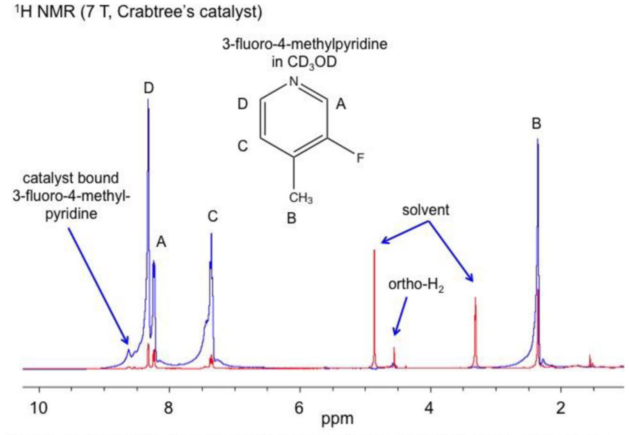

1H NMR spectra of hyperpolarized 3-fluoro-4-methylpyridine in presence of Crabtree's catalyst (blue) and the thermal spectrum (red).

Opposite phases are observable when apply [IrIMesCODCl].

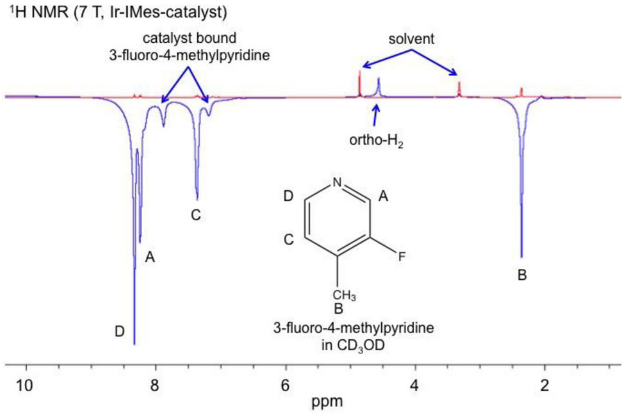

1H NMR spectra of hyperpolarized 3-fluoro-4-methylpyridine in presence of the [IrIMesCODCl] complex (blue) and the thermal spectrum (red).

With the latter named complex, the highest signal enhancements were calculated (SE > 50).

19F NMR spectra allow the investigation of an interaction between a fluorinated ligand and the catalyst. Because of the large chemical shift range in 19F NMR, signals of the "free" pyridine derivative as well as the complex-bounded molecules can be distinguished. The consideration of the signs of the signal integrals leads to the realization that opposite observations can be made in 19F NMR spectroscopy in comparison to the 1H NMR. Enhanced signals with positive phases are detectable when [IrIMesCODCl] is used, while negative phases are observable in presence of Crabtree's catalyst.

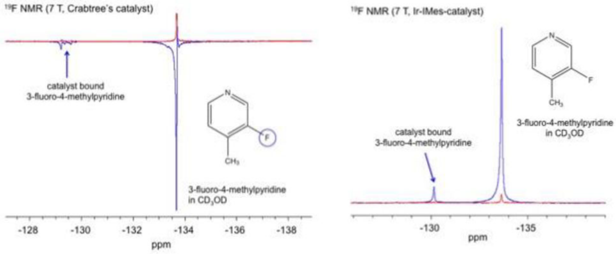

19F NMR spectra of hyperpolarized 3-fluoro-4-methylpyridine (blue) and the thermal spectrum (red).

Discussion/Conclusion: Less is known about the hyperpolarization transfer from the ^{1}H protons of para-H$_2$ to nuclei of the ligand system. The effect of the molecular structure of the catalyst system concerning the phases/signs of the enhanced MR signals was investigated here. Opposite signs were detected when using the Crabtree´s catalyst or using the [IrIMesCODCl] complex. Couplings to the ^{31}P nucleus in the Crabtree catalyst have a significant impact. The controlled influencing of the signal phases by choice of the catalyst is of great importance for MR imaging, since mixed-phase signals lead to quenching.

References:

1. RW Adams et al., Science 2009; 323: 1708–1711.
2. J-B Hövener et al., Angew. Chem. Int. Ed. 2018; 57:11140–11162.
3. AN Pravdivtsev et al., J. Magn. Reson. 2015; 261: 73–82.

S11 Scientific Session

10:50–12:20 *Room 4 - Plate & Van der Vorm Zaal*

Abdomen, Thorax & Pelvis

S11.02

Assessment of liver fibrosis stage using machine learning and feature extraction of gadoxetate-enhanced MR images

M. Karlsson, Y.-C. Lu, P. Lundberg
Linköping University, Department of Medical and Health Sciences, Linköping, SWEDEN

Purpose/Introduction: There is a need for non-invasive alternatives to needle biopsies when evaluating liver fibrosis in chronic liver disease (CLD) patients. Gadoxetate is a liver specific MRI contrast agent commonly used for characterizing lesions in the liver. Quantitative measurements of the relative enhancement (RE) of the gadoxetate–enhanced images have previously been used to detect liver fibrosis.[1] However, RE reflects liver function rather than fibrosis accumulation. An alternative approach, to use radiomics, i.e. to extract different image features from the MR images, have recently shown promise with regards to assessing advanced liver fibrosis.[2] The purpose of this work was therefore to implement a feature-based method for assessing advanced liver fibrosis.

Subjects and Methods: 91 patients, with suspected CLD were prospectively included. They underwent an MR-examination (Philips, 1.5T), immediately followed by a liver biopsy. The MR-examination included 2-point Dixon images (Fig. 1), acquired before and 20 min after gadoxetate injection.

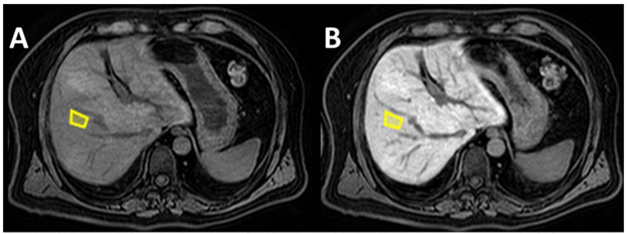

Examples of MR images before (A) and 20 minutes after (B) gadoxetate injection. The yellow square is an example of ROI.

Regions of interest (ROIs) were placed in the liver and RE = (SI20-SI0)/SI0 was calculated, where SI0 and SI20 are the signal intensities before and 20 min after gadoxetate injection.

For the feature analysis, an ROI covering the whole liver was used. In order to increase the number of data points, the dataset was augmented by using each individual slice from each patient as an independent datapoint. For training and validation, the dataset was then divided into a training set with slices from 73 patients and a test set with slices from 18 patients.

For each liver voxel, a total of 29 features were extracted using the Gray-Level Co-Occurrence Matrix3 and the Gray-Level Run Length Matrix4, with Bin size = 64, Window size = 15 × 15, and Distance = 1. Each matrix was applied four times using different rotations (0°, 45°, 90°, 135°). For each feature, the value was averaged across the four rotations, as well as across all liver voxels. Lastly, using the 29 extracted features, an Adaboost classifier was trained to separate patients with and without advanced fibrosis.

Results: Table 1 shows the diagnostic performance of the Adaboost classifier and RE, and Fig. 2A shows receiver operation characteristic curves, all with regards to the validation data set. The results show that the classifier is better than RE. Figure 2B shows a confusion matrix for the Adaboost classifier.

	SENSITIVITY (%)	SPECIFICITY (%)	AUROC	ACCURACY (%)
Adaboost	80	89	0.9	88
RE	73	71	0.76	73

Diagnostic performance of the Adaboost classifier and RE, with respect to identify patients with advanced fibrosis; AUROC: Area Under the Receiver Operating Characteristic Curve

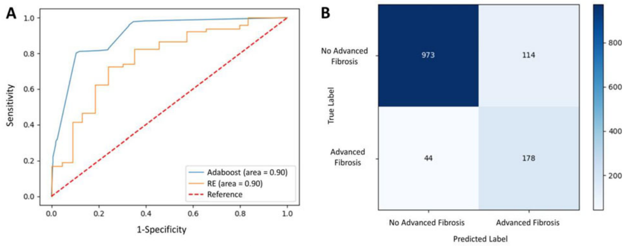

(A) Receiver operating characteristic curves for the Adaboost classifier and RE, using the validation data set. (B) A confusion matrix for the Adaboost classifier.

Discussion/Conclusion: We have demonstrated the potential of using machine learning and feature extraction of gadoxetate–enhanced MRI to identify patients with advanced fibrosis. In the present cohort, the feature–based method outperformed the simplistic use of RE. Future work should include more data from different scanners and field strengths in order to verify the generalizability of the method.

References:

[1] Feier 2013 Radiology
[2] Park 2018 Radiology
[3] Haralick 1973 IEEE Trans Syst Man Cybern
[4] Xiaoou 1998 IEEE Trans Image Process

S11.03

Supervised risk prediction of transition zone cancer lesions in the prostate using GOIA-sLASER ^{1}H MR spectroscopic imaging without endorectal coil

N. Gholizadeh[1], P. Greer[2], J. Simpson[2], O. Al-iedani[1], P. Lau[3], **A. Heerschap**[4], S. Ramadan[1]
[1]University of Newcastle, Health and Medicine, New Castle, AUSTRALIA, [2]University of Newcastle, Radiation Oncology, New Castle, AUSTRALIA, [3]University of Newcastle, Radiology, New Castle, AUSTRALIA, [4]Radboud University Nijmegen, Radiology and Nuclear Medicine, Nijmegen, NETHERLANDS

Purpose/Introduction: In the diagnosis of prostate cancer (PCa) by multiparametric MRI (mpMRI) the PIRADS-V2 scoring system, including T2 weighted, diffusion and DCE-MRI, plays a key role [1]. However, the reproducibility of PCa diagnosis using PI-RADS criteria is only moderate, with least performance in the transition zone (TZ) [2]. Moreover, DCE-MRI has little value in mpMRI and Gd carries a safety risk [3]. Recently, improved 3-dimensional ^{1}H MR Spectroscopic Imaging (3D ^{1}H MRSI) of the prostate has been presented, employing a semi-LASER sequence with gradient-modulated offset-independent adiabatic (GOIA) pulses [4, 5].

Aim: to evaluate the GOIA-sLASER sequence in detecting and diagnosing PCa's in the TZ and to develop risk models to differentiate (a) normal vs cancer, (b) low risk vs high risk cancer, (c) low risk vs intermediate risk cancer and (d) intermediate risk vs high risk cancer voxels.

Subjects and Methods: Multiparametric MRI including 3D ^{1}H MRSI using GOIA-sLASER (nominal voxels ~ 0.34 cc) was performed on 36 patients with biopsy-proven low and high risk TZ cancers (age: 53–72 years) using a 3T MRI system with an external phased-array coil. Cancer lesions were selected by an experienced radiologist. For each voxel within the ROI, the MR spectra were fitted with LCModel and seven metabolite ratios were calculated and split into a subset for training and another for testing. Four support vector machine (SVM) models were built using four training datasets. The accuracy, sensitivity and specificity for each model were calculated using the test dataset.

Results: With an 8 min GOIA-sLASER acquisition we obtained high quality spectra for the whole prostate (Fig. 1). The normal vs cancer diagnostic model for TZ lesions achieved a high predictive performance with an accuracy, sensitivity and specificity of 96.2%, 95.8% and 93.1%, respectively. The accuracy, sensitivity and specificity of the low risk vs high risk cancer and low risk vs intermediate risk cancer models were 82.5%, 89.2% and 70.2% and 73.0%, 84.7% and 60.8%, respectively. The intermediate risk vs high risk cancer model yielded lower accuracies, sensitivities and specificities: 49.1%, 54.3% and 42.7%, respectively.

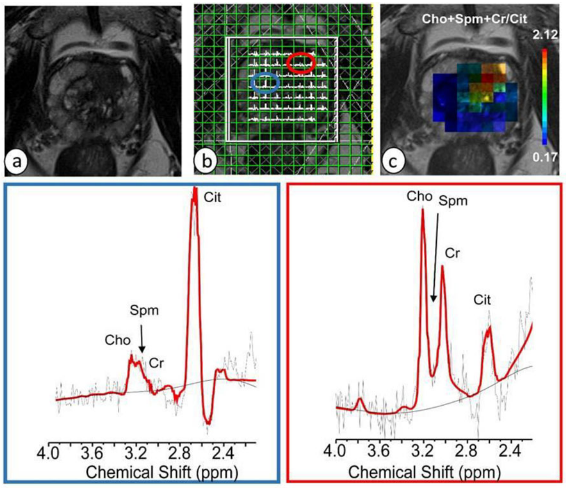

Prostate MRSI of patient with PCa (Gleason 4+5, left side transitional zone). a) Axial T2WI. b) Spectral map. c) color coded map Cho+Spm+Cr/Cit. Bottom: Spectra with LCModel fit (expansion of encircled spectra in b).

Discussion/Conclusion: The GOIA-sLASER sequence with an external phased-array coil is an excellent combination for robust MRSI assessment of TZ cancers. The classification results demonstrate that this MRRSI approach is a valuable diagnostic tool for discriminating normal vs cancer, low risk vs high risk cancer and low risk vs intermediate risk cancer and therefore may improve mpMRI of the prostate.

References:

1. Barentsz, J.O., et al., Urology. 2016, 69(1): p. 41–49.
2. Rosenkrantz, A.B., et al., Radiology, 2016. 280(3): p. 793–804.
3. Turkbey et al. Eur, Urology 2019, in press.
4. Steinseifer IK, et al. Magn Reson Med. 2015 Oct;74(4):915–24.
5. Tayari N et al., Invest Radiol. 2017 Oct;52(10):640–646.

S11.04

MR Elastography of the liver: correlation with T_1 mapping

C. Kremser, M. Plaikner, B. Henninger
Medical University of Innsbruck, Radiology, Innsbruck, AUSTRIA

Purpose/Introduction: Magnetic Resonance Imaging (MRI) represents a widely available noninvasive method for the evaluation of diffuse liver disease. In recent years, beside methods for hepatic iron and fat quantification, also MR elastography (MRE) was increasingly used for the additional detection and classification of fibrosis. As a biomarker for fibrosis, T_1 mapping was suggested as an alternative approach by several authors (1, 2). The purpose of our work was to correlate MRE findings with T_1 mapping and to investigate the influence of factors other than tissue stiffness on T_1 values.

Subjects and Methods: After approval by our local institutional review board, 216 patients with clinical suspicion of diffuse liver disease were investigated on a 1.5T MR scanner (MAGNETOM AvantoFit, Siemens, Germany). For iron quantification a fat-saturated multi-gradient-echo sequence with 12 echoes (T_R = 200 ms; T_{En} = 0.99 ms + n*1.41 ms, flip-angle: 20°) was used. Hepatic R_2* values were calculated using custom written ImageJ plugins. For fat quantification MR spectroscopy was performed using a T_2-corrected multi-echo single-voxel STEAM spectroscopy (SVS) sequence (five echoes: T_E = 12/24/36/48/72 ms, T_R = 3000 ms, voxel size: 20 × 20 × 20 mm^3, single breath-hold of 15 s) (3). Liver T_1 values were obtained using a fast T_1 mapping sequence as described by Deichmann et al. (4). MRE was acquired using a 2D-SE-EPI protocol(T_R = 1000 ms, T_E = 45 ms) with 60 Hz acoustic excitation using a commercial driver system (Resoundant, Inc., USA). Stiffness maps were automatically calculated during image reconstruction and tissue stiffness values were provided in kPa.

Results: 58/216 patients had fibrosis of different stages (stiffness values > 2.5 kPa). For all patients a significant ($p < 0.001$) moderate correlation ($r = 0.46$) between tissue stiffness and hepatic T_1 values was found.

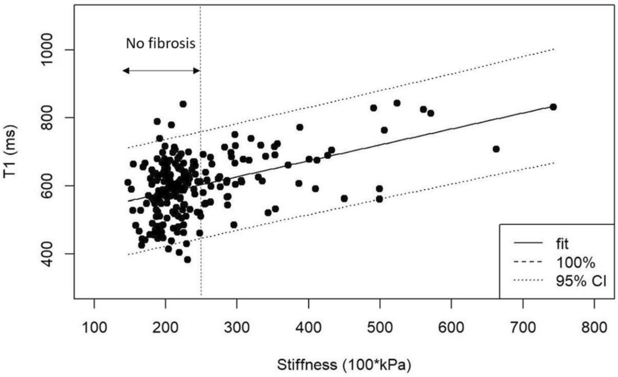

For all patients a significant (p<0.001) moderate correlation (r=0.46) between tissue stiffness and hepatic T1 values was found.

A high variability of T1 values was observed (range: 383–839 ms) for patients without fibrosis (stiffness values < 2.5 kPa). By excluding these patients (n = 158) the correlation between tissue stiffness and T1 values slightly improved to $r = 0.517$ ($p < 0.001$). Patients without fibrosis showed significantly ($p < 0.001$) different T1 values between different iron or fat combinations: iron overload resulted in markedly decreased T1 values and hepatic fat deposit without iron overload lead to increased T1 values.

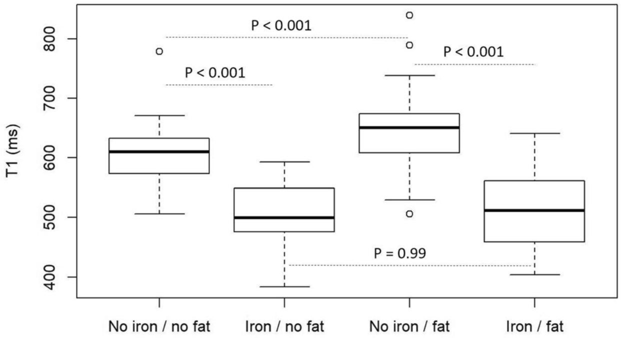

T1 values for patients without fibrosis for different iron and fat situations. Iron overload resulted in markedly decreased T1 values and hepatic fat deposit without iron overload lead to increased T1 values.

Discussion/Conclusion: Our data show that hepatic T_1 values depend on partly opposing factors such as iron overload, fat deposition and tissue stiffness and might not be a reliable biomarker for fibrosis.

References:

[1] Banerjee R, et al., Journal of Hepatology 2014; 60: 69–77
[2] Rauscher I, et al. EJR 2014; 83 : 900–904
[3] Pineda N, et al. Radiology 2009; 252(2) :568–576
[4] Deichmann R, et al. JMR 1992 : 96 :608–612

S11.05

Accelerated free-breathing self-gated 4D-lung MRI with wave-CAIPI

J. A. J. Richter[1], T. Wech[1], A. M. Weng[1], M. Stich[1], S. Weick[2], H. Köstler[1]

[1]University Hospital Würzburg, Department of Diagnostic and Interventional Radiology, Würzburg, GERMANY, [2]University Hospital Würzburg, Department of Radiation Oncology, Würzburg, GERMANY

Purpose/Introduction: Dynamic 4D MR imaging of the lung usually requires long scan times to resolve multiple breathing phases at sufficient spatial resolution, e.g., for radiotherapy treatment planning. Parallel imaging can be used to accelerate the image acquisition, but is accompanied by an additional noise penalty. We propose the implementation of the wave-CAIPI technique (1) for retrospectively self-gated dynamic 4D lung MRI to mitigate the increase in noise.

Subjects and Methods: A wave-CAIPI k-space trajectory was implemented in a 3D FLASH pulse sequence by applying sinusoidal gradient oscillations on the phase-encoding directions during readout. For respiratory gating, a DC signal was acquired immediately after the excitation pulse. A Conjugate Gradient SENSE Algorithm (2) was applied and coil sensitivity maps were estimated using the Berkley Advanced Reconstruction Toolbox (3). Gradient system imperfections were compensated for by the gradient system transfer function (4). All experiments were performed on a 3T MR scanner (MAGNETOM Prisma, Siemens Healthcare GmbH, Erlangen, Germany). To compare the wave-CAIPI acquisition with Cartesian sampling, two density-weighted (5) scans of a healthy volunteer were performed with a matrix size of 224 × 224 × 120 and 2.23 mm isotropic resolution. The data was gated into 8 breathing phases. The acquisition time was set to 05:10 min and was retrospectively accelerated up to 01:05 min. Noise estimation was performed using the pseudo multiple replica approach (6).

Results: Figure 1 shows a comparison of the Cartesian and the wave-CAIPI scans at various acquisition times. Specifically for large accelerations, the wave-CAIPI images are superior in image quality, especially in regard of undersampling artifacts. In Fig. 2, a maximum-intensity-projection across 7 adjacent axial slices is shown, indicating that small vessels are displayed more clearly in the accelerated wave-CAIPI images, due to the lower noise level. A quantitative investigation of image noise is presented in Fig. 3, showing a reduced noise level (up to 20% in the thorax) for the wave-CAIPI technique.

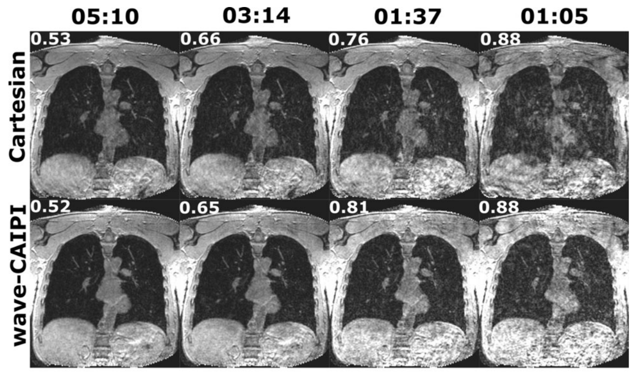

Fig. 1. Comparison of a Cartesian and a wave-CAIPI scan in end-inspiration at various acquisition times (top row; units: min). The respective fraction of missing k-space lines is shown in each image at the top left corner.

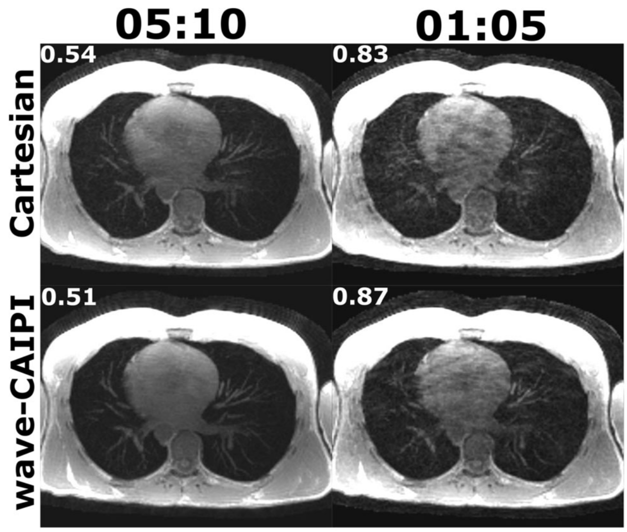

Fig. 2. Maximum-intensity projection across 7 axial slices at end-expiration for different acquisition times. The undersampling rate is shown in the respective top left corner. The wave-CAIPI image exhibits a reduced noise level.

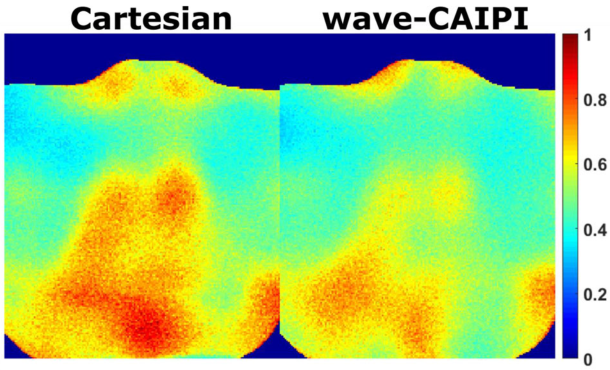

Fig. 3. Image noise in a Cartesian and a wave-CAIPI scan (coronal slice) at end-inspiration. The acquisition time is 01:05 min, the undersampling rate in both cases is 0.88. The wave-CAIPI image exhibits a reduced noise level.

Discussion/Conclusion: The wave-CAIPI k-space trajectory entails a wide spread of aliasing artifacts, thereby exploiting coil sensitivity variations in all three spatial dimensions, which ultimately leads to a more stable parallel imaging reconstruction. We demonstrate that by using the wave-CAIPI technique instead of Cartesian sampling, full coverage of the lung can be achieved in a shorter time at decreased noise enhancement due to parallel imaging.

References:

1. Bilgic B et al., Magn Reson Med 2015, 73(6), p. 2152–62
2. Pruessmann KP et al., Magn Reson Med 2001, 46(4), p. 638–51
3. Uecker M et al., Proc. Intl. Soc. Mag. Reson. Med. 2015, 23, p. 2486
4. Stich M et al., Magn Reson Med 2018, 80(4), p. 1521–1532
5. Breuer K et al., Phys Med Biol. 2018, 63(7), p. 075002 (12 pp)
6. Robson PM et al., Magn Reson Med 2008, 60(4), p. 895–907

S11.06

Feasibility of a non-invasive Short MRI Surveillance (SMS) protocol as a screening tool for hepatocellular carcinoma (HCC) in high risk patients

F. Willemssen, Q. de Lussanet de la Sablonière, F. Fiduzi, C. Els, G. Krestin, R. Dwarkasing
Erasmus University Medical Center, Radiology, Rotterdam, NETHERLANDS

Purpose/Introduction: Imaging surveillance in patients at risk for HCC is aimed at detecting early HCC in order to increase patient survival. Leading consensus guidelines (1, 2) recommend ultrasound every six months. The hypothesis of this study is that a Short MRI Survaillance (SMS) protocol consisting of axial T2 W fat saturation, DWI, and T1 W in-and oppose phase measurements (without contrast agent injection), with an aquisition times of less that 10 min, will suffice for detection of lesions suspect for HCC.

Subjects and Methods: From 2010 to 2019 patients were recruited who received yearly MRI of the liver with contrast-enhcandement (CE-MRI) for HCC screening in a surveillance program. These patients must have recieved more than two full CE-MRI liver protocols. MRI with HCC on first detection, and the second to last MRI in HCC naive patients were included for evaluation. Imaging data consisting of the SMS sequences (T2 W fat saturation, DWI ($b = 0$ and 600, 800) and T1 W in-and oppose phase) was anonymized and uploaded on a separate research server. Two radiologist with different levels of experience (reader 1: 12 years, tertiary center; reader 2: 4 years, general hospital) reviewed the imaging data independently and blinded for all patient data, in a dedicated research software environment "openclinica". Confidence scores on presence, size and type of lesions per MR sequence were attributed to a five-point scale: (1) HCC, (2) probably HCC, (3) uncertain, (4) benign, (5) no lesions. Results were compared to the reference standard (full CE-MRI liver protocol). Intra-reader agreement, sensitivity, specificity, false negative and false positive values were calculated with use of Excel and SPSS.

Results: $N = 215$ patients were included; of whom 78 (83%) had cirrhosis and the remaining 37 patients had non-cirrhotic hepatitis. Thirty-nine patients (18.1%) had true HCC. The intra-class correlation coefficient (ICC) was good (0.82). Reader 1 scored better (sens. 94%, spec. 80%, false neg. 6%, false pos. 20%) than reader 2 (89%, 72%, 11%, 29% respectively). When "uncertain" lesions were also included as suspect for HCC then specificity increased for both readers, albeit with loss of sensitivity (reader 1: sens. 78%, spec. 95%, false neg. 22%, false pos. 5%; and reader 2: 72%, 94%, 28%, 4%, respectively).

Discussion/Conclusion: Our proposed Short MRI Surveillance (SMS) protocol yields a robust sensitivity and specificity for detection of early HCC with respect to what is typically reported for ultrasound, both for the experienced and in-experienced observer.

References:

1. EASL Clinical Practice Guidelines: Management of hepatocellular carcinoma. J Hepatol. 2018;69(1):182. Epub 2018 Apr 5.
2. 2018 Practice Guidance by the American Association for the Study of Liver Diseases. Hepatology. 2018;68(2):723.

S11.07

Comparative evaluation of multifrequency MRE parameters for the assessment of fibrosis and inflammation in a small animal model of nonalcoholic steatohepatitis

F. Julea[1], M. Dioguardi Burgio[2], V. Paradis[3], S. Doblas[1], G. Pagé[1], V. Vilgrain[2], B. van Beers[2], P. Garteiser[1]
[1]Laboratory of Imaging Biomarkers, UMR1149 INSERM-University Paris Diderot, Paris, FRANCE, [2]Radiology department, Hôpital Beaujon, AP-HP, Clichy, FRANCE, [3]Histopathology department, Hôpital Beaujon, AP-HP, Clichy, FRANCE

Purpose/Introduction: In hepatology, there is a lack of imaging methods to diagnose nonalcoholic fatty liver disease (NAFLD) and steatohepatitis (NASH). Although the steatosis and fibrosis components are quite well characterized[1, 2] the diagnosis of inflammation and ballooning (necroinflammation) still lacks validated markers. Viscoelastic parameters determined with MR elastography (MRE) (loss modulus) were recently proposed[3]. Here we evaluate the frequency response of viscoelastic parameters as potential markers of necroinflammation in an animal model of NAFLD.

Subjects and Methods: Experiments were approved by the Institutional Ethics Committee. Mice under a high fat, choline-deficient, methionine supplemented (CDA-HFD) diet (or normal diet (ND) controls) were examined with MRE prior to histopathological examination (fibrosis, ballooning, inflammation) at 5 ($N = 8$, $N = 7$ ND), 11 ($N = 10$) and 16 ($N = 10$) weeks of diet. MRE was acquired at 7T ($300\ \mu m^3$, $TR/TE = 1$ s/30 ms, 4 time steps, 3d encoding, 400, 600 and 800 Hz frequencies acquired sequentially). Liver viscoelastic parameters (storage modulus G', loss modulus G″, stiffness $|G^*|$) were calculated[4], and multifrequency coefficients ("slopes") were extracted by fitting a powerlaw (i.e. $G(\omega) \approx \omega^{\gamma}$). Single frequency results analysis was carried out on 400 Hz data only. Multifrequency results analysis were carried out on $\gamma_{G'}$ only. Kruskall-Wallis tests were used to evaluate differences between diet time points, and Mann–Whitney tests and ROC analyses were used to evaluate the relationships with histologic features.

Results: Mechanical properties at 400 Hz tended to increase with increasing diet durations (G' (kPa): 0.39 ± 0.09, 0.61 ± 0.12, 0.72 ± 0.16, 0.69 ± 0.16, $p = 0.00085$; G'' (kPa): 0.27 ± 0.08, 0.43 ± 0.10; 0.56 ± 0.12, 0.53 ± 0.17, $p = 0.00072$; $|G^*|$ (kPa): 0.50 ± 0.12; 0.77 ± 0.16; 0.96 ± 0.21; 0.90 ± 0.24, $p = 0.000941$ for ND, CDA-HFD at weeks 5, 11 and 16, respectively). $\gamma_{G'}$ decreased during diet (1.21 ± 0.48; 0.83 ± 0.21; 0.59 ± 0.18; 0.84 ± 0.39, $p = 0.034$), Fig. 1. $|G^*|$ at 400 Hz was connected to fibrosis ($p < 0.0001$, $AUC = 0.87$[0.76–0.99]), while G″ was connected to inflammation ($p < 0.0001$, $AUC = 0.96$[0.91–1]) and ballooning ($p = 0.0012$, $AUC = 0.80$[0.66–0.93]) (Fig. 2). $\gamma_{G'}$ was only correlated to inflammation ($p = 0.002$, $AUC = 0.80$ [0.64–0.96]).

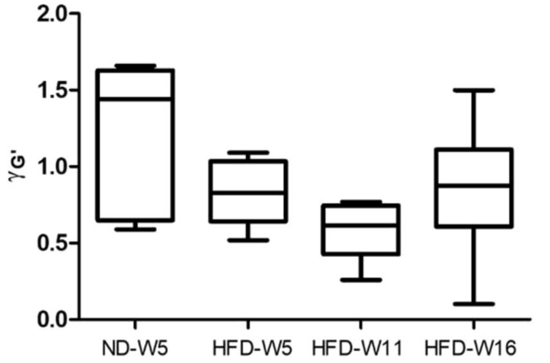

Fig.1 γG' for the control group (ND-W5) and the high fat diet groups at the various tested timepoints (HFD-W5, HFD-W11 and HFD-W16). A trend towards a decreased value is observed as the diet duration increases.

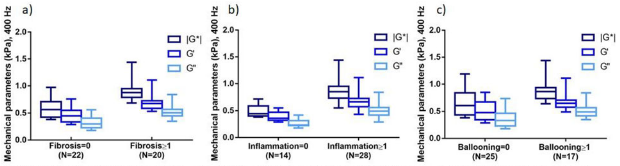

Fig.2 Box plots of mechanical parameters (|G*|, G', G") at 400 Hz in all experimental groups according to absence or presence of fibrosis (a), inflammation (b) and ballooning (c).

Discussion/Conclusion: Our results are in line with recent literature results where stiffness and loss modulus were proposed to assess fibrosis and lobular inflammation[5]. Despite its small size and the relative sparseness in histology results, our study additionally suggests loss modulus as a good indicator of ballooning. $\gamma_{G'}$ was a promising and potentially specific marker of inflammation rather than ballooning. The combination of single and multi-frequency MR elastography could potentially provide a better characterization of necroinflammation in NAFLD and NASH.

References:

[1]Yokoo, Radiol., 2009
[2]Park, Gastroenterology, 2017
[3]Yin, Eur. Radiol., 2019
[4]Sinkus, MRI, 2005
[5]Salameh, Radiol., 2009

S11.08

Assessment of local human brown adipose tissue changes after cold exposure

A. S. D. Sardjoe Mishre[1], J. Burakiewicz[1], G. Abreu-Vieira[2], L. G. Janssen[2], K. J. Nahon[2], M. R. Boon[2], A. G. Webb[1], P. C. N. Rensen[2], H. E. Kan[1]
[1]Leiden University Medical Center (LUMC), Radiology, Leiden, NETHERLANDS, [2]Leiden University Medical Center (LUMC), Division of Endocrinology, Leiden, NETHERLANDS

Purpose/Introduction: Brown adipose tissue (BAT) plays a role in energy metabolism in humans upon cold exposure, as it generates heat by burning free fatty acids. Hence, BAT activation has gained attention as a potential therapeutic target in cardiometabolic diseases. Changes in MRI-derived fat fraction (FF) and T2* have been reported in the human supraclavicular BAT (scBAT) depot after cold exposure[1–2]. Usually, overall changes in FF and T2* of the scBAT repository are quantified, regularly with the use of initial FF thresholds to focus on BAT rather than white adipose tissue. However, it is unclear at what initial FF and T2* most changes after cold exposure occur, making these thresholds arbitrary. By co-registering pre-and post-cold images, we now aimed to asses local FF-and T2* changes after cold exposure.

Subjects and Methods: Ten healthy Europid male volunteers were included (22.9 ± 0.7 years). Each participant underwent a personalized cooling protocol for BAT activation. Pre- and post-cooling images were acquired on a 3T scanner (Philips, Ingenia) using 3D 6-point Dixon: TR = 15 ms, TE1 = 1.98 ms, ΔTE 1.75 ms, FA 8°, FOV 480 mm × 300 mm × 90 mm and 1.1 mm isotropic resolution. Using a large ROI encompassing the scBAT region (fig. 1), analysis was performed using two methods: (i) image registration for voxel-wise comparison (FF_{loc} and $T2^*_{loc}$) and (ii) binary mask deformation for global volume, FF and T2* analysis (VOL_{glob}, FF_{glob} and $T2^*_{glob}$). For both analysis methods voxels below 20% FF were excluded. The distribution of FF_{loc} changes after cold-exposure was assessed using K-means clustering and scBAT volume, FF_{glob} and $T2^*_{glob}$ before and after cold exposure were assessed using paired-sample t-tests ($p < 0.05$).

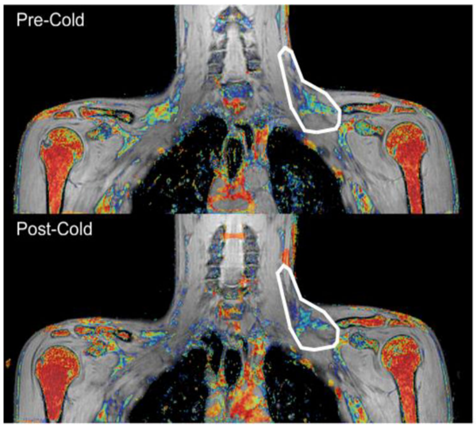

Figure 1. scBAT ROI placement. For both methods, ROIs were only delineated on the pre-cooling scan. For voxel-wise analysis, the post-cooling images were deformed, while for the global analysis only the ROIs were deformed.

Results: Voxel-wise analysis showed that FF changes after cold-exposure occurred along nearly the entire initial FF range (Fig. 2A), but that most decreases in FF occurred at the higher initial FFs 69.1 ± 16.1. $T2^*_{loc}$ analyses showed that decreases in FF_{loc} after cold exposure were accompanied by increases in T2* (Fig. 2B). For the global analysis, mean FF_{glob} decreased (Fig. 3), but no significant changes were present in VOL_{glob} and $T2^*_{glob}$.

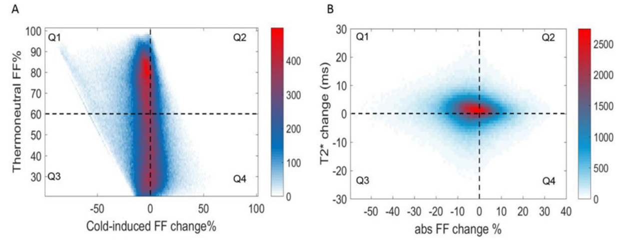

Figure 2. Voxel-wise analysis resulted in 3D voxel-density plots, where in Figure 2.A each point represents voxel counts related to an initial FF and absolute FF change. Voxels associated to FFloc and T2*loc dynamics are shown in Figure 2.B.

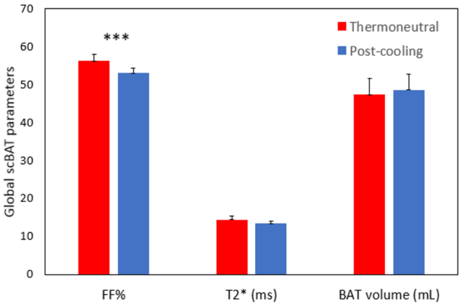

Figure 3. Global BAT volume, FF-and T2* values of the scBAT depot before and after cooling. Values are presented as mean±SE; * p<0.05, ** p<0.01 and *** p<0.0001.

Discussion/Conclusion: Global analysis showed that, as expected, cold exposure decreased overall FF, but did not change BAT volume and T2*. Voxel-wise analysis showed that the changes in FF are mostly due to decreases in FF at initial FFs of above 69%. The association between locally decreased FFs and increased T2* values might be indicative of BAT activity, possibly due to intracellular lipolysis for lipid combustion and increased perfusion[2–3].

References:

1. PMID: 25928226.
2. PMID: 23255760.
3. PMID: 26092667.

S11.09

A single-center large retrospective analysis on biparametric prostate MRI

F. Pesapane[1, 2], G. M. Agazzi[3], P. Tantrige[4], M. Acquasanta[1], M. Codari[5], C. Mattiuz[5], A. Esseridou[5], F. Sardanelli[6]
[1]Università degli Studi di Milano, Postgraduation School in Radiodiagnostic, Milan, ITALY, [2]-, -, -, ITALY, [3]Universita degli Studi di Brescia, Radiology Department, Brescia, ITALY, [4]King's College Hospital, Interventional Radiology, London, UNITED KINGDOM, [5]IRCCS Policlinico San Donato, Radiology Department, San Donato Milanese, ITALY, [6]Università degli Studi di Milano, Department of Biomedical Sciences for Health, Milan, ITALY

Purpose/Introduction: Dynamic contrast-enhancement (DCE) sequences have a limited role in the detection of prostate cancer (PCa) and there is growing interest in performing multiparametric MRI (mpMRI) without DCE, termed biparametric MRI (bpMRI). We aimed to compare the diagnostic performance of bpMRI against mpMRI in patients with elevated PSA levels.

Subjects and Methods: Single-center 1.5-T images of prostate-MR in 431 men (mean age: 61.5 years, SD: 8.3;) with PSA ≥ 4.0 ng/mL (mean PSA 12.0 ng/mL, free PSA: 19%) were included in a retrospective analysis. Complete studies (mpMRI) and the same studies with the DCE sequences removed (bpMRI) were independently assessed in separate reporting sessions ≥ 1 month apart and in a random order by 2 radiologists of 5 (R1) and 3 (R2) years experience. The results were recorded and compared using the PI-RADSv2 criteria. Histopathological analysis or ≥ 2 -years of follow-up served as a reference standard. Using a dichotomized score with PI-RADS score ≥ 3 as the threshold for a positive exam, diagnostic performance was calculated and compared between mpMRI and bpMRI for each reader. Cohen's k were used to calculate interobserver agreement.

Results: Our final study population consisted in 195/431 (45, 3%) histopathologically proven PCa, with 62/195 (31.8%) high-grade PCa (GS ≥ 7b) and 133/195 (68.2%) low-grade (GS = 6/7a). PCa could be excluded by histopathology in 58/431 (13.5%) patients and by follow-up in 178/431 (41.3%) patients. For bpMRI, the sensitivity was 164/195 (84%, 95% CI 79–89%) for R1 and 156/195 (80%, 95% CI 74–86%) for R2; the specificity was 182/236 (77%, 95% CI 72–82%) for R1 and 175/236 (74%, 95% CI 68–80%) for R2. For mpMRI, the sensitivity was 168/195 (86%, 95% CI 81–91%) for R1 and 160/195 (82%, 95% CI 77–87%) for R2; the specificity was 184/236 (78%, 95% CI 73–83%) for R1 and 177/236 (75%, 95% CI 69–81%) for R2. The bpMRI resulted in 4 more false negative cases, compared to mpMRI, for both R1 and R2 and all of these were low-grade PCa. No high-grade PCa was missed with bpMRI. High and similar accuracy of bpMRI (80% for R1 and 77% for R2) and mpMRI (82% for R1 and 78% for R2) indicated clinically relevant predictive characteristics for both approaches. Interobserver agreement was substantial for both bpMRI ($\kappa = 0.802$) and mpMRI ($\kappa = 0.787$).

Discussion/Conclusion: The diagnostic accuracies of bpMRI and mpMRI were similar, especially in the detection of high-grade PCa. The use of bpMRI could eliminate the retention and the adverse events of gadolinium-based contrast agents, shorten examination time and reduce costs, possibly resulting in increased accessibility of MRI for biopsy-naïve men with elevated PSA levels.

References:

J.C. Weinreb et al. Eur Urol 69(1) (2016) 16–40.
J.E. Thompson D. et al. J Urol 192(1) (2014) 67–74.
P. De Visschere et al. Clin Radiol 72(1) (2017) 23–32.
B. Turkbey, et al. Eur Urol, in press (2019).

L03 Lightning Talks

10:50–11:50 *The Stage*

Diffusion, Perfusion & CEST

L03.01

Characterization of heating artifacts in opto-fMRI studies

D. Schache, F. Albers, L. Wachsmuth, C. Faber
Westfälische Wilhelms-Universität Münster, Institut für klinische Radiologie, Münster, GERMANY

Purpose/Introduction: In optogenetic applications such as opto-fMRI, laser light to control light-sensitive proteins is often delivered directly to the brain via a fiber. This can lead to a heating of the surrounding tissue due to the introduced laser power and therefore cause fMRI responses in the absence of optogenetic activation. This effect is called apparent BOLD or heating artifacts and must be distinguished from true BOLD activation [1] [2].

Subjects and Methods: The experiments were performed on 7 Fisher rats under medetomidine sedation at 9.4T. Optical stimulation with a green laser (λ = 552 nm, 183 mW/mm^2, 9 Hz, 100 ms pulse duration) and electrical fore paw stimulation (1.5 mA, 9 Hz, 1 ms pulse duration) were applied. A block design paradigm consisting of 10 s rest, 5 s stimulation and 15 s rest (10-5-15) was repeated 20 times. A GE-EPI sequence with TR 250 ms, TE 18 ms, FA 30°, 2–3 slices (n_{elek} = 18, n_{opt} = 18) and a diffusion-weighted SSE sequence with TR 250 ms, TE 35.85 ms, FA 150°, Δ 15 ms, δ 2 ms, b 500 s/mm^2, 2–3 slices (n_{elek} = 20, n_{opt} = 18) were used; each of these had a slice thickness of 1.2 mm and a resolution of 0.325 × 0.35 mm^2.

The recorded data was statistically evaluated after preprocessing by SPM12 using a t-test. The area of the most contiguous pixels was selected as a ROI in each relevant layer and the time courses were calculated, normalized to 1 and displayed in MATLAB.

Results: Electrical stimulation resulted in positive signal changes in both EPI and DWI. Signal changes were delayed with respect to stimulus onset according to the expected hemodynamic response; additionally, EPI signal was delayed with respect to diffusion signal (Fig. 1 right).

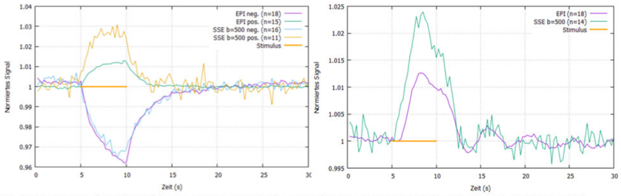

Fig. 1: Time courses for EPI and SSE measurements in the fiber slice for optical stimulation (left) and electrical stimulation (right).

Optical stimulation resulted in pronounced negative signal changes, but also positive changes with lower amplitude (Fig. 2). No delayed onset with respect to start of stimulation was observed. There was also no delay between EPI and diffusion signal (Fig. 1 left).

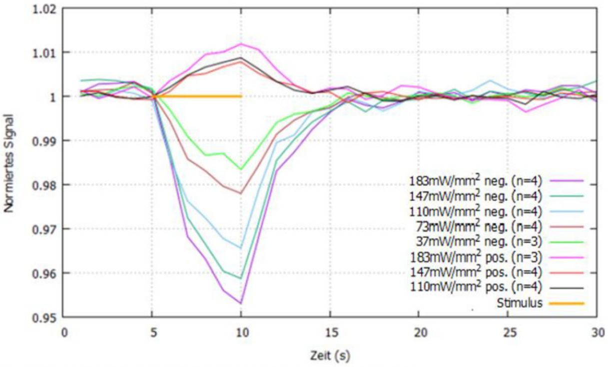

Fig. 2: Time courses for EPI measurements (TE 1s) in the fiber slice at different laser powers.

Using electrical stimulation, the maximum signal change was observed shortly after the onset of the stimulation for both sequences, whereas with optical stimulation the maximum signal change was observed within the last 0.5 s of the stimulation period (Fig. 1).

Both the amplitude (Fig. 2) and spatial extent of the signal changes increased with increasing laser power. Signal changes extended from the fiber slice to neighboring slices with a detectable time lag.

Discussion/Conclusion: Observable signal changes in optical (i.e. heat application) and electrical stimulation differ significantly for both EPI and DW SSE sequences. Signal changes in DW measurements upon electrical stimulation are therefore not (exclusively) due to heat effects. The injected laser power results in measurable signal changes.

References:

[1] Christie IN, Neuroimage (2013), 1(66):634–41.
[2] Schmid F, Magn Reson Med (2017), 77(1):126–36.

L03.02

Comparison of MEMRI and diffusion MRI evaluation of a feeding/fasting paradigm in glioblastoma bearing rats

S. González, **I. Guadilla**, T. Navarro-Hernanz, P. López-Larrubia
Instituto de Investigaciones Biomédicas Alberto Sols CSIC-UAM, Madrid, SPAIN

Purpose/Introduction: Magnetic resonance imaging (MRI) allows carrying out studies of neuronal activity in response to certain stimuli, such as the regulation of appetite, which is involved in numerous disorders of the global energy balance. Manganese-enhanced MRI (MEMRI) [1] and diffusion tensor imaging (DTI) [2], are approaches that enable the study of the brain functionality. On the other hand, HRMAS ex vivo analysis can identify metabolites as surrogate markers of healthy and pathological brain conditions [2].

Subjects and Methods: Wistar adult male rats were distributed in three groups (n = 12): i) controls without Mn^{2+}; ii) healthy animals with $Mn^{2+}$and iii) orthotopic glioma bearing rats [3] with Mn^{2+}. Animals were studied in two experimental conditions: fed ad libitum and fasted. $MnCl_2$ was injected intraperitoneally 24 h before the MRI evaluation in a 7T system. T1 parametric maps were generated for MEMRI evaluation (7TR/TE = 150–6000/12 ms). DTI studies were acquired by applying diffusion gradients in 6 directions (TR/TE = 3000/40 ms; Δ/δ = 16/4 ms; 3b (0–1000 s/mm2). Images were computed with homemade software and ROIS were manually selected and statically analyzed.

Animals were sacrificed with a high-power microwave, brain excised and regionalized. 1H HRMAS CPMG spectra of the different regions were acquired in a 11.7T system and processed with LCModel.

Results: The accumulation of manganese in brain yielded to a significant decrease of T1 in all groups (healthy and glioma bearing), experimental condition (fed and fasted) and brain areas evaluated (fig. 1a, 3a). In healthy and tumor rats the T1 decreased due to the fasting status reaching statistical significance in several regions (fig. 1b, 3a). Regarding on diffusion studies, mean diffusivity (MD) values were sensitive to fasting in healthy animals with a significant decrease (Figs. 2a, 3b); but the ability to detect this metabolic status was lost in the presence of Mn^{2+} (Figs. 2b, 3b). Data from HRMAS spectra also identified changes in metabolites linked to alterations in the global energy metabolism (GABA, glutamate, glutamine), and/or the presence of inflammatory processes (myo-inositol).

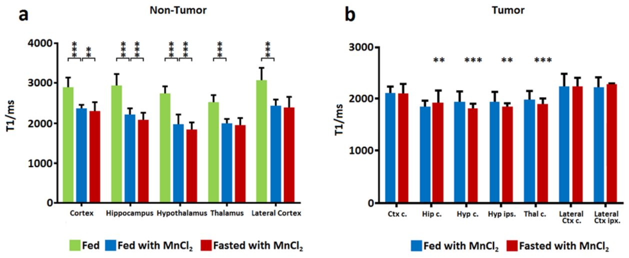

Figure 1. T1 values for MEMRI evaluation in cortex, hippocampus, hypothalamus, thalamus and lateral cortex. a) Non-tumor bearing rats: fed without manganese infusion (green), fed with manganese infusion (blue) and fasted with manganese infusion (red). b) Tumor bearing rats: fed with manganese infusion(blue) and fasted with manganese infusion (red). In this case the results are shown as contralateral and ipsilateral.

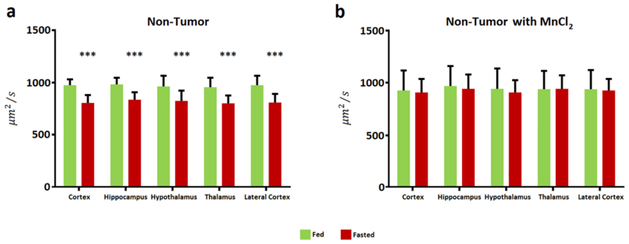

Figure 2. Mean diffusivity values obtained from DWI studies in fed (green) and fasted (red) conditions from non-tumor bearing rats in cortex, hippocampus, hypothalamus, thalamus and lateral cortex. a) Without manganese infusion and b) With manganese infusion.

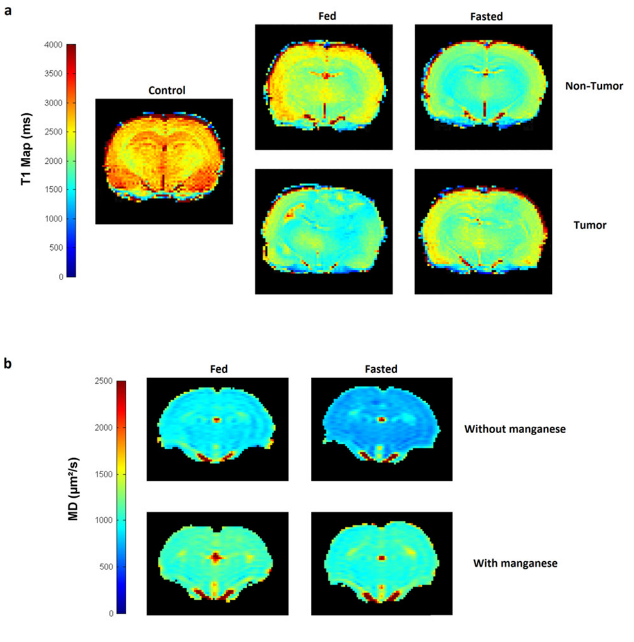

Figure 3. Parametric maps from MEMRI and Diffusion evaluation. a) T1 maps. Control animal (non-tumor bearing, non manganese infusion, fed condition) compared with the different conditions with manganese infusion: non-tumor (up) and tumor (down) bearing animals in fed (left) and fasted (right) conditions. b) Mean diffusivity maps for non-tumor bearing animals without manganese (up) and with manganese infusion (down) in fed (left) and fasted (right) conditions.

Discussion/Conclusion: MEMRI allows to study the brain functionality associated to voltage dependent channels because of the Mn^{2+} competition with Ca^{2+}. In our study, there was a higher neuronal activation (lower T1) in fasted condition. DTI corroborated this by detecting the astrocyte swelling [4], but the presence of Mn^{2+} affects the diffusion parameters avoiding this functional detection. The obtained results evidence the contraindication of performing diffusion MRI evaluation when manganese has been used as contrast agent.

References:

[1] Koretsky AP, et al. NMR Biomed. November 2004; 17(8):527–31.
[2] Bihan AR, et al. PLOS Biol. July 2015; 13(7):e1002203.
[3] Borges AR, et al. Am J Neuroradiol. January 2012; 33(1):24–36.
[4] Lizarbe B, et al. NeuroImage. January 2013; 64:448–57.

L03.03

Improved accuracy of fibers tractography with use of BSD-DTI method: a study on a human muscle

R. Obuchowicz[1], A. Krzyżak[2]
[1]*Collegium Medicum of Jagiellonian University, Kraków, POLAND,*
[2]*AGH University of Science and Technology, Kraków, POLAND*

Purpose/Introduction: In a biological settings many tissues play a role of solutions and fluids conductors with elementary structure of narrow tubes generally called fibers. Fibers limit diffusion multidirectionally with unrestricted water transport in the one direction which can be effectively imaged with use of EPI sequence.

With use of the deterministic tractography, representation of the given biological fiber is built along the vectors of known largest secondary eigenvalue.

Unfortunately, representation of the fibers eigenvalue magnitude and eigenvector position is strongly influenced by systematic errors, in prevalence induced by concomitant field and eddy currents.

Uncontrolled b-matrix alterations make imaged fibers tracts unrepresented or misshapen. Bammer for the first time turned attention on heterogeneity of the non uniformity of the gradients, generated by gradient coils with suspected errors in subsequent measurements (1).With the novel idea of correction of the systematic errors (BSD-DTI) with use of anisotropic phantoms, we are able to present significant improvement of the representation of visualized fibers (2, 3). Aim of this study was to present the impact of BSD-DTI correction of diffusion tensor shape on the visualization of biological fibers on the example of muscle tissue.

Subjects and Methods: Experiment was conducted on calf muscles of healthy volunteer.

Calibration was carried out using a phantom consisting of 20 µm diameter glass tubes filled with water, aligned parallelly and enclosed in glass sphere. The b-matrices were determined for consecutive voxels by determination of indiscrete variables, corresponding to the number of row, column and slice, what was performed by solving of at least 6 equations (1, 2).

Results: Fig 1. Representation of muscle fibers calculated with use of the same parameters. The left image (a) with BSD-DTI approach, the right image (b) with standard approach.

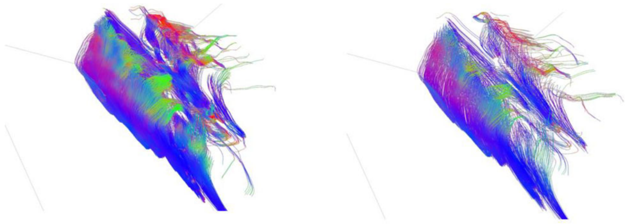

F1

Fig 2. Differences in visualization of muscle fibers (markedly enlarged view) calculated with use of the same parameters. The left image (a) with BSD-DTI approach, the right image (b) with standard approach.

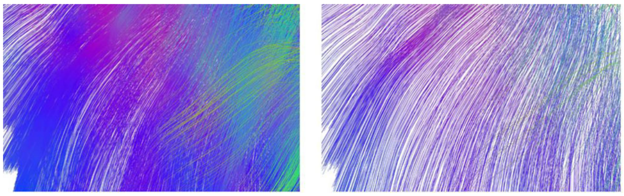

Discussion/Conclusion: Our results present that improvement of the b matrix shape with correction of the systematic errors results in marked improvement in the accuracy of the visualization of fiber tracts of the muscle.

Conslusion: with BSD DTI technique much more accurate, in comparison to standard DTI technique, presentation of the fibers of living tissue is possible.

References:

1. Bammer et al., Magn Reson Med, vol. 50, no. 3, pp. 560–569, Sep. 2003.

2. Borkowski K, Krzyżak AT. J Magn Reson. 2018 Nov;296:23–28.

3. Krzyzak AT, Olejniczak Z, Magnetic Resonance Imaging 2015; 33:286–295.z

Acknowledgements: The work was partly financed by the National Centre of Research and Development, contract no. STRATEGMED2/265761/10/NCBR/2015

L03.04

WITHDRAWN

L03.05

Variability of NODDI metrics between AMICO and original NODDI in UK Biobank data

I. I. Maximov, L. T. Westlye

University of Oslo, Oslo, NORWAY

Purpose/Introduction: Diffusion MRI is very promising tool for non-invasive probing and visualisation of living tissue such as human brain. Many different diffusion models are developed and applied in clinical studies, for example, CHARMED^{1}, WMTI^{2}, RSI^{3}. Neurite orientation distribution diffusion imaging (NODDI) has gained popularity due to its simple and elegant theoretical description of white matter architecture$^{4, 5}$. The original NODDI model^{4} is computationally demanding and time consuming. As a result, the Accelerated Microstructure Imaging via Convex Optimization (AMICO)^{6} model was proposed, which estimates the same parameters with substantially lower computational demands. However, NODDI has been reported to suffer from numerical issues related to degeneracy in the case of multi-compartmental diffusion models$^{7, 8}$. In the present study we aim to compare relevant NODDI parameters between the original NODDI and AMICO models using human brain diffusion MRI from the UK Biobank (UKB) ^{9}.

Subjects and Methods: We included 182 subjects. Two datasets were post-processed along two diffusion pipelines: an optimised diffusion pipeline (OP)^{10} and original UKB pipeline^{9}. The AMICO metrics released by the UKB includes neurite density (ND), isotropic water fraction (ISO), and orientation distribution parameter (ODI). For data processed using our OP we computed the same metrics using both the original NODDI and AMICO algorithms. Voxel-wise statistical comparisons between diffusion metrics derived from OP and UKB were carried out using TBSS^{9}. In addition, we correlated the mean skeleton values from the different pipelines and models.

Results: Figure 1 shows results from the TBSS analysis. On the left panel, we present a comparison between NODDI AMICO algorithm for OP and UKB pipelines. On the right panel, the results for two NODDI algorithm are shown using OP processed data. Figure 2 shows a distribution of the mean diffusion metrics averaged over the TBSS skeletons prepared by OP.

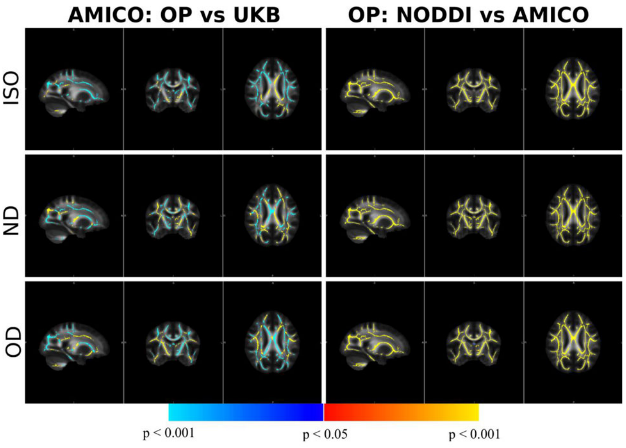

Figure 1. TBSS analysis between NODDI metrics. Left: difference between two pipelines for AMICO. Right: difference between orig. NODDI and AMICO for OP.

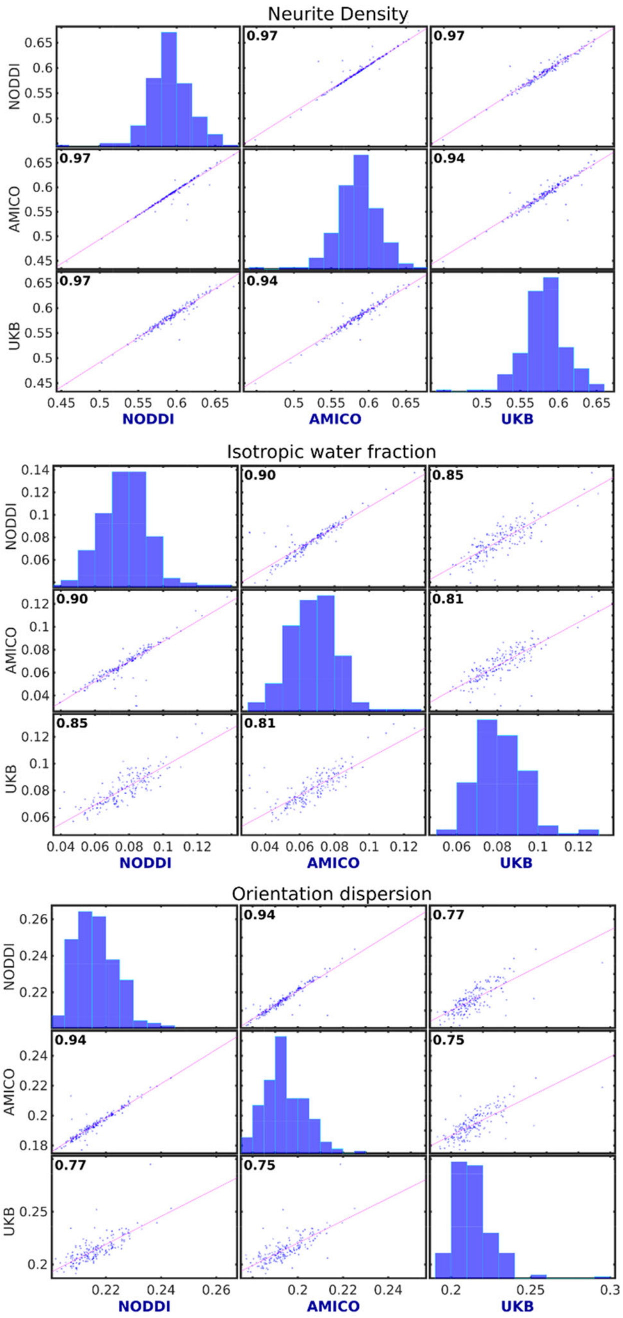

Figure 2. Correlation plots and Pearson correlation coefficients for NODDI metrics estimated from optimised pipeline (NODDI and AMICO) and original UKB data (UKB; AMICO).

Discussion/Conclusion: Diffusion MRI models offer remarkable opportunities to characterise and visualise brain tissue geometry, but the reliability of the models influences the biological interpretations and validity of the tissue representation. Here, our comparison revealed robust differences in ND, ODI and ISO between the original NODDI algorithm and the AMICO model, respectively. Interestingly, that original NODDI algorithm possesses a good correlation with both AMICO data for all metrics. In conclusion, we stress here that NODDI model is very sensitive to the pipeline and chosen algorithm.

References:

1 Assaf and Basser, NI 27 (2005) 48.
2 Fieremans et al., NI 58 (2011) 177.
3 White et al., HBM 34 (2013) 327.
4 Zhang et al., NI 61 (2012) 1000.
5 Tariq et al., NI 133 (2016) 207.
6 Daducci et al., NI 105 (2015) 32.
7 Jelescu et al., NI 107 (2015) 242.
8 Jelescu et al., NMR Biomed 29 (2016) 33.
9 Miller et al., Nature Neurosci 19 (2016) 1523.
10 Maximov et al., bioRxiv 511964.

L03.06

MR tractography and MR neurography of brachial plexus

I. Ibrahim[1], J. Tintera[1], J. Beran[1], A. Skoch[1], M. Nagy[1], E. Rolencova[1], I. Humhej[2], V. Flusserova[3], M. Hajek[1]
[1]IKEM, MR Unit, Prague, CZECH REPUBLIC, [2]J. E. Purkyně University, Masaryk Hospital, Department of Neurosurgery, Usti nad Labem, CZECH REPUBLIC, [3]IKEM, Department of Neurology, Prague, CZECH REPUBLIC

Purpose/Introduction: The goal of the study was to visualize and assess the integrity of brachial plexus (BP) using advanced MR techniques sensitive to water diffusion (MR tractography—MRT) combined with high-resolution 3T MR neurography (MRN) technique (1).

Subjects and Methods: Eight subjects (7 controls. mean age 39.3 ± 7.3 years and 1 patient with C7-Th1 roots avulsion, age 33 years) underwent MR examination on a 3T MR scanner (Siemens Magnetom Trio) using phased-array body coil with following protocol:

1. Diffusion-weighted imaging using spin-echo echo-planar imaging (SE-EPI) sequence with the acquisition parameters: voxel size of $3 \times 3 \times 3$ mm^3, TR/TE of 7500/82 ms, number of diffusion directions 64 and two b values: 0. 800 s/mm^2.
2. T2 weighted 3D STIR sequence used for high-resolution MRN with the voxel size of $1 \times 1 \times 1$ mm^3. TE of 149 ms. TR of 2000 ms and TI of 160 ms.

The DTI data were corrected for distortions and eddy current effects using FSL (www.fmrib.ox.ac.uk/fsl/index.html). To reconstruct the fiber pathway, regions of interest (ROIs) were manually selected in the EPI at different levels of the spinal cord nerves.

The diffusion data were calculated from C5 to C8 bilateral reconstructed spinal nerves using DSI studio (http://dsi-studio.labsolver.org/). The indices based on diffusion and density (normalized quantitative anisotropy—NQA), fractional anisotropy (FA), generalized fractional anisotropy (GFA), mean diffusivity (MD), axial diffusivity (AD) and radial diffusivity (RD) in the BP nerves were calculated and statistically analyzed with two-tailed t-test.

MR neurograhy has been done in MedINRIA and enhanced with 3D mode – maximum intensity projection (< a href = "http://med.inria.fr/" > http://med.inria.fr/).

Results: The two-tailed t-test found no significant effect of laterality of the BP in the control subjects ($p = 0.45$ for NQA and $p = 0.68$ for FA. $p = 0.49$ for GFA. $p = 0.94$ for MD. $p = 0.91$ for AD. $p = 0.82$ for RD, Table 1, Fig. 1). Diffusion indices values calculated in the left C5–C8 and C5–6 (right) nerves in the patient with C7-Th1 avulsion were (left/right side): NQA (0.09/0.12), FA (0.18/0.24), GFA (0.08/0.89), MD ($2.72/2.20 \times 10^{-3}$ mm^2/s), AD ($3.18/2.67 \times 10^{-3}$ mm^2/s), and RD ($2.51/1.96 \times 10^{-3}$ mm^2/s). Patient shows higher diffusivity in the left BP with avulsions. The results of the MRT and MRN are shown in Fig. 1.

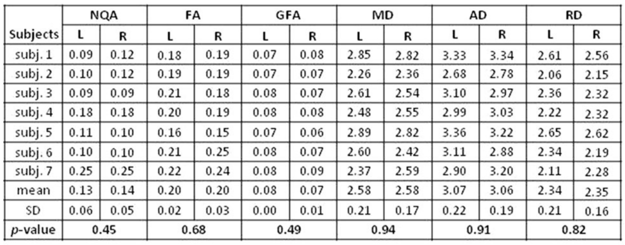

Subjects	NQA		FA		GFA		MD		AD		RD	
	L	R	L	R	L	R	L	R	L	R	L	R
subj. 1	0.09	0.12	0.18	0.19	0.07	0.08	2.85	2.82	3.33	3.34	2.61	2.56
subj. 2	0.10	0.12	0.19	0.19	0.07	0.07	2.26	2.36	2.68	2.78	2.06	2.15
subj. 3	0.09	0.09	0.21	0.18	0.08	0.07	2.61	2.54	3.10	2.97	2.36	2.32
subj. 4	0.18	0.18	0.20	0.19	0.08	0.08	2.48	2.55	2.99	3.03	2.22	2.32
subj. 5	0.11	0.10	0.16	0.15	0.07	0.06	2.89	2.82	3.36	3.22	2.65	2.62
subj. 6	0.10	0.10	0.21	0.25	0.08	0.07	2.60	2.42	3.11	2.88	2.34	2.19
subj. 7	0.25	0.25	0.22	0.24	0.08	0.09	2.37	2.59	2.90	3.20	2.11	2.28
mean	0.13	0.14	0.20	0.20	0.08	0.07	2.58	2.58	3.07	3.06	2.34	2.35
SD	0.06	0.05	0.02	0.03	0.00	0.01	0.21	0.17	0.22	0.19	0.21	0.16
p-value	0.45		0.68		0.49		0.94		0.91		0.82	

Table 1. Mean normalized quantitative anisotropy (NQA), fractional anisotropy (FA), generalized fractional anisotropy (GFA), mean diffusivity (MD $\times 10^{-3}$ mm^2/s), axial and radial diffusivities (AD and RD $\times 10^{-3}$ mm^2/s) values calculated in C5-C8 nerve roots in seven examined volunteers in the left (L) and right (R) brachial plexus.

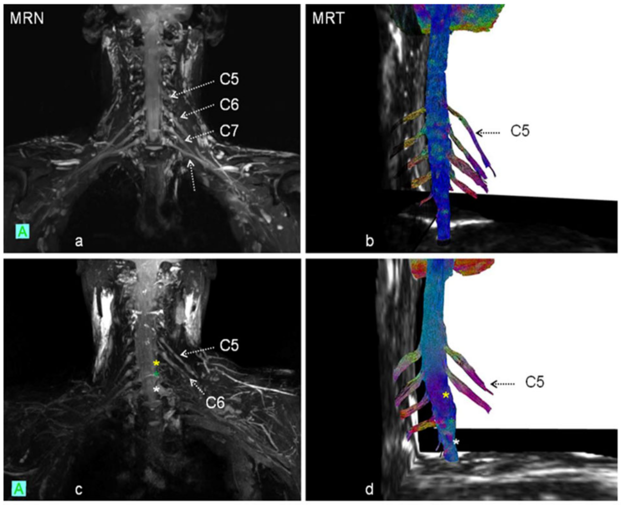

Fig 1. 3D MR neurography (MRN) reconstruction from a coronal 3D STIR SPACE dataset in a 20-year-old healthy volunteer (a) and MR tractography (MRT) results (b) show the architectural configuration of the reconstructed brachial plexus (C5-C8). The images (c and d) show the corresponding results of MRN and MRT in a 33-year-old patient with C7-Th1 avulsion roots of the left brachial plexus (asterisks - yellow, green and white).

Discussion/Conclusion: MR tractography and MRN are shown to be able to successfully visualize and assess the integrity of PN structures. These techniques can help in decision making in many peripheral nerves pathologies in terms of correct diagnosis establishment, conservative versus surgical treatment, pre-surgical planning and post-operative follow-up.

“Supported by Ministry of Health of the Czech Republic, grant No. 17-28587A and MHCZ-DRO 00023001IKEM.”

References:

1). Mallouhi Aet al. 3T MR tomography of the brachial plexus: structural and microstructural evaluation. Eur J Radiol. 2012 Sep;81(9):2231–45.

L03.07

A comparison of response function tensor models for multi-tissue spherical deconvolution

J. Morez, J. Sijbers, B. Jeurissen
University of Antwerp, Department of Physics, imec-Visionlab, Antwerp, BELGIUM

Purpose/Introduction: Multi-tissue spherical deconvolution[1] (MT-SD) estimates the white matter (WM) fiber orientation density function (fODF) and the apparent densities of gray matter (GM) and cerebrospinal fluid (CSF) by assuming that each tissue fODF can be retrieved through deconvolving the diffusion weighted (DW) signal with the tissue response functions (RF). Currently, Zonal Spherical Harmonics (ZSH) are used to represent the RFs for each tissue type[2]. As ZSH only model the angular dependencies of the signal, it requires the DW sampling to be shell-wise. Models that can describe both the angular and radial dependencies of the signal responses can enable MT-SD of non-spherically sampled data[3], broadening the range of DW datasets that can be analysed with MT-SD[4, 5]. In this work, we assess the ability to describe WM, GM and CSF RFs of different (high order) tensor models[6] and investigate the effect of choosing these models on the estimated fODFs.

Subjects and Methods: Using a multi-shell data set (b = 0, 250, 500, 1000, 2000, 3000 and 4000 s/mm^2 in 11, 45, 45, 45, 45, 66 and 66 directions, respectively), we compared 3 models that can describe the radial dependence of the signal to the ZSH model: 1) a 2nd order tensor model (DT2); 2) a 4th order tensor model (DT4); and 3) a 4th order tensor model with offset (DT4+ offset). Each tensor model was simplified by imposing axial symmetry for WM and isotropic symmetry for GM and CSF. The resulting RFs were then used to perform MT-SD and the resulting apparent tissue densities were compared.

Results: Figure 1 shows that the WM and GM responses requires a 4th order tensor model to accurately describe the non-monoexponential decay in these tissues types observed at high b-values. For CSF, the offset is required to describe the noise floor. The root-mean-square-errors (RMSE) of the RFs with respect to the ZSH for DT2, DT4, DT4 + offset are respectively: 5.117, 0.871, 0.773 (WM). For GM: 5.237, 1.429, 1.419. For CSF: 7.623, 5.987, 1.641. Figure 2 shows that the apparent tissue densities estimated with DT4 + offset are very close to the state-of-the-art ZSH, whereas the densities estimated using DT2 and DT4 show over- and underestimations up to 15%. Figure 3 illustrates that the fODFs estimated using DT4+ offset and ZSH are practically indistinguishable.

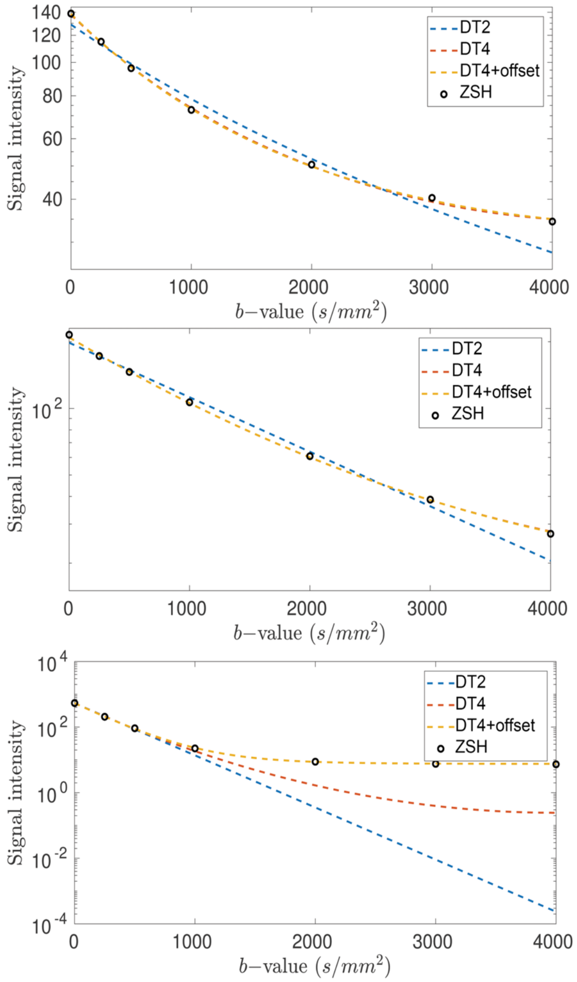

Figure 1: Radial RFs for each tissue type (WM: top; GM: middle; CSF: bottom) compared to those obtained with the ZSH model.

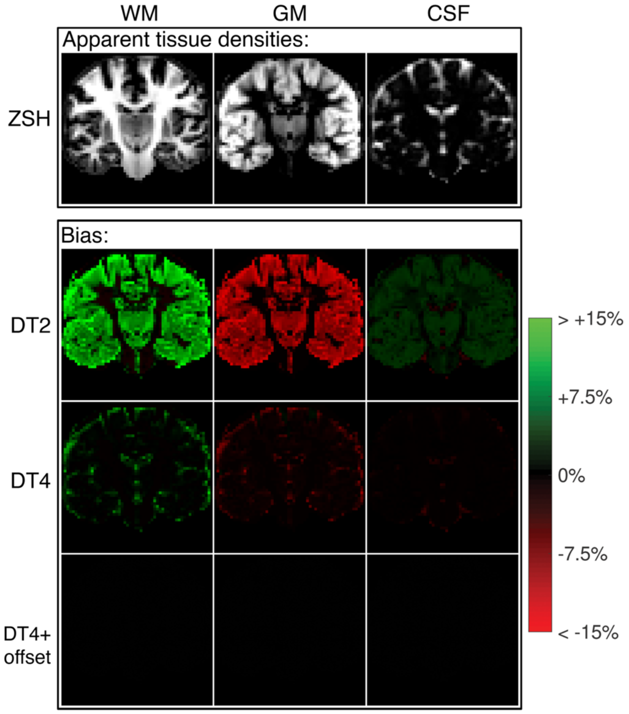

Fig. 2. Apparent tissue densities of WM, GM and CSF estimated using the ZSH RF (top row) and relative deviations from these densities when using the DT2, DT4 and DT4+offset RFs (second to fourth rows).

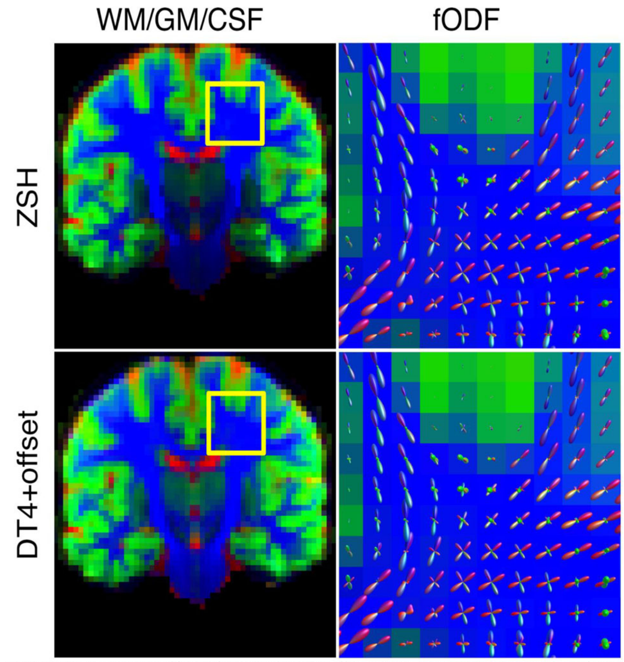

Figure 3: Apparent tissue densities (CSF: red; GM; green; WM: blue) and fODFs (directionally encoded colour) obtained using ZSH RFs (top) and DT4+offset RFs (bottom).

Discussion/Conclusion: The 4th order tensor model + offset provides fODFs that match the state-of-the-art ZSH on shell-based data, while also taking into account the radial dependencies. This enables MT-SD of non-spherically sampled data.

References:

[1] Jeurissen, B. et al. (2014), NeuroImage, 103, 411–426.

[2] Tournier, J.D. et al. (2007), NeuroImage, 35, 1459–1472.
[3] Morez, J. et al. (2017), ISMRM, Volume 25, 66.
[4] Scherrer, B et al. (2012) PLoS ONE 7, e48232.
[5] Wedeen, V.J. et al. (2008), Neuroimage, 41, 1267–77.
[6] Jensen, J.H. et al. (2005), MRM, 53, 1432–1440.

L03.08

Application of anisotropic phantoms with laminar and cylindrical pores to determination of important parameters characterizing porous media

W. Mazur, A. T. Krzyżak
AGH University of Science and Technology, Department of Fossil Fuels, Krakow, POLAND

Purpose/Introduction: Diffusion Tensor Imaging (DTI) and relaxometry are widely used in clinical applications. To improve these methods of imaging in order to explore microscale structures, many approaches have been developed that include application of phantoms. In the work we introduce new anisotropic phantoms that can mimic porous structures with different, well-defined microgeometries- planar and cylindrical, which were tested in different magnetic field strengths in order to determine different physical quantities.

Subjects and Methods: Two water-filled phantoms were measured in low, medium and high magnetic field (0.05 T, 0.6 T and 9.4 T respectively) in terms of diffusion or relaxation. Planar geometry was achieved by separating 99 glass plates (SiO_2) by using cylindrical separators, ensuring water thickness between plates to be equal to 20 μm. Cylindrical geometry was achieved by close packing of 824 photonic fibers (SiO_2), each containing 300 tubes with a diameter of 30 μm. Anisotropic part is a 1 cm × 1 cm × 1 cm cube, which is placed in a Plexiglas enclosure. We measured relaxation in each field strength. DTI was performed in a high field for 6 and 30 diffusion sensitizing directions.

Results: Trimodal relaxation spectrum was obtained in a medium field (Fig. 1A). The low field relaxometry revealed multimodal spectrum with additional peaks associated with surface processes and dipolar interactions (Fig. 1B). Voxel-by-voxel T_2-mapping has shown heterogeneous T_2 spatial distribution and helped to identify regions in which bulk or surface relaxivity dominates (Fig. 2). The application of the BSD-DTI calibration method [1] for 6 diffusion gradient directions allowed us to observe a significant improvement in tractography of cylindrical pores compared to standard DTI for 30 directions.

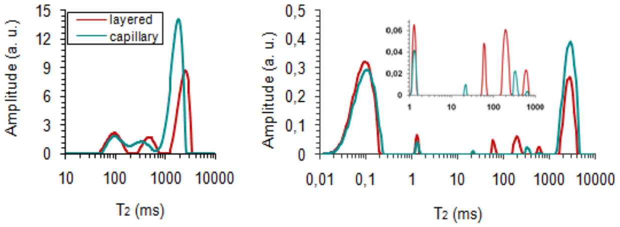

Fig. 1. Relaxation spectrum: A- 0.6 T, B- 0.05 T.

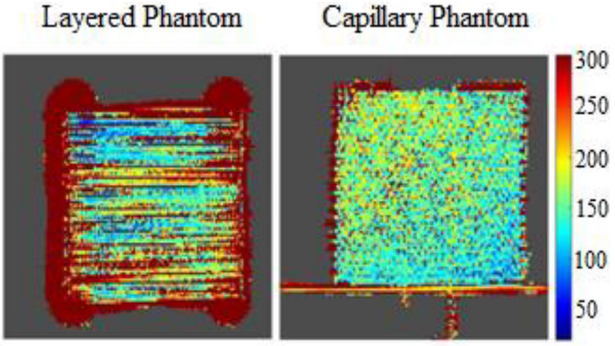

Fig. 2. Voxel-based T2-mapping of phantoms (9.4 T).

Discussion/Conclusion: Anisotropic phantoms presented in the work proved to be very useful for the studies of the behavior of water present in the microscale pore with the vicinity of macroscale pore and interacting with siliceous walls. They can be used for the accurate determination of physical quantities, such as surface relaxivities. The phantoms also evidenced to be excellent standards of diffusion tensor and can be used for verification of new imaging methods.

References:

[1] A. T. Krzyżak and Z. Olejniczak, *Magn. Reson. Imaging*, vol. 33, no. 3, pp. 286–295, 2015.

Acknowledgements: The work was partly financed by the National Centre of Research and Development, contract no. STRATEGMED2/265761/10/NCBR/2015. W.M. has been partly supported by the EU Project POWR.03.02.00-00-I004/16.

L03.09

Combined functional and structural evaluation of language processing augmented with network analysis reveals task-specific lateralization differences: a DTI-fMRI correlation study

G. Gyebnár, L. R. Kozák
Semmelweis University, MR Research Center, Budapest, HUNGARY

Purpose/Introduction: It is a common concept that about 95% of right handers and 75% of left handers show left lateralized language processing. However, the issue of lateralization is more complicated, it depends on the balance of overlapping brain networks subserving the processing of different aspects of language [1]. Here we aimed to investigate whether network analysis can be relevant in the discussion of language processing, especially with respect to pre-surgical lateralization estimation.

Subjects and Methods: We evaluated 39 consecutive patients retrospectively from our clinical database who all underwent routine pre-surgical workup including BOLD fMRI with picture naming, synonym matching, speech comprehension and auditory decision tasks at 3 mm isotropic spatial and 3 s temporal resolution; and diffusion weighted imaging with 32 encoding directions, b = 800 s/mm2, and 2 mm isotropic resolution.

fMRI analysis was performed in SPM12 [2] with standard parameters, then the individual unthresholded activation maps were further analyzed using the ICN_Atlas toolbox [3] with ROIs defined by the AAL atlas labels [4].

DWI data was processed and corrected with ExploreDTI [5] including whole brain DTI tractography and calculating connectivity matrices using the same ROIs.

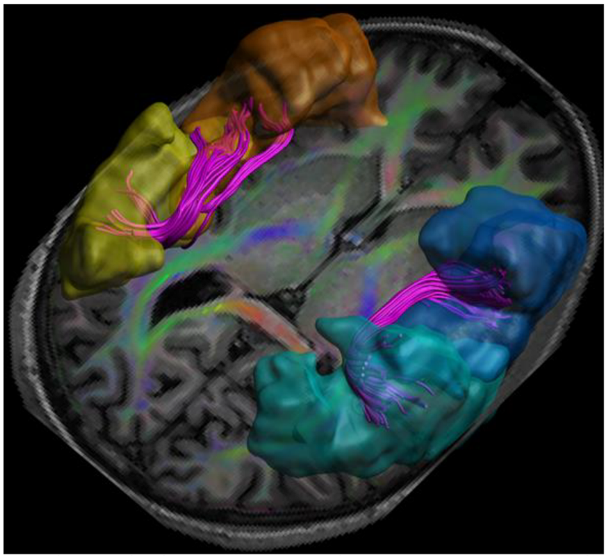

Bilateral ROIs created by fusing frontal and temporo-parietal labels of the AAL-atlas were used to delineate the arcuate fasciculi

Network characteristics of the whole DTI-based structural connectome were calculated with the Brain Connectivity Toolbox [6] and were compared to fMRI-based speech lateralization using conventional parametric statistics in Matlab, focusing on the bilateral AAL labels corresponding to Broca's and Wernicke's areas.

Results: fMRI-based lateralization correlated with structural network parameters in a task dependent fashion: frontal lateralization patterns of the picture naming and synonym tasks, and temporal lateralization patterns of the speech comprehension and auditory decision tasks showed significant positive correlations with the network metrics-based laterality indices of the temporo-parietal regions. The lateralization of the structural descriptors of arcuate fasciculi (AF) correlated with the lateralization of frontal functional language areas.

Discussion/Conclusion: The observed functional-structural correlations in the temporo-parietal network hubs and the prominent correlations between AF structural parameters and frontal fMRI activations are in line with previous literature [7, 8]. Our findings underline the importance of including both functional and structural evaluation augmented with network analysis for the pre-surgical evaluation of language processing.

References:

1. Friederici, Physiol Rev 91: 1357–1392, 2011.
2. https://www.fil.ion.ucl.ac.uk/spm.
3. Kozák et al., NeuroImage, 163:319–341.
4. Tzourio-Mazoyer et al., Neuroimage 15(1):273–89.
5. Leemans et al., ISMRM 2009 p3537.
6. Rubinov & Sporns, NeuroImage 52:1059–69.
7. Wylie KD & Regner, J Neurosci 34 (47) 15505–15507.
8. Propper er al., Brain Cogn 73: 85–92.

L03.10

Optimization of b-values for characterization of glioma by intravoxel incoherent motion (IVIM)

O. Jalnefjord[1], J. Arvidsson[1], I. Björkman-Burtscher[2], M. Ljungberg[1]

[1]University of Gothenburg, Department of Radiation Physics, Gothenburg, SWEDEN, [2]University of Gothenburg, Department of Radiology, Gothenburg, SWEDEN

Purpose/Introduction: Intravoxel incoherent motion (IVIM) analysis of diffusion-weighted images has shown potential for grading of brain tumors [1]. In particular the blood-volume related IVIM parameter f (the perfusion fraction) has been able to differentiate between low-grade and high-grade glioma in multiple studies [2–4]. However, the b-value schemes used in previous studies have in general been typical for exploratory studies including many different b-values not specifically chosen for the tissue or pathology under study.

The aim of this study was to evaluate the potential of b-value optimization for improved estimation precision for the IVIM perfusion fraction f with focus on glioma grading.

Subjects and Methods: IVIM parameter values for each tissue type were obtained from the literature (table 1): low-grade (LG) and high-grade (HG) glioma for b-value optimization, and additionally gray matter (GM), white matter (WM) and cerebrospinal fluid (CSF) for simulations.

An optimized b-value scheme for LG and HG glioma was derived by error propagation as described previously [5]. The optimization aimed to minimize the sum of relative errors of IVIM f from the two tumor types, while keeping the expected estimation bias less than 10%. The optimization was set to produce a b-value scheme with the same number of b-values as the reference scheme below and was limited to the same maximum b-value.

A quantitative analysis of the effect of b-value optimization was performed by simulating data for each tissue type with the optimized b-value scheme and with a reference scheme typical for previous studies that includes 16 b-values (b = 0, 10, 20, 40, 80, 110, 140, 170, 200, 300, 400, 500, 600, 700, 800, 900 s/mm^2; approximate scan time 3 min) [3]. Further, a qualitative assessment was performed by generating artificial data with a digital brain phantom [6]. SNR was set to 40 for all simulations.

Estimates of the perfusion fraction f were obtained by segmented IVIM model fitting where b $\geq$ 200 s/mm^2 were used in the first step [7].

	GM	WM	LG	HG	CSF
D [µm^2/ms]	0.8	0.8	1.2	0.8	3.0
f [%]	8	6	8	13	40
D^* [µm^2/ms]	10	10	10	10	50

Table 1. IVIM parameter values used for optimization and simulation. GM: Gray matter, WM: White matter, LG: Low-grade glioma, HG: High-grade glioma, CSF: Cerebrospinal fluid. Parameter values from refs [3,8]

Results: The optimized b-value scheme consisted of three unique b-values that were repeated (number of repetitions × b-value): 3 × 0 s/mm^2, 8 × 309 s/mm^2, 5 × 900 s/mm^2.

Optimization of the b-value scheme resulted in a precision improvement of approximately 45% for all tissue types and a reduced estimation bias (Fig. 1). The improved parameter precision was clearly visible in parameter maps (Fig. 2).

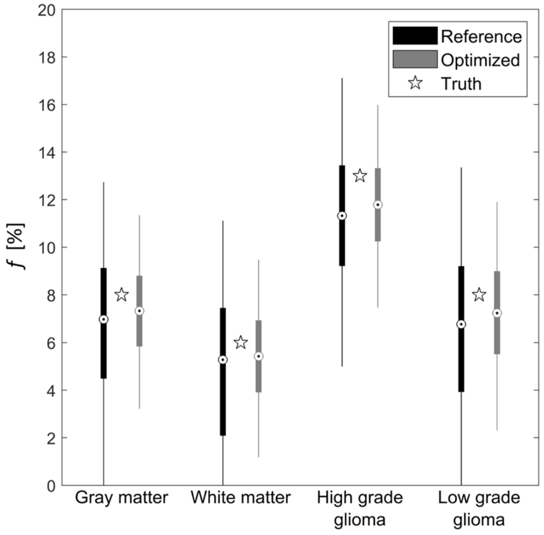

Figure 1. Estimated perfusion fraction values in different tissue types and for different b-value schemes (reference and optimized); CSF not shown. The whiskers of the boxplots extend to the 5th and 95th percentiles, respectively

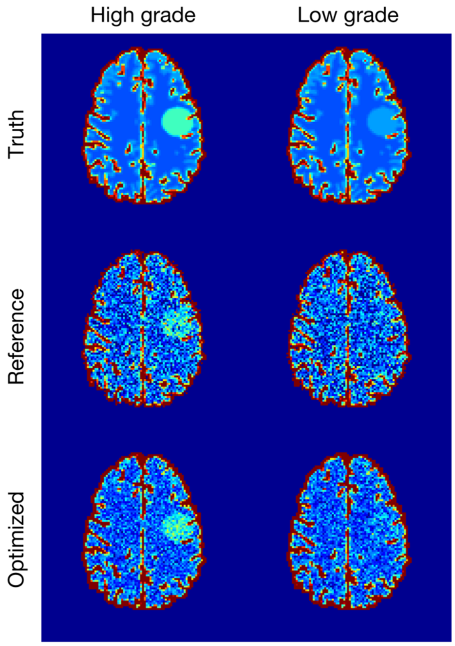

Figure 2. Estimated perfusion fraction maps obtained with the two compared b-value schemes (reference and optimized) and the ground truth. The displayed parameter range is 0 to 30 %

Discussion/Conclusion: Optimization of b-values is essential for IVIM-based glioma grading and can be used to improve the precision of the IVIM perfusion fraction or to reduce scan time.

References:

1. Paschoal 2018 NeuroImage: Clinical
2. Bisdas 2013 Neuroradiology
3. Federau 2014 Am J Neuroradiology
4. Togao 2016 Neuro-Oncology
5. Jalnefjord 2019 ISMRM
6. Aichert 2013 IEEE NSS/MIC
7. Pekar 1992 MRM
8. Rydhög 2017 PhD thesis

L03.11

Prognostic value of dynamic perfusion MRI imaging in patients with local advanced rectal cancer in the assessment of chemo-radiation treatment: comparison with ADC-map values

P. P. Arcuri[1], A. Sikora[2], S. Roccia[3], G. Fodero[1], C. Bertucci[1], E. Mazzei[4], V. Aiello[5], D. Lagana’[2]

[1]A.O. Pugliese Ciaccio, Radiology, Catanzaro, ITALY, [2]Magna Graecia University, Radiology, Catanzaro, ITALY, [3]A.O. Pugliese Ciaccio, Epidemiology, Catanzaro, ITALY, [4]A.O. Pugliese Ciaccio, Radioterapy, Catanzaro, ITALY, [5]Magna Graecia University, Medicine, Catanzaro, ITALY

Purpose/Introduction: the aim of our study was to investigate the value of dynamic contrast-enhanced perfusion-MRI parameters, in comparison with ADC-map values, in evaluation of the response to chemo-radiation therapy in patients with local advanced rectal cancer.

Subjects and Methods: We evaluated, retrospectively, thirty-eight patients affected by rectal adenocarcinoma (confirmed by biopsy) studied with dynamic contrast-enhanced MR sequence performed on 1.5T MRI system, before (MR-T0) and after chemo-radiation therapy (MR-T1). The protocol included Dynamic T1 gadolinium-enhanced images, obtained by axial fat-sat THRIVE sequence. Diffusion (DWI) and the corresponding Apparent Diffusion Coefficient (ADC) maps were reconstructed. A region of Interest (ROI) was manually drawn on tumor tissue and normal rectal wall. The following parameters were calculated and statistically analyzed: maximum enhancement (ME), relative enhancement (RE), time to peak (TTP), whash-in rate (W-inR) and whash-out rate (W-outR). Data were expressed in terms of median value ± range. Kruskal–Wallis non-parametric test was performed. Sensitivity, specificity and accuracy were assessed. Fisher’s exact test was used to evaluate statistical significance. A p value < 0.05 was considered statistically significant. The biopsy of the masses was the gold standard reference.

Results: Thirteen tumors (35%) showed complete or subtotal regression (TRG1–2) at histology and classified as responders; twenty-five tumors (65%) were classified as non-responders (TRG3–5). Perfusion MRI parameters were significantly higher in the tumor tissue than healthy tissue in MR-T0 and MR-T1 ($p < 0.05$). At baseline (MR-T0), no significant difference in perfusion parameters was found between responders and non-responders. After six months post chemo-radiation therapy, (MR-T1), responders showed significantly ($p < 0.05$) lower perfusion values. Sensitivity, specificity and diagnostic accuracy were respectively: ME = 81%, 78%, 83%; RE = 77%, 75%, 73%; TTP = 78%, 81%, 84%, W-inR = 69%, 72%, 74%; W-outR = 71%, 68%, 74%. In non-responders, there was no significant difference between perfusion values at MR-T0 and MR-T1.

DWI obtained sensitivity 78%, specificity 69%, PPV 41% NPV 85% and accuracy 67%.

Discussion/Conclusion: DCE-MRI improves the performance and confidence of radiologists in selecting the patients with a pathological complete tumor response after chemoradiation for locally advanced rectal cancer. Nevertheless, the combination of DCE-MRI + DWI could be of additional value for the clinical assessment of these patients.

References:

1) Birlik B, Obuz F, Elibol FD et al. *Magn Reson Imaging. 2015 Feb;33(2):201–12.*

2) Engin G, Sharifov R. *World J Clin Oncol. 2017 Jun 10;8(3):214–229.*

3) Lambregts DMJ, Boellaard TN, Beets-Tan RGH. *Insights Imaging. 2019 Feb 13;10(1):15.*

4) Tarallo N, Angeretti MG, Bracchi E. et al. *Pol J Radiol. 2018 Dec 17;83:e600–e609.*

L03.12

Evaluation of Manganese dimercaptosuccinate (Mn-DMSA) complex as contrast agent for paramagnetic enhancement in MRI studies of malignant tumors in animals

W.-Y. Ussov[1], V. D. Filimonov[2], A. Kovalenko[1], M. L. Belyanin[2], A. Bezlepkin[3], Y. Rogovskaya[4], N. L. Shimanovsky[5]

[1]Tomsk Medical Research Center/Institute of Cardiology, MRI Res. Lab, Tomsk, RUSSIAN FEDERATION, [2]National Research Tomsk Polytechnic University, Biotechnology and Organic Chemistry, Tomsk, RUSSIAN FEDERATION, [3]"Aibolit" Veterinary Clinic, Tomsk, RUSSIAN FEDERATION, [4]Tomsk Medical Research Center/Institute of Cardiology, Dept. of anatomic pathology, Tomsk, RUSSIAN FEDERATION, [5]N.I.Pirogov Moscow Medical Research University, Molecular Pharmacology, Moscow, RUSSIAN FEDERATION

Purpose/Introduction: We attempted to develop a Mn-based paramagnetic contrast agent for imaging of tumor processes, employing avidity of dimercaptosuccinic acid (DMSA) to various neoproliferative structures, and for this aim tested the paramagnetic complex Mn-DMSA in animals with fibrooseous nasal tumors

Subjects and Methods: Complex Mn-DMSA was obtained using nanopowder technology from manganese (II) carbonate and dimercaptosuccinic acid mixed together with addition of trace amounts of water, and then dissolved in buffered saline, delivering finally the 0.5 M solution of Mn-DMSA at pH = 6.5. The Mn-DMSA was injected intravenously slowly to sleeping animals (7 cats and 2 dogs, all veterinary patients, with fibroepithelial nasopharingeal tumors), as much as 0.05 ml of 0.5 M solution per Kg of BW. MRI scanning in T1-weighted spin-echo mode has been carried out with TR = 500 ms and TE = 15 ms, in sagittal, axial and frontal slices as thin as 2–2.5 mm, to the matrix 256 × 256, with the field of view not larger than 200 × 200 mm. The uptake was reported visually as change in intensity of T1-w MRI scans and quantitatively, with calculating for the T1-w MRI images the index of enhancement (IE) of intensity per voxel, as : IE = (MeanInt of T1-w.MRI)Mn-DMSA/(MeanInt of T1-w.MRI).

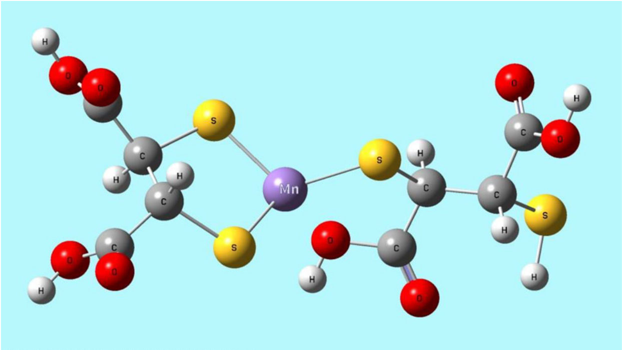

Structure of Manganese - dimercaptosuccinate complex

Results: The R1 relaxivity of Mn-DMSA was obtained as 3.2 $^{1}/_{(s*mM)}$. Visually on whole-body T1-w. SE scans the Mn-DMSA induced increase of intensity of the tumor, most prominent in the peripheral areas of tumor and less intense over the central non-perfused areas. The values of the *IE* were over 1.29 (*IE* = 1.62 ± 0.12) for all peripheral parts of tumors, whereas only 1.23 ± 0.08 in central regiones. The peripheral vascularised parts of tumors demonstrated relatively higher uptake of Mn-DMSA. The normal musculoskeletal tissues did not enhance after Mn-DMSA injection, with *IE* = 1.07 ± 0.03. The uptake $k_{blood\text{-}tissue}$ constants were as little as < 0.12 ml/min/100 g for non-tumor tissues and over 0.24 ml/min/100 g in vascularised regions of tumors, with slow back diffusion and $k_{tissue\text{-}blood}$<0.04 ml/min/100 g.

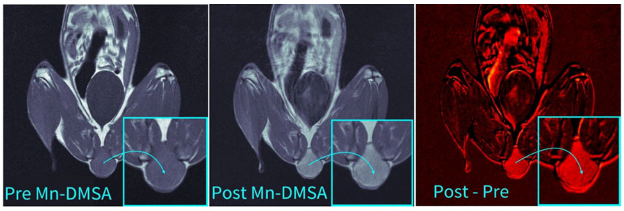

Mn-DMSA contrast enhancement of a pelvic fibroepithelial tumor in a cat

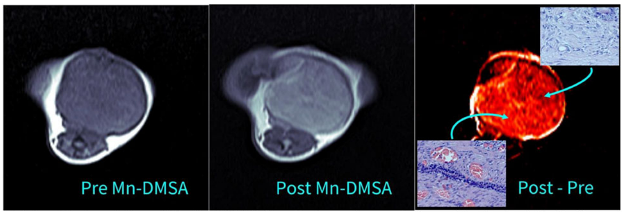

Axial slices of the tumor, before and after Mn-DMSA injection, with microscopic preparates from peripheral and central parts of tumor superimposed

Discussion/Conclusion: Paramagnetic complex Mn-DMSA provides obvious intense enhancement of musculoskeletal tumors in T1-SE MRI, demonstrates intermediate relaxivity R1, is non-toxic and makes possible to image tumor processes in animals. The Mn-DMSA complex can be suggested as basic molecule for design of Mn-based non-gadolinium paramagnetic agent for tumor imaging.

References:

1. Samuilov F.D., Nikiforova V.I., Nikiforov E.A. Effect of paramagnetic additives on the spin-lattice relaxation of protons of intracellular water. Biofizika. 1979; 0.24(2): 270–273.

2. Belyanin M.L., Stepanova E.V., Filimonov V.D., Valiev R.R., Ågren H., Borodin O.Y, Ussov W.Y. Design, synthesis and evaluation of a new Mn contrast agent for MR imaging of myocardium based on DTPA-Phenylpentadecanoic acid complex. Chemical Physics Letters. 2016; 665: 111–116.

L03.13

On the diagnostic capability of a dinuclear blood pool GBCA in a pathological model of rat cerebral ischemia

F. La Cava[1], **A. Fringuello Mingo**[2], S. Colombo Serra[2], P. Irrera[1], A. Di Vito[2], C. Cabella[2], L. Miragoli[2], E. Terreno[1], L. Poggi[2]

[1]Università di Torino, Department of Molecular Biotechnology and Health Center, Torino, ITALY, [2]Bracco Imaging spa, Colleretto Giacosa, ITALY

Purpose/Introduction: Gadolinium based contrast agents (GBCAs) have been widely used in clinic to boost the visibility of pathology and delineation of lesions in Magnetic Resonance Imaging acquisitions. Approximately, 40 million administrations are made worldwide every year and search for new candidates is still active.[i-iii]

Subjects and Methods: $(GdDTPA)_2$-Chol, a dinuclear gadolinium(III) chelate containing two moieties of diethylenetriaminepentaacetic acid (DTPA), covalently conjugated to an analogue of deoxycholic acid was synthesized and characterized in vitro. Relaxivity (r_1) resulted improved by an increment of the size of the contrast agent; moreover, r_1 further increased by the occurrence of a noncovalent binding with plasma proteins, resulting in a fairly high relaxivity in plasma (approx. 20 $mM^{-1}s^{-1}$, 20 MHz, 310 K). $(GdDTPA)_2$-Chol was tested for its in vivo bio-distribution and pharmacokinetic on healthy rats[iv] and showed unexpectedly long elimination half-life. In this work, the diagnostic capability of $(GdDTPA)_2$-Chol was tested in a pathological model of permanent cerebral ischemia in rats with a 3 T scanner equipped with a dedicated brain surface coil.

Results: Ischemia was successfully induced after *i.v.* perfusion of Rose Bengal and cortical irradiation by green light in n = 11 Sprague–Dawley rats. The onset of the pathology was assessed by T_2-weighted images 1 week later and administration of $(GdDTPA)_2$-Chol (0.05 mmol/kg, n = 5) and of a commercial macrocyclic GBCA (0.1 mmol/kg, n = 6) was performed 12 days after induction, when the lesion reached the chronic stage of the disease, corresponding to an increase in blood brain barrier permeability.[iv] $(GdDTPA)_2$-Chol T_1-contrast enhancement was monitored for 90 min in continuous and evaluated 24 h post *i.v.* administration, while commercial GBCA enhancement was followed for 60 min in continuous.

Discussion/Conclusion: Even if the molecular rotational motion contribution to r_1 is valued at low-to-intermediate magnetic field strength, $(GdDTPA)_2$-Chol enhancement was comparable to the macrocyclic commercial agent, injected at double the dose. Moreover, a difference in distribution and accumulation of the compound into the lesion can be observed: $(GdDTPA)_2$-Chol accumulated slowly into the lesion as a result of the increased molecular size after binding with serum albumin, and reached a plateau after about 20 min, according to the durable availability of the compound characterized by a long elimination rate. The strong binding to albumin and the slow accumulation into fibrotic tissue observed after administration of $(GdDTPA)_2$-Chol are valuable features and could be exploited for different applications into cerebral pathology staging and follow-up.

References:

[i] Runge, V. M. Invest. Radiol. (2017) 52:317 − 323.
[ii] Parac-Vogt T.N. et al. Chem. Eur. J. (2005) 11:3077–3086.
[iii] Longo D. et al. Biomaterials (2016) 75:47–57.
[iv] Lee et al. Chonnam Med. J. (2011) 47:90–98.

L03.14

Repeatability of perfusion measurements in gliomas using pulsed and pseudo-continuous arterial spin labelling MRI

A. Alsaedi[1], D. Thomas[1], E. De Vita[2], J. Panovska-Griffiths[3], S. Bisdas[1], X. Golay[1]
[1]UCL Queen Square Institute of Neurology, Department of Brain Repair & Rehabilitation, London, UNITED KINGDOM, [2]King's College, Biomedical Engineering Department, London, UNITED KINGDOM, [3]University College London, Department of Applied Health Research, London, UNITED KINGDOM

Purpose/Introduction: To facilitate and justify the use of arterial spin labelling (ASL) for absolute tumour blood flow (aTBF) quantification, the repeatability of aTBF and relative TBF (rTBF) measurements must be estimated. This work (a) investigates the extent to which pulsed-ASL (PASL) and pseudo-continuous ASL (PCASL) techniques can produce repeatable measures of aTBF; and (b) determines the impact of the internal reference ROI size and its positioning on rTBF.

Subjects and Methods: 40 adult glioma patients were recruited for this study; 16 were scanned using PASL (9 high grade, 7 low grade), and 24 using PCASL (9 high grade, 15 low grade). Repeatability was assessed through splitting of the multiple repetitions of the ASL datasets in 2 subsets considered independent. The variability and repeatability in the contralateral normal appearing hemisphere (CNAH) was measured in normal cerebral blood flow (CBF), in the tumour itself (aTBF), and in the normalised rTBF to large ROIs (total grey matter (GM) and white matter (WM) of the CNAH) and to small ROI (caudate nucleus (caud) from the CNAH). The repeatability was assessed using intra-class correlation coefficient (ICC; two-way mixed effect, absolute agreement), while the variability was measured as Within-Coefficient-of-Variation (WCoV) and quantified in the same unit as the measured values as Coefficient of Repeatability (CR), expressed in Table 1. As the patients involved in the PASL scanning were not the same as those involved in the PCASL scanning, repeatability was assessed separately for each ASL method.

Results: Overall, both PASL and PCASL demonstrated high reliability ($ICC > 0.9$) in all of the normal CBF, aTBF and rTBF. However, the variability (WCoV) was higher in the tumour (both aTBF, rTBF) than in the normal CBF from large ROIs but not than normal CBF of the small ROI. Furthermore, aTBF variability was higher than rTBF variability when we used large ROIs for normalisation, especially when the GM was used, however, the reverse was true when rTBF was normalised using small ROI. Furthermore, the lowest RC was for the rTBF that normalised to the GM.

Discussion/Conclusion: The higher variability of aTBF compared to rTBF poses a caveat for quantitative ASL-based tumour characterisation. Using rTBF normalised by a large segmented GM ROI may be more reliable than performing absolute quantification.

L03.15

Glx dynamics in visual cortex after single stimulus. fMRI and ^{1}H fMRS study

M. Ublinskiy[1], N. Semenova[2], A. Manzhurtsev[2], A. Yakovlev[3], P. Menshchikov[1], T. Akhadov[1]
[1]Clinical and Research Institute of Urgent Pediatric Surgery and Trauma (CRIEPST), Radiology, Moscow, RUSSIAN FEDERATION, [2]Institute of Biochemical Physics (IBCP), Russian Academy of Sciences (RAS), Moscow, RUSSIAN FEDERATION, [3]Moscow State University (MSU), Moscow, RUSSIAN FEDERATION

Purpose/Introduction: Glutamate (Glu) is the main excitatory neurotransmitter in the human brain. Metabolically, Glu is stored as Gln in glia, and the balanced cycling between these two neurochemicals is essential for normal functioning of brain cells [1]. The glutamate-glutamine (Glx) signal on ^{1}H MRS can therefore be used as a measure for central glutamatergic neurotransmission.

The aim of this study was to analyze dynamics of Glx in visual cortex of normal brain after single visual stimulus.

Subjects and Methods: 10 healthy volunteers (3 males, 7 females, mean age = 21 years) comprised test group. Study was performed on clinical Phillips Achieva 3.0 T MRI scanner. Volume of interest in visual cortex was localized on the base of fMRI study (EPI FFE, TR = 3000 ms, TE = 30 ms) as the zone of activation caused by visual stimuli (flashing chessboard, duration = 3 s) with the 21 s periodicity. The BOLD signal was measured each 3 s. ^{1}H MR spectra (PRESS, TE = 30 ms TR = 2000 ms) were obtained; FID signals for time points t = −1, 1, 3, 5, 7, 9, 11, 13, 15, 17, 19, 21 s before/after stimulus were summarized. Thus, we received metabolic responses to single stimulus in BOLD dynamics. FMRI data were processed using SPM12 on purpose to obtain values of activated visual cortex (AVC). For FID processing LCModel software was used. Glx signal intensities for each time point were normalized twice: first—to corresponding Cr signal intensities; second—to their values at t = 0. Time points differences were estimated using Mann–Whitney criterion with the level of significance $p < 0.0$****5.

Results: We found a longitudinal (during 15 s after stimulus) statistically significant ($p < 0.05$) increase of relative Glx/Cr ratio in response to stimulus (Fig. 1).

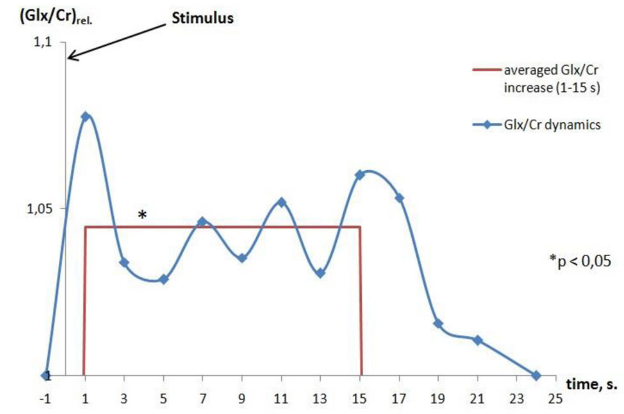

Relative Glx/Cr dynamics in response to visual stimulus

Statistical analysis showed significant correlation (R = 0.85, $p < 0.05$) between averaged Glx/Cr ratio (1–15 s after stimulus) and partial volume of activated visual cortex (Fig. 2).

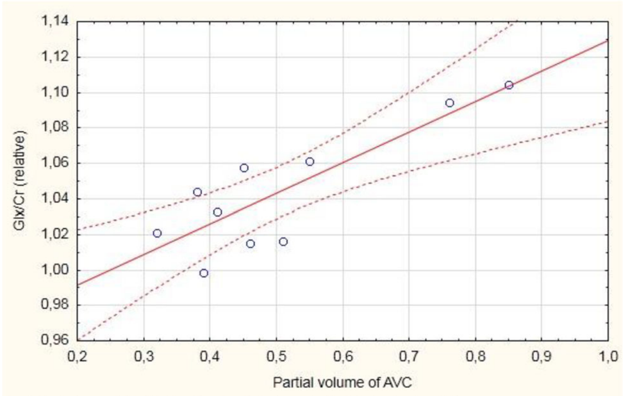

Correlation between relative Glx/Cr ratio and partial volume of activated visual cortex (AVC)

Discussion/Conclusion: We found that dynamics of Glu/Cr ratio positively correlates with BOLD effect in response to video stimulus. This fact may be explained by increased energy demands performed by oxidative metabolism during neuroactivation [2, 3].

References:

1. Ramadan S. https://doi.org/10.1002/nbm.3045.
2. Bednařík P. https://doi.org/10.1177/0271678x17695291.
3. Bednařík P. https://doi.org/10.1038/jcbfm.2014.233.

L03.16

Shimming scheme effect on single shot EPI-based pCASL perfusion measurement

H. Doshi[1], **L. Lamalle**[2]
[1]Université Grenoble Alpes, SFR RMN biomédicale et Neurosciences, UMS IRMaGe, Grenoble, FRANCE, [2]Inserm, US 17, Grenoble, FRANCE

Purpose/Introduction: ASL-based brain perfusion MRI relies on measuring subtle (< 4%) signal differences between label (Lbl) and control (Ctl) acquisitions. Using single shot spatial encoding is common although the long readout duration increases B_0 inhomogeneity effects. At 3T, the latter are mitigated by high-order shimming. B_0 inhomogeneity also affects the behavior of spins flowing through the labelling slab and thus labelling efficiency[1]. We study on a clinical scanner the effect on EPI pCASL perfusion mapping of various B_0 shimming schemes, which influence both labelling efficiency and EPI signal quality.

Subjects and Methods: 3T Philips Achieva dStream system (32-channel head coil). B_0 shimming options and multi-slice pCASL-EPI sequence as of software R5.4.1. Subject (M, 31 y.o.) inclusion conformed with ethics rules. After a T_1-weighted anatomical scan, pCASL-EPI, proton density M_0 and B_0 data were collected under 5 automatic shim procedures described in Fig. 1 and Table 1 (col.2). TE/TR: 20.3/4850, 1650 ms Lbl duration, 1600 ms post Lbl delay, $(256\ \mathrm{mm})^2$ field of view, $(4\ \mathrm{mm})^2$ in-plane resolution, 4 mm slice thickness. TR for M_0 was 10 s. For each shimming scheme GE scans were acquired for B_0 mapping with $(4\ \mathrm{mm})^2$ in-plane resolution, 5 mm slice thickness, TE/TR: 4.61/650 with ΔTE of 3 ms. Processing pipeline is described in Fig. 2. Perfusion maps were generated according to [2]. Spatial mean and SD values were computed over masks: Fig. 2A Grey Matter (GM) for perfusion, Fig. 2C tissue for B_0 values.

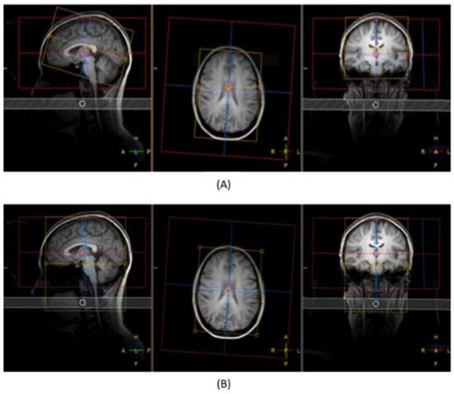
(A)
(B)

Figure 1. Imaging, labelling and shimming volumes are shown as a red, a hashed, or a yellow box, respectively. Imaging and labelling volumes do not change. Shimming box targets brain (A) or brain and labelling (B) volumes.

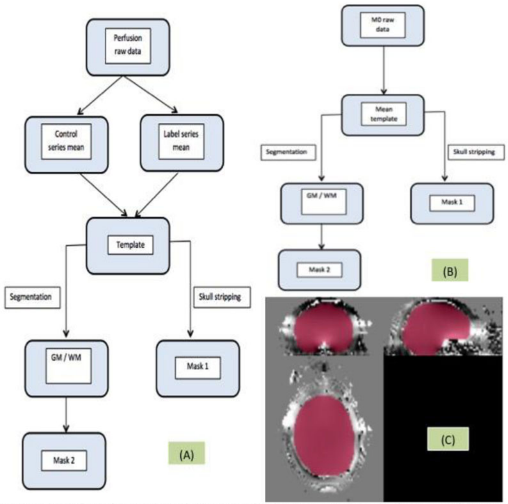

Figure 2. Processing pipeline for perfusion (A) and proton density (B) data, and an example (C) of magnitude GE and derived skull-stripped thresholded mask used for B0 map statistics.

Results: Table 1 reports: (Col.1&2) shimming scheme, mean and SD of perfusion values over GM (Col.3) and of B_0 values over GE mask (Col.4), mean Ctl-Lbl (Col.5) and M_0 (Col.6) image intensities over GM, (Col.7) ratio of mean perfusion values relative to that obtained with scheme 1. M_0 signal was highest in 2 and decreased through 3, 4, 1, 5. Ctl-Lbl difference was highest in 5, and decreased through 2, 1, 3, 4.

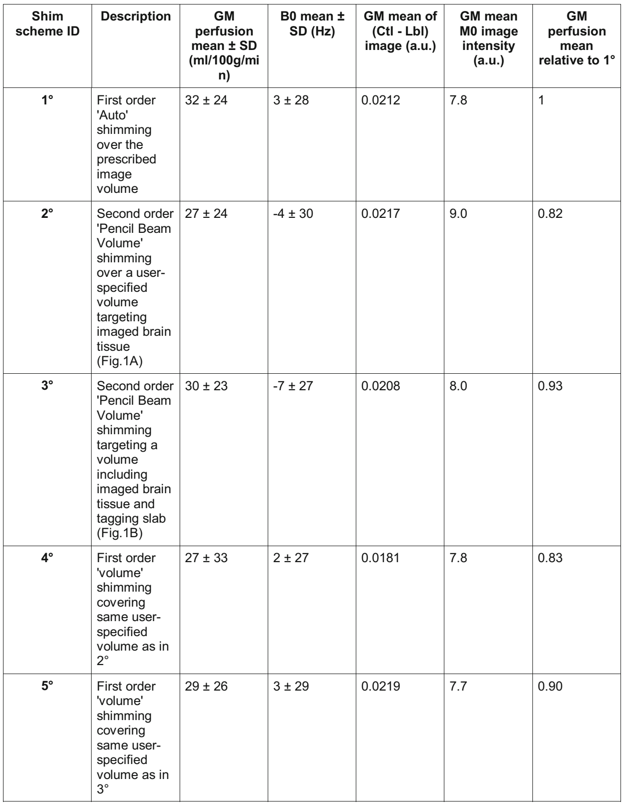

Shim scheme ID	Description	GM perfusion mean ± SD (ml/100g/min)	B0 mean ± SD (Hz)	GM mean of (Ctl - Lbl) image (a.u.)	GM mean M0 image intensity (a.u.)	GM perfusion mean relative to 1°
1°	First order 'Auto' shimming over the prescribed image volume	32 ± 24	3 ± 28	0.0212	7.8	1
2°	Second order 'Pencil Beam Volume' shimming over a user-specified volume targeting imaged brain tissue (Fig.1A)	27 ± 24	-4 ± 30	0.0217	9.0	0.82
3°	Second order 'Pencil Beam Volume' shimming targeting a volume including imaged brain tissue and tagging slab (Fig.1B)	30 ± 23	-7 ± 27	0.0208	8.0	0.93
4°	First order 'volume' shimming covering same user-specified volume as in 2°	27 ± 33	2 ± 27	0.0181	7.8	0.83
5°	First order 'volume' shimming covering same user-specified volume as in 3°	29 ± 26	3 ± 29	0.0219	7.7	0.90

Volume mean and standard deviation of perfusion and B0 values and mean Ctl-Lbl and M0 image intensities across different shim settings

Discussion/Conclusion: Quantitative analysis of B_0 maps was complicated by phase-unwrapping-related problems at some pixels. Assuming stable subject perfusion between scans, shimming scheme altered the labelling efficiency, the EPI image GM signal and GM perfusion estimates. Basic 1st order 'Auto' scheme seems a good practical compromise. Otherwise, shimming targeting a user-defined volume benefits from 2nd order shimming and a large volume including both brain and labelling plane should be preferred to targeting a volume covering brain tissue only.

References:

1. Jahanian et al., NMR Biomed. 2011 **24** 1202; 2. Alsop et al., Magn Reson Med 2015 **73** 102.

L03.17

Quantification of multiple boli arterial spin labelling in mice and rats

S. Paterson[1], A. Vallatos[2], W. Holmes[1]

[1]*University of Glasgow, Institute of Neuroscience and Psychology, Glasgow, UNITED KINGDOM,* [2]*University of Edinburgh, Edinburgh, UNITED KINGDOM*

Purpose/Introduction: High SNR ASL sequences are crucial for CBF quantification. We introduce a quantitative model for a high SNR ASL sequence (mbASL) in rats and mice, which uses a train of adiabatic pulses to label multiple boli of arterial water[1]. mbASL is a hybrid of PASL and CASL: either as a multiple PASL with limited labelling thickness or a large thickness CASL. We have quantified this technique in mice and rats by describing mbASL signal as a sum of limited thickness PASL signals[2] using a modification of Buxton's kinetic model to account for multiple boli slice-selective labelling.

Subjects and Methods: Variable labelling slice thickness mbASL experiments were performed using CD1 mice (n = 6) & Wistar rats (n = 6). The distance between labelling and imaging slice was kept constant. Exploration of the labelled bolus arrival at different post-label delay times used 1-shot mbASL with an inversion time (CI) of 500 ms and a time after inversion TI = 50:500:4050 ms (NA = 10). CBF maps were produced using a T1 map and a 4-shot mbASL (NA = 10, CI = 5000 ms, TI = 50 ms). mbASL was compared with FAIR, NA = 10, TI = 1750 ms.

Results: By modifying Buxton's kinetic model (Fig. 1) and using a varying labelling thickness and value of average velocity, theoretical predictions shows the hybrid nature of the mbASL sequence. The experimental data in Fig. 2 shows the distribution of signal at 3 different thicknesses for a mouse, with the data from rats showing a similar trend. The peak signal moves as the labelling thickness increases. The sequence has shown high SNR and is able to be used to produce CBF maps (Fig. 3) with values that compare to literature. With its adaptable nature for signal distribution, there is high potential for this sequence to be adapted for different animal strains and clinical use. mbASL can measure CBF non-invasively with a higher SNR and accuracy compared to the standard ASL sequences.

$$\Delta M_i(t) = \begin{cases} 0 & \text{for } 0 < t < \delta+(i-1)*(t_p+t_{wait}) \\ 2Mb_0(t-\delta)\alpha e^{\frac{-t}{T_{1b}}}\dfrac{e^{kt}(e^{-k\delta}-e^{-kt})}{k(t-\delta)} & \text{for } \delta+(i-1)*(t_p+t_{wait}) < t \text{ \& } t < \delta+\tau+(i-1)*(t_p+t_{wait}) \\ 2Mb_0\tau\alpha e^{\frac{-t}{T_{1b}}}\dfrac{e^{kt}(e^{-k\delta}-e^{-k(\tau+\delta)})}{k\tau} & \text{for } t > \delta+\tau+(i-1)*(t_p+t_{wait}) \end{cases}$$

$$\Delta M_{mbASL}(t) = f\sum_{i=1}^{nbp} M_{i,PASL}(t)$$

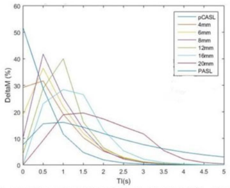

Figure 1: Equations describing the modified Buxton Kinetic Model for mbASL and the calculation of CBF using mbASL. The graph shows varying signal distributions dependent on labelling slice thickness.

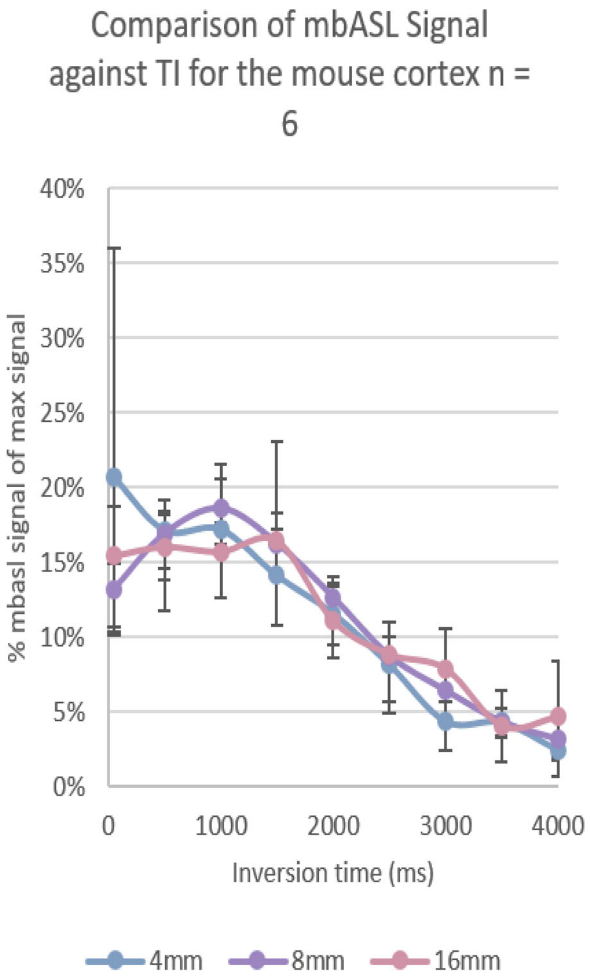

Figure 2: mbASL signal against TI for various slice thicknesses for mice

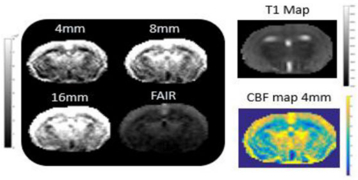

Figure 3: ASL perfusion maps acquired using mbASL at multiple thickness and FAIR.(left) T1 map for the same animal used to produce the CBF map in for 4mm thickness. (top and bottom right)

Discussion/Conclusion: We have been able to fully quantify the mbASL sequence and produce quantitative CBF maps for mice and rats which agree with literature values[3, 4].

References:

[1]Vallatos, A et al. (2017), [2]Buxton, R. B. et. al. (1998), [3]Muir, E. R. et al. (2008), [4]Sicard, K. M et al. (2005).

L03.18

ASL-BIDS, the brain imaging data structure extension for arterial spin labeling

P. Clement[1], M. Castellaro[2], T. Okell[3], D. Thomas[4], C. Gorgolewski[5], S. Appelhoff[6], J. Petr[7], M. Chappell[8], H.-J. Mutsaerts[9]

[1]Ghent University, Dep. of Diagnostic Sciences, Radiology, Ghent, BELGIUM, [2]University of Padova, Padova Neuroscience Center, Padova, ITALY, [3]University of Oxford, Oxford, UNITED KINGDOM, [4]University College London, London, UNITED KINGDOM, [5]Stanford University, Stanford, UNITED STATES, [6]Max Planck Institute for Human Development, Berlin, GERMANY, [7]Helmholtz-Zentrum Dresden-Rossendorf, Dresden, GERMANY, [8]Institute of Biomedical Engineering, University of Oxford, Oxford, UNITED KINGDOM, [9]Amsterdam University Medical Center, Leiden, NETHERLANDS

Purpose/Introduction: The Brain Imaging Data Structure (BIDS) is a recently developed data storage standard, that meets the need for a structured manner to organize imaging data in the age of big datasets and data sharing (https://bids.neuroimaging.io).[1] This abstract presents a BIDS extension for ASL, which only supports ASL approaches as recommended in the ASL acquisition consensus paper, and several M0 calibration approaches.[2]

Subjects and Methods: A group of ASL experts initiated this extension by defining several concepts and preparing a first draft. This draft was shared online from May 2017 until March 2019 with the international ASL community, and several teleconference and face-to-face meetings were organised. Per BIDS convention, existing BIDS fields were reused for the ASL-BIDS extension if possible. The BIDS fields names were based on the NEMA ASL DICOM fields, where possible. Additionally, three example datasets were collected[3] and efforts were initiated to adapt existing ASL analysis tools and the BIDS validator for ASL-BIDS compatibility.

Results: Six concepts were defined to allow a uniform yet flexible ASL-BIDS specification. First, it was decided to focus solely on the implementation of the ASL approaches discussed in the ASL consensus paper: single- and multi-delay, pulsed, continuous, and pseudo-continuous ASL.[5] Second, the BIDS-structure consists of two mandatory files and several optional files (Fig. 1). Third, it is obligatory to keep the ASL time series in the original acquisition order in a 4D NIfTI file, including any M0, if it was part of the original ASL time series. If an M0 image was acquired separately, it should be stored as a separate NIfTI file. The ASL-context BIDS field explains the content of each volume in the ASL time series. Fourth, the derivative images DeltaM and CBF are considered to be raw images if the ASL-sequence or vendor only provided derivative images, lacking raw data. This principle follows the prioritization shown in Fig. 2. Fifth, all ASL data need to be stored in at least 32 bit floating point, without any scale slopes. Some vendor implementations store scaled ASL data to increase the precision of the stored data within the traditional 12 bit DICOM files. It is the responsibility of the DICOM to BIDS conversion to apply any existing scale slopes. Sixth, it is recommended to specify as much information as labeling as possible: the exact location of the labeling plane and the labeling efficiency.

```
my_dataset
    dataset_description.json
    participants.tsv
    sub-<label>
            sub-<label>_sessions.tsv
            ses-<label>
                    asl
                            sub-<label>_ses_<label>_acq-<label>_rec-<label>_run-<index>_asl.nii.gz
                            sub-<label>_ses_<label>_acq-<label>_rec-<label>_run-<index>_asl.json
                            sub-<label>_ses_<label>_acq-<label>_rec-<label>_run-<index>]_MZeroScan.nii.gz
                            sub-<label>_ses_<label>_acq-<label>_rec-<label>_run-<index>]_MZeroScan.json
                            sub-<label>_ses_<label>_acq-<label>_rec-<label>_run-<index>]_MZeroScanR.nii.gz
                            sub-<label>_ses_<label>_acq-<label>_rec-<label>_run-<index>]_MZeroScanR.json
                            sub-<label>_ses_<label>_acq-<label>_rec-<label>_run-<index>]_labeling.jpg
```

Fig.1 - ASL-BIDS structure consisting two mandatory files (_asl.nii[.gz] and _asl.json). All other files are optional, depending on the data acquisition approach. Grey-shaded files and text are optional.

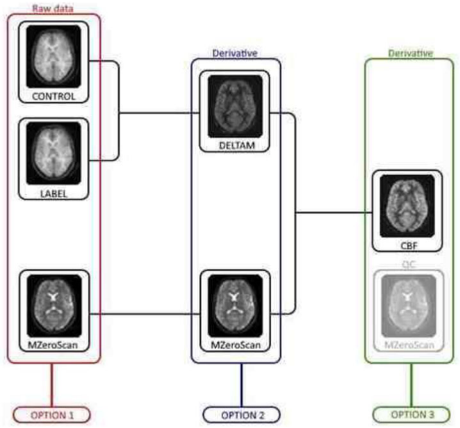

Fig. 2 - The control, label and the M0 image should be stored as raw data (Option 1). When these are (partly) lacking, the DeltaM and M0 images should be provided as raw data (Option 2), or the CBF image should be stored as raw data (Option 3).

Discussion/Conclusion: The current ASL-BIDS extension is restricted to the ASL approaches recommended by the consensus paper.[1] With the current development of more advanced ASL approaches, such as time-encoded and velocity-selective ASL, the ASL-BIDS may be extended for these technique. Also, a derivatives extension for ASL is anticipated.

References:

1. Gorgolewski, KJ. (2016) 2. Alsop, DC. (2015) 3. Abaei, M. (2019).

L03.19

How to quantify ASL values in a perfusion phantom

X. Golay[1], A. Oliver-Taylor[1], Y. Susuzi[2], M. Chappell[2]
[1]*Gold Standard Phantoms Ltd, London, UNITED KINGDOM,*
[2]*Oxford University, Institute of Biomedical Engineering, Oxford, UNITED KINGDOM*

Purpose/Introduction: Over the last four years, we have been developing an Arterial Spin Labelling (ASL) perfusion phantom aiming at providing reference values for quality assurance (QA) of ASL data in the clinics (1). Preliminary data acquired during a round robin experiment (2) where quantified using the 'White Paper' ASL equations (3), while realising that some of the assumptions behind these equations were not valid for the phantom. Here, we show that the original equations from the General Kinetic Model (GKM) (4) can be used to quantify the ASL signal in the QASPER phantom (1).

Subjects and Methods: The general hypotheses behind the GKM are that the signal can be described as:

$$\Delta M(t) = 2\ M_{0b} f\ \{c(t) * [r(t)\ m(t)]\}$$

With $*$ = convolution operator, $c(t)$ = delivery function, which can here be defined as a plug flow, $m(t) = e^{-t/T}1$, and the residue function $r(t) = e^{-ft/\lambda}$. Now, r(t) is defined as such based on the hypothesis that the outflow of any labelled magnetization out of a voxel will be well mixed, which is hte case here as no exchange is modelled. In human physiology, the outflow of magnetization is going through the venous system. In the QASPER phantom, the magnetization is flowing to an adjacent voxel, as no direct venous system is modelled. However, the assumption stands, with a theoretical λ = 0.32 (= void volume of the porous plastic used to simulate the microvasculature).

Data were acquired on a Philips 3T scanner (Achieva, R5.3). Two pCASL sequences with labelling time (LT) = 800/1800 ms, and post-labelling delay (PLD) = {50, 250, 500, 750, 1000, 1250, 1500, 1750, 2000, 2250, 2500 ms} was designed. Other parameters were: Multi-slice EPI, Matrix = 64 × 64, FOV = 192 mm, 20 3 mm slices, 4 averages.

Data were analysed using BASIL (www.fmrib.ox.ac.uk/fsl/BASIL), using a Variational Bayesian algorithm (5), with $T_1 = T_{1b}$ = 1900 ms and a prior on BAT of 1000 ms (100 ms variance).

Results: The calculated perfusion and BAT maps are shown in Figs. 1 and 2 respectively. The values associated with a set pump flow rate of 350 mL/min are of the 500–600 mL/min/100 g on average for all voxels with LT = 800 and 1800 ms resp. Excluding the signal from the 'arteries' for the PLD = 800 ms case lead to an equivalent perfusion distribution for both PLDs.

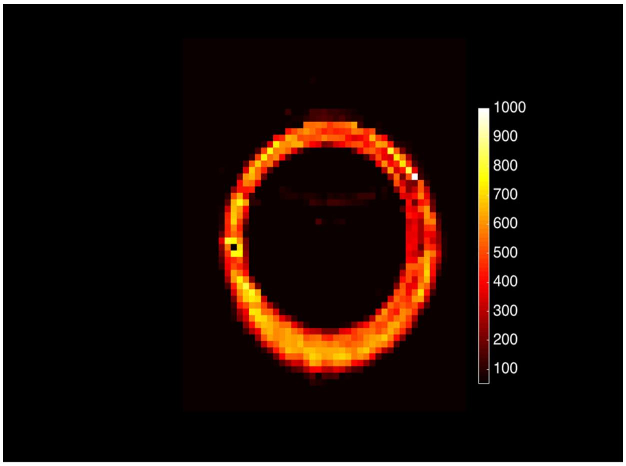

Fig. 1: Calculated CBF image for LT = 1800ms

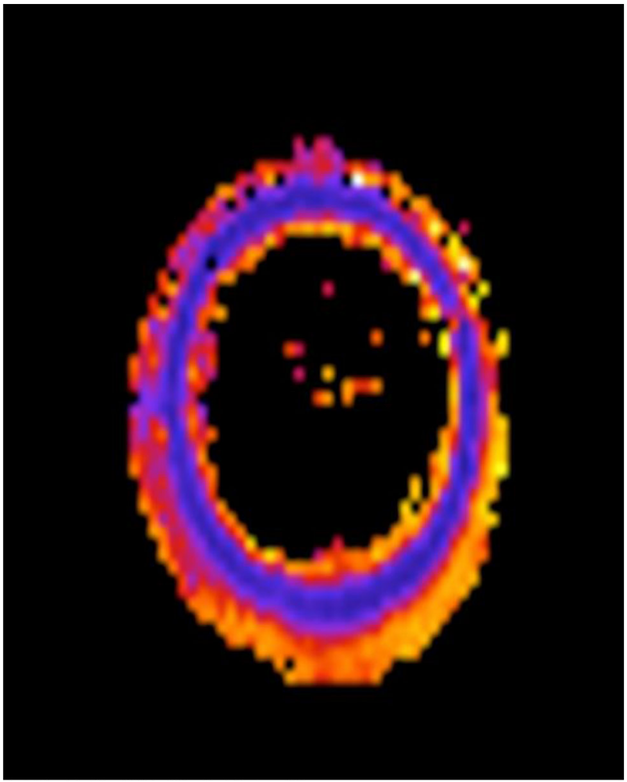

Fig. 2: Bolus Arrival Time (BAT) for 1800ms (scaled between 0-2s)

Discussion/Conclusion: The general kinetics given by the perfusion phantom can be seen in Fig. 3. In this figure, 4 ROIs taken at different distance from the phantom's 'arterioles' show a behaviour in line with that predicted by the GKM. While the CBF values measured are an order of magnitude larger than grey matter CBF ones, the general aspects of the tracer kinetics are in line with expected physiological values.

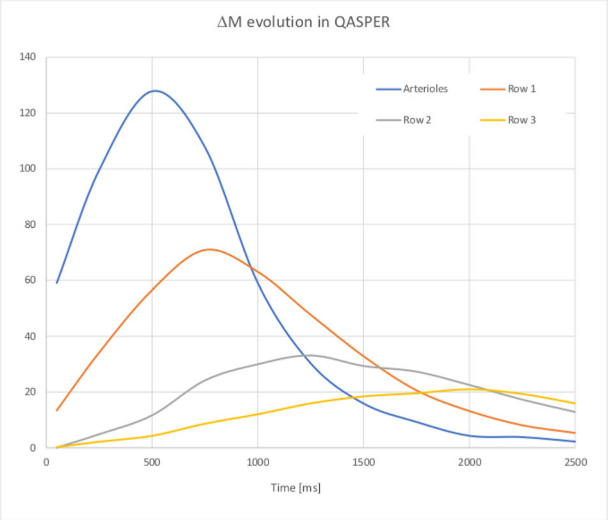

Fig. 3: Signal time curves for 4 ROIs from the centre of the arterioles to the outer 'tissue' part

References:

1. Oliver-Taylor et al. Proc. #0681, ISMRM 2017
2. Oliver-Taylor et al. Proc. #5028, ISMRM 2019
3. Alsop et al. Magn Reson Med. 73:102–16, 2015
4. Buston et al. Magn Reson Med. 40:383–96, 1998
5. Chappell et al. IEEE Transactions on Signal Processing 57(1):223–236, 2009.

L03.20

Investigating the existence of bias in ASL sequences: evaluation of perfusion measurements in phantom with 2D and 3D EPI pseudo-continuous ASL sequences

I. Brumer[1], J. Chacon-Caldera[1], S. Hubertus[1], T. Uhrig[1], M. Dziadosz[2], M. Barth[3], L. R. Schad[1], F. G. Zöllner[1]
[1]Computer Assisted Clinical Medicine, Medical Faculty Mannheim, Heidelberg University, Mannheim, GERMANY, [2]Magnetic Resonance Spectroscopy and Methodology, Department of Biomedical Research, University of Bern, Bern, SWITZERLAND, [3]School of Information Technology and Electrical Engineering and Centre for Advanced Imaging, University of Queensland, Brisbane, AUSTRALIA

Purpose/Introduction: Arterial spin labelling (ASL) allows non-invasive quantification of perfusion, which is a valuable parameter for diagnosis and monitoring of blood flow altering physiologies, such as cancer or dementia[1]. However, due to the multitude of available sequences, this technique is not yet widely used in the clinical routine. The ASL signal measured in vivo is influenced by various technical parameters (labelling scheme, plane, duration) and physiological parameters (motion, blood pulsation, background tissue signal). Perfusion measurements in phantom are useful for investigating the technical variation sources in isolation and can provide useful information for calibrating different ASL sequences. In this work, we investigate two pseudo-continous ASL (pCASL) sequences for bias and reproducibility using multiple repeated measurements in a perfusion phantom.

Subjects and Methods: Measurements were performed in a 3T MR scanner using the spine array (MAGNETOM Trio, Siemens Healthineers). Two sequences were used: (1) pCASL with 2D-EPI readout and (2) pCASL with 3D-EPI readout[2]. The perfusion phantom (Fig. 1) consisted of a closed system of circulating water with a dialysis filter (HelixoneFX800, Fresenius Medical Care, Germany) and a peristaltic pump[3]. The rotation velocity was set to 400 rpm. For each sequence, the perfusion phantom was scanned sagittally 15 times in sequence (Fig. 1). Acquisition parameters are listed in Table 1. Perfusion maps were calculated with the formula presented by Alsop et al[1], assuming T1 = 4000 ms for water. The three central slices were averaged and an ROI was placed in the middle of the phantom to calculate mean perfusion values (Fig. 2).

Results: Mean perfusion values are shown in Fig. 2. Higher perfusion values were obtained with the 2D EPI readout than with the 3D EPI readout (120–135 mL/100 g/min and 78–105 mL/100 g/min, respectively). Overall, standard deviations were lower for the 2D EPI (6–12 mL/100 g/min) than for the 3D EPI (8–15 mL/100 g/min) except for one measurement (17 mL/100 g/min). In terms of reproducibility, mean perfusion and standard deviations between the 15 measurements were 124 ± 4 and 98 ± 6 mL/100 g/min for the 2D EPI and 3D EPI, respectively.

Discussion/Conclusion: The values obtained with the 3D EPI readout agree well with previous measurements performed with the same phantom using dynamic contrast-enhanced MRI[3]. The higher values obtained for the 2D EPI suggest an intrinsic bias, which would have to be accounted for in in vivo measurements. The good reproducibility of perfusion values within each sequence demonstrates their robustness in absence of physiological variabilities. In future work, other ASL sequences will be evaluated using the same procedure, which could help calibrate and optimise them for use in the clinical routine.

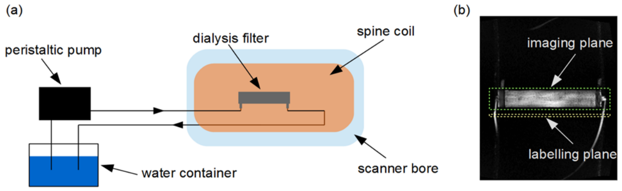

Figure 1: (a) Schematic of the measurement set up with the perfusion phantom and (b) localiser image of the phantom with imaging and labelling planes.

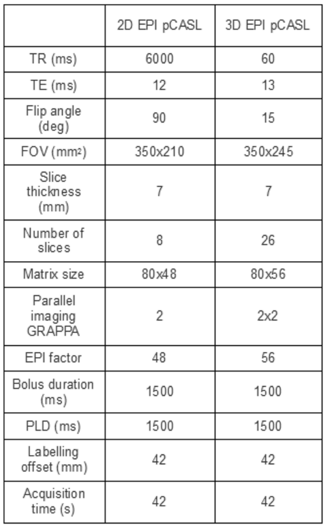

	2D EPI pCASL	3D EPI pCASL
TR (ms)	6000	60
TE (ms)	12	13
Flip angle (deg)	90	15
FOV (mm²)	350x210	350x245
Slice thickness (mm)	7	7
Number of slices	8	26
Matrix size	80x48	80x56
Parallel imaging GRAPPA	2	2x2
EPI factor	48	56
Bolus duration (ms)	1500	1500
PLD (ms)	1500	1500
Labelling offset (mm)	42	42
Acquisition time (s)	42	42

Table 1: Acquisition parameters of the pCASL sequences used in this work. The echo time TE was set to the minimal possible value in both cases. All ASL parameters were chosen to be the same to allow a meaningful comparison of perfusion values.

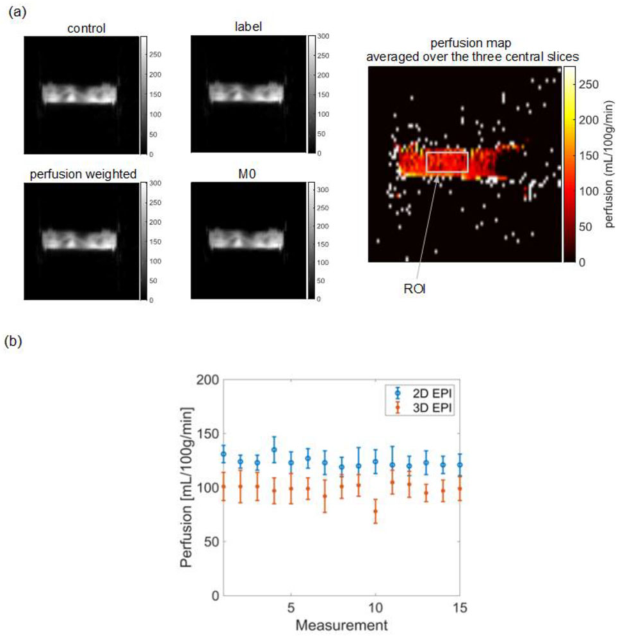

Figure 2: (a) Images of the phantom obtained with the 3D EPI and calculated perfusion map with ROI. (b) Mean perfusion calculated over the three central slices for the 15 measurements. The error bars indicate the corresponding standard deviations.

References:

[1] Alsop et al. Magn Reson Med 2015.
[2] Poser et al. Neuroimage 2010.
[3] Uhrig et al. Proc DGMP Nüremberg 2018.

L03.21

Unsupervised clustering on measurements derived from ASL and structural MR imaging of the brain can identify separated patterns in a cohort of MCI and SCI subjects

P. Bosco[1], L. Biagi[1], G. Cioni[1], M. Matteoli[2], M. Tosetti[1], &. the Train the Brain Consortium[3]
[1]IRCCS Stella Maris Foundation, Pisa, ITALY, [2]Institute of Neuroscience of the CNR, Pisa, ITALY, [3]the Train the Brain Consortium, Pisa, ITALY

Purpose/Introduction: Both Mild cognitive impairment (MCI) and Subjective Cognitive Impairment (SCI) are conditions that may precede Alzheimer's Disease (AD) or dementia.
For this reason, differential diagnosis of both MCI and SCI subjects is crucial for patient prognosis and management.
Subjects and Methods: A cohort of 111 elderly subjects (65 ÷ 89 years, mean 74.7 ± 5.2) was recruited. According to current guidelines [1, 2], 79 were confirmed at the neurological examination as MCI, 32 as SCI.
Besides clinical evaluation, all subjects underwent a MR exam of the brain at a 1.5T scanner (GE healthcare, HDx). MRI protocol included a T1-weighted 3D FSPGR sequence (TR/TE = 12650/5300 ms, prep time = 700 ms, NEX = 1, isotropic voxel = 1 × 1 × 1 mm^3) and a 3D pseudo-continuous Arterial Spin Labeling (pCASL) (TR/TE = 4850/10 ms, NEX = 4, pld = 2025 ms, spiral acquisition with 512 sampling points on eight spirals, spatial resolution = 3.64 mm, slice thickness = 4 mm). The gray matter was segmented on T1-weighted scans through the FreeSurfer recon-all utility [3] and 87 ROIs (19 subcortical and 68 cortical) were identified. After ASL and T1-weighted registration, for each ROI, the gray matter volume (normalized to the supratentorial volume) and the median of the ASL signal was measured. The ASL and the gray matters volumes data were separately processed through an unsupervised clustering method to identify homogeneous subgroups of subjects. The clustering approach was based on k-means algorithm. Since k-means algorithm requires a predetermined number of clusters and produces different solutions depending on the starting point, we iterated 4000 times the clusterization by varying both the number of clusters (from 2 to 10) and the starting points. In order to pick a final clustering solution a new clusterization was performed on the clusters co occurrence matrix of the subjects Fig. 1.

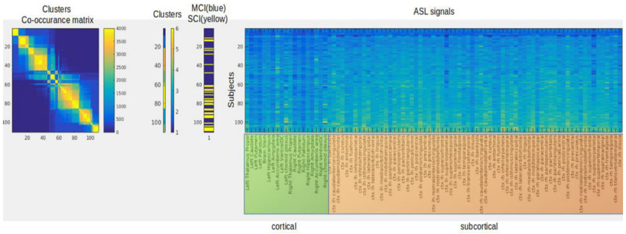

Co-occurance matrix on the iterative k-means clusterization process on the 111 subjects (left) with the final clusterization, the SCI/MCI reordered labels and the ASL median signals on the ROIs reordered accordingly.

Results: Unsupervised clustering identified 6 different clusters on both ASL and gray matter volume data. Perfusion showed to be

variable in the different clusters and showed dissimilar patterns at subcortical and cortical levels (Fig. 2). On the other hand, the patterns of atrophy showed peculiar characteristics in different clusters (atrophy limited to subcortical areas, widespread, limited to cortical areas but with deep structures spared from degeneration etc.).
The identified clusters showed to be different also when compared at clinical level, with higher Mini Mental Score Examination (MMSE) and Rey Auditory Verbal Learning Test values, and lower ADAS-cog values in clusters with higher perfusion levels (Fig. 3) and lower atrophy.

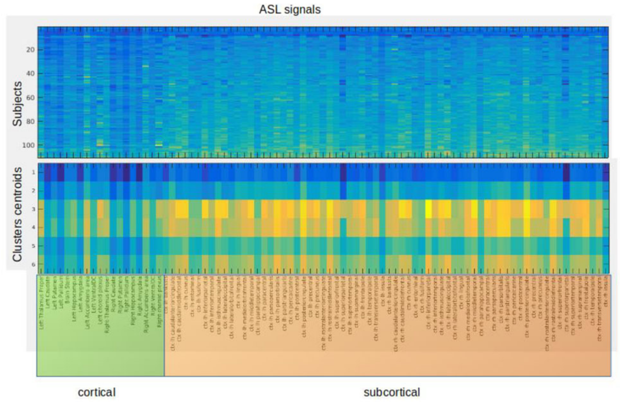

ASL signals on the entire data set and the centroids (the arithmetic mean of the signal in each ROI of the subjects belonging to cluster) of the identified 6 clusters.

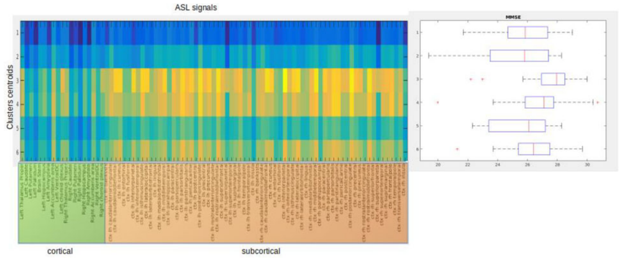

Centroids of the ASL identified clusters and the corresponding distributions of MMSE scores. Subjects with higher brain perfusion (cluster 3 and 4) show higher scores in neuropsychological assessment.

Discussion/Conclusion: Unsupervised clustering of ASL and structural MR imaging of the brain seems to be beneficial in differential diagnosis of subjects at risk of dementia.

References:

1-Sperling et al. Alzheimer's and Dementia, 7(3), 270–279, 2011.
2-Jessen et al. Alzheimer's and Dementia, 10(6):844–52, 2014.
3-Fischl et al. Neuron, 33(3):341–55, 2002.

L03.22

Characterization and validation protocol for a perfusion phantom used in arterial spin labeling experiments

L. Petitclerc, W. M. Teeuwisse, M. J. P. van Osch
Leids Universitair Medisch Centrum, C.J. Gorter Center for High Field MRI, Leiden, NETHERLANDS

Purpose/Introduction: Arterial Spin Labeling (ASL) is used to quantify perfusion in the brain. However, sequences and protocols differ between sites and vendors, making comparison of the results hazardous.[1] This is especially problematic for new sequences for which no ground truth is known. This has prompted the creation of the perfusion phantom QASPER (Quantitative Arterial Spin Labelling Perfusion Reference, Gold Standard Phantoms, London, UK), with the objective of allowing calibration and uniformization of quantification. In order for an ASL researcher to adopt such a phantom, it must exhibit characteristics and behaviours comparable to the human brain when imaged. This study aims to define a protocol for validation and characterization of an ASL phantom's relevant properties such as timing of label-arrival, B1-dependency, and flow crushing characteristics of the readout.

Subjects and Methods: All images were acquired on an Achieva dStream 3T scanner (Philips Healthcare, Best, the Netherlands). Three protocols were used: a Look-Locker (LL) sequence, a series of acquisitions with variable labeling flip angle (FA), and scans including crusher gradients, see Table 1. These were acquired in the phantom (beta testing version) and a healthy volunteer (female, age 25) who provided written informed consent. The LL sequence was used to compare the time-dependent behaviour of the signal to the volunteer data and the variable FA scans were acquired to estimate labeling efficiency. Also, the influence of flow-crushers on the signal was assessed. Images were processed in MATLAB. Threshold-based masking was applied on both datasets for signal averaging.

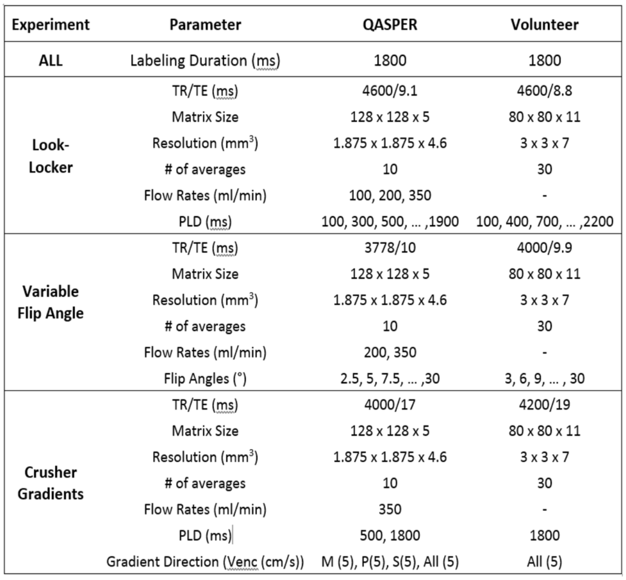

Experiment	Parameter	QASPER	Volunteer
ALL	Labeling Duration (ms)	1800	1800
Look-Locker	TR/TE (ms)	4600/9.1	4600/8.8
	Matrix Size	128 x 128 x 5	80 x 80 x 11
	Resolution (mm^3)	1.875 x 1.875 x 4.6	3 x 3 x 7
	# of averages	10	30
	Flow Rates (ml/min)	100, 200, 350	-
	PLD (ms)	100, 300, 500, … ,1900	100, 400, 700, … ,2200
Variable Flip Angle	TR/TE (ms)	3778/10	4000/9.9
	Matrix Size	128 x 128 x 5	80 x 80 x 11
	Resolution (mm^3)	1.875 x 1.875 x 4.6	3 x 3 x 7
	# of averages	10	30
	Flow Rates (ml/min)	200, 350	-
	Flip Angles (°)	2.5, 5, 7.5, … ,30	3, 6, 9, … , 30
Crusher Gradients	TR/TE (ms)	4000/17	4200/19
	Matrix Size	128 x 128 x 5	80 x 80 x 11
	Resolution (mm^3)	1.875 x 1.875 x 4.6	3 x 3 x 7
	# of averages	10	30
	Flow Rates (ml/min)	350	-
	PLD (ms)	500, 1800	1800
	Gradient Direction (Venc (cm/s))	M (5), P(5), S(5), All (5)	All (5)

Table 1. Sequence parameters

Results: Figures 1 and 2 show the results of the LL and FA experiments, respectively. The ASL signal map of a slice of the phantom and the brain is seen on top of both figures, and the average signal as a function of either PLD or FA on the bottom. The outer ring of signal in the QASPER images (label leakage) was excluded from the analysis. Time-dependence of signal for the recommended flow rate of 350 ml/min for QASPER approaches that of the volunteer the closest, with the latter seemingly exhibiting shorter transit times. FA data demonstrates a high similarity between the labeling efficiency of the phantom and volunteer, especially evident in the normalized signal graph. Crushing had visible effects on the phantom signal at a short PLD while leaving it unaffected at a typical pCASL PLD (not shown).

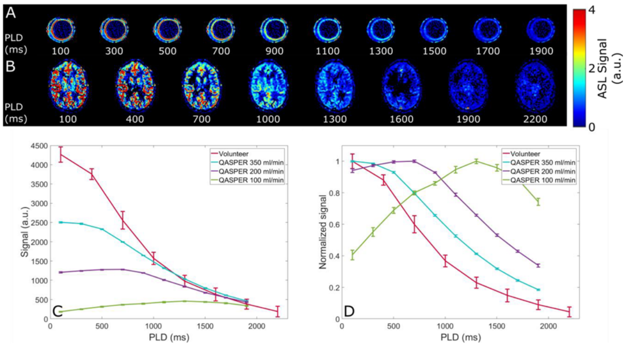

Figure 1. Perfusion maps for QASPER (a) and the subject (b) for all PLD's. Average signal as a function of PLD in absolute value (C) and normalized to the maximum (D) is also presented. Errorbars are the standard deviation over the averages.

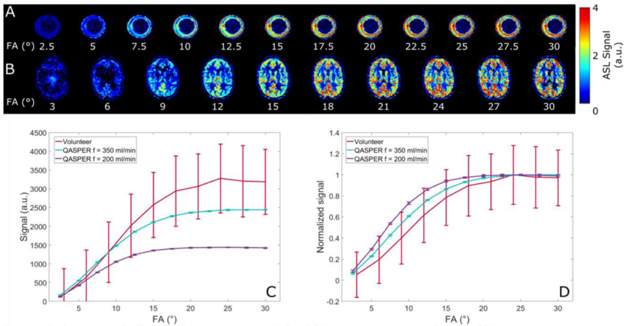

Figure 2. Perfusion maps for QASPER (a) and the subject (b) for all FA's. Average signal as a function of FA in absolute value (c) and normalized to the maximum (d) is also presented. Errorbars are the standard deviation over the averages.

Discussion/Conclusion: Comparison of the results for this protocol reveals good agreement of temporal variation of the signal, labeling efficiency as well as flow crushing. In the future, we will expand this method to measure the impact of more variables on the phantom signal. In particular, the effect of background suppression and the impact of off-resonance effects at the labeling plane will be studied. Results will also be tested for reproducibility.

References:

1. Fan, A. P., et al., (2016). JCBFM.

L03.23

3D GRASE readout optimization for time-encoded pCASL

A. M. Paschoal[1], S. Schmid[1], S. L. Franklin[1], M. C. van der Plas[1], R. F. Leoni[2], **M. J. van Osch[1]**

[1]C.J. Gorter Center for High Field MRI, Department of Radiology, Leiden University Medical Center, Leiden, NETHERLANDS, [2]InBrain Lab, Department of Physics, University of Sao Paulo, Ribeirao Preto, BRAZIL

Purpose/Introduction: 3D Gradient and Spin Echo sequences (GRASE) [1] are one family of recommended readout strategies [2] for arterial spin labeling (ASL), since they provide optimal background suppression by only use a single excitation per TR and also result in higher SNR compared to 2D echo planar images (EPI). Furthermore, Hadamard time-encoded labeling is preferable for providing multiple post-labeling delays (PLD) images [2], providing dynamic information. In this study, we aimed to optimize 3D GRASE readout for time-encoded pseudo-continuous ASL (pCASL) and to compare the performance to 2D EPI. We also analyzed the effect of flow compensation (FC) and the segmentation number for 3D GRASE acquisitions.

Subjects and Methods: Five volunteers (4 females, age 25.4 ± 4.3 years) were scanned using a time-encoded Hadamard 8 pCASL labeling sequence with single-shot, two shot and three shot 3D GRASE. The total labeling duration was 3500 ms, which was divided into blocks of 1800 ms, 800 ms, 400 ms, 2 ×150 ms and 2 ×100 ms and a minimum PLD of 260 ms. Two background suppression were applied at 1831 ms and 3135 ms. 2D EPI (TE (ms)/TR (s) = 9.2/4.1) and 3D GRASE using 1, 2 and 3 shots were acquired (TE (ms)/TR (s) = 9.2/4.1, 13.9/3.9 and 10.5/3, 9 respectively; all with first-order FC enabled). For all acquisitions, total scan time was kept around 6 min using 8, 6, 3 and 1 averages respectively. Two-shot 3D GRASE scans were acquired with and without FC. Post-processing and calculation of temporal SNR (tSNR) was done in MATLAB. FSL/BASIL was used to quantify the CBF and arterial blood volume (aBV).

Results: Figure 1 shows time-encoded pCASL maps for two slices at multiple PLDs for each used readout. From these ASL maps, we quantified the CBF and aBV (Fig. 2). tSNR was better for 2 and 3 segmented GRASE with FC (Fig. 3).

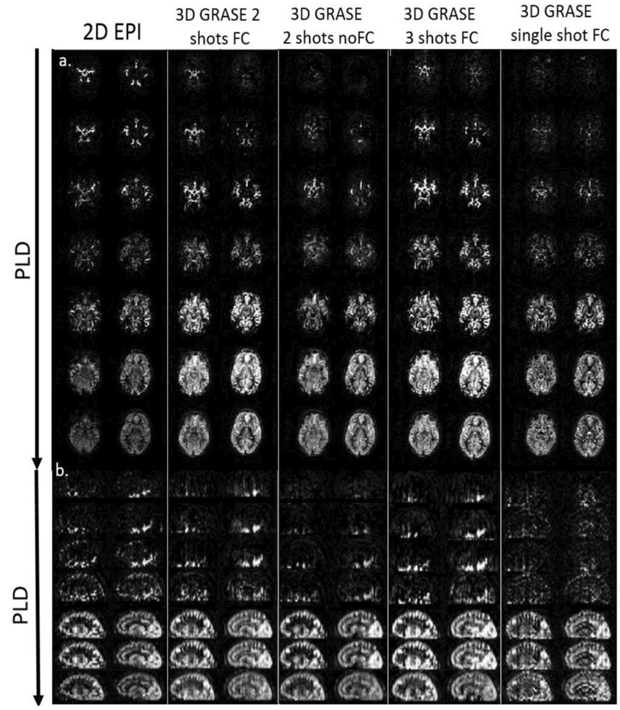

Figure 1 - Two representative slices of all PLD acquired for each different readout used in time-encoded pCASL. (a) Axial view; (b) Sagittal view.

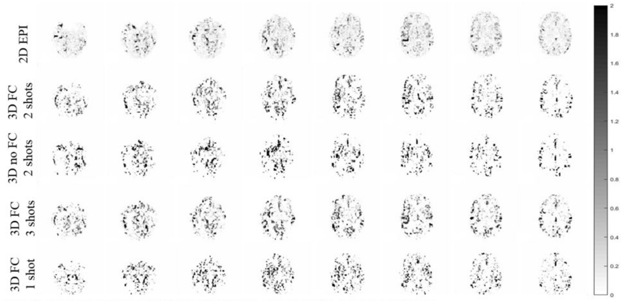

Figure 2 - Arterial blood volume (aBV) quantified for time-encoded pCASL for all readouts used.

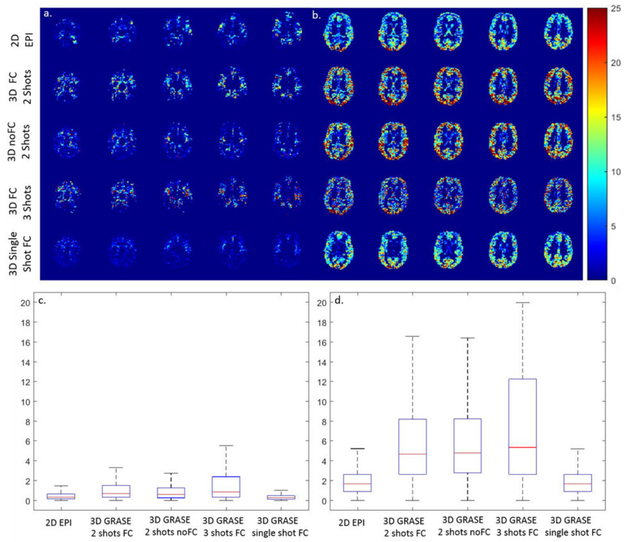

Figure 3 - Temporal SNR calculated for all readouts at (a) and (c) PLD of 360 ms and (b) and (d) PLD of 1860 ms

Discussion/Conclusion: Besides its lower SNR in comparison to 3D readouts, 2D EPI showed good results for time-encoded pCASL, allowing the visualization of both arterial and perfusion signal. For single shot 3D GRASE tSNR was comparable to 2D EPI for perfusion signal (Fig. 3b, b), but worse for arterial signal (Fig. 3a, c). On the other hand, segmented GRASE resulted in a higher tSNR for both perfusion and arterial signal. However, without first order FC the arterial signal was not well visualized (Figs. 1 and 2). Flow crushing properties of the GRASE readout module should therefore be carefully controlled when applying it for time-encoded pCASL. Based on our results we recommend the use of 2 or 3 shot 3D GRASE *with* FC. When single-shot readout is needed, GRASE and MS-EPI provide similar quality.

References:

[1] Gunther et al. MRM 2005; [2] Alsop et al. MRM 2015.

L03.24

Contrast enhanced dynamic MRI of the lacrimal drainage system

J. Martin[1], Y. Kazempour[2], V. Juniat[3], H. Lewis[4], M. Mills[1], S. Rajak[3], L. M. Harris[1]

[1]Brighton & Sussex University Hospitals NHS Trust, Medical Physics, Brighton, UNITED KINGDOM, [2]Brighton & Sussex Medical School, Brighton, UNITED KINGDOM, [3]Brighton & Sussex University Hospitals NHS Trust, Department of Ophthalmology, Brighton, UNITED KINGDOM, [4]Brighton & Sussex University Hospitals NHS Trust, Department of Imaging, Brighton, UNITED KINGDOM

Purpose/Introduction: Epiphora, the overflow of tears onto the face, is a common malady that can cause blurred vision, ocular discomfort, skin irritation and social embarrassment. One cause is an occlusion of the lacrimal drainage system. Dacryocystograms (DCG) and dacryscintigraphy (DSG) are variably used to investigate blockage and poor flow but have major limitations and both contribute an ionising radiation dose to the eye. Previous studies[1–4] have highlighted the potential for using magnetic resonance dacryocystography (MRDCG) but clinical uptake has been limited compared to DCG and DSG, possibly due to the difficulty of producing comparable dynamic images. In this feasibility study we investigate the efficacy of dynamic MRDCG using volumetric interpolated breath-hold examinations (VIBE).

Subjects and Methods: 15 volunteers with no lacrimal symptoms and 5 patients with unilateral epiphora were prospectively recruited. Currently, 10 asymptomatic volunteers have been scanned. Dotarem contrast agent (Gadoteric acid 0.5 mmol/mL) was diluted 50 fold in normal saline and infused from an Alaris GH syringe pump machine (infusion rate of 3mls/h) through a cannula onto the patient's eyes. The VIBE sequence ($\alpha = 10°$, *TE = 2.5 ms, TR = 5.0 ms*) was used to visualise contrast flow through the lacrimal drainage system on a 1.5T *Siemens Aera* MRI scanner. 18 oblique slices (*pixel size* $0.71 \times 0.71\ mm^2$*, matrix size* 224×228*, slice thickness 1.5 mm*) provide imaging of the volume containing the lacrimal system at a temporal resolution of 12 s.

Results: Dynamic MRDCG with VIBE provides multi-slice dynamic videos that reliably demonstrate contrast flow that is physiological and gives good anatomical data. The nasolacrimal passage was visible in 90% of volunteers following contrast being dripped into their eyes (1 failed due to volunteer movement). Figure 1 shows 6 slices for one volunteer after contrast was dripped in the left and right eyes with the lacrimal sac visible for each. Figure 2 shows a 6 slice fusion image (*0.75 mm x 0.75 mm x 9 mm*) for a single volunteer after contrast was dripped into the left eye.

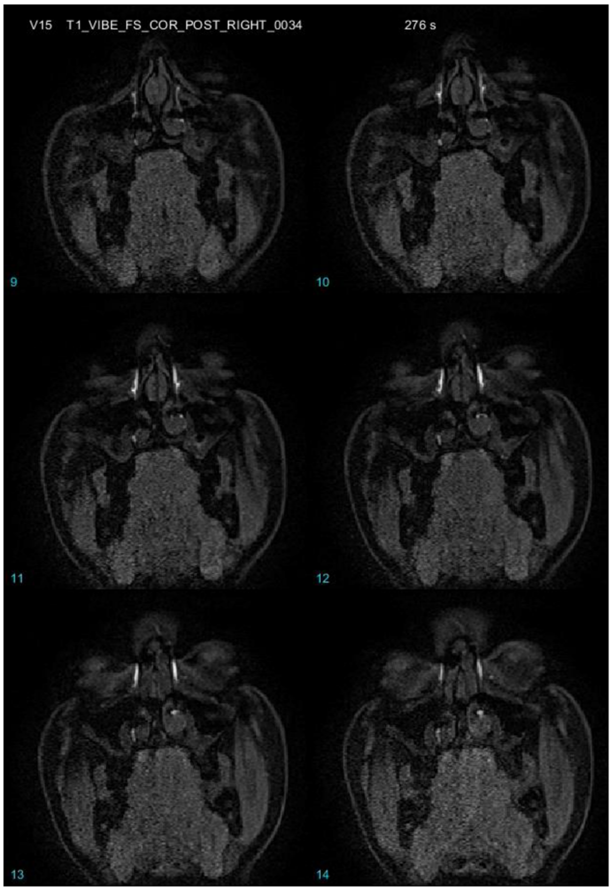

Figure 1 shows 6 slices of (0.75 mm x 0.75 mm x 1.5 mm) of the lachrymal system from a MRDCG VIBE Sequence 240 s after contrast had been dripped in the left eye and 100s post drip in right eye. The Sac and nasolacrimal duct are clearly visible

Figure 2 shows a multislice MRDCG fusion image (0.75 mm x 0.75 mm x 9 mm) of the lachrymal system from a VIBE Sequence 140 s after contrast was dripped into their left eye. The nasolacrimal and sac are visible.

Discussion/Conclusion: Dynamic MRDCG provides using VIBE sequences shows good structural and temporal resolution of the drainage system. It has the potential to be used as a routine clinical investigation of patients with epiphora that can safely and quickly provide better functional and anatomical information than existing imaging modalities of the tear drainage system and surrounding region.

References:

[1] Karagülle, Tuba, et al. “Nasolacrimal system: evaluation with gadolinium-enhanced MR dacryocystography…” 2002, European radiology.

[2] Goldberg, Robert Alan, et a. “Gadolinium magnetic resonance imaging dacryocystography.” 1993, American journal of ophthalmology.

[3] Manfrè, Luigi, et al. “MR dacryocystography: comparison…” 2000, American Journal of neuroradiology (AJR).

[4] Coskun, B., et al. “MR dacryocystography in the evaluation…” 2012. AJR.

L03.25

Accelerating CEST by 2D CAIPIRINHA: a simulation study on Z-spectra from 3D whole brain CEST-MRI

K. M. Nam, A. Hendriks, D. Klomp, E. Wiegers, J. Wijnen
University Medical Center Utrecht, Utrecht, NETHERLANDS

Purpose/Introduction: The standard 3D acquisition method of chemical exchange saturation transfer (CEST) imaging [1] for a whole brain can be time-consuming. To save scan time, it is beneficial to use acceleration techniques such as SENSE [2] and 2D CAIPIRINHA [3]. However, such acceleration methods may induce errors in the Z-spectrum due to the folding artifacts introduced by the undersampling pattern. Therefore, this work compared the Z-spectra of 3D CEST MRI images that were under-sampled with SENSE and 2D CAIPIRINHA to reduce scan time.

Subjects and Methods: We obtained 3D fast gradient echo MRI with 48 frequency offsets on a 7T MRI system (Philips, Best, The Netherlands) with an 8 transmit channel and a 32 receive channel head coil (Nova Medical, Wilmington, USA). Coil sensitivity maps were generated by ESPIRiT [4] using raw data from the first frequency offset (unsaturated). The sequence parameters were as follows: TE = 1.5 ms, TR = 3.35 ms, a 3 μT saturation block pulse of 1.4 s and the saturated volumes were acquired followed by 47 frequency offsets of between -1252 Hz and 1252 Hz. The acquired fully sampled data was retrospectively undersampled in MATLAB (The MathWorks, Natick, MA, USA), using SENSE and 2D CAIPIRINHA patterns that are described before [2, 3].

Results: In Fig. 1a, a 3D fully encoded CEST image of the brain is shown. The overlap maps of the SENSE and CAIPIRINHA reconstructed images with reductions factors R = 1, 2, and 4 are shown in Fig. 1b–l. In most cases, there is less overlap in the 2D CAIPIRINHA reconstructions, as compared to SENSE. The inverse g-factor maps in Fig. 2 correspond to reconstructed images using SENSE and 2D CAIPIRINHA with R = 1 (a), 2 (b–d), and 4 (e–k). When the optimal undersampling pattern is selected for R = 1–4, scan time can be reduced with a maximum g-factor penalty of less than 1.5 (as denoted in red in Fig. 2). The Z-spectra are shown in Fig. 3. The error in the Z-spectrum was calculated as the root-mean-square error (RMSE) on the Z-spectrum between the fully sampled 3D CEST-MRI and undersampled reconstructed image.

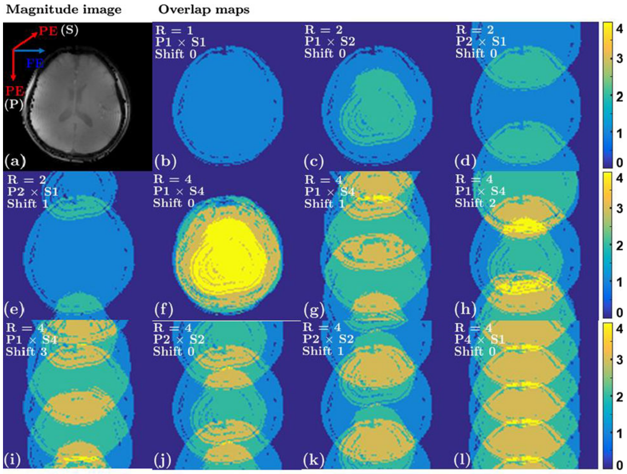

Fig 1: Transverse image of a 3D fully CEST-MRI with phase encoding (PE) in the AP direction and frequency encoding (FE) in the RL direction and the second phase encoding (PE) is in the FH direction (a). Reconstructed images using 2D CAIPIRINHA sample pattern with reduction factors R = 1, 2, and 4 (b-l). R indicates the reduction factor, P and S indicate the two phase encoding directions and the shift indicates the sampling position shift.

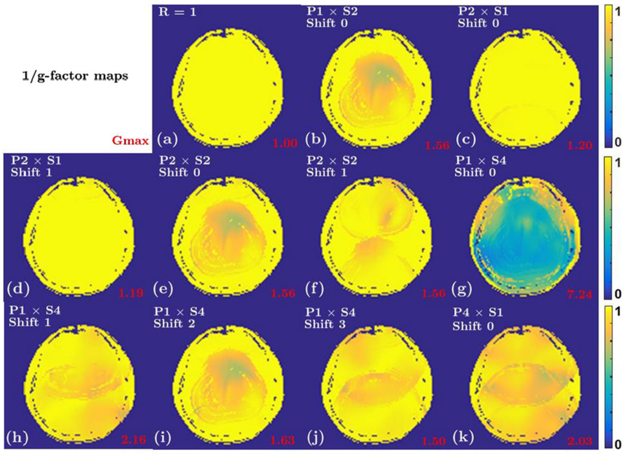

Fig 2: Inverse g-factor maps for different reduction factors: R = 1 (a), 2 (b-d), and 4 (e-k). The maximum value of the g-factor in the 3D whole brain image is displayed in red on the right bottom of each figure.

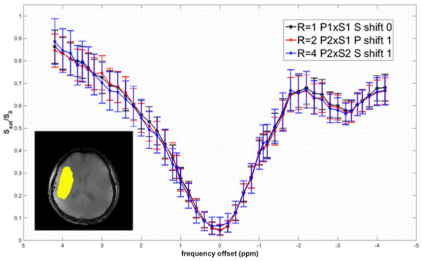

	$R_y x R_z$ dir. shift	RMSE
SENSE	P1xS2 S shift 0	0.0569
SENSE	P2xS1 P shift 0	0.0136
CAIPIRINHA	P2xS1 P shift 1	0.0135
SENSE	P1xS4 S shift 0	0.1767
CAIPIRINHA	P1xS4 S shift 1	0.0453
CAIPIRINHA	P1xS4 S shift 2	0.0624
CAIPIRINHA	P1xS4 S shift 3	0.0596
SENSE	P2xS2 S shift 0	0.0622
CAIPIRINHA	P2xS2 S shift 1	0.0414
SENSE	P4xS1 S shift 0	0.0486

Fig 3: Z spectra of the region of interest (ROI) in the brain. Only the 3 z-spectra with the lowest RMSE for R=1, 2, and 4 are shown. The standard deviation of the RMSE within the ROI is displayed on top of each frequency offset in the z-spectrum. All RMSE values are described in the right table with R = 1, 2, and 4 with SENSE and 2D CAIPIRINHA.

Discussion/Conclusion: In practice, 3D whole brain CEST imaging has been limited by long acquisition times because it requires multiple RF saturation offsets. In this work, we demonstrate that the scan time of CEST-imaging can be reduced by using SENSE and 2D CAIPIRINHA. Most successful acceleration is achieved through 2D CAIPIRINHA. However, note that the RMSE may change depending on the location of the ROI and will be lowest when aliasing artifacts are avoided. In conclusion, the acceleration of CEST-MRI up to R = 4 is feasible with an RMSE of less than 0.05.

References:

1. Jinyuan Zhou et al., 2003, Nature Medicine.
2. Klaas P. Pruessmann et al., 1999, MRM.
3. Felix A. Breuer et al., 2006, MRM.
4. Martin Uecker et al., 2017, MRM.

L03.26

Positive chemical exchange experiments using steady state RACETE

S. Mayer, F. T. Gutjahr, F. Hörner, P. M. Jakob
University of Wuerzburg, Experimental Physics 5, Würzburg, GERMANY

Purpose/Introduction: Chemical exchange saturation transfer (CEST) experiments allow the detection of low concentrated substances with exchangeable protons (called solute pool) which exhibit a chemical shift. The water pool is indirectly saturated by radiofrequency irradiation of the solute pool [1]. Very recently a new method with positive chemical exchange image contrast was proposed [2]. The Refocused Acquisition of Chemical Exchange Transferred Excitation (RACETE)-Method is based on a stimulated echo method. The first two 90°-pulses (called Excitation Transfer Modul, ETM) are applied on the resonance of the solute pool. Protons which exchange to the water pool after that excitation are read-out by a 90°-pulse on the water resonance and produce a stimulated echo, the RACETE-signal. The signal can be accumulated manifold by repeatedly playing out multiple ETM. After each read-out a waiting period is required so that the system reaches thermal equilibrium before the next preparation is started. In this work an extension to steady state RACETE imaging is demonstrated, where ETM-signal preparation is interleaved with small-flip-angle RACETE read-outs, eliminating the need for any waiting periods (see Fig. 1).

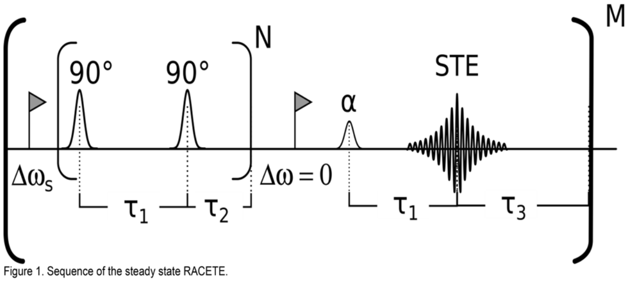

Figure 1. Sequence of the steady state RACETE.

Subjects and Methods: The steady state RACETE-sequence was analyzed using Extended Phase Graph (EPG) simulations and analytical calculations, assuming a two pool system using the Bloch-McConnell equations [3, 4]. The efficiency (steady state signal per square root of unit time) was derived and, similar to the well known Ernst-angle in steady state MRI, an efficiency optimum can be found for the steady state RACETE with an optimum T1-dependent flip angle.

Results: In Fig. 2 the simulated time-normalized signal for a typical set of parameters (e.g. T1 = 1 s) and the optimal flip angle is depicted. A significant improvement compared to the normal RACETE sequence can be observed for a broad range of 20–600 ETMs corresponding to preparation times of about 140 ms to 4.2 s only.

As a side note the analytically derived solutions were successfully reproduced by the EPG-simulations. In addition first phantom measurements containing iopamidol were performed demonstrating an increased efficiency using steady state RACETE.

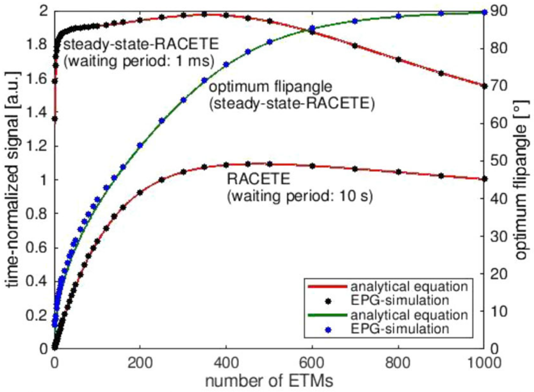

Figure 2. Simulated time-normalized RACETE signal compared to the steady state signal (and optimum flipangle) for a typical set of parameters.

Discussion/Conclusion: The proposed method can increase the efficiency of RACETE-imaging significantly, for a broad range of ETM-numbers, which facilitates future in vivo experiments.

References:

[1] Zijl P.: Chemical Exchange Saturation Transfer (CEST): what is in a name and what isn't. Magn Reson Med (2011); 65(4): 927–48.

[2] Gutjahr F.: Positive chemical exchange contrast in MRI using Refocused Acquisition of Chemical Exchange Transferred Excitations (RACETE). Z Med Phys (2018).

[3] Weigel M.: Extended phase graphs: Dephasing, RF pulses, and echoes—Pure and simple. JMR (2015).

[4] Malik S.: Extended Phase Graph Formalism for Systems With Magnetization Transfer and Exchange, Magn Reson Med 80:767–779 (2018).

L03.27

Dual-contrast RACETE for simultaneous positive- and negative-contrast chemical exchange imaging

F. T. Gutjahr[1], **S. Mayer**[2], P. M. Jakob[2]
[1]Universityhospital/University of Wuerzburg, Comprehensiv Heart Failure Center/Experimental Physics 5, Würzburg, GERMANY,
[2]University of Wuerzburg, Experimental Physics 5, Würzburg, GERMANY

Purpose/Introduction: Chemical Exchange Saturation Transfer (CEST)-MRI is the backbone of chemical exchange imaging [1]. In CEST, the magnetization of exchangeable solute protons is saturated and transferred to the water pool multiple times, resulting in a significantly decreased MRI signal intensity and thus a negative contrast. Just recently the RACETE-sequence, a novel method capable of generating a positive chemical exchange contrast was proposed [2]. This sequence makes use of stimulated echoes to refocus only the magnetization of the transferred protons (see Fig. 1a). Just like CEST, the RACETE sequence enhances its contrast by repeated excitation. In this work a Dual-Contrast-RACETE sequence with positive and negative chemical exchange contrast is proposed, which allows to acquire both RACETE-type and CEST-type signals simultaneously.

Subjects and Methods: The RACETE-pulse-diagram is depicted in Fig. 1a. The selection-gradient G_s is used to rephase only water spins previously present in the solute pool, which delivers the RACETE-signal. By adding a refocusing pulse after the RACETE-readout and an additional gradient G_s, only saturated water signal is refocused, yielding a CEST-weighted image (Fig. 1b). Experiments were performed on a 750 MHz tomograph (Bruker BioSpin, Ettlingen, Germany) using a phantom containing the x-ray contrast agent Iopamidol (100 mmol, Bracco Imaging, Konstanz) and crosslinked Bovine Serum Albumin (BSA, 5%). To calculate $CEST_{asym}$ imaging was performed at several frequency offsets, while RACETE-images are acquired in a single measurement.

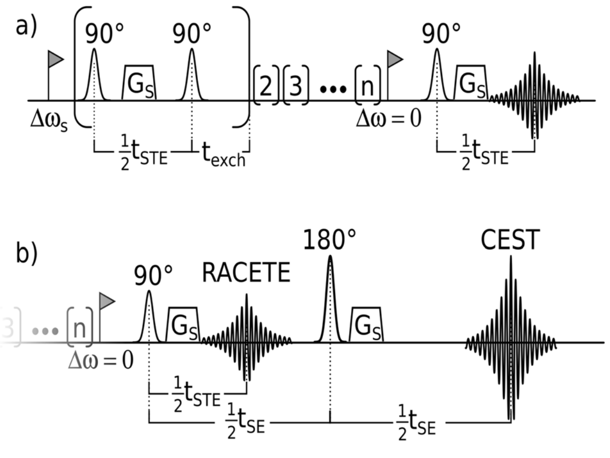

Fig.1 a) RACETE-sequence diagram. b) Extension to refocus a CEST weighted contrast

Results: In Fig. 2 the RACETE- and $CEST_{asym}$-images from the Dual-Contrast-RACETE measurement are shown next to images from stand-alone CEST and RACETE experiments. The images are of almost identical quality, however the RACETE-image from the combined measurement shows a lower SNR than in the stand-alone measurement.

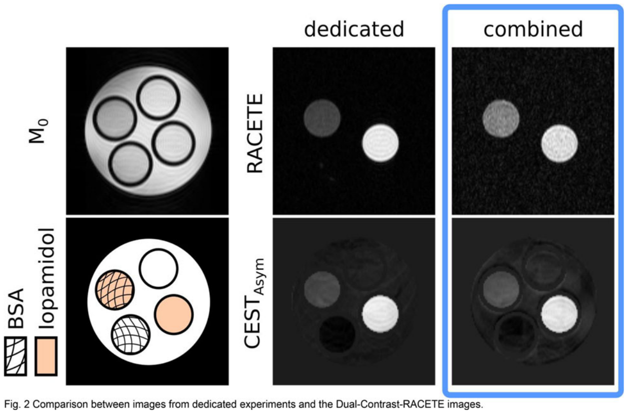

Fig. 2 Comparison between images from dedicated experiments and the Dual-Contrast-RACETE images.

Discussion/Conclusion: In this work the proposed Dual-Contrast-RACETE-technique is demonstrated to be capable of generating both a CEST- and RACETE-type contrast in a compact experiment. This feature comes for almost free and adds a new degree of freedom to future chemical exchange experiments.

In addition, this feature might allow mitigating certain shortcomings such as difficulties of the CEST-asymmetry-analysis in presence of NOE or low RACETE-signal for extremely high exchange rates.

References:

[1] Van Zijl, P. C. M., & Yadav, N. N. (2011). Chemical exchange saturation transfer (CEST): What is in a name and what isn't? MRM, 65(4), 927–948. https://doi.org/10.1002/mrm.22761.

[2] Gutjahr, F. T., Munz, E., & Jakob, P. M. (2018). Positive chemical exchange contrast in MRI using Refocused Acquisition of Chemical Exchange Transferred Excitations (RACETE). Z MED PHYS. https://doi.org/10.1016/J.ZEMEDI.2018.05.005.

L03.28

An optimized multislice sequence for 3D MRI-CEST imaging

D. Villano[1], F. Romdhane[1], L. Consolino[1], P. Irrera[2], W. Dastrù[1], D. Longo[3]

[1]University of Turin, Molecular Biotechnology and Health Sciences, Turin, ITALY, [2]University of Campania "Luigi Vanvitelli, Biostructures and Bioimages Institute, CNR, Naples, ITALY, [3]Italian National Research Council (CNR), Institute of Biostructures and Bioimaging (IBB), Turin, ITALY

Purpose/Introduction: MRI-CEST is a novel approach for interrogating several molecules with large potential clinical translation in cancer imaging. However, the long scan times needed (due to long RF pulses and multiple offsets sampling) reduce the volume coverage capability, hence the functional information and assessment of 3D heterogeneity that is recognized as an important biomarker of cancer aggressiveness. At preclinical level only few multislice CEST sequences have been implemented to solve this issue, but still limited by low SNR [1], geometry distortions [2] or strict applicability hypothesis [3]. To overcome these limitations, we have implemented an uneven irradiation scheme, as in [1], within a RARE readout and validated it in vitro and in vivo for pH imaging [4].

Subjects and Methods: The sequence was implemented for a Bruker 7T scanner by alternating a first long saturation pulse followed by repeated short pulses for each acquired slice. In vitro experiments were carried out on an Iopamidol containing phantom to optimize different parameters combinations. The optimized sequence was compared in term of Zspectra homogeneity along slices, SNR, presence of geometrical distortion and scan time with two previously reported sequences: a 2D RARE-based approach iterated along slices to obtain 3D data [5] and a multislice EPI-based scheme. Sequence accuracy along the third dimension was further tested on a pH varying Iopamidol phantom. In vivo validation was performed in acidoCEST and glucoCEST applications by acquiring multislice images of whole tumors following iopamidol or glucose injection.

Results: Figure 1 compares different acquisition approaches. The 2D RARE method showed the highest spectra homogeneity and SNR and absence of distortion, but the longest scan time. For the EPI scheme, T1 relaxation induced a noticeable loss of contrast, in addition to distortion. Moreover, the SNR was almost three times lower for the EPI readout. Our proposed sequence showed the best trade-off between scan time and image quality. Good homogeneity in terms of CEST contrast along slices is showed in Fig. 2. The optimized fast multislice sequence was applied in vivo to obtain multislice pH images following iopamidol injection (Fig. 3A). The 3D data set was exploited for 3D pH rendering of the tumors (Fig. 3B) and allowed to assess the pH gradient in the tumoral region, hence providing heterogeneity measurement of tumor acidosis (Fig. 3C).

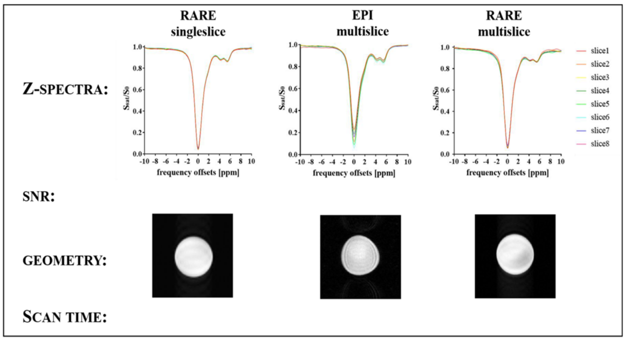

Figure1: Comparison of conventional single slice and EPI multislice sequences with the proposed one in term of Z-spectra homogeneity along the slices, SNR, presence of geometrical artifacts and acquisition duration of a single offset.

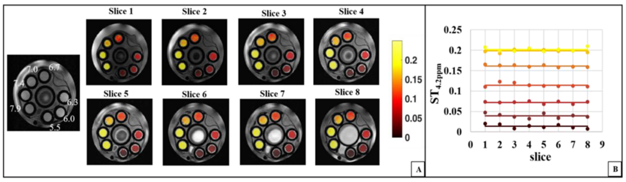

Figure2: CEST contrast 2D maps at 4.2 ppm. Comparison between mean contrast calculated inside each compartment as function of the slice (points) and its mean value calculated along slices (lines).

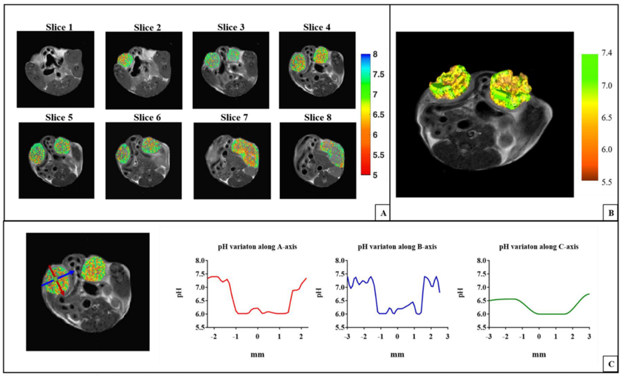

Figure3: Multislice 2D pH maps in the kidneys region superimposed onto the anatomical image (A). pH map 3D rendering (B). pH gradients along three directions (A-axis and B-axis: in plane and C-axis: across slices) in the tumoral region (C).

Discussion/Conclusion: A fast multislice CEST MRI sequence was tested and validated in vivo allowing high volume coverage, good sensitivity and homogeneity along slices in feasible times (~ 10 min). The optimized sequence allows accurate 3D imaging for an improved in vivo characterization of tumor heterogeneity.

References:

1 Sun et al.; Magn Reson Med 2011, 65, 588.

2 Sun et al.; Magn Reson Med 2008, 59, 1175.

3 Randtke et al.; Magn Reson Med 2017, 78, 106.

4 Longo et al.; Cancer Res 2016, 76, 6463.

5Longo et al.; Magn Reson Med 2011, 65, 202.

L03.29

In Vivo 3D chemical exchange saturation transfer for human brain studies at 3T

Y. Wu[1], T. Wood[2], J. A. Hernandez-Tamames[1], G. J. Barker[2], M. Smits[1], E. A. H. Warnert[1]
[1]Erasmus MC, University Medical Centre Rotterdam, Department of Radiology & Nuclear Medicine, Rotterdam, NETHERLANDS,
[2]King's College London, Centre for Neuroimaging Science, London, UNITED KINGDOM

Purpose/Introduction: Chemical Exchange Saturation Transfer (CEST) imaging is a novel MRI technique with great potential for measuring amide proton content. CEST research is commonly performed at ultra-high field strength (7 Tesla or higher) so for clinical applicability, CEST sequences need to be optimized at 3 Tesla. In the current work, 3D CEST sequences with different parameterization were compared for the detection of amide protons (+3.5 ppm) at 3 Tesla.

Subjects and Methods: All measurements were performed on a 3 Tesla scanner with a 32-channel head coil (General Electric, Chicago, USA). A phantom (egg white) and one healthy volunteer (female, 30 years) were scanned. CEST experiments were performed using 3D pulsed saturation schemes similar to [2] with different readouts (full k-space trajectory with 1 or 2 k-space lines per CEST preparation and Snapshot sequence using spiral reordering [3]). Common acquisition parameters: frequency off-sets ($\Delta\omega$): -6 to 6 ppm, TR = 13.2 ms, TE = 6.3 ms, 12 slices, resolution $1.875 \times 1.875 \times 5$ mm^3, B_1 power of 1 uT. Additionally, B_1 of 0.6, 1.2 and 1.8 μT were tested for B_1 optimization under Snapshot. Using $B_1 = 1.2$ uT, the amount of magnetization transfer (MT) pulses (duration of 20 ms each, ranging from 10 to 80 pulses) was also tested. Voxel-wise B_0 inhomogeneity correction and magnetization transfer ratios (MTR_{asym}) calculation were performed with freely available software [4]. Two images acquired without saturation were used to normalize the images with saturation for the calculation of Z-spectra.

Results: The application of Snapshot, higher B_1 and more MT pulses shows higher CEST effects in the phantom experiment (Fig. 1). The same conclusion holds in the human study (Figs. 2, 3).

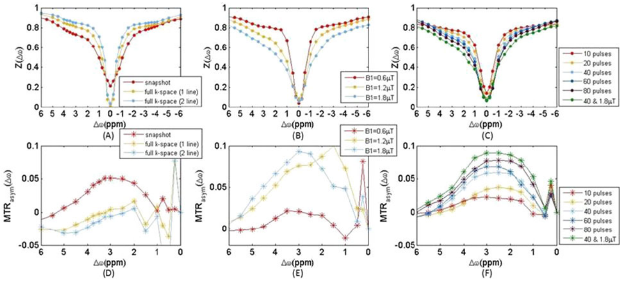

Figure 1 Influence of k-space trajectories, B1 and MT pulses on Z-spectra and MTR_{asym} in the phantom study. In MT pulses comparison, an additional series with 1.8 μT B1 power and 40 MT pulses was tested. Metrics were averaged in the region of interest circled in the centre of phantom.

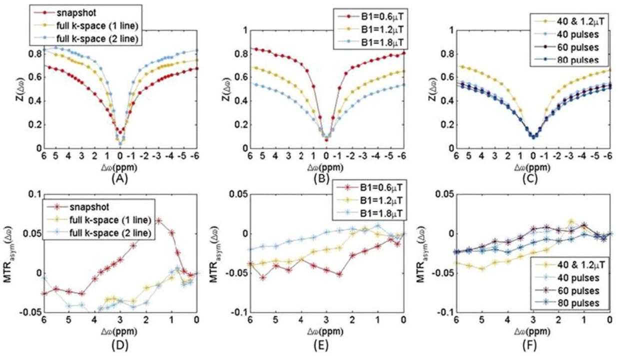

Figure 2 Comparison of sequences under different parameters in the human study (in grey matter region in one slice of the brain). In (E) and (F), the result of the series with 1.2 μT and 40 MT pulses was added while other results are series with 1.8 μT B1 power and different MT pulses.

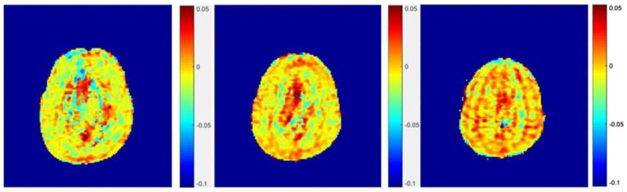

Figure 3 In vivo MTR_{asym} map of human brain. Three slices were shown from the brain of the healthy volunteer.

Discussion/Conclusion: The snapshot CEST acquisition scheme showed stronger amide signal (at 3.5 ppm) and decreased 20% of acquisition time than full k-space trajectory. Compared with applying 80 MT pulses, using 40 MT pulses gave a 30% reduction in scanning time bringing the total acquisition under 4 min. Compensating for the decreased CEST signal with less MT pulses can be done by using a higher B_1 power of 1.8μT. Future work includes further optimization of B_1 power and sampling schemes of CEST frequency offsets.

References:

1. Jones, C. K et al. *Magn. Reson. Med.* **67,** 1579–1589 (2012).
2. Deshmane, A et al. *Magnetic resonance in medicine*, **81**(4), pp.2412–2423.
3. CEST-Sources (2018, October 20), retrieved from cest-sources.org.

L03.30

GagCEST imaging in the upper ankle joint in patients with ostheochondral lesions and healthy volunteers

A. Müller-Lutz, C. Schleich, L. Radke, J. Stabinska, H.-J. Wittsack
University Dusseldorf, Medical Faculty, Department of Diagnostic and Interventional Radiology, D-40225 Düsseldorf, GERMANY

Purpose/Introduction: To optimize a gagCEST protocol for imaging of glycosaminoglycans at a clinical 3 Tesla MRI and to compare gagCEST values between patients with ostheochondral lesions and healthy volunteers.

Subjects and Methods: The study was approved by the local ethics committee and written informed consent was obtained from all volunteers and patients.

We used Bloch-McConnell simulations for the optimization of the gagCEST protocol (https://github.com/cest-sources/BM_sim_fit/) [1].

Therefore, T1 and T2 relaxation times of cartilage[2] were used: T1 = 1.2 s, T2 = 0.039 s.

11 volunteers (age 24 ± 5 years) and 4 patients (age 32 ± 9 years) with ostheochondral lesions were investigated with the optimized gagCEST protocol. In addition, T1 and T2 values were determined in order to evaluate, if the relaxation times used in the simulation were accurate.

Sequence parameters of the FLASH-based pulsed gagCEST sequence were: FOV = 160 × 160 mm^2, slice thickness = 5 mm, TE/TR = 3.5 ms/7.2 ms. 25 CEST images with the frequency offsets between -3 ppm and 3 ppm and a reference image at -300 ppm were recorded. An acquisition of an additional water saturation shift referencing[3] sequence was used for B0 inhomogeneity correction.

Results: The optimization with the Bloch-McConnell simulations showed an optimal B1 amplitude of 0.8 µT and a pulse and an interpulse duration of 300 ms using 8 saturation pulses. We found a mean T1 time of (0.88 ± 0.13) s and a mean T2 time of (0.033 ± 0.005) s. These values were significantly different from those used in the simulation. Nevertheless, further simulations revealed the same optimal pulse sequence parameters for the CEST sequence. Healthy volunteers showed a significantly higher gagCEST effect compared to patients (volunteers: $MTR_{asym} = (1.40 \pm 0.71)\ \%$; patients: $MTR_{asym} = (0.05 \pm 0.28)\ \%$; p-value < 0.01) (see Fig. 1)

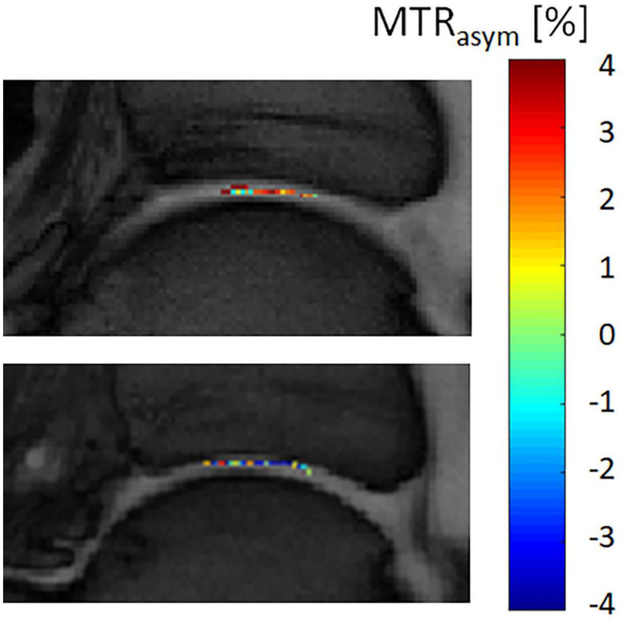

Figure 1. GagCEST values overlaid with the anatomical image in the upper ankle joint

Discussion/Conclusion: The proposed gagCEST technique showed good performance and could distinguish between volunteers and patients with ostheochondral lesions. A larger patient cohort is desirable to confirm these initial findings.

References:

[1] Zaiss, M, Angelovski, G, Demetriou, E, McMahon, MT, Golay, X and Scheffler, K (2017), QUESP and QUEST revisited – fast and accurate quantitative CEST experiments. Magn Reson Med. https://doi.org/10.1002/mrm.26813.

[2] Stanisz GJ, Odrobina EE, Pun J, Excaravage M, Graham SJ, Bronskill MJ, Henkelman RM (2005), T1, T2 Relaxation and Magnetization Transfer in Tissue at 3T. Magn Reson Med. https://doi.org/10.1002/mrm.20605.

[3] Kim M, Gillen J, Landman BA, Zhou J, van Zijl PC. Water Saturation Shift Referencing (2009), Water saturation shift referencing (WASSR) for chemical exchange saturation transfer (CEST) experiments. Magn Reson Med. https://doi.org/10.1002/mrm.21873.

I15 Teaching Session

13:50–15:20 *Room 1 - Willem Burger Zaal*

More Than Just a Scan

I15.01

Model-based multi-contrast methods, fingerprinting and quantitative imaging

A. Sbrizzi[1, 2]
[1]UMC Utrecht, Utrecht, NETHERLANDS, [2]UMC Utrecht, Imaging Division, Utrecht, NETHERLANDS

Learning Objectives: Understanding the mechanisms of signal generation and reconstruction, which play a role in multi-parametric quantitative MR.

Understanding how this field evolved during the last 15 years.

Body: In this lecture, I will give an overview of multi-parametric quantitative MR methods, which are based on a single scan to reconstruct T1, T2 and proton density maps.

The starting point will be the methods based on analytical signal models [9, 13, 14] and their acceleration by acting on more efficient k-space encodings [4]. Afterwards, I will briefly introduce the Compressed Sensing paradigm [5] and show how the concepts of sparsity, incoherence and over-completeness could be applied jointly to k-space encoding and time to accelerate quantitative mapping [3]. A natural development along this line is MR Fingerprinting [8, 6] and I will show how the concept of incoherence plays a role also in the MRF framework [11]. Recently proposed multi-parametric reconstruction paradigms are leaning towards an inversion theoretic approach [1, 15] and ultimately towards a parametric quantification which acts directly on k-space (or time-domain) data [10].

Finally, the reproducibility and the clinical deployment of the fast multi-parametric techniques will be addressed [2, 7, 12].

References:

[1] Assländer, J., et al. (2018). *Magnetic resonance in medicine*, *79*(1), 83–96.
[2] Buonincontri, G., et al. (2019). *NeuroImage*.
[3] Doneva, M., et al. (2010). *Magnetic Resonance in Medicine*, *64*(4), 1114–1120.
[4] Ehses, P., et al. (2013). *Magnetic resonance in medicine*, *69*(1), 71–81.
[5] Lustig, M., et al. (2007). *Magnetic Resonance in Medicine*, *58*(6), 1182–1195.
[6] Jiang, Y., et al. (2015). *Magnetic resonance in medicine*, *74*(6), 1621–1631.
[7] Jiang, Y., et al. (2017). *Magnetic resonance in medicine*, *78*(4), 1452–1457.
[8] Ma, D., et al. (2013). *Nature*, *495*(7440), 187.
[9] Schmitt, P., et al. (2004). *Magnetic Resonance in Medicine 51*(4), 661–667.
[10] Sbrizzi, A., et al. (2018). *Magnetic resonance imaging*, *46*, 56–63.
[11] Stolk, C. C., & Sbrizzi, A. (2019). *IEEE transactions on medical imaging*.
[12] Tanenbaum, L. N., et al. (2017). *American Journal of Neuroradiology*, *38*(6), 1103–1110.
[13] Warntjes, et al. (2007). *Magnetic Resonance in Medicine 57*(3), 528–537.
[14] Warntjes, J. B. M., et al. (2008). *Magnetic Resonance in Medicine 60*(2), 320–329.
[15] Zhao, B., et al. (2016). *IEEE transactions on medical imaging*, *35*(8), 1812–1823.

I15.03

Interpretation and application of multi-contrast MRI

A. Tisell[1, 2]
[1]Linköping University, CMIV, Linköping, SWEDEN, [2]Linköping University, Medical radiation physics, Linköping, SWEDEN

Learning Objectives: What synthetic MRI is, and how to generate synthetic MRI.

How to implement synthetic MRI in clinical practice.

How to apply synthetic and quantitative MRI in clinical studies.

Body: In conventional MRI, contrast between different types of tissues are manly achieved by implementing MR sequences that are sensitive to the inherent T1 and T2 differences between tissue typs. And, the different images are denoted to which parameters that have the strongest effect on the contrast i.e. T1 weighted (T1w), T2w, PDw, etc. However, all image contrasts are alos deepened on a number of scanner related parameters such as Coil sensitivity, B0, B1 homogeneity, etc. Using quantitative MRI imaging this scanner related effects can be mitigated and also all image contrast can be synthesised form a single MR sequence.

This presentation will be based on discussion of using the qMRI method presented in [1, 2] for generating synthetic MRI and for tissue classification for brain imaging. However, in principle any method for any body part generating qMRI values [3, 4] could be used in this manner.

How Do We Calculate syMRI?

The Bloch equations can be used to set up signal equations for conventional MRI sequences. This, have been done for optimising conventional MRI but it can also be used to calculate *"synthetic"* MRI for quantitate MRI [1, 5, 6].

Can syMRI Replace the Conventional MRI?

It has been shown that the image quality of syMRI is comparable to conventional MRI [7–10]. However, synthetic T2 FLAIR images has a problem with partial volume effects [8].

How Can We Use qMRI for Tissue Classification and Volume Estimations?

QMRI can also be used for automatic, user independent tissue classification and brain parenchymal fraction (BPF) quantifications [11–14]. Moreover, myelin volume can be estimated using qMRI [14–17]. The BPF quantification can be used for following developing brains or disease progression [18–22].

How Can We Find Biomarkers Using syMRI and qMRI?

Since the synthetic MRIs are base on qMRI there are a perfect registration between synthetic MRI and the quantitative parameters maps. This can be utilised for drawing ROI in the synthetic and perform quantitative statistical test on using the qMRI [23–28].

References:

1. Warntjes, MRM, 2008.
2. Krauss, MRI, 2015.
3. Deoni, MRM, 2008.
4. Ma, Nature, 2013.
5. Gulani, InvRad, 2004.
6. Hacklander, Acad Rad, 2005.
7. Hagiwara, , AJNR, 2017.
8. Tanenbaum, AJNR, 2017.
9. Krauss, Eur Radiol, 2018.
10. Wallaert, L., MRM Sci, 2018.

11. West, Eur Radiol, 2012.
12. West, PLoS One, 2013.
13. Warntjes, AJNR 2014.
14. Saccenti, Neurorad 2019.
15. Warntjes, Front Neurol, 2016.
16. Warntjes, AJNR, 2017.
17. Hagiwara, Sci Rep, 2018.
18. Vagberg, AJNR, 2013.
19. Vagberg, PLoS One, 2015.
20. Granberg, AJNR, 2016.
21. Vagberg, J Neuroradiol, 2016.
22. Hakansson, I., J Neuroinf, 2018.
23. Engstrom, M. PLoS One, 2014.
24. West, PLoS One, 2014.
25. Blystad, AJNR, 2016.
26. Blystad, PLoS One, 2017.
27–28. Hagiwara, AJNR, 2017.

S12 Scientific Session

13:50–15:20 *Room 2 - Van Weelde Zaal*

Molecular & Cellular Imaging

S12.02

Sodium MRI reveals therapy induced changes in Multiple Sclerosis lesions

A. Mennecke[1], A. Nagel[2], J. Wegmann[1], R. Linker[3], D.-H. Lee[3], N. Kästle[1], K. Huhn[3], A. Dörfler[1], T. Engelhorn[1]
[1]*Universitätsklinikum Erlangen, Neuroradiologie, Erlangen, GERMANY,* [2]*Universitätsklinikum Erlangen, Radiologie, Erlangen, GERMANY,* [3]*Universitätsklinikum Erlangen, Neurologie, Erlangen, GERMANY*

Purpose/Introduction: In multiple sclerosis, the increase of sodium in the white matter correlates with disease markers.(1) Therefore, sodium MRI is likely to provide insights into neuroaxonal pathophysiology. During an acute episode, the medication aims in delaying, inhibiting or even reversing the pathophysiological processes. The purpose of the current study is to investigate the different types of multiple sclerosis lesions and their longitudinal time course during the recovery from an acute multiple sclerosis episode.

Subjects and Methods: We included 29 patients in the study who were admitted to the hospital with acute multiple sclerosis relapse or primary diagnosis of multiple sclerosis and showed acute disturbances of the blood-brain-barrier in contrast enhanced T1 weighted imaging (T1CE). The subjects were scanned with a sodium MRI protocol at the beginning of the therapy with a 3T MR scanner, a dual-tuned head coil and a 3D density-adapted 3D radial acquisition technique(NA1).(2) 12 subjects were additionally scanned on one or more follow-up measurements between 1 and 100 days afterwards and 20 patients were scanned with a sodium inversion recovery sequence (IR) to suppress the free sodium and access the tighter bound intracellular sodium in the brain.(1) Lesions were demarcated in the T1CE, the proton fluid attenuated inversion recovery (Flair, FL +) and the sodium image (NA +). At least 10 regions of interest were drawn in the normal appearing white matter of the flair of every patient (naWM). All images were linearly transformed to the NA1 of the patient. The mean NA and IR signal of the lesions were calculated and normalized by the mean of the naWM regions (nNA and nIR) of the patient, respectively.

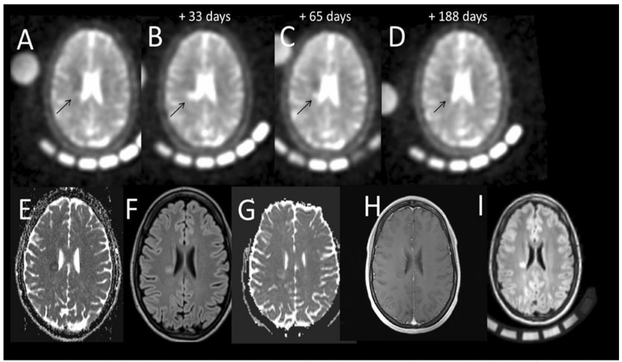

Temporal evolution (A-D) of a lesion (arrow) showing both, therapy fail(A->B) and successful recovery (B->C->D). ADC decrease (E) and FL+ (G) at the time of NA1, ADC (G) and T1CE (H) at the time of NA3, Flair at the time of Na4 (I)

Results: At the first visit during the acute episode, the NA+, FL+ and the T1CE+ lesions showed increased nNA. During recovery, the nNA of the visually detectable sodium hyperintense lesions decreased significantly, while the nNA of the T1CE+ lesions did not change. In the T1 normal Flair lesions, nIR was slightly increased. Despite the therapy, nIR of the NA+ lesions decreased from visit 1 to 2.

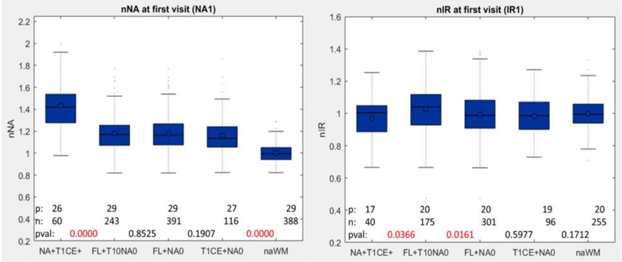

Box-whisker-plots of nNA and nIR for the first visit. Na+: visibly detectable Na-enhancing lesion; T1CE+: hyperintens in T1CE; FL+: hyperintense in Flair; T10: T1CE normal; NA0: not NA+T1CE+; p: number of patients, n: number of lesions, see fig 3

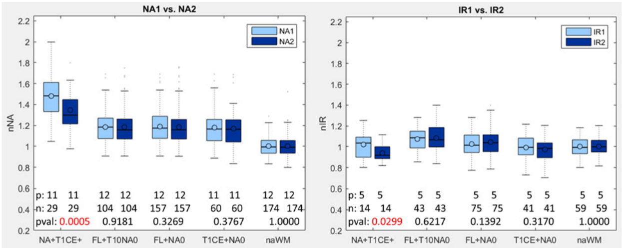

Box-whisker-plots of nNA and nIR for the first (1) and second visit (2). see fig.2 pval: p-values of the paired t-test. Red: pval < 0.05. Only the nNA and nIR of the initially visibly detectable sodium enhancing lesions differ between 1 and 2.

Discussion/Conclusion: Sodium imaging, especially with the inclusion of an inversion recovery sequence, holds the potential to gain insight to the pathological processes in acute multiple sclerosis episodes. With increased field strength and sophisticated signal acquisition methods sodium imaging is a gadolinium-free method to access the recovery status of multiple sclerosis lesions.

References:

1. Petracca M, Vancea RO, Fleysher L, Jonkman LE, Oesingmann N, Inglese M. Brain intra- and extracellular sodium concentration in multiple sclerosis: a 7 T MRI study. Brain : a journal of neurology 2016;139(Pt 3):795–806.
2. Nagel AM, Laun FB, Weber MA, Matthies C, Semmler W, Schad LR. Sodium MRI using a density-adapted 3D radial acquisition technique. Magnetic resonance in medicine 2009;62(6):1565–1573.

S12.03

Unusual nanoparticle structure results in fast in vivo clearance of single-resonance 19F perfluorocarbon nanoparticles

X. Staal[1], S. Temme[2], O. Tagit[1], K. Cortenbach[1], K. Becker[2], A. Veltien[3], N. K. van Riessen[1], U. Fögel[2], M. Srinivas[1]
[1]*Radboudumc, Tumor Immunology Lab, Nijmegen, NETHERLANDS,* [2]*Heinrich-Heine-University, Department of Molecular Cardiology, Düsseldorf, GERMANY,* [3]*Radboudumc, Department of Radiology, Nijmegen, NETHERLANDS*

Purpose/Introduction: Fluorine-19 Magnetic Resonance Imaging (^{19}F MRI) is an upcoming imaging modality, using [1] the 100%

naturally abundant and stable fluorine-19 isotope, that can be imaged as a result of its spin magnetic moment [2]. MRI has low sensitivity, therefore most of the used imaging agents are composed of heavily fluorinated molecules. These molecules preferably contain chemically identical fluorine bonds to give a single resonance peak. Unfortunately, these perfluorocarbons have clearance half-lives of 200 days, leading to regulatory and safety concerns, which in turn hamper clinical adaptation [3]. Here we show multicore PFCE containing nanoparticles that are cleared faster by their unique structure.

Subjects and Methods: NPs, consisting of poly(D, L-lactide-co-glyolide) (PLGA) polymer and the single resonance perfluoro-15-crown-5-ether (PFCE), and egg-lecithin PFCE nanoemulsions (NE), were synthesized using a miniemulsion technique. Equivalent amounts of PFCE (20 mg nanoparticles dissolved in 400 µl 0.9% NaCl and 3, 3% PFCE nanoemulsions) were injected into the tail vein of wild type C57Bl/6 mice. At 6 timepoints spanning 2 weeks biodistribution was measured using an optimized ^{19}F 3D RARE sequence (12:48 min scan time). With the aid of a reference tube with a known concentration of imaging agent, fluor signal is corrected for injected dose. Nanoparticles were dissolved in phosphate buffered saline and agitated at 37 °C for 2 weeks to study in vitro degradation through hydrolysis.

Results: The synthesized nanoparticles are, 200 nm diameter in size and contain 30wt % PFCE, the nanoemulsions are 130 nm diameter. Fluoride concentration and MRI signal are linear (R^2 0.99 for linear fit) allowing quantification based on a reference. 2 h after injection, the liver contains 40% of the injected dose for both NE and NP, spleen contains 2, 5% and 11% of injected dose for NE and NP respectively. Over the time course of 2 weeks the liver signal halved and the spleen signal was reduced to 1/5 of the initial signal for NPs, for NEs the liver concentration stayed stable and the spleen concentration dropped below the detection threshold. Nanocapsules, revealed causative mechanisms behind the enhance clearance of the NPs to be the structure, not the PLGA polymer. Degradation experiments show a unique degradation profile when compared to conventional PLGA particles. NPs degrade into smaller domains, averaging around 50 nm diameter, while retaining PFCE.

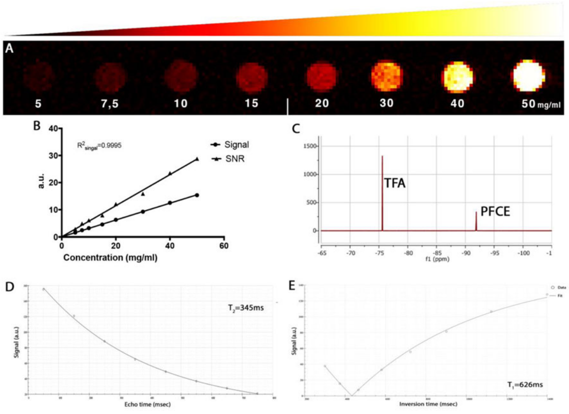

MRI characterisation. A, Phantoms containing a known amount of NPs B, Signal to known concentration of NP is linear C, 19F NMR D,E, relaxation properties

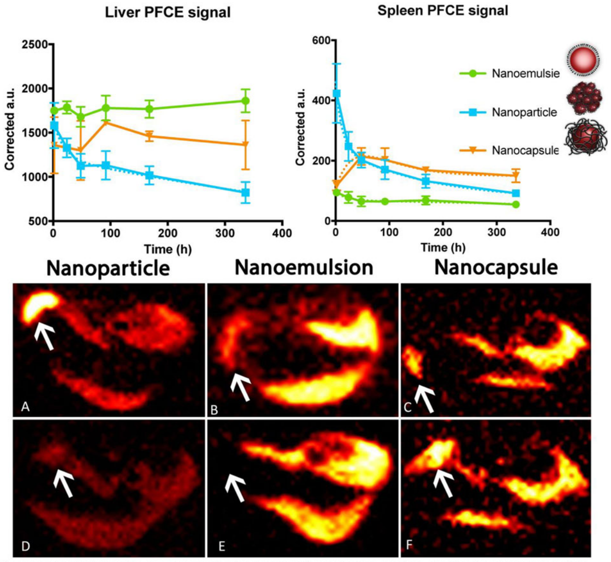

In vivo mouse biodistribution. Top row: corrected fluorine content for liver and spleen over time, showing clearance of only the NPs. A,B,C, representative image of liver and spleen 2 hours after injection, D,E,F 2 weeks after injection

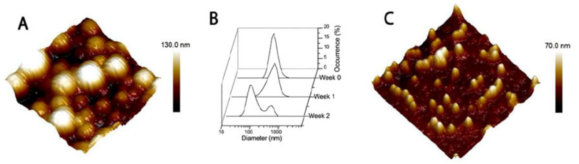

AFM and DLS analysis of degradation of NPs. A, NPs dissolved in PBS at day 0. B, DLS size over 2 weeks time; first the NPs swell as is typical of PLGA NPs, later they degrade in smaller domains, which is

Discussion/Conclusion: PFC-based ^{19}F imaging agents are cleared by exhalation. Single resonance PFCs, such as PFCE and the commercially available perfluoropolyether are excreted slowly via this process. Here we show a PLGA nanoparticle, containing PFCE with a half-life of only 2 weeks. A unique degradation profile is hypothesized to facilitate faster clearance.

References:

https://doi.org/10.1002/nbm.1570.
Holland et al. 19F MRI 1977.
https://doi.org/10.1002/nbm.3059.

S12.04

Investigation of cerebral lithium distribution in patients with bipolar disorder: a Lithium-7 magnetic resonance imaging study at 7 Tesla

J. Stout[1], F. Hozer[2], A. Coste[1], F. Mauconduit[1], E. Duchesnay[1], C. Rabrait-Lerman[1], J. Houenou[2], F. Bellivier[3], **F. Boumezbeur**[1]
[1]Centre d'études de Saclay, NeuroSpin, bâtiment 145, Gif-sur-Yvette, FRANCE, [2]Hôpital Fernand Widal, Paris, FRANCE, [3]Université Paris-Descartes, INSERM UMRS-1144, Paris, FRANCE

Purpose/Introduction: Lithium (Li) is the first-line mood stabilizer to treat bipolar disorder (BD) patients. However, its mechanisms of action remains poorly understood. ^{7}Li MRI is the only non-invasive method to assess brain Li distribution in vivo [1–2]. In this study, we acquired ^{7}Li MRI at 7 Tesla using a 3D SSFP Twisted Projection Imaging (TPI) sequence from a cohort of euthymic BD patients treated with Li for at least 2 years.

Subjects and Methods: Euthymic type I and II BD patients (n = 21, 41 ± 12 years) were recruited from Lariboisière-Fernand Widal University Hospital (Paris, France). BD patients were systematically scanned 12 h after their last Li_2CO_3 treatment (800 to 1400 mg/day). MRI data were acquired on a 7T scanner (Siemens Healthineers, Germany) with a dual-resonance ^{1}H/^{7}Li RF birdcage coil (Rapid Biomedical, Germany). ^{7}Li MRI were acquired using a 3D UTE SSFP Twisted Projection Imaging (TPI) SSFP TPI sequence [3] (TE/TR = 0.3/200 ms, FA = 20°, 1769 projections, linear fraction of 50%, 352 points per spoke, 10.6 ms readout duration). Global T_1 and T_2 relaxation times were estimated from non-localized MR spectra acquired from five BD patients using the progressive saturation technique (TR ranging from 0.4 to 20 s) and by varying the echo-time (TE ranging from 30 to 120 ms). Non-Cartesian reconstruction was performed using a regridding algorithm [4] while brain [Li] quantification was estimated using a modified phantom replacement approach accounting for global T_1 and T_2 relaxation effects [5, 6]. Individual [Li] maps were aligned with their T_{1w} anatomical reference, interpolated and co-registered to the MNI-152 template space provided by SPM [7] in order to evaluate the average concentrations over seven regions-of-interest as well as the averaged normalized Li distribution across patients (Fig. 1).

Results: As reported in previous studies [1, 2] and illustrated by Fig. 1, brain lithium distribution was quite heterogeneous. Despite significant differences in absolute concentrations amidst our BD patients, the brainstem, cerebellum and mid-brain regions consistently exhibited the highest Li content (Table 1). A somewhat strong correlation was observed between the average cerebral and plasmatic lithium content (Fig. 2 : $[Li]_{brain} \sim 0.42^*[Li]_{plasma}$, PCC = 0.7).

ROI	Average [Li] (mmol/L)
Brainstem	0.46 ± 0.17
Cerebellum	0.36 ± 0.08
Frontal lobe	0.28 ± 0.05
MidBrain	0.39 ± 0.10
Occipital lobe	0.33 ± 0.07
Parietal lobe	0.32 ± 0.06
Temporal lobe	0.34 ± 0.08
Whole Brain	0.33 ± 0.06

Discussion/Conclusion: This study confirms the feasibility of mapping Li brain content using ^{7}Li MRI and hints at the trove of information that could be exploited when combined with ^{1}H MRI and MRS acquisitions so as to better understand the action mechanism of lithium in BD patients.

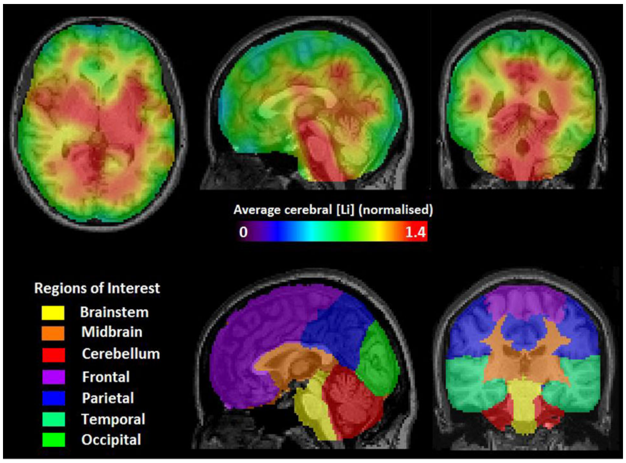

Above, the average cerebral distribution of normalized [Li] concentration over 21 bipolar subjects. Below, an illustration of the regions of interest used in the analysis of lithium concentration levels.

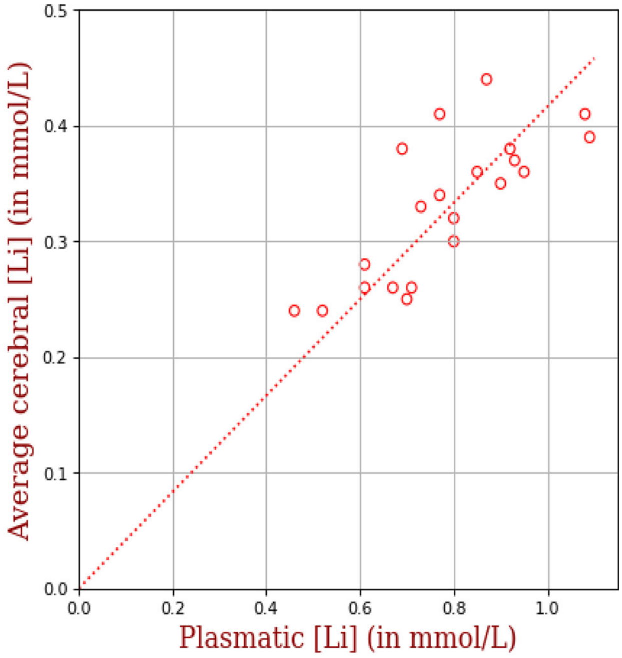

Linear regression of the average plasmatic [Li] vs cerebral [Li] in subjects

References:

1. Lee et al., MRM 2012
2. Smith et al., Mol Psychiatry 2018
3. Boada et al., MRM 1997
4. Jackson et al., IEEE TMI 1991
5. Stout et al. NMR in Biomed, 2016
6. Soher et al., Man Reson Med 1996
7. http://www.fil.ion.ucl.ac.uk/spm/.

S12.05

Multicolor 19F-MRI for in vivo imaging of immune cells activity in a model of multiple sclerosis

L. Chaabane[1], C. Chirizzi[2], P. Metrangolo[3], F. Baldelli Bombelli[3], G. Comi[2]

[1]Ospedale San Raffaele, Institute of Experimental Neurology (INSPE) and Imaging Center (CIS), Milano, ITALY, [2]Ospedale San Raffaele, Institute of Experimental Neurology (INSPE), Milano, ITALY, [3]Politecnico di Milano, Department of Chemistry, Materials, and Chemical Engineering, Milano, ITALY

Purpose/Introduction: Multiple sclerosis (MS) is a chronic autoimmune disease of the central nervous system (CNS) characterized by progressive neuronal demyelination and degeneration mainly attributed to neuroinflammation activity. Fluorine (19F) MRI has been shown to be a potential imaging tool for detecting inflammation with the use of fluorine probes (1–3). In the present work, we explored multicolor 19F-MRI with two formulations of nanoparticles (19F-NPs)(4) to track the dynamic of immune cells infiltration in the CNS of the experimental autoimmune encephalomyelitis (EAE) in mice, a model of multiple sclerosis (MS).

Subjects and Methods: 19F-NPs were produced by direct sonication of fluorocarbons with a surfactant and fluorescent dye for cytometric analysis (FCM). EAE was induced in C57BL/6 mice (n = 14) through immunization with myelin oligodendrocyte glycoprotein peptide (MOG_{35-55}) and pertussis toxin. In vivo MRI were performed in heathy (n = 6) and EAE after a first dose of a 19F-NPs, given at disease onset, and a second dose, given at peak/chronic phase. The signal of 19F-NPs was quantified in the brain, at different levels of the spinal cord, lymphoid organs and liver. At the end, all these organs were collected for flow cytometry (FCM) and fluorescent microscopy.

Results: EAE mice showed different levels of motor impairments from weakness to complete paralysis of hind limbs. MR images of each 19F-NPs were obtained thanks to the distinct resonance frequency of fluorine atoms. From 19F-MRI, an important 19F signal was observed along the spinal cord and in the brain of animals with a high motor disability. Indeed, 19F signal correlated with the expected increment of leukocytes infiltration in the CNS, as measured by FCM, and especially high with 19F-NPs administrated after EAE onset. From FCM, 19F-NPs were mainly found in monocytes and neutrophils. In mice treated simultaneously with both 19F-NPs, fluorine signal along the spinal cord co-localized. In addition, both 19F-NPs formulations demonstrated the same ability to label leukocytes. In all EAE mice, a strong 19F-signal was also observed in the salivary lymph nodes, confirming the high immune response.

Discussion/Conclusion: The present work demonstrates the potentiality of multicolor 19F-MRI to track inflammation during different phases of disease in a model of Multiple Sclerosis. The proposed 19F-NPs is also a promising tool for labelling therapeutic cells and to monitor their efficacy and localization over time.

References:

1. Temme S and al., WIREs Nanomed Nanobiotechnol; 2012.
2. Weise G et al., Experimental Neurology; 2011.
3. Waiczies H, et al. Sci Rep. 2013;3:1280.
4. Chirizzi C., et al. Radiology 2019.

S12.06

Chemical exchange saturation transfer imaging with silent three-dimensional zero echo time acquisition: a pilot study of amide proton transfer weighted imaging

W. Dou[1], X. Wei[1], **J. J. van Asten**[2], A. Heerschap[2], C.-Y. E. Lin[1], Y. Fan[1], B. Wu[1]

[1]GE Healthcare, MR Research, Beijing, CHINA, [2]Radboud University Medical Center, Department of Radiology and Nuclear Medicine, Nijmegen, NETHERLANDS

Purpose/Introduction: Chemical exchange saturation transfer (CEST) imaging[1], relying on proton exchange between specific biocompounds and bulk water, generates image contrast in a "label free" fashion. When exchangeable protons in amide groups of proteins are employed in CEST imaging, it is called amide-proton-transfer weighted (APT) imaging, being widely applied for brain tumor assessment[2,3].

So far, echo-planar-imaging[2] or spin-echo[3] readouts are commonly used in APT imaging. However, these readouts may suffer from image distortions, low signal and long scan, negatively affecting CEST imaging.

3D zero-echo-time (ZTE) imaging, due to its intrinsic properties, is well known for high signal and low sensitivity to local field inhomogeneities. As both features are expected to be beneficial for CEST imaging, we aimed to develop a 3D ZTE-CEST sequence and to investigate its feasibility in APT imaging at clinical 3T.

Subjects and Methods: A schematic diagram of 3D ZTE-CEST sequence is shown in Fig. 1.

Three patients (mean age: 56 ± 4 years) with high grade gliomas were recruited for APT imaging. Written informed consent was obtained.

3D ZTE-CEST, as well as T2-weighted FLAIR imaging was performed on a 3T-MRI system (Discovery 750 W, GE Healthcare, USA), using a 24-channel head coil. The ZTE-CEST parameters were: field-of-view = 220 × 220 mm, 32 slices with a slice thickness of 4 mm, image resolution = 2 × 2 mm, flip angle = 4degree, spokes-per-segment = 512 and segment numbers = 10. Six-offset frequencies were applied including ± 4 ppm and ± 3.0 ppm (1 NEX), and ± 3.5 ppm (2 NEX) for higher APT signal. For B_0 correction[5], a slightly modified CEST module with one saturation pulse (amplitude/duration: 0.5μT/200 ms), occurring before segment 1, 3, 8 during signal acquisition, was applied at ± 1.5 ppm (step = 0.2 ppm), while other scan parameters were identical. Total scan time was 5 min 38 s.

The corresponding magnetic transfer ratio asymmetry (MTR_{asym}) images were obtained with custom-written Matlab scripts.

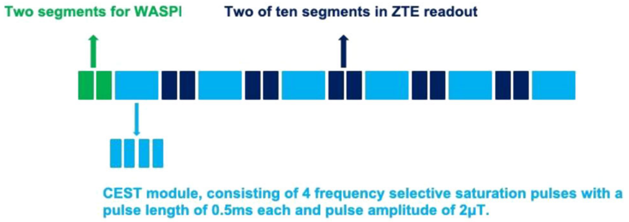

Figure 1. The schematic diagram of 3D ZTE-CEST sequence: A developed CEST module, consisting of four frequency selective saturation pulses each with a pulse length of 500 ms (2 s in total) and pulse amplitude of 2 μT, was incorporated prior to each two segments of ZTE acquisition as well as an extra two-segment data acquisition using water- and fat-suppressed solid-state proton projection imaging (WASPI) method[4] recovering the central region of k-space lost in the receiver dead time.

Results: On T2-weighted FLAIR images the brain lesions are clearly visible (Fig. 2A). Applying the ZTE-CEST sequence we observed strong CEST effects at 3.5 ppm for these lesions, reflected by a high MTR_{asym} averaged over the whole lesion (3.7 ± 0.3%; Fig. 2B). Similar results were obtained with saturation pulses applied over a 3–4 ppm range as shown in averaged MTR_{asym} images (3.3 ± 0.3%; Fig. 2C).

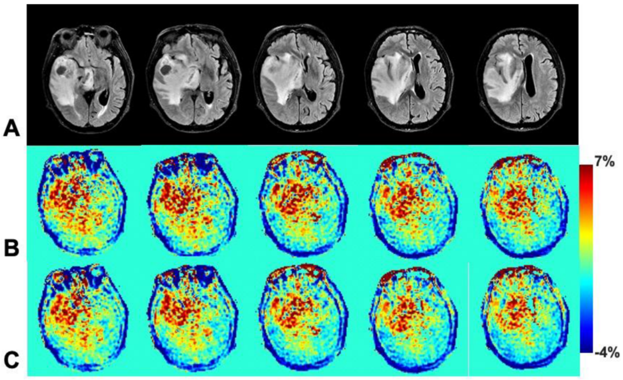

Figure 2. Representative T2-weighted FLAIR images (A) showed lesions at five continuous slices for a male patient (66 years old) clinically confirmed with high grade glioma. Using ZTE-CEST sequence, strong CEST effect was found in these lesion regions, indicating by strong MTR_{asym} of 3.7%. The MTR_{asym} images at 3.5 ppm (B) were shown correspondingly, covering a similar region as shown in FLAIR images. The corresponding averaged MTR_{asym} images over 3 -4 ppm (C) were also shown (MTR_{asym} of 3.3%).

Discussion/Conclusion: We conclude that ZTE-CEST is feasible for silent clinical APT imaging and provides excellent results, comparing favorably with previous CEST imaging of brain tumors[2, 3]. More applications are needed to evaluate its real potential.

References:

1. Ward K. et al. J Magn Reson. 143:79–87 (2000).
2. Su L. et al. World Neurosurg. 116 :e814–23 (2018).
3. Zhou J. et al. J Magn Reson. 38:1119–28 (2013).
4. Wu Y. et al. Magn Reson Med. 50 :59–68 (2003).
5. Kim M. et al. Magn Reson Med. 61:1441–50 (2009).

S12.07
WITHDRAWN

S12.08
Targeting cell surface receptor CD177 for non-invasive imaging of neutrophil granulocytes by ^{19}F MRI

P. Bouvain[1], V. Flocke[1], S. Kadir[1], Z. Ding[2], W. Krämer[3], R. Schubert[3], J. Schrader[2], U. Flögel[1], **S. Temme**[1]
[1]University of Düsseldorf, Molecular Cardiology/Experimental Cardiovascular Imaging, Düsseldorf, GERMANY, [2]University of Düsseldorf, Molecular Cardiology, Düsseldorf, GERMANY, [3]Albert-Ludwigs-University, Pharmaceutical Technology and Biopharmacy, Freiburg, GERMANY

Purpose/Introduction: Neutrophil granulocytes are essential for protective immune response against infectious pathogens but also contribute to the development/progression and resolution of inflammatory diseases like atherosclerosis or myocardial infarction. However, excess neutrophils can cause severe tissue damage. To further unravel the role of neutrophils under inflammatory conditions, the aim of the present study was to target perfluorocarbon nanoemulsions (PFCs) to CD177—which is specifically expressed by neutrophil granulocytes—to enable the in vivo visualization of neutrophil granulocytes by $^{1}H/^{19}F$ magnetic resonance imaging (^{19}F MRI).

Subjects and Methods: Peptides against human (hNGP) and murine (mNGP) CD177 [1, 2] as well as control peptides (NGC) were equipped with n-terminal carboxyfluorescein and c-terminal -GGG-cysteine spacer. Coupling to PFCs was performed via the c-terminal cysteine of the peptides and maleimide residues on the particle surface (Mal-PFCs). Binding studies were performed by flow cytometry and ^{19}F MRI using human neutrophils from healthy volunteers and patients after myocardial infarction. Murine neutrophils were obtained from blood of C57BL/6 mice or isolated from LPS-doped matrigel plugs. MR experiments were performed at a 9.4 T Bruker AVANCEIII Wide Bore NMR spectrometer and datasets were acquired using a 25 mm birdcage resonator tuneable to ^{1}H and ^{19}F.

Results: Binding studies with ^{hNGP}PFCs and ^{mNPG}PFCs showed specific labeling of neutrophil granulocytes from humans and mice. We also found that inflammatory stimuli like LPS or myocardial infarction upregulated the cell surface expression of CD177 on neutrophils in humans and mice. Increased cell-surface expression of CD177 also led to strongly enhanced cellular uptake of ^{hNGP}PFCs. To visualize NGP-labeled neutrophils in vivo in mice, we implanted neutrophils into matrigel/LPS plugs and analyzed the ^{19}F signal over time. ^{19}F MRI of the matrigel plugs revealed strong ^{19}F signals that decreased within 1 week. Moreover, we were also able to image the infiltration of neutrophils into the infarcted heart after cardiac ischemia/reperfusion injury by in vivo non-invasive $^{1}H/^{19}F$ MRI.

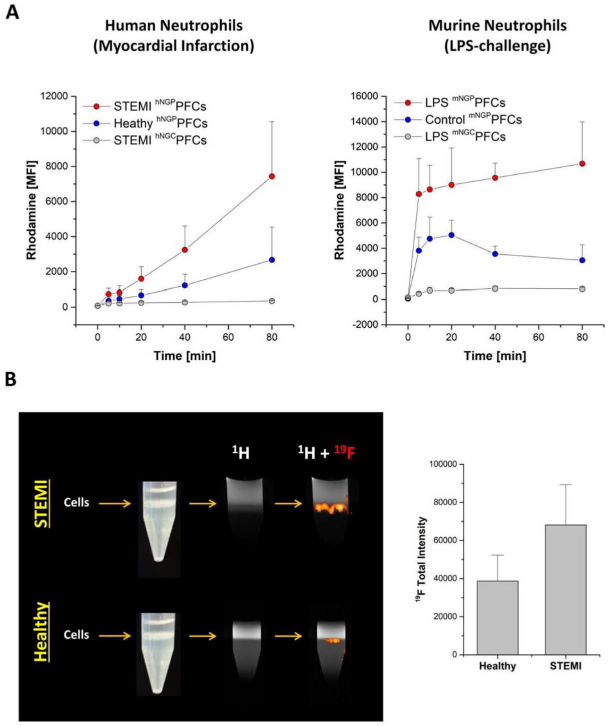

Inflammatory stimuli increase the labelling of neutrophil granulocytes by NGP-PFCs: A) Flow cytometry of human and mouse neutrophils incubated with NGP-PFCs or control-PFCs (NGC) B) 1H/19F MRI of neutrophils

Discussion/Conclusion: We show that neutrophil granulocytes can be specifically labeled with ^{NGP}PFCs which target the cell surface receptor CD177. Cell-surface expression of CD177 is upregulated under inflammatory conditions which supports the tracking of $CD177^{+}$ neutrophils by ^{19}F MRI in particular under inflammatory conditions.

References:
[1] Mazzucchelli L, Burritt JB, Jesaitis AJ, Nusrat A, Liang TW, Gewirtz AT, Schnell FJ, Parkos CA. Cell-specific peptide binding by human neutrophils. Blood. 1999; 93(5):1738–48.
[2] Miettinen HM, Gripentrog JM, Lord CI, Nagy JO. CD177-mediated nanoparticle targeting of human and mouse neutrophils. PLoS One. 2018 Jul 10;13(7).

S12.09

Metallated doped conjugated polymer nanoparticles as bimodal imaging agent for cancer detection: application in a preclinical glioblastoma model

L. E. Ibarra[1], **N. Arias-Ramos[2]**, M. J. Guillen Gomez[2], G. Morales[3], C. Chesta[3], V. A. Rivarola[1], P. Lopez-Larrubia[2], R. Palacios[3]
[1]Instituto de Biotecnología Ambiental y Salud CONICET-UNRC, Río Cuarto, ARGENTINA, [2]Instituto de Investigaciones Biomedicas Alberto Sols CSIC/UAM, Madrid, SPAIN, [3]Instituto de Investigaciones en Tecnologías Energéticas y Materiales Avanzados CONICET-UNRC, Río Cuarto, ARGENTINA

Purpose/Introduction: The possibility of bringing together several functions into a single nanostructure offers great potential in theranostic nanomedicine. Fluorescence and magnetic resonance dual-modal imaging nanoprobes are highly desired materials in molecular imaging, but also have potential use in clinical diagnosis with high precision and accuracy. Conjugated polymer nanoparticles (CPNs) possess many useful properties including high brightness, excellent photostability, good water-dispersibility, low cytotoxicity, and easy synthesis and functionalization, showing promising application in bioimaging and photo-assisted anticancer therapy[1−3]. Through the incorporation of an appropriate metal core into CPNs, its application as a T1/T2-enhanced magnetic resonance contrast agent could be possible.

Subjects and Methods: Our purpose was to develop, characterize and evaluate in vivo CPNs doped with iron oxide, cobalt nanoparticles or metallated porphyrin as potential dual-imaging contrast agents in tumor bearing mice.

CPNs were synthetized as we described previously[1]. Iron oxide nanoparticles (IONp)[4], cobalt TurboBeads™ Vinyl (CoTB) or octaethylporphyrin (PtoEH) were used as dopants to incorporate into CPNs synthesis. A fully characterization was perform: DLS, AFM, TEM, and relaxation times measurements for T1 and T2 in MRI applications.

Glioma in vivo model was developed injecting C6 cells in the flank of NOD SCID mice. Tumor growth was followed by T2 W MRI in a 7 T system and when tumors reached an appropriated size, CPNs were injected intravenously (IV) or intratumorally (IT) at doses of 0.25 mg/kg or 0.1 mg/kg respectively. The biodistribution and arrival of CPNs to the tumor tissue were evaluated by MRI and fluorescence in vivo imaging system at different time points.

Results: All the doped CPNs had narrow size diameter about 50 – 100 nm and showed good colloidal stability after several months. IONp doped CPNs induced a shortening of T2 relaxation time of water and also were visible by IVIS imaging, so, were selected to continue with MRI and IVIS fluorescence assays (Table 1).

	T1 (ms)	T2 (ms)
IONp doped CPNs	2952.24	36.55
CoTB doped CPNs	4945.76	195.35
PtoEH doped CPNs	3638.58	230.29

Table 1: Relaxation time measures of metallated doped CPNs

In tumor bearing mice, CPNs biodistribution could be followed by in vivo MRI and fluorescence imaging with an increased accumulation in tumors over time allowing dual-modal detection of tumors in a living body (Fig. 1).

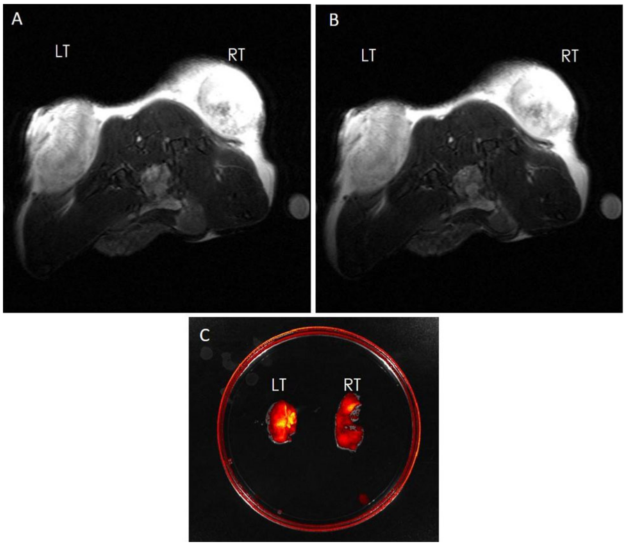

CPNs IT injection induced a greater T2 negative contrast (Fig. 2).

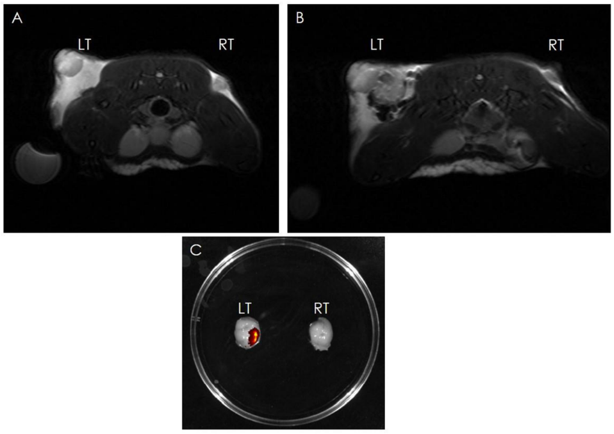

Figure 2: T2W images before (A) and 1 h after (B) CPNs 0.1 mg/kg intratumoral injection. C) IVIS imaging of tumors. LT: left tumor, RT: right tumor

Discussion/Conclusion: Our results, incorporating fluorophore and metal complex or other functional unit into one CPNs, provide a potential design strategy to fabricate dual/multi-modality theranostic agents for in vitro and in vivo applications in future.

References:
1. Ibarra LE, et al. *Nanomedicine*. 2018;13(6):605–624.
2. Spada RM, et al. *Dye Pigment*. 2018;149:212–223.
3. Ponzio RA, et al. *Methods Appl Fluoresc*. 2017;5(2):024001.
4. Mascolo MC, et al. *Materials (Basel)*. 2013;6(12):5549–5567.

I16 Teaching Session

13:50–15:20 *Room 3 - Ruys & van Rijckevorsel Zaal*

Applications of Machine Learning in Neuroscience

I16.01

Machine Learning in Diffusion MRI

K. H. Maier-Hein
German Cancer Research Center (DKFZ), Heidelberg, GERMANY

Learning Objectives: - How ML can help us to better understand dMRI data.
- Clinical applications.
- Applications in basic research.
- What is the potential of and what are the challenges for ML in dMRI.

Body: Diffusion-Weighted MRI reveals information on the brain tissue structure at a microscopic scale. In combination with sophisticated computing technology, this leads to exciting opportunities in basic neuroscience research as well as in clinical applications. Machine learning and deep learning techniques are increasingly applied in diffusion MRI, offering important benefits to the more traditional methods used for processing diffusion MRI. The presentation will contain some successful applications of machine learning in brain diffusion MRI and also discuss the potential of machine learning in this field in the future.

References:

Jäger et al., “Revealing Hidden Potentials of the Q-Space Signal in Breast Cancer.”, MICCAI 2017.
Bickelhaupt, Jaeger et al. “Radiomics with adapted Kurtosis Fitting on DWI Clarifies Majority of Mammographic Findings”. Radiology, 2018.
Kamphenkel, Jaeger et al., “Model-Based Domain Adaptation for Large-Scale Application of Deep Learning-based Lesion Classification on Diffusion-Weighted MR Images”, submitted to Breast Image Analysis, 2018.
Alexander et al., “Image Quality Transfer and Applications in Diffusion MRI.”, NeuroImage 2017.
Maier-Hein et al., “The Challenge of Mapping the Human Connectome Based on Diffusion Tractography”, Nature Communications 2017.
Neher et al. “Fiber Tractography Using Machine Learning.”, NeuroImage 2017
Poulin, Philippe, et al. “Learn to Track: Deep Learning for Tractography.”, MICCAI 2017.
Wasserthal et al. “Fast and accurate white matter tract segmentation.”, NeuroImage 2018.
Wasserthal et al. “Combined tract segmentation and orientation mapping for bundle-specific tractography”, submitted to MedIA.

I16.03

Machine Learning for the Detection of Brain Abnormalities

H. Kuijf
UMC Utrecht, Image Sciences Institute, Utrecht, NETHERLANDS

Learning Objectives: The purpose of this lecture is twofold. First to demonstrate how machine learning can be applied to measure brain abnormalities; ranging from simple to advanced methods. Second to provide a standardized assessment and comparison of automated WMH segmentation techniques; and insights learned from dozens of methods that have been analysed.

Body: Magnetic Resonance Imaging as a clinical diagnostic method is one of the greatest innovations of the twentieth century. In Europe, millions of images are made yearly and the number is steadily increasing. Assessment of medical images relies on visual inspection, which can be time-consuming and subjective. Automated machine learning solutions have proven essential towards reliable detection and quantification of brain pathology.

Brain abnormalities–associated with stroke, dementia, and ageing–have been a key application for machine learning solutions in medical image analysis. Various automated analysis techniques have been developed, to provide quantitative measurements and replace time-consuming, observer-dependent delineation procedures. Such techniques exist, or are currently being developed, for white matter hyperintensities (WMH), microbleeds, microinfarcts, and more.

References:

Kuijf, H. J., Biesbroek, J. M., de Bresser, J., Heinen, R., Andermatt, S., Bento, M., … & Collins, D. L. (2019). Standardized assessment of automatic segmentation of white matter hyperintensities; results of the wmh segmentation challenge. *IEEE transactions on medical imaging*.
Smith, E. E., Biessels, G. J., De Guio, F., de Leeuw, F. E., Duchesne, S., Düring, M., … & Thrippleton, M. J. (2019). Harmonizing brain magnetic resonance imaging methods for vascular contributions to neurodegeneration. *Alzheimer's & Dementia: Diagnosis, Assessment & Disease Monitoring*, *11*, 191–204.
Wardlaw, J. M., Smith, E. E., Biessels, G. J., Cordonnier, C., Fazekas, F., Frayne, R., … & Black, S. E. (2013). Neuroimaging standards for research into small vessel disease and its contribution to ageing and neurodegeneration. *The Lancet Neurology*, *12*(8), 822–838.
Pantoni, L. (2010). Cerebral small vessel disease: from pathogenesis and clinical characteristics to therapeutic challenges. *The Lancet Neurology*, *9*(7), 689–701.
Weaver, N. A., Zhao, L., Biesbroek, J. M., Kuijf, H. J., Aben, H. P., Bae, H. J., … & Duering, M. (2019). The Meta VCI Map consortium for meta-analyses on strategic lesion locations for vascular cognitive impairment using lesion-symptom mapping: Design and multicenter pilot study. *Alzheimer's & Dementia: Diagnosis, Assessment & Disease Monitoring*, *11*, 310–326.
The WMH segmentation challenge: https://wmh.isi.uu.nl/
The MRBrainS18 segmentation challenge: https://mrbrains18.isi.uu.nl/.

S13 Scientific Session

13:50–15:20 *Room 4 - Plate & Van der Vorm Zaal*

Cardiovascular Applications

S13.02

In vivo visualization of early alterations in the extracellular matrix after myocardial infarction by magnetic resonance chemical exchange saturation transfer

U. Flögel[1], C. Jacoby[1], J. Müller[2], A. Petz[2], Z. Ding[1], M. Grandoch[2], J. Fischer[2], J. Schrader[1]
[1]*Heinrich Heine University, Experimental Cardiovascular Imaging, Düsseldorf, GERMANY,* [2]*Heinrich Heine University, Pharmacology, Düsseldorf, GERMANY*

Purpose/Introduction: The extracellular matrix (ECM) provides a three dimensional scaffold to the heart that forms a stable microenvironment facilitating the function of both cardiomyocytes and non cardiomyocytes[1]. Upon ischemic injury the ECM is acutely damaged and during the subsequently initiated ECM remodeling, especially *de novo* formation and crosslinking of collagenous matrix, stabilizes the infarct scar and is important for adaptation[1]. Here, we attempted to adjust MRI chemical exchange saturation transfer (CEST) techniques to monitor early alterations in cardiac ECM after I/R injury in mice at 9.4T.

Subjects and Methods: Although the CEST signal is not specific for a certain matrix component, the amount of exchangeable protons is especially high in hydroxylated sugar moieties of hyaluronan (HA) and glycosaminoglycans. Phantom experiments revealed that HA gives rise to the strongest CEST contrast whereas proteoglycans and other compounds of the ECM result in much weaker CEST signals. To further enhance specificity and to avoid contaminations from 'CEST-active' components in the blood (in particular sugars), before induction of saturation, a 'black blood preparation' was initiated for suppression of all signals from circulating blood. Adjustment to fluctuations of the heart rate (HR) were carried out via a variable delay after detection of the QRS complex to ascertain reproducible saturation conditions.

Results: This procedure turned out to be extremely robust and allowed the acquisition of CEST images from the murine thorax in excellent quality. 24 h post I/R injury (50 min) strong CEST signals could be detected in the infarcted left ventricle with lower intensity in the border zone and almost no signal in the remote myocardium (Fig. 1).

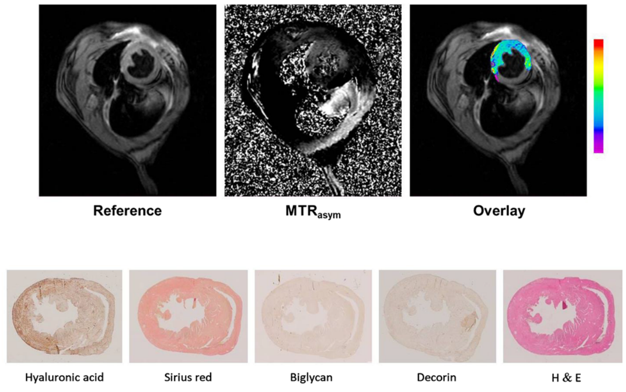

Figure 1: CEST contrast and histology 24 h post I/R

Whereas histochemistry detected HA accumulation already 24 h post I/R, the stainings of other ECM molecules were not yet upregulated. To confirm that predominantly HA contributes to this early CEST signal, we subjected mice treated with a pharmacologic inhibitor of HA synthesis (4-MU) or lacking HA synthase 2 ($\mathrm{HAS2}^{-/-}$) to I/R injury. Fig. 2 demonstrates that both 4-MU and HAS2 deficiency caused a strong reduction of cardiac CEST signals during the first 72 h post I/R. Interestingly, later on CEST signals in both groups approach those of controls representing the increasing accumulation of other ECM components such as proteoglycans, glycoproteins etc.

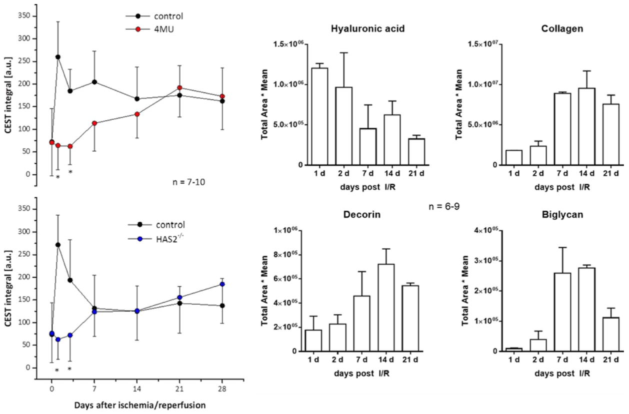

Figure 2: Temporal development of CEST signal and components of the ECM after I/R

Discussion/Conclusion: These data indicate that cardiac CEST imaging allows to monitor HA accumulation post I/R especially in the first 2–3 days post I/R. In summary, we present a non-invasive approach to image the provisional HA matrix after I/R by applying CEST with black blood adjustment, which permits the sensitive detection of alterations in the ECM already 24 h after I/R.

References:

1. Frangogiannis NG. The extracellular matrix in myocardial injury, repair, and remodeling. *J Clin Invest* 2017;127:1600–1612.

S13.03

Investigation of carotid atherosclerotic plaque microstructure using diffusion tensor imaging

B. Tornifoglio[1], A. J. Stone[1], S. Shahid[2], L. Iacob[3], J. Clarke[3], A. O'Callaghan[3], S. O'Neill[3], C. Kerskens[4], C. Lally[1]
[1]Trinity College Dublin, Trinity Centre for Bioengineering and Department of Mechanical and Manufacturing Engineering, Dublin, IRELAND, [2]Emory University, School of Medicine, Department of Neurology, Atlanta, UNITED STATES, [3]St. James Hospital, Vascular and Endovascular Surgery, Dublin, IRELAND, [4]Trinity College Dublin, Trinity College Institute of Neuroscience, Dublin, IRELAND

Purpose/Introduction: Smooth muscle cells (SMCs) play a critical role in the progression and stability of atherosclerotic plaques [1]. This stability can change quickly as cellular metabolism and composition vary; which in turn affect the turnover of the extracellular matrix and allow for the accumulation of lipoproteins in the vessel wall [2]. These alterations lead to mechanically weak points where SMC and collagen content decrease and macrophages and lipoproteins increase [3]. Current stability and rupture risk metrics are largely based on the percent stenosis and are not indicative of true plaque vulnerability [1, 4]. The aim of this study is to use diffusion tensor imaging to characterise the microstructure of arterial tissues with a view to identify alterations in cellular content, which may be more indicative of plaque stability.

Subjects and Methods: Ex vivo porcine carotid artery (PCaA) tissue models and excised human carotid plaque specimens from carotid endarterectomy patients were scanned using a 7 T Bruker BioSpec system. PCaA models included native and decellularized vessels. All sample tissues were imaged with a 3D DTI sequence with the following parameters: TE/TR: 17.7/1000 ms, image size: 96 × 96 × 60, field of view: 16 × 16 × 10 mm3, resolution: 0.167 mm^3, b-value: 800 s/mm2, 10 b-directions, and acquisition time: 17 h 26 min. Raw data was denoised and Gibbs ringing correction performed prior to the calculation of fractional anisotropy (FA) and mean diffusivity (MD) in ExploreDTI.

Results: The mean FA decreased markedly between native and decellularised (0.30 ± 0.09 to 0.07 ± 0.03) while the MD increased (7.30 ± 1.05 to 10.0 ± 1.28 x1e-4 mm2/s) (Fig. 1).

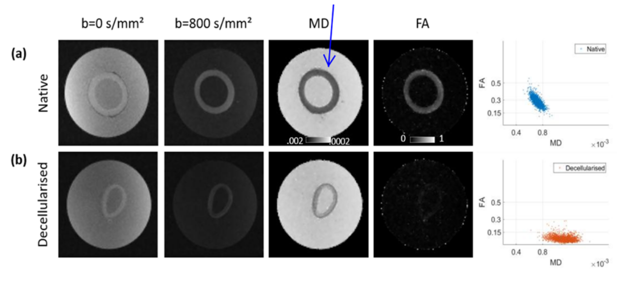

PCaA tissue models. (a) Native and (b) decellularised tissue models and single slice representative b=0 s/mm2, b=800 s/mm2, MD, FA maps and FA vs. MD plots.

The lipid core (LC) of the plaques (red regions, Fig. 2) had FA values of 0.10 ± 0.06 and 0.11 ± 0.06 and MD values of 5.96 ± 1.70 and 5.40 ± 1.76 x1e-4 mm2/s. In the fibrotic media (FM) (blue regions, Fig. 2), the FA values were 0.09 ± 0.04 and 0.12 ± 0.06 and MD values were 11.0 ± 2.16 and 9.23 ± 2.72 x1e-4 mm2/s, respectively.

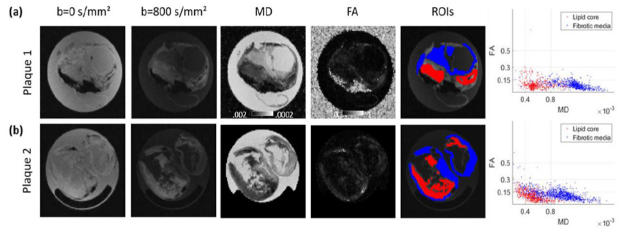

Two human atherosclerotic plaque specimens. (a, b) Single, representative slice b=0 s/mm2, b=800 s/mm2, MD and FA maps for each plaque. Lipid core (red) and fibrotic media (blue) regions of interest were masked and plotted for FA vs. MD.

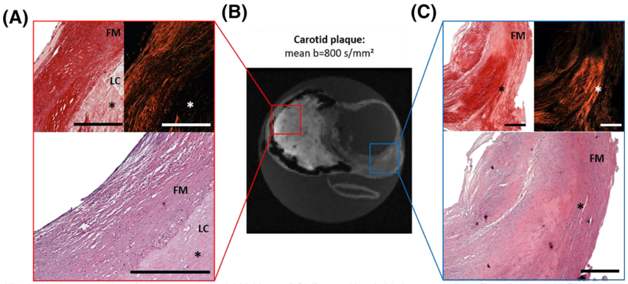

Histological representation of plaque specimen. (a) Lipid core (LC) (from red box in b) shows no cells or fibre alignment. (c) Fibrotic media (FM) (from blue box in b) shows fibre alignment with decreased cell content. Scale bars: 500 µm.

Discussion/Conclusion: The tissue models demonstrated an observable difference in mean FA and MD values, suggesting the presence of cells allowed for measurable anisotropic behaviour and hindered diffusion to lower the MD. Adapting this approach to plaque tissue highlighted the potential for using FA and MD as markers for cell content and a potential indicator for vessel wall stability. While the diffusion profile of the LC was unlike both tissue models (Fig. 3a), some regions of the FM were unique while others showed characteristics in line with those of the decellularised tissue (Fig. 3c). Future work will look at additional plaques to ascertain the sensitivity of this imaging technique for identifying vulnerable regions of plaques.

References:

[1] Wang et al., Diagn Histopathol, 18(11):461–467, 2012.
[2] Douglas, Medicine, 42(9):480–484, 2014.
[3] Davies, Heart, 63(5):377–381, 1993.
[4] Mughal et al., Expert Rev Cardiovasc Ther, 9(10):1315–1330, 2012.

S13.04

Identification of USPIO-uptake in calcified atherosclerotic plaques

P. P. R. Ruetten[1], A. Cluroe[2], A. Usman[1], J. H. Gillard[1], M. J. Graves[1]
[1]University of Cambridge, Radiology, Cambridge, UNITED KINGDOM, [2]Cambridge University Hospital, Pathology, Cambridge, UNITED KINGDOM

Purpose/Introduction: Ultrasmall paramagnetic iron oxide (USPIO) particles can image inflammation in carotid artery plaques. USPIO-uptake increases R_2*-values and reduces the signal on T_2*w images. However, a comparison of images acquired before and after contrast agent administration is required to distinguish areas of paramagnetic USPIO-uptake (positive susceptibility) from diamagnetic calcification (negative susceptibility). We show that Quantitative Susceptibility

Mapping (QSM) can identify and quantify USPIO uptake and distinguish it from calcification.

Subjects and Methods: Four patients with carotid artery disease were scanned at 1.5T (MR450w, GE Healthcare, Waukesha, WI). Two MRI examinations were performed per patient, before and 48 h after 5 mg/kg USPIO-injection (Ferumoxytol, AMAG Pharmaceuticals, Lexington MA).

Parameter	3D axial multi-echo gradient-echo	3D Time-of-Flight	Black-Blood fat-suppressed T1w FSE
TR [ms]	88	20	580
TE [ms]	TE1 = 4.4, Echo Spacing = 2.1	3.2	15.0
Number of Echoes	6	6	24
Spatial Resolution [mm3]	0.625x0.625x2 (1 interpolated)	0.625x0.625x1.4	0.625x0.625x1.4
Receiver Bandwidth [kHz]	+/-83.3	+/-15.63	+/-31.25

Sequence Parameters

The study protocol comprised:3D Time-of-Flight (TOF) MRA; black-blood, fat suppressed T_1w CUBE; 3D multi-echo gradient echo acquisition (SWAN), used for QSM, T_2*w images, and R_2*-mapping. In two cases histology was available. An in-house developed QSM reconstruction consisted of IDEAL water-fat separation to estimate ΔB, background field removal, and dipole field inversion(1, 2). R_2*-mapping was performed on a voxel-by voxel and a quadrant basis.

Results: In two cases, the plaque was lightly calcified. QSM easily identified USPIO-uptake as hyperintensities, and calcifications as hypointensities using the post-contrast acquisition alone (Fig. 1). Calcification and USPIO-uptake both decreased T_2*w signal intensity and hence increased R_2*-values.Areas of USPIO uptake were identified by comparing pre-and post-contrast acquisitions. Histological analysis was available and confirmed presence and location of calcification and iron particles (Fig. 1).

The other two patients had heavily calcified plaques. QSM identified USPIO-uptake by increased susceptibility and distinguished it from areas containing only calcification (Fig. 2). On T_2*w images and R_2*maps, USPIO uptake could not be easily differentiated from calcification. Furthermore, insufficient SNR results in failure to estimate R_2* correctly (red voxels). Quadrant analysis confirmed an overall increase in R_2*-value in areas of QSM-identified USPIO-uptake (Fig. 2). Histological analysis confirmed the uptake of iron particles interspersed with heavy calcification (Fig. 2).

The multi-contrast protocol confirmed the presence and location of calcification and USPIO in all cases.

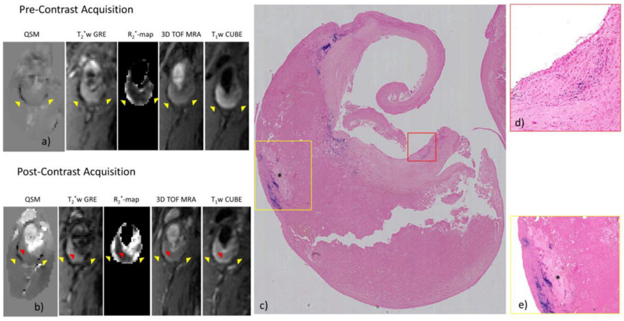

QSM distinguishes USPIO-uptake (red arrow, positive susceptibility) from calcification (yellow arrow, negative susceptibility). Other MRI sequences confirm this. Histology shows calcification as a pale area (e) and USPIO with a blue stain (d).

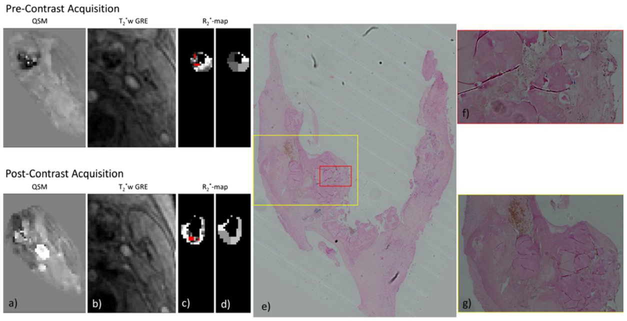

USPIO increases susceptibility in the calcified plaque (a). Histology (e) confirms the presence of calcification (pink nodules, g) and iron

Discussion/Conclusion: QSM-identified USPIO-uptake and calcification was confirmed with R_2*-mapping and T_2*w images. In heavily calcified plaques QSM identified and distinguished calcification and USPIO-uptake, whereas a quadrant-based analysis was necessary when only T_2*w images and/or R_2* maps were used. Hence we have shown that the positive contrast provided by QSM improves the visualisation of USPIO uptake.

References:

1 Reeder, et al. MRM 51.1 (2004): 35–45.
2 Wang, et al. MRM 2015:73:82–101.

S13.05

Pharmacokinetic analysis of black-blood DCE-MRI of atherosclerotic plaques

J. Schoormans[1], C. Calcagno[2], G. Strijkers[1], K. H. Zheng[3], A. Nederveen[4], B. Coolen[1]
[1]Amsterdam UMC, Biomedical Engineering and Physics, Amsterdam, NETHERLANDS, [2]Icahn School of Medicine at Mount Sinai, Translational and Molecular Imaging Institute, New York, NY, UNITED STATES, [3]Amsterdam UMC, Vascular Medicine, Amsterdam, NETHERLANDS, [4]Amsterdam UMC, Radiology and Nuclear Medicine, Amsterdam, NETHERLANDS

Purpose/Introduction: Atherosclerotic plaque microvascularization and permeability are characteristic features of vulnerable plaques with increased risk of cardiovascular events, such as myocardial infarction and stroke. The DCE-derived parameters K_{trans} and the area-under-the-curve (AUC) have been used to assess plaque vulnerability. We previously developed a compressed sensing accelerated high-resolution golden-angle radial turbo field echo with iMSDE preparation for high spatiotemporal resolution DCE-MRI of vessel wall. However, black blood in this sequence—necessary for reliable vessel-wall delineation—prevents simultaneous measurement of the blood arterial input function (AIF).

Aim: In this study we investigated the applicability of the Reference Region Method (RRM [1]) and the constrained extended RRM (CERRM [2]) to derive DCE-parameters of the vessel wall without AIF.

Subjects and Methods: The dynamic signal evolution was simulated for different tissues (muscle, healthy vessel wall(VW), fibrous tissue, intraplaque-hemorrhage, necrotic core), with tissue parameters in the range of published values. Sequence parameters: TR/TE = 7.2/3.2 ms, FA = 15 ms, T_{imsde} = 11 ms. We investigated whether the different tissues can be distinguished from their kinetic parameters by Patlak, RRM, CERRM, and AUC analyses. The analysis was also performed on DCE-MRI data of atherosclerotic plaques in the femoral artery of patients.

Results: Both reference models provided estimated K_{trans} values for different tissues with smaller distributions and better separation than the Patlak model (Fig. 1).

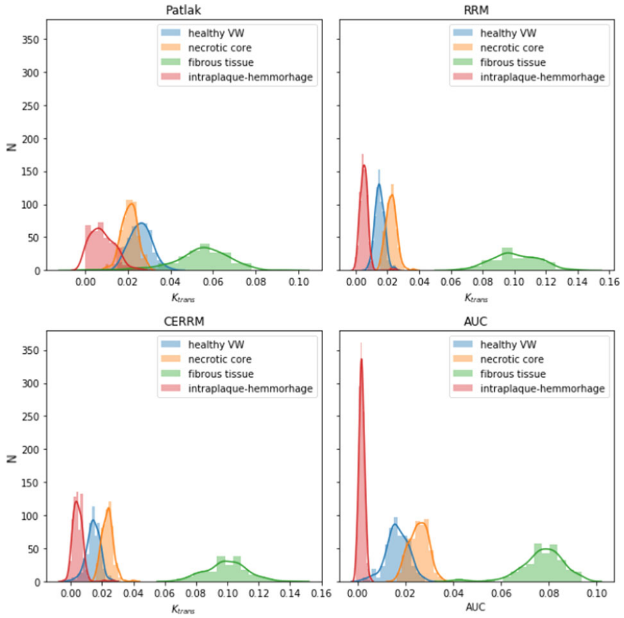

Figure 1: Histogram of simulation. The Patlak model shows the largest spread of estimated values, and therefore discriminating between the different types of healthy and diseased tissues is more difficult than either RRM, or even the AUC.

Interestingly, also the AUC method provided good separation between different tissues. This suggests that discrimination of different plaque components is more easily achieved by either reference region method or the AUC than by Patlak analysis. However, Patlak-derived K_{trans} values were more accurate (correlations with true K_{trans}: Patlak/RRM/ERRM = 0.98/0.88/0.89). Nevertheless, the reference models and AUC incorporate differences in T_1, T_2, and v_e, v_p which resulted in a higher discriminating power.

The Patlak and CERRM approaches were subsequently applied to patient DCE-MRI data (Fig. 2). The mean correlation between RRM K_{trans} and a Patlak K_{trans} with a model AIF (in 65 femoral atherosclerotic plaques) was 0.57 ± 0.22.

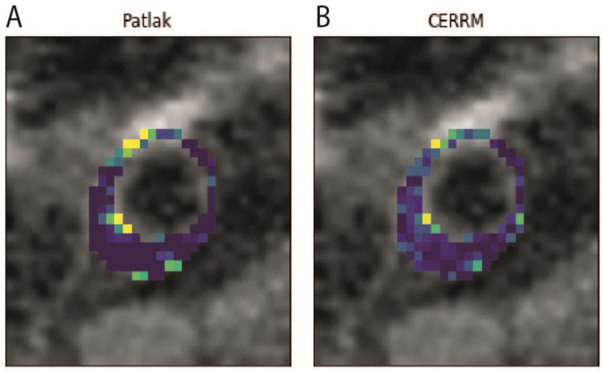

Figure 2: Comparison of Ktrans in a atherosclerotic patient. The high Ktrans values in both methods were spatially correlated. Over all plaque and vessel wall in 65 patient and controls, the correlation between Patlak and CERRM was 0.57±0.22.

Discussion/Conclusion: The RRM and CERRM are applicable for analyzing vessel wall and atherosclerotic plaque DCE-MRI, and result in easier separation of tissue types than the Patlak model.

References:

[1] Yankeelov, et al." *MRI* 23.4 (2005).
[2] Ahmed et al. *NMR in Biomed.* 31.7 (2018).

S13.06

3D MRI velocity measurements in coronary stent designs for the validation of numerical analyses

K. John[1], M. Bruschewski[1], L. Quirin[1], J. Oldenburg[2], F. Borowski[2], K.-P. Schmitz[2], M. Stiehm[2], S. Grundmann[1]
[1]University of Rostock, Institute of Fluid Mechanics, Rostock, GERMANY, [2]Rostock University Medical Center, Institute for Biomedical Engineering, Rostock, GERMANY

Purpose/Introduction: Restenosis and thrombosis forming due to pathologically altered blood flow are common post-operational complications of implanting coronary stents. Therefore, one of the primary emphases in stent designing is to examine the influence of the implant on the flow topology. Computational Fluid Dynamics (CFD) is an important method to analyze internal flows. However, the reliability of numerical models can only be proven through experimental data. Magnetic Resonance Imaging (MRI) is a promising method to provide such three-dimensional velocity datasets. The long-term aim of our current research is to establish MRI as a standard method for the optimization of flow-conducting implants.

Subjects and Methods: This study compares MRI measurements of three simplified stent designs presented in [1] with the velocity fields obtained from CFD. The models are shown in Fig. 1. Scaling the stent models 15 times the size of an original stent ensured sufficient signal intensity and resolution in the MRI measurement. Such an approach is possible according to fluid dynamics similarity laws: Incompressible, stationary flows of the original and scaled model are similar if the Reynolds number is the same. A flow circuit connected the stent models inside the MRI scanner with a 100-liter tank and a pump. The flow medium was a mixture of water and glycerine with a kinematic viscosity of 6.04*10–5 m^2/s and a flow rate of Q = 47 l/min. The resulting Reynolds number was 460. Measurements were performed on a 3T Magnetom Trio (Siemens) at the Institute of Fluid Mechanics, University of Rostock. A conventional phase contrast (PC) MRI method similar to the one presented in [2] was used to capture three-dimensional velocity fields. Numerical data was produced with an incompressible laminar Navier–Stokes solver using the OpenFOAM software package.

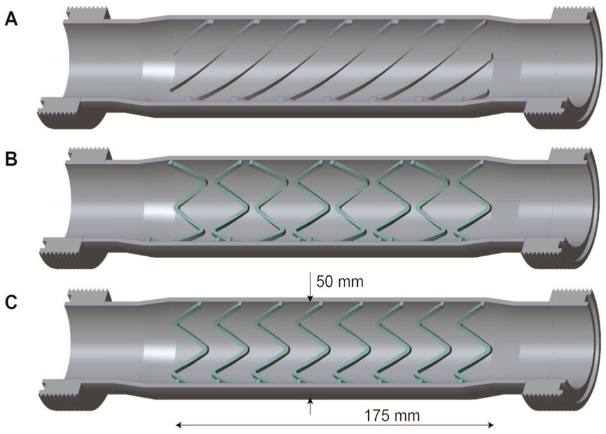

Figure 1: Large-scale models of the investigated stent designs: (A) Helical struts, (B) Mirror-pattern, (C) Row-pattern.

Results: Figure 2 illustrates the excellent agreement of the numeric approach and MRI measurement. The main flow proximal and distal to the stent model was within 6% deviation. After the validation, the high-resolution CFD data was used to extract secondary flow information; in particular, the wall shear stress (WSS). Although all stent designs have the same square cross-section, a considerable influence of the stent design on WSS distribution could be observed (Fig. 3). As a result, it was possible to identify the potential of thrombus formation in the stent patterns using validated CFD.

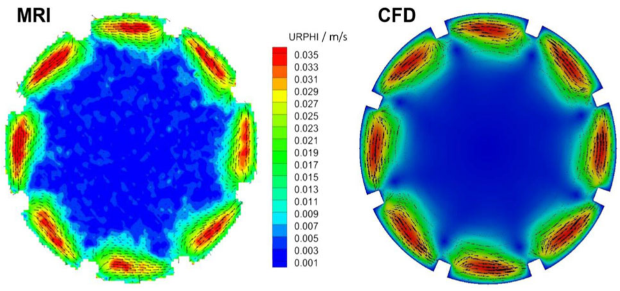

Figure 2: Comparison of MRI and CFD results. The circumferential velocity field in the cross-sectional plane of the stent with helical pattern is shown.

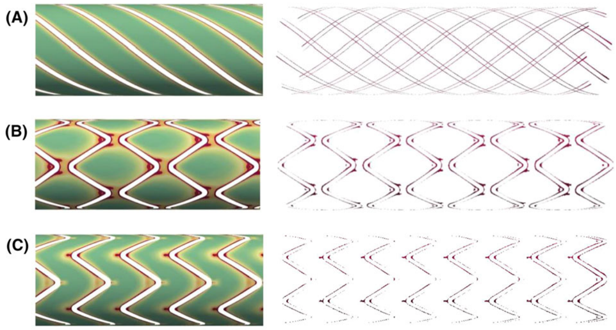

Figure 3: Qualitative comparison of the wall shear stress distribution obtained from CFD. Red colors indicate large stress.

Discussion/Conclusion: This study demonstrates the combination of in vitro MRI data and high-resolution CFD data. This kind of flow analysis is regarded as a reliable method to support the numerical optimization of future stent designs.

References:

[1] Stiehm, M., Numerische Simulation der Durchströmung koronarer Stents, Untersuchung der Einflussparameterfür das Restenosepotential. MENZEL-Verlag 2014.

[2] Markl M., et al. 4D flow MRI. J Magn Reson Imaging 2012;36:1015–1036.

S13.07

Phase-specific aorta segmentation based on 4D flow MRI: Inter-examination reproducibility in healthy volunteers

J. Juffermans[1], J. Westenberg[1], P. van den Boogaard[1], R. van der Palen[2], A. Roest[2], H. van Assen[1], H. Lamb[1]
[1]Leiden University Medical Center, Radiology, Leiden, NETHERLANDS, [2]Leiden University Medical Center, Pediatric Cardiology, Leiden, NETHERLANDS

Purpose/Introduction: Hemodynamic aorta parameters can be derived from 4D flow MRI and requires lumen segmentation. In commercial 4D flow MRI software tools, segmentations are mostly (semi-)automatically generated and subsequently manually improved. The aim of this study was to determine the inter-examination reproducibility of phase-specific aorta segmentation of 4D flow MRI in healthy volunteers.

Subjects and Methods: Ten healthy volunteers (26.5 ± 2.6 years) underwent aortic 4D flow MRI at 3T MRI (Ingenia, Philips Healthcare) twice, planned consecutively with a 5 min break. The 4D flow acquisition parameters were: respiratory navigator-gated, retrospective ECG-gated, velocity encoding: 200 cm/s, isotropic spatial resolution: 2.5 mm, temporal resolution: 35.1–36.1 ms and field of view: 350 × 250 × 75 mm. Thoracic aorta was segmented at five systolic phases using CAAS MR 4D flow v1.1 (Pie Medical Imaging BV). By positioning six perpendicular planes on the segmentation's centerline the aorta was divided into five anatomical segments; 1. proximal ascending aorta, 2. distal ascending aorta, 3. aortic arch, 4. proximal descending aorta and 5. distal descending aorta (pAAo, dAAO, AoA, pDAo and dDAo respectively; see Fig. 1). In order to evaluate the inter-examination variability the image analysis of both 4D flow acquisitions was performed by a single observer. Finally, the centerline length (CL) and mean diameter (MD) were determined for each segment using an in-house developed Python-based tool. The MD was derived from perpendicular cross-sections with a 2 mm spacing, see Fig. 2. The paired T-test (TT), absolute mean difference (DIFF), coefficient of variation (COV) and interclass correlation coefficient (ICC) were calculated for MD and CL between both examinations for each segment and phase over all subjects.

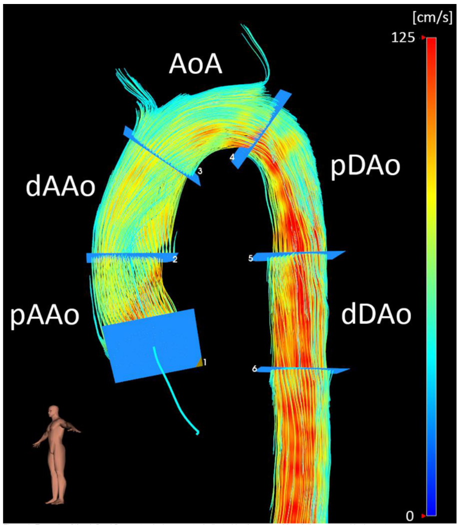

Figure 1. Example of the defined five anatomical segments, indicated by the same abbreviations as used in the text.

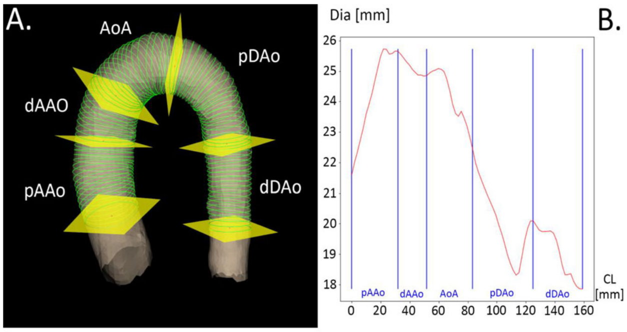

Figure 2. Example of a thoracic aorta segmentation. A: Visualization of a segmentation displaying the positioned planes (yellow) and cross-sections (green) to derive the diameter and centerline length. B: Plot of the cross-section diameter (Dia) over

Results: The TT showed no significant ($p > 0.05$) group difference between both examinations, except for AoA MD at the fifth systolic phase ($p = 0.027$, see Table 1). The inter-examination analysis showed for MD low DIFF (0.1–1.2 mm), low COV (1.6–8.8%), with good-to-excellent ICC (0.78–0.99) over all phases, excluding pAAo which had moderate-to-good ICC (0.53–0.77). For CL low DIFF (0.0–1.6 mm), intermediate-to-low COV (7.5–15.2%) with good-to-strong ICC (0.71–0.91) were found over all phases, excluding pAAo which had a poor ICC (0.36–0.48).

Segment	MD - DIFF [mm]	MD - TT [p]	MD - COV [%]	MD - ICC	CL - DIFF [mm]	CL - TT [p]	CL - COV [%]	CL - ICC
pAAo	0.3 - 1.2	0.133 - 0.653	5.2 - 8.8	0.53 - 0.77	1.2 - 1.6	0.229 - 0.378	13.1 - 15.2	0.36 - 0.48
dAAo	0.1 - 0.4	0.089 - 0.828	1.8 - 4.0	0.87 - 0.97	1.1 - 1.3	0.166 - 0.273	9.9 - 12.3	0.71 - 0.76
AoA	0.0 - 0.6	0.027 - 0.906	2.7 - 5.5	0.78 - 0.94	0.4 - 0.9	0.287 - 0.607	7.6 - 8.7	0.89 - 0.91
pDAo	0.2 - 0.4	0.082 - 0.624	1.6 - 5.2	0.88 - 0.99	0.0 - 0.3	0.777 - 0.981	7.4 - 8.5	0.89 - 0.91
dDAo	0.1 - 0.4	0.151 - 0.755	2.7 - 3.7	0.95 - 0.97	0.3 - 0.7	0.443 - 0.657	7.9 - 8.7	0.73 - 0.80

Table 1. Inter-examination MD and CL results of DIFF, COV and ICC per anatomical segment. Results displayed as ranges over all five systolic phases (minimum - maximum). All abbreviations are used as indicated in the text.

Discussion/Conclusion: In general, for MD and CL a good-to-excellent reproducibility was found for all segments and phases, except for pAAo. This observation can be explained by ease-of-use image analysis within the applied software, resulting in DIFF well below the spatial acquisition resolution. The reduced reproducibility of pAAo is most likely related to pronounced systolic stretching and lumen distension in the ascending aorta. Besides, the observer experienced difficulties while positioning planes at the aortic valve level.

References:

Not included.

S13.08

4D MR velocimetry and numerical simulations for studying swirling flows in blood vessel models

A. Khe[1], V. Vanina[2], A. Cherevko[1], D. Parshin[1], A. Tulupov[3], A. Chupakhin[1]

[1]Lavrentyev Institute of Hydrodynamics, Novosibirsk, RUSSIAN FEDERATION, [2]Novosibirsk State University, Novosibirsk, RUSSIAN FEDERATION, [3]International Tomography Center, Novosibirsk, RUSSIAN FEDERATION

Purpose/Introduction: Several studies of the structure of the blood flow show the existence of the helical (rotational-translational) character of the flow in certain parts of the human cardiovascular system (e.g., in the aorta) [1, 2]. In this work a framework for studying the helical character of the blood flow in human vessels using magnetic resonance imaging is analyzed.

Subjects and Methods: A set of experimental data was obtained by studying the flow in silicone models of blood vessels with a 3-tesla MRI scanner. The flow in models was generated by a programmable pump, which allows one to create non-stationary fluid flow profiles, similar to the flow in blood vessels. A 40% glycerol solution with water was used as a blood mimicking liquid. A silicone tube with a homemade swirl generator and a real-size silicone model of a common carotid artery bifurcation were used in our experiments.

For each model, several series of experiments were carried out using the 4D Qflow scanning protocol, from which the temporal-spatial velocity field was reconstructed. For processing DICOM files, we developed a MATLAB code.

The flow domain was reconstructed from MRI scans and used for the numerical simulation. The flow was modeled with the Navier–Stokes equations, which were solved in the ANSYS CFX software.

Results: A comparison of the results of the numerical calculation and the data obtained in the experiment using MRI showed that the conclusion about the character of the fluid flow was made correctly. Numerical simulations with different flow rates were performed. The comparison showed that with the increase of the flow rate, the length of the helical region increases.

Assessment of the accuracy of the MRI measurements was performed by comparing the flow rate computed from the experimental data against the one generated by the pump. According to the graphs, the experimentally obtained results are close to the prescribed exact ones.

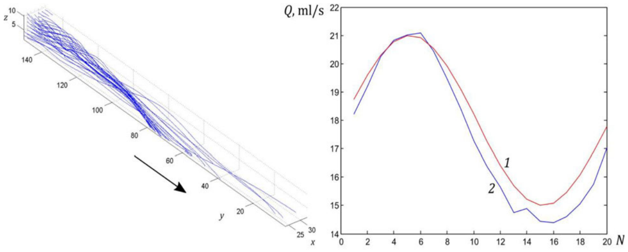

Streamlines of the flow in tube with swirl generator Generated (1) and measured (2) flow rate

Streamlines and flow rate

Discussion/Conclusion: The paper demonstrates the possibility of studying the three-dimensional unsteady structure of the flow in blood vessel models by means of magnetic resonance imaging. In particular, the use of this method allows one to determine the existence of a swirling (helical) component of the fluid flow.

The framework can be used for investigations aimed at studying the flow structure in cerebral vessels. Rotational flows and their influence on formation and evolution of pathologies can be studied.

This work was supported by the Russian Science Foundation (grant 17-11-01156).

References:

[1] Gataulin YA, Zaitsev DK, Smirnov EM, Fedorova EA, Yukhnev AD. Weakly swirling flow in a model of blood vessel with stenosis: Numerical and experimental study. *St Petersburg Polytechnical University Journal: Physics and Mathematics*. 2015;1(4):364–371.

[2] Kirsanov RI, Kulikov VP. Helical (spiral or swirling) blood flow in cardiovascular system. *Uspekhi Fiziologicheskikh Nauk*. 2013;44(2):62–78. (in Russian)

S13.09

^{19}F-MRI of inflammation with PFCE-loaded PLGA nanoparticles: quantification and intracellular localization

M. R. Daal[1], X. H. Staal[2], B. F. Coolen[1], A. J. Nederveen[3], M. Srinivas[2], N. N. van der Wel[4], R. C. Wüst[1], G. J. Strijkers[1]

[1]Amsterdam UMC, University of Amsterdam, Biomedical Engineering and Physics, Amsterdam, NETHERLANDS, [2]RIMLS, Tumor Immunology Lab, Nijmegen, NETHERLANDS, [3]Amsterdam UMC, University of Amsterdam, Radiology and Nuclear Medicine, Amsterdam, NETHERLANDS, [4]Amsterdam UMC, University of Amsterdam, Medical Biology, Amsterdam, NETHERLANDS

Purpose/Introduction: ^{19}F-MRI with fluorine-loaded nanoparticles(NP) has proven a powerful tool to study inflammation and for in vivo tracking of labeled cells[1]. Although the ^{19}F-MRI signal can be readily quantified, quantification of inflammatory disease activity or number of labeled cells is more difficult, as it requires knowledge on ^{19}F in the cells[2]. The spleen is important in this respect, as it is a center of activity of the immune system. The purpose of this study was to investigate correlation of ^{19}F signal with injected dose and association of the NP with leukocytes in the spleen by transmission electron microscopy (TEM) in mice with myocardial infarction.

Subjects and Methods: C57BL/6 J mice were iv. injected once with a varying dose of PFCE-loaded PLGA NP. A control (n = 3) and disease group (n = 5) that underwent 30 min ischemic/reperfusion myocardial infarction surgery were used. After 24–48 h the mice were scanned with a dual-tuned ^{1}H/^{19}F coil in a 7T MR Solutions preclinical scanner. MRI consisted of: ^{1}H 3D FLASH for anatomical imaging, LGE for myocardial infarct detection and 3D bSSFP for ^{19}F with the SNR determined in the spleen. The spleen was fixed and embedded in Epon for TEM to determine the number of cells labeled with NP and of NP per cell. Values are mean ± std.

Results: All mice had a positive ^{19}F signal in the spleen which correlated linearly ($R^2 = 0.74$) with the injected PFCE dose independent of group conditions (Fig. 1). ^{19}F signal was observed in infarct mice in the myocardial wall near the infarct border (Fig. 2.), indicative for the presence of inflammatory cells in agreement with previous observations in infarct mice. TEM of the spleen in 2 mice injected with 5.5 and 14.8 mg PFCE revealed 26.4 ± 3.6 and 39.1 ± 12.1% of the leukocytes (granulocytes and monocytes) contain NP, while the mean number of NP per cell was 16.9 ± 4.3and 42.1 ± 7.4 ($p = 0.03$) respectively (Fig. 3).

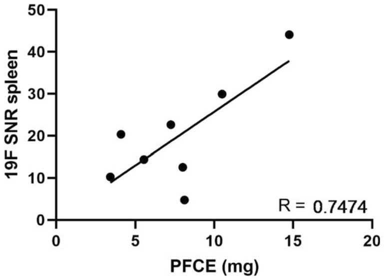

Figure 1. Correlation of 19F SNR in the spleen and injected PFCE dose.

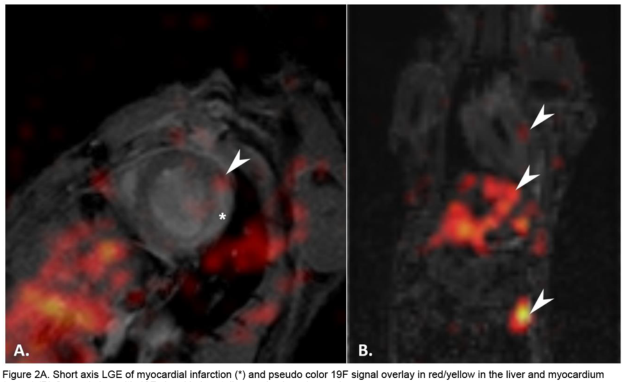

Figure 2A. Short axis LGE of myocardial infarction (*) and pseudo color 19F signal overlay in red/yellow in the liver and myocardium (arrow).(B) Coronal view with 19F signal in heart, liver and spleen (arrows).

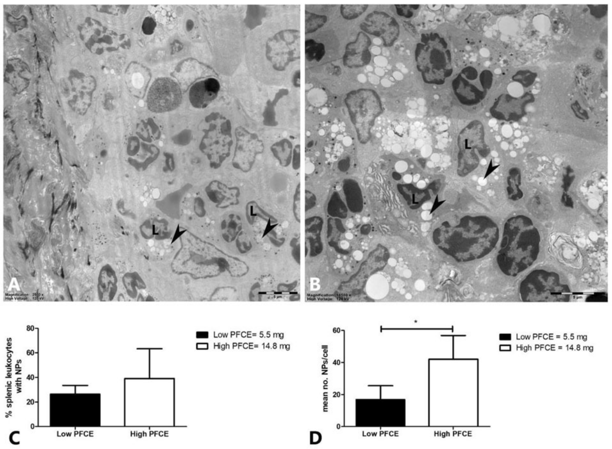

Figure 3. TEM. Spleen from mouse with (A) 5.5 and (B) 14.8mg PFCE injection. Leukocytes (L) containing NP (arrows). (C) Percentage labeled cells. (D) Number of NP per cell.

Discussion/Conclusion: We established linearity of ^{19}F signal in the spleen with injected NP dose. NP in the spleen can be found in both granulocytes and monocytes. Although quantification remains challenging, the results are indicative of the cell loading efficiency. For higher doses, the number of labeled cells seems to stay approximately the same, but the number of NP per cell increases. This needs to be considered when using ^{19}F-MRI as readout of inflammatory disease activity.

References:

1 Wüst et al., ATVB in press
2 Srinivas et al. 2012.

L04 Lightning Talks

13:50–14:40 *The Stage*

Brain Imaging

L04.01

T2 relaxation and volumetry of the brain: age-related changes in patients with hypertension

A. Sabisz[1], P. Naumczyk[2], A. Marcinkowska[1], B. Graff[3], D. Gasecki[4], A. Jankowska[1], K. Jodzio[5], E. Szurowska[1], K. Narkiewicz[3]
[1]Medical University of Gdańsk, 2nd Department of Radiology, Gdańsk, POLAND, [2]University of Gdańsk, Institute of Psychology, Gdansk, POLAND, [3]Medical University of Gdańsk, Department of Hypertension and Diabetology, Gdańsk, POLAND, [4]Medical University of Gdańsk, Department of Neurology of Adults, Gdańsk, POLAND, [5]University of Gdańsk, Institute of Psychology, Gdańsk, POLAND

Purpose/Introduction: Morphometry provides detailed information on the atrophy of the brain. Whereas quantification of the T2 relaxation time characterizes properties of the tissue. Combining both of these methods in the hypertensive population tells us more about aging processes and the impact of continuous elevated blood pressure on the brain. In this study, we wanted to answer the question of whether the values of T2 and volumes of brain regions vary in patients with hypertension with respect to different age groups.

Subjects and Methods: 189 participants took part in the study: 87 healthy controls (CON) and 102 patients with hypertension (SUB) with well-controlled blood pressure levels. Participants were divided into three age subgroups (Table 1).

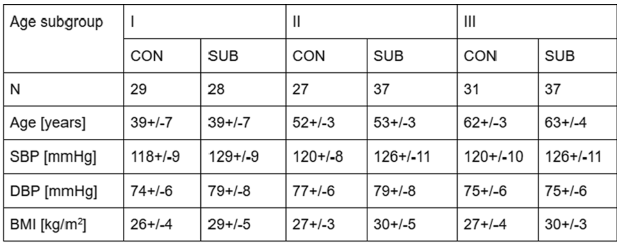

Age subgroup	I		II		III	
	CON	SUB	CON	SUB	CON	SUB
N	29	28	27	37	31	37
Age [years]	39+/-7	39+/-7	52+/-3	53+/-3	62+/-3	63+/-4
SBP [mmHg]	118+/-9	129+/-9	120+/-8	126+/-11	120+/-10	126+/-11
DBP [mmHg]	74+/-6	79+/-8	77+/-6	79+/-8	75+/-6	75+/-6
BMI [kg/m^2]	26+/-4	29+/-5	27+/-3	30+/-5	27+/-4	30+/-3

Table 1. Characteristics of the participants.

T1w TFE and T2w multiecho TSE sequences were acquired on 3T Philips Achieva TX scanner. The T1w sequence was used to calculate volumes of brain regions in Freesurfer and T2w images were used for mapping of the relaxation time. Analysis steps are presented in Fig. 1.

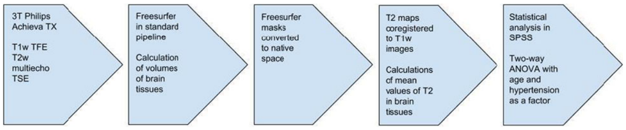

Figure 1. Methodology steps for quantification of volumes and T2 values of brain structures.

The effect of age and hypertension factors on quantified values were tested by two-way ANOVA.

Results: There was no significant interaction between the effects of age and hypertension on volumes of the brain structures. The main effect of age on the volume was significant in almost all of the regions, only white matter cerebellum of left and right hemisphere, corpus callosum, brain white matter of left and right hemisphere did not show age dependency. The main effect of hypertension was not significant in any of the comparisons.

The similar pattern was found in the analyses of mean values of T2 in different brain tissues. There wasn't any significant interaction between the effects of age and hypertension, also the main effect of hypertension wasn't significant. Statistical analysis showed the main effect of age on relaxation times. The values decreased with age.

Discussion/Conclusion: This study focused on the morphometry and T2 relaxation time in aging patients with hypertension. Patients with well-controlled hypertension don't differ from the healthy control group. The results confirmed shrinkage of the brain tissue with age in the study population as well as a decrease in T2 relaxation time. Atrophy and changes in T2 values in HTN follow the control pattern.

References:

[1] Naoko Saito et al. "Relaxo-volumetric multispectral quantitative magnetic resonance imaging of the brain over the human lifespan: global and regional aging patterns" https://doi.org/10.1016/j.mri.2009.05.006.

[2] Guillaume Bonnier et al. " The Combined Quantification and Interpretation of Multiple Quantitative Magnetic Resonance Imaging Metrics Enlightens Longitudinal Changes Compatible with Brain Repair in Relapsing–Remitting Multiple Sclerosis Patients" https://doi.org/10.3389/fneur.2017.00506.

L04.02

Simultaneous glucoCEST and fiber photometry of glucose in the healthy mouse brain

A. Eleftheriou[1], M. T. Wyss[1], G. Warnock[1], S. A. Vinogradov[2], B. Weber[1]
[1]University of Zurich, Institute of Pharmacology and Toxicology, Zurich, SWITZERLAND, [2]University of Pennsylvania, Perelman School of Medicine & Department of Chemistry, School of Arts & Sciences, Department of Biochemistry & Biophysics, Philadelphia, UNITED STATES

Purpose/Introduction: Glucose is the brain's main energy source and its uptake and metabolism are sensitive biomarkers for neurodegenerative diseases. Glucose Chemical Exchange Saturation Transfer (glucoCEST) is an MRI-based approach used to amplify glucose detectability and it has been proposed for tumor imaging, mainly because it is radioactivity-free and there is a large availability of MR scanners[1]. The main principle of glucoCEST is clear, but the exact compartmental origin of the signal needs further investigation in the brain[2].

3-O-methyl-D-glucose (3OMG) is used as a glucoCEST contrast agent. It is also known to trans-accelerate the glucose transporter GLUT1 in erythrocytes. Trans-acceleration occurs when hexose molecules are presented on the *trans* side, which allows the transporter to return faster to the *cis* side with a bound substrate. In practice, the extracellular presence of 3OMG stimulates the exit of intracellular glucose leading to a decrease of the fluorescent nanosensor signal. The initial slope of this reduction, can be used as a marker for the rate of glycolysis in astrocytes and neurons.

The aim of this study was to assess astrocytic and neuronal glucose levels and metabolic rates upon administration of 3OMG using fiber photometry and correlate these measurements with glucoCEST, to determine the contribution of astrocytes and neurons to the overall brain signal.

Subjects and Methods: We performed simultaneous glucoCEST and photometry measurements of intracellular glucose concentration in the mouse neocortex upon intravenous infusion of 3OMG, insulin and glucose with galactose, successively.

For the photometry recordings, the genetically encoded Förster Resonance Energy Transfer (FRET) nanosensor FLIIP was used[3]. Constructs coding for this sensor were injected into somatosensory cortex of adult mice using an adeno-associated viral approach and specific promotors were used for either astrocytic (short GFAP promotor) or neuronal (human Synapsin promotor) expression.

Results: We observed trans-acceleration in astrocytes (mainly expressing GLUT1) and neurons (mainly expressing GLUT3).

Insulin and glucose with galactose were used to reach the minimum and maximum of the nanosensor dynamic range, for two-point calibration. Normalization to these points revealed higher baseline FLIIP signals in astrocytes.

Discussion/Conclusion: We demonstrate the feasibility of simultaneous glucose level measurements using fiber photometry and glucoCEST in vivo.

Fluorescence measurements during glucoCEST MRI give immediate validation of the influx of 3OMG into neurons and astrocytes, by observation of trans-acceleration. Despite lower baseline FLIIP measurements in neurons than in astrocytes, both cell types exhibited trans-acceleration.

References:

1. Van Zijl, P. C. M. et al., *Magn Reson Med* 65 (2011),
2. Nasrallah, F. A. et al., *J. Cereb Blood Flow Metab* 33 (2013),
3. Takanaga, H. et al., *Biochimica et Biophysica Acta, Biomembranes* 1778 (2008).

L04.03

MRI features of hemo- and cerebrospinal fluid dynamics in patients with idiopathic intracranial hypertension and idiopathic normal pressure hydrocephalus

K. Kolpakov[1], O. Bogomyakova[2], M. Amelin[3], M. Rezakova[4], **A. Tulupov**[2]
[1]Novosibirsk State University, Nobosibirsk, RUSSIAN FEDERATION, [2]Laboratory of Medical Diagnostic, International Tomography Center, Siberian Branch of Russian Academy of Sciences, Nobosibirsk, RUSSIAN FEDERATION, [3]FSBI, Nobosibirsk, RUSSIAN FEDERATION, [4]State Scientific-Research Institute of Physiology and Basic Medicine, Nobosibirsk, RUSSIAN FEDERATION

Purpose/Introduction: Idiopathic intracranial hypertension (IIH) and idiopathic normal pressure hydrocephalus (iNPH) both are the functional brain diseases with unclear pathogenesis [1, 2]. Nowadays their diagnostics is based on a clinical manifestation and exclusion of organic lesions [2, 3]. The alteration of CSF dynamics plays a significant role in several pathological process [1, 2]. Nevertheless, the exact mechanisms of its dysfunction are not clearly defined. The purpose of this study was to reveal the most important defects of the hemo- and CSF dynamics in patients with IIH and iNPH.

Subjects and Methods: The two groups of volunteers were formed: the patient group consisted of 10 patients with clinical/radiological signs of either IIH or iNPH without any organic lesions of the brain and the control group that consisted of 12 persons without any neurological disorders. This study was performed on Philips "Ingenia" 3.0T scanner using the phase-contrast MRA for the quantitative evaluation of the hemoand cerebrospinal fluid dynamics. A number of parameters were analyzed including Pulsatility Index (PI), Arterio-Venous Delay (AVD), Stroke Volumes (SV) and Intracranial Complaince (ICC). Data were analyzed with the Mann–Whitney test.

Results: ICC decreased by 58% ($p < 0.01$) and the total venous outflow was 52% higher ($p < 0.05$) in all patients compared with the control group. In the IIH patients the AVD is 37% lower ($p < 0.05$) and PI on the great occipital foramen and cervical area is 15% lower ($p < 0.05$) than in the control group. In the iNPH patients PI on the aqueductal area increased nearly by 2.3 times ($p < 0.05$) as compared with the healthy people. In the iNPH patients the PI on the straight sinus increased by 40% ($p < 0.05$) as compared with the control group.

Discussion/Conclusion: Decreasing of ICC is the most common feature of functional disturbances of the cerebrospinal fluid dynamics. These patients have a congestion of fluid inside the intracranial volume that has to be compensated by increasing the venous outflow. In the IIH patients the excess fluid accumulates in the brain interstitial space, while in the iNPH patients it accumulates mostly in the lateral ventricles and primarily the straight sinus compensates this congestion.

The work was supported by Russian Science Foundation (the project #19-75-20093).

References:

1. Bräutigam K., Vakis A., Tsitsipanis C. Pathogenesis of idiopathic Normal Pressure Hydrocephalus: A review of knowledge//Journal of Clinical Neuroscience. Berlin: Elsevier, 06.11.2018 г. Vol. 61. pp 10–13.
2. Chan J.W. Current concepts and strategies in the diagnosis and management of idiopathic intracranial hypertension in adults//Journal of Neurology. Phoenix: Springer, 31.01.2017 г. 8. Vol. 264. pp. 1622–1633.
3. Keong N.C.H., Pena A., Price S.J. Imaging normal pressure hydrocephalus: theories, techniques, and challenges//Neurosurgical Focus. - Singapore : JNS, 09.2016 г. 3:Vol. 41.

L04.04

Delayed 24 h post-contrast retention of gadolinium in brain tumors as sign of malignancy, cell lysis and enhanced intratumoral level of free metals

W.-Y. Ussov[1], M. L. Belyanin[2], T. N. Trofimova[3], A. S. Chirikov[4], V. D. Filimonov[2], N. V. Savello[5], N. L. Shimanovsky[6]
[1]Tomsk Medical Research Center/Institute of Cardiology, MRI Res. Lab, Tomsk, RUSSIAN FEDERATION, [2]National Research Tomsk Polytechnic University, Biotechnology and Organic Chemistry, Tomsk, RUSSIAN FEDERATION, [3]I.P.Pavlov Medical University, Saint-Petersburg, RUSSIAN FEDERATION, [4]Tomsk Regional Clinical Hospital, Neurosurgery, Tomsk, RUSSIAN FEDERATION, [5]R-Pharm Co., Saint, Petersburg, RUSSIAN FEDERATION, [6]N.I.Pirogov Moscow Medical Research University, Molecular Pharmacology, Moscow, RUSSIAN FEDERATION

Purpose/Introduction: We evaluated the hypothesis the elevalted intratumoral amount of biological microelements induces the transmetallation of Gadolinium contrast agents, release of free Gd and prolonged delay of it in the tumor. As the malignant brain tumors demonstrate significantly higher degree of cell lysis and release of Zn, Co, Cu and Mn into extracellular marix [1], the malignant tumors are thought to demonstrate higher degree of delayed 24-h Gd delay, than bening ones

Subjects and Methods: Twenty-seven patients with brain tumors were referred for ths study, among them twelwe with meningiomas, all below 40 mm in diameter, and fourteen with glioblatoma multiforme (3), low-grade glomas (9) or lung cancer metastases(2), all as little as < 30 mm..

In everybody the contrast-enhance MRI study of the brain has been carried-out, in particular employing T1-w.protocols (TR = 500 ms, TE = 12–15 ms), with contrast enhancement using 2 ml of 0.5 M Gd complexes per 10 kg BW and acquisition of post-contrast scans in 15–20 min post-injection as well as in 24 h post injection. Th retention index was calculated as ratio of scan intensities per voxel: IR = $\{(\text{Tumor/Norm})_{24\text{h}}\}/\{(\text{Tumor/Norm})_{15\text{min}}\}$, using RadiAnt (Medixant, Poznan, Poland) software. In seventeen (all meningiomas and five low-grade gliomas) the neurosurgical intervention was carried out soon, and the contents of Zn, Co, Cu and Mn was measured spectroscopically.

Results: All benign tumors demonstrated prominent contrast enhancement at 15–20 min after the contrast injection, but full washout without significant retention of contrast at 24 h T1-w scan (image.1). The IR = {(Tumor/Norm)24 h}/{(Tumor/Norm)15 min} was in this group as low as 0.63 ± 0.12 in this group.

In the malignant brain lesion the 24 h scans demonstrated progredient retention of the paramagnetic agent (image.2), with IR = 1, 12 ± 0.09 ($p < 0.02$, if compared to group of benign tumors). This difference provided sure delineation of malignant lesions from the benign ones in every case.

The IR correlated significantly ($r = 0.49$, $p < 0.05$) with overall sum of concentrations of Zn, Co, Cu and Mn ions in the tissue.

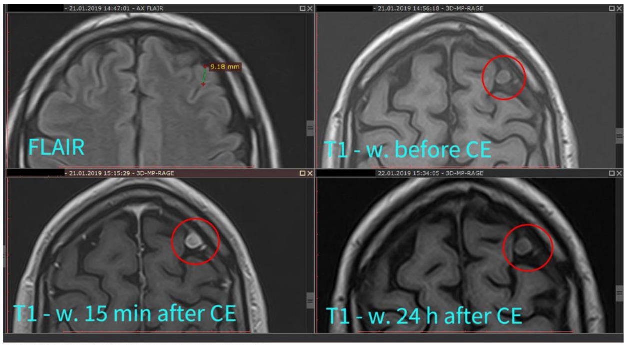

Typical 24-h dynamic of contrast retention in meningeoma

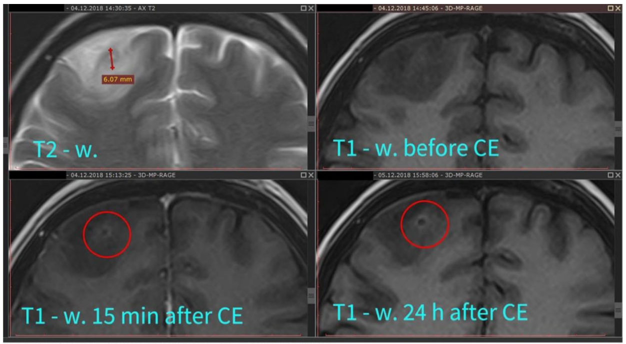

Progredient increase of Gd retention in little malignant low grade glioma

Discussion/Conclusion: Thus we conclude the delayed 24 post-CE T1-w scans of brain tumors provide simple and useful technique for detection of tumor malignancy, due to intratumoral Gd transmetallation with free microelements released to tumor interstitial space. Further more extensive and detailed study is in progress

References:

1. Varfolomeev S.D., Gurevich S.K. Biokinetics. Moscow. Moscow State University Publ. 2009. 571 P.

L04.05

Synthetic diffusion-weighted imaging (MAGIC DWI) in stroke imaging: study of 52 cases

R. Vadapalli[1], R. b. Annamraju[2], a. s. Vadapalli[3]
[1]*Vijaya Diagnostics, Radiology, Hyderabad, INDIA,* [2]*GE Healthcare, Digital innovations in affordable care, Bangalore, INDIA,* [3]*Medway Maritime Hospital Windmill Road Gillingham Kent, Orthopaedic surgery, Hyderabad 500020, INDIA*

Purpose/Introduction: To evaluate the role of Multi b value synthetic diffusion-weighted Imaging in the evaluation of stroke

Subjects and Methods: 52 patients who presented with symptoms suggestive of stroke in the age group of 39–81 years with the mean age 49.5 + _10 years with M: F ratio of 2.3 were evaluated by dedicated stroke protocol and supplemented by an additional 2-min synthetic magic DWI multi b value protocol after a waiver from IRB. The parameters of synthetic DWI sequence are as follows:

Multi b value DWI acquisition with b values of 0 1000 and synthesis of b values of 1500, 2000 with maximum b value not exceeding 2500. Magic DWI sequence is used in addition to conventional stroke protocol with an additional penalty of 2 min and retrospective post processing and generation of multiple b value images for instance b = 500, 750 or 2500.

The sensitivity of detection of infarcts on conventional DWI was compared to Magic DWI

Results: Of 52 Patients 31 patients had multiple acute lacunar infarcts in MCA territory and MCA and PCA watershed zones and 21 patients in the infratentorial region including brain stem and cerebellum and six patients with a sensitivity of 92 per cent and specificity of 97percent with conventional DWI.

Using the Magic DWI with the synthesis of multiple b values between 1000 to 2500 the sensitivity and specificity have significantly improved to 97 per cent and specificity of 99 per cent with an NPV of 99 per cent.

Midbrain pontine and medullary lacunar strokes showed significant increased conspicuity and yield rate of detection.

High b value imaging, especially between 1500 and 2000, allowed additional detection of acute lacunar infarcts in eloquent strategic locations like media; midbrain(Claude's syndrome,)anterior cerebral peduncle in addition to the medial midbrain (Benedict's syndrome) and medial and lateral-medullary infarcts

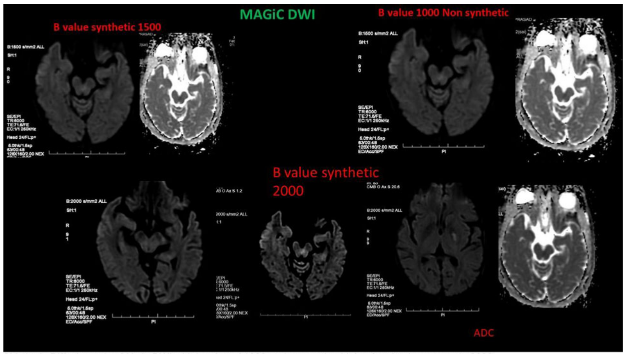

SYnthetic Diffusion using MAgic DWI with b value of 1000 and generating higher b value images up to 2000

Discussion/Conclusion: MultiB value Ultra fast Synthetic DWI - Magic DWI which is a synthetic diffusion technique that generates multiple synthetic b values from a single DWI scanned series allowing the user to view the diffusion contrasts changes in real time even after the data acquisition with no time or SNR penalties.

This is a powerful adjunct tool to the conventional stroke protocol offering the user a retrospective synthetic slider to generate multi b value data from 100 to 2500 increasing the sensitivity of stroke detection with no time or SNR penalties.

References:

Chilla GS, Tan CH, Zu C, Poh CL. Diffusion-weighted magnetic resonance imaging and its recent trend—a survey. Quant Imaging Med Surg. 2015 Jun; 5(3):407–22.

L04.06

Microstructural disorders in thalamus in the acute phase of pediatric mild traumatic brain injury. DTI study

O. Vasiukova[1], **A. Manzhurtsev**[2], P. Menshchikov[3], M. Ublinskiy[4], T. Akhadov[4], N. Semenova[2], I. Melnikov[4], O. Bozhko[4]
[1]National Research Nusclear University MEPHI, Moscow, RUSSIAN FEDERATION, [2]Emanuel Institute of Biochemical Physics of the Russian Academy of Sciences, Moscow, RUSSIAN FEDERATION, [3]Semenov Institute of Chemical Physics of the Russian Academy of Sciences, Moscow, RUSSIAN FEDERATION, [4]Clinical and Research Institute of Emergency Pediatric Surgery and Traumatology, Moscow, RUSSIAN FEDERATION

Purpose/Introduction: Wide-spread visualization methods which are computed tomography (CT) and magnetic resonance imaging (MRI) are not sensitive to mild traumatic brain injury (mTBI). However, mTBI may cause changes in cerebral microstructure that could be found using diffusion tensor imaging (DTI).

The aim of this study is to reveal possible microstructural disorders in grey and white cerebral matters of children in the acute phase of mTBI (no more than 72 h), not accompanied by any structural brain injury.

Subjects and Methods: Subjects: 11 healthy subjects and 11 patients with mTBI (up to 41 + 19 h since the injury), mean age 16 + 2. Philips Achieva dStream 3.0T and 32-channel SENSE head coil were used. The standard TBI MRI protocol was applied. No pathological changes in brain tissue of any subject were found.

DTI was performed in 32 directions and processed in Philips Intellispace Portal. The fractional anisotropy (FA) and apparent diffusion coefficient (ADC) values were obtained in corpus callosum (CC), corticospinal tract (CST) and in thalamus.

Statistical analysis was performed in STATISTICA 12 (Statsoft). The nonparametric Mann–Whitney criterion was used to reveal the significance of group differences, p-value < 0.05 was considered significant.

Results: The results of the quantitative analysis for FA and ADC are provided in tables 1 and 2. In Table 1 the white matter analysis is demonstrated. One may observe the trend to the FA increase in corpus callosum in mTBI group and the absence of any changes in this parameter in corticospinal tract. ADC in both CC and CST is unchanged.

Region	FA controls	FA mTBI	p-value	ADC controls	ADC mTBI	p-value
CC	0.43±0.02	0.45±0.02	0.08	0.88±0.05	0.87±0.04	0.53
CST	0.52±0.02	0.52±0.02	0.24	0.80±0.05	0.82±0.05	0.15

Table 1. FA and ADC values in white matter (Median ± range)

Table 2 summarizes the data on FA and ADC measured in thalamus as a sample of grey matter. Both FA and ADC parameters are sensitive to mTBI in this region: FA is increased and ADC decreases in the acute phase after mTBI.

FA controls	FA mTBI	p-value	ADC controls	ADC mTBI	p-value
0.42±0.02	0.44±0.03	0.006*	0.85±0.02	0.83±0.02	0.042*

Table 2. FA and ADC in thalamus (Median ± range), * - p<0.05

Discussion/Conclusion: The results of this study signify the presence of microstructural damage in thalamus. The changes in diffusion parameters arise from the cytotoxic swelling, that happens because of the alterations in metabolic processes caused by the traumatic impact [1]. The trend to the growth of FA revealed in this work may witness for the process of microstructural damage “maturation”, causing these changes to be observed as significant at a later stage after injury [1, 2, 3].

References:

1. Z. Chu. Voxel-Based Analysis of Diffusion Tensor Imaging in Mild Traumatic Brain Injury in Adolescents. AJNR Am J Neuroradiol. 2010 Feb;31(2):340–6.
2. Henry LC, Tremblay J, et al. (2011) Acute and chronic changes in diffusivity measures after sports concussion. J Neurotrauma. (10):2049–59.
3. Mayer AR, Ling J, Mannell MV, et al. (2010) A prospective diffusion tensor imaging study in mild traumatic brain injury. Neurology.;74(8):643–50.

L04.07

Assessment of microcirculatory changes in patients with multiple sclerosis by perfusion MRI

L. Vasilkiv, **A. Tulupov**, O. Bogomyakova
International Tomography Center Siberian Branch of Russian Academy of Sciences, Novosibirsk, RUSSIAN FEDERATION

Purpose/Introduction: Multiple sclerosis (MS) is one the most common demyelinating diseases in young adults accompanied by disseminated demyelination foci. The purpose of the study was to assess morphofunctional changes in demyelinating lesions of the central nervous system using perfusion MRI.

Subjects and Methods: The MRI study was performed on the Ingenia (Philips) scanner 3.0T using pseudontinuous arterial blood spin-marking and dynamic contrast susceptibility (DSC) techniques. The study included 12 healthy volunteers and 45 patients with MS (9 patients with clinically isolated syndrome, 31 patients with remitting-recurrent MS and 5 patients with secondary progressive MS) in age from 18 to 50 years. A quantitative and qualitative assessment of the cerebral blood flow rate (CBF) and volume (CBV), contrast transit time (MTT) and peak concentration time (TTP) in demyelination foci and in the normal-appearing white matter (NAWM) in the frontal, parietal, temporal and occipital lobes of the brain were evaluated. Data were processed using non-parametric methods of analysis.

Results: In patients with clinically isolated syndrome and in the acute stage with remitting multiple sclerosis, there was a significant increase in CBF to 65, 2% and CBV to 78, 1% in active foci of demyelination; in remission stage, there was a 25, 2% decrease in CBF and a 18, 1% decrease in CBV in the inactive demyelination foci. Under dynamic observation, an increase in hypoperfusion was observed in NAWM in all patients, which was more pronounced in the secondarily progressive course. Perfusion maps revealed asymmetric zones of hypo-/hyperperfusion indicating the pathological processes in the white matter of the brain.

Discussion/Conclusion: In this work the data of the changes in qualitative and quantitative parameters of perfusion in the healthy white matter and in the demyelination foci in various types of multiple sclerosis were obtain. A dynamic changes in perfusion indices in patients with clinically isolated syndrome, multiple sclerosis with remitting-recurrent and secondary-progressive course were studied. Evaluation of cerebral perfusion allows to suggest the role of the vascular component in the process of formation of focal inflammatory changes in the brain in MS. Perfusion data improves informativeness of the routine MRI and provides a comprehensive assessment of the pathogenesis of MS.

References:

The work was supported by Russian Science Foundation (the project #19-75-20093).

L04.08

Resting state fMRI, voxel-based morphometry and neuropsychological examination in patients with anorexia nervosa

T. Salomatina[1], N. Ananyeva[1], L. Akhmerova[1], E. Andreev[1], A. Pichikov[2], Y. Popov[2], M. Wasserman[3], A. Popova[3]
[1]Federal State Budgetary Institution "V.M. Bekhterev National Medical Research Center for Psychiatry and Neurology" of the Ministry of Health of the Russian Federation, Department of Neurophysiology, Neurovisual and Clinical and Laboratory Studies, Saint-Petersburg, RUSSIAN FEDERATION, [2]Federal State Budgetary Institution "V.M. Bekhterev National Medical Research Center for Psychiatry and Neurology" of the Ministry of Health of the Russian Federation, Department of adolescent psychiatry, Saint-Petersburg, RUSSIAN FEDERATION, [3]Federal State budgetary Educational Institution of Higher Education "St. Petersburg State Pediatric Medical University", Saint-Petersburg, RUSSIAN FEDERATION

Purpose/Introduction: The significant increase in the number of adolescents with AN requires a deeper understanding of structural and functional disorders in these patients. In our work, using a multidisciplinary approach, we have identified neuromorphofunctional features in young girls suffering from anorexia nervosa.

Subjects and Methods: MRI Toshiba 1.5 T with MPRAGE, using VBM (Freesurfer) and fMRIrs was applied to 50 females: 31-AN and 19- controls (average age-16).Neuropsychological examination included: ACE-R III, Stroop test, proof test, dichotic test, TIP, State-Trait Anxiety Inventory (STAI).

Results: VBM in AN group: the cerebellum was reduced by 20%, l amygdala–18%, r amygdala–17%, thalamus—11% and r hippocampus—13%; pallidum—10%, III ventricle—14%; l entorhinal cortex—14%, r entorhinal cortex—28%, r parahippocampal gyrus—20%, l frontal pole—12%, r frontal pole—16%. l middle frontal gyrus—11%, r middle frontal gyrus—13%, r fusiform gyrus—14%. FMRIrs ROI to ROI data analysis in AN group showed an increased activation in precuneus and cuneal, a decreased in supramarginal gyrus in sensomotory network, in default mode network—higher activation of the r medial prefrontal cortex; in visual network—increased activation in the l precuneus and reduced in the r frontal pole. In the Salience network- increased activation in middle frontal gyrus, pre-, postcentral gyrus, additional motor cortex of the l hemisphere. In the dorsal attention network- increased activity in the precentral gyrus. In the executive control network- the paracingular gyrus of the l hemisphere and the l frontal pole is increased. In the language network- increased activity of the posterior cingulate gyrus, right superior frontal gyrus, supramarginal gyrus in r hemisphere ($p \leq 0.05$).The neuropsychological data analysis showed the significant differences between two groups: lower summary scale in ACE-R III, subscales "attention", "memory", "verbal fluency", higher coefficient of interference in the Stroop test and in "situational anxiety"scale in STAI in AN group

Discussion/Conclusion: Significant reductions in the volume of structures indicate a pathological change in the brain in AN and it affects the connectivity of the neural networks. Also the significant differences in neuropsychological scales which are mostly in cognitive functions may prove all these morphological changes. It will contribute to the selection of structural and functional markers in anorexia nervosa. Further research of morphofunctional correlates may provide a deeper understanding of pathogenesis of anorexia nervosa and find new ways for a therapy of this disease.

References:

Phillipou A., Abel L.A., Castle D.J., Hughes M.E., Nibbs R.G., Gurvich C., Rossell S.L. Resting state functional connectivity in anorexia nervosa. Psychiatry Res Neuroimaging. 2016 May 30;251:45–52.

L04.09

Computation of the texture features in Glioblastoma grade 4 and Oligodendroglioma grade 2 based on T1 weighted post contrast images

M. Grzywińska[1], A. Sabisz[2], N. Borof[3], E. Szurowska[2]
[1]Medical University of Gdansk, Department of Human Physiology, Gdansk, POLAND, [2]Medical University of Gdansk, 2nd Department of radiology, Gdansk, POLAND, [3]The Provincial Integrated Hospital, Elblag, POLAND

Purpose/Introduction: The study aims to find statistical differences between texture features in two types of grade and types of tumour. The texture in medical images describes the internal structure of human tissues or organs. Textural analysis and the measurement of conventional parameters from imaging studies is based on a series of algorithms related to a series of images (Szomolanyi et al. 2009).

Subjects and Methods: For analysis, we used twenty retrospective examination, the patients had also histopathology examination. All MR acquisition was performed using a 1, 5 Tesla magnet (MAGNETOM Aera, Siemens Healthcare GmbH, Erlangen, Germany).

For correct field inhomogeneity, we used N4 Algorithm (Tustison and Gee 2009). For texture analysis, we used Pyradiomics (version 2.0.0), where we use a relative bound and bin width fixed (bW = 2) (Kickingereder et al. 2016), and the same size of ROI.

Statistic analysis was performed using IBM SPSS Statistic 25. We used 110 texture parameters for each patient. Data was checked to a normal distribution Shapiro–Wilk test, t-student test was performed.

Results: Obtain result show us a significant difference between some texture parameter in two types of grade and types of tumour. In this texture features: GLDM_DependenceNonUniformity ($t(18) = 10.142$, $p < 0.001$), GLDM_GrayLevelNonUniformity ($t(18) = 3.686$, $p = 0.002$), GLCM_JointEntropy ($t(18) = 8.328$, $p < 0.001$), GLCM_JointEnergy ($t(18) = -5, 793$, $p < 0.001$), FirstOrder_Energy ($t(18) = 4.012$, $p < 0.001$), FirstOrder_Entropy ($t(18) = 2.875$, $p < 0.005$), FirstOrder_Variance ($t(18) = 1.736$, $p = 0.050$), GLRLM_GreyLengthNonUniformity ($t(18) = 3.759$, $p = 0.002$), GLSZM_ZoneEntropy ($t(18) = 5.217$, $p < 0.001$) and NGTDM_Complexity ($t(18) = 2.702$, $p = 0.007$).

Discussion/Conclusion: Our preliminary research shows that textural analysis can be a potential tool for diagnosing and differentiating grade of pathological lesions. However, the method of texture analysis should be standardised, and the influence of acquisition parameters, size of ROI, binning and others, on structural parameters should be tested.

References:

Kickingereder, P., Burth, S., Wick, A., Götz, M., Eidel, O., Schlemmer, H.-P., Bonekamp, D. 2016 Radiomic Profiling of

Glioblastoma: Identifying an Imaging Predictor of Patient Survival with Improved Performance over Established Clinical and Radiologic Risk Models. *Radiology*, *280*(3), 880–889.

Leijenaar, Ralph T.H., Nalbantov, G., Carvalho, S., van Elmpt, W. J. C., Troost, E.G. C., Boellaard, R., Lambin, P. 2015 'The Effect of SUV Discretization in Quantitative FDG-PET Radiomics:The Need for Standardized Methodology in Tumor Texture Analysis'.

Nioche, C., Orlhac, F., Boughdad, S., Reuze, S., Goya-Outi, J., Robert, C., Buvat, I 2018. 'Lifex: A Freeware for Radiomic Feature Calculation in Mulmodality Imaging to Accelerate Advances in the Characterization of Tumorti Heterogeneity'. *Cancer Research* 78(16): 4786–89.

Tustison, Nicholas J, and James C Gee. 2009. *N4ITK: Nick's N3 ITK Implementation For MRI Bias Field Correction*.

L04.10

Motor mapping for pre-surgical planning using seed-based resting-state fMRI approach

V. Malekian, A. Nasiraei Moghaddam

Institute for Research in Fundamental Sciences, School of Cognitive Sciences, Tehran, IRAN, ISLAMIC REPUBLIC OF

Purpose/Introduction: In the recent years, utilizing functional maps, obtained from task-based fMRI (tsfMRI) in pre-surgical planning, has been highlighted as a major clinical application [1, 2]. However, performing task paradigm in patients with the massive brain tumor close to the corresponding functional regions is challenging. In a few studies, resting-state fMRI (rsfMRI) have been used instead of tsfMRI to localize the functional regions [2, 3]. Here, we utilized the seed-based analysis method to obtain functional map from rsfMRI data for patients with tumor in the motor regions. The results look promising for localization of the motor areas close to tumor.

Subjects and Methods: rsfMRI was performed on two patients with tumors, invaded motor part of their brains by 3T MRI scanner using EPI protocol with parameters: TR/TE = 2000/30 ms, FOV = 224 * 224 mm^2, FA = 80°, Voxel size = 3 × 3 × 3 mm^3, TR = 2 s and 240 measurements. All the preprocessing and analysis steps were performed using FSL. Motion correction, temporal filtering and spatial smoothing (FWHM = 5 mm) were applied as a preprocessing step. Motor mask was created to generate a seed using Juelich atlas in MNI space, and was then converted into the functional space to calculate the mean time-course of the seed. Lastly, dual regression was performed to generate z-maps which was then converted to the anatomical space.

Results: In Fig. 2, the motor mask and the related seed were shown by red and blue respectively. In Fig. 3, motor mapping in our rsfMRI approach were indicated for two patients. Seeds were selected in the opposite side of the tumor in the motor regions that were placed in left side in both cases here. In addition to the regions close to the seeds, the map for motor activity is also seen around the tumor in the right part of the brain for both cases.

Discussion/Conclusion: Finger tapping is the common approach to localize the motor cortex before surgery [4]. Suitable performance of the task depends on patient ability, tolerance and cooperation during the experiment. rsfMRI is an alternative method to help patients unable to follow the task paradigm related to the part of brain, invaded by tumor. Here, we utilized the seed at the opposite side of the tumor in the motor cortex and calculate the correlation between the seed time-course and the rest of the brain voxels. As can been seen in Fig. 3, the proposed approach can help to investigate the motor mapping in the neighborhood of the brain tumor due the functional connectivity in motor network. In conclusion, rsfMRI can localize the motor cortex as an alternative approach which takes advantage of simple data acquisition but more complicated data processing in comparison to tsfMRI.

References:

[1] Glover, *Neurosurgery Clinics* 22.2 (2011): 133–139.
[2] Shimony, et al., *Academic radiology* 16.5 (2009): 578–583.
[3] Kamran, et al., *Neuroimaging Clinics* 24.4 (2014): 655–669.
[4] Qiu, et al., *Acta neurochirurgica* 156.12 (2014): 2295–2302.

L04.11

Multiple quantum filtered sodium MRI of multiple sclerosis at 7T

A. Shymanskaya[1], **W. A. Worthoff[2]**, J. O. Cleary[3], Y. Blunck[4], R. K. Glarin[4], S. Kolbe[5], L. Johnston[4], N. J. Shah[6]

[1]Forschungszentrum Jülich GmbH, Institute of Neuroscience and Medicine, 11, Jülich, GERMANY, [2]Forschungszentrum Jülich GmbH, Institute of Neuroscience and Medicine, 4, Jülich, GERMANY, [3]Guy's and St. Thomas' NHS Foundation Trust, Department of Radiology, London, UNITED KINGDOM, [4]Melbourne Brain Centre Imaging Unit (MBCIU), University of Melbourne, Department of Medicine and Radiology, Melbourne, AUSTRALIA, [5]Monash University, Department of Neuroscience, Melbourne, AUSTRALIA, [6]Forschungszentrum Jülich, Institute of Neuroscience and Medicine, 4, Jülich, GERMANY

Purpose/Introduction: Multiple sclerosis (MS) is an autoimmune condition of the central nervous system (CNS). Demyelination and axonal dysfunction, characteristic of MS, disrupt nerve transmission and sodium flux. Non-invasive assessment of sodium distribution in intra- and extracellular spaces may provide insight into the disease. We compare an RRMS and a healthy subject (HS) using enhanced SISTINA (1).

Subjects and Methods: A female RRMS patient (age 48) and a HS (male, age 40) were imaged in accordance with human research ethics committee approval. A 7T system with a transmit/receive ^{23}Na/^{1}H head coil and 32 channel receive ^{1}H coil was used.

Na images (see Fig. 1) were acquired using an enhanced SISTINA imaging protocol (1). Preparatory time and evolution time were t = 6 ms and d = 40 µs, TR = 120 ms.

MP2RAGE images were acquired for registration with FSL FLIRT (2) and for segmentation of the Na images. In the patient, one lesion was segmented. In both subjects, a region in normal appearing white matter (NAWM) was manually segmented.

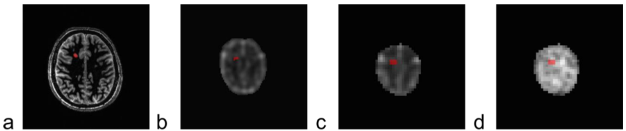

Fig.1: MRI images of the MS patient: (a) MP2RAGE, (b) Na UTE image, (c) Na SQ-weighted image, (d) Na TQ-weighted image. Red: mask of the segmented lesion

Fits of the multi-echo data were used to estimate T^*_2 relaxation times and MQF-derived parameters in the NAWM and the lesion in both the patient and HS.

Results: MP2RAGE of the MS patient demonstrated multiple characteristic white matter lesions. The results are provided in Table 1; Table 2 shows the corresponding parameter ratios of the lesion and NAWM between the patient and the HS.

Compared to the HS, NAWM showed a decrease in T^*_{2f}, ISMF and ISVF, as well as a strong increase in T^*_{2s}, and a moderate increase in concentrations c_{in} and c_T. In the lesion, a decrease in T^*_{2f} was prominent; in ISMF and ISVF the decrease was moderate. There was no change in T^*_{2s} and a strong increase in c_{in} and c_T.

Subject	T*_2f (ms)	T*_2s (ms)	ISMF	c_T (mmol/L)	c_in (mmol/L)	ISVF
Patient (lesion)	0.58±0.35	26.03±7.77	0.66	39.58±4.19	28.94±1.67	0.90
Patient (NAWM)	2.09±0.69	37.73±2.99	0.66	27.22±3.57	19.19±1.43	0.93
HS (NAWM)	2.74±0.94	23.83±3.10	0.74	22.62±3.00	17.47±1.40	0.96

Tab.1: Na tissue parameters estimated in HS and patient.

	T*_2f/T*_2f,HS	T*_2s/T*_2s,HS	ISMF/ISMF_HS	c_T/c_T,HS	c_in/c_in,HS	ISVF/ISVF_HS
lesion	0.21	1.09	0.89	1.75	1.66	0.94
NAWM	0.76	1.58	0.89	1.20	1.10	0.97

Tab.2: Na tissue parameter ratios comparing lesion and NAWM of the patient to NAWM of a HS.

Discussion/Conclusion: In line with previous work, the MS patient showed a distinct relative increase of TSC within both the lesion and NAWM (3). This change can originate from processes, which cannot be separated by measuring total Na alone. The enhanced SISTINA sequence enables estimation of relaxation times in tissue and extends previous QF approaches by providing complementary Na parameters in one acquisition (4). Our results suggest an increased intracellular concentration in MS patients with a corresponding increase in regional T^*_{2s} value, which may be due to increased Na entry into axons via voltage gated channels or reduced excretion by the Na/K pump.

The enhanced SISTINA sequence was applied at 7T in an MS patient and a HS, and the simultaneous estimation of relaxation times and relative Na concentration was achieved. This may increase the precision of multi-compartment assessments in sodium MRI of MS.

References:

1. Worthoff, Shymanskaya, Shah. MRM 2019;81(1):303–315.
2. Jenkinson, et al. Neuroimage 2002;17(2):825–841.
3. Inglese, et al. Brain 2010;133(3):847–857.
4. Petracca, et al. Brain 2016;139(3):795–806.

L04.12

Structural connectivity assessment in Diabetes Mellitus type 2: a DKI study

R. Loução, A.-M. Oros-Peusquens, N. J. Shah
Forschungszentrum Jülich, Institute of Neurosciences and Medicine 4, Jülich, GERMANY

Purpose/Introduction: Type II diabetes mellitus (T2DM) is a metabolic disorder associated with obesity. The characteristic high blood glucose levels seen in diabetics have been shown to affect the underlying tissue microstructure of the brain[1, 2, 3], and therefore, alterations in the brain's structural network can be expected.

In this initial study, we aim to assess changes in the structural network of the brain as a consequence of T2DM using diffusion kurtosis imaging (DKI), network-based statistics[4] (NBS) and graph topological metrics.

Subjects and Methods: Data sets were selected from the 1000BRAINS[5] population-based cohort, a study investigating ageing. Seven subjects with previously undiagnosed T2DM were matched with seven age, gender and education control subjects unaffected by T2DM (all male, age = 69.6 ± 5.5 and 67.3 ± 5.8, respectively). All subjects were scanned twice, with a 2-year interval, resulting in 4 data groups (controls and T2DM, 1st and 2nd time points). MRI at 3T included T1-weighted MPRAGE and a DKI acquisition, as described in 4.

Brain parcellation was performed using Freesurfer[6] on the T1 data, from which 97 ROIs were selected, and later registered to diffusion images using affine transformation[7]. Diffusion weighted images were processed using DKIu[8], with a DKI-based tractography reconstruction[9].

The metrics analysed included the local metrics node degree, clustering coefficient, and betweenness centrality; and the global metrics small worldness and global efficiency[10].

Network comparison was performed using NBS. Node level statistics were performed using the Mann–Whitney U test.

Results: Figure 1 shows a glass brain representation of the regions with significant changes in local metrics between the two groups (red for increase, blue for decrease), for both time points. A number of cortical regions were identified.

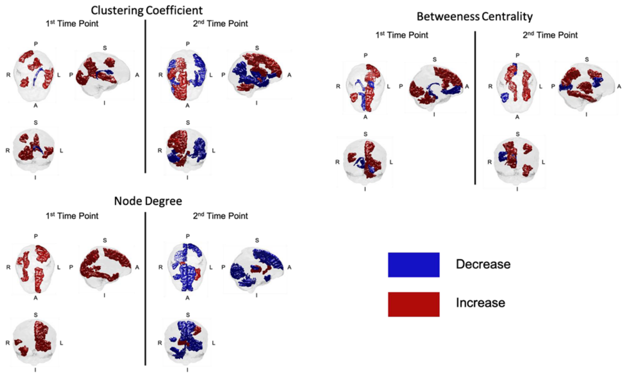

Figure 1 – Glass brain representation of regions of altered local connectivity metrics. A – anterior; P – posterior; S – superior; I – inferior; L – left; R – right.

Global metrics are summarised in Table 1 and did not differ significantly between the groups and the time points. NBS analysis showed no significant changes when comparing between the groups at the 1st time point. A trend towards significance was observed ($p < 0.1$) at the 2nd time point.

	1st time point		2nd time point	
	Controls	T2DM	Controls	T2DM
Small Worldness	3.21 ± 0.58	3.44 ± 0.30	3.42 ± 0.48	3.50 ± 0.19
Global Efficiency	0.34 ± 0.02	0.32 ± 0.03	0.34 ± 0.02	0.32 ± 0.04

Table I - Global metrics. Neither small wordlness nor global efficiency showed statistically significant differences.

Discussion/Conclusion: This initial study suggests T2DM has an impact on the structural network of the brain, as evidenced by local changes in its topological metrics. No significant global changes were found with NBS analysis, small worldness or global efficiency, at either time point.

Investigating a larger cohort over a longer time period would allow one to characterise the interplay between structural and functional alterations within a connectivity framework.

References:

1.DeJong RN Postgrad Med. 1977 2.Oros-Peusquens AM et al. Proc.ISMRM 2018 3.Xie Y et Am J Neurorad 2017 4.Zalesky A et al. NeuroImage 2010 5.Caspers S et al. Frontiers in AN, 2014 6.Fischl B et al. Neuron 2002 7.Jenkinson M et al. NeuroImage 2002 8.Neto-Henriques et al. MAGMA 2015 9.Lazar M et al. MRM 10.Rubinov M, Sporns O, NeuroImage 2010.

L04.13

Body mass index and longitudinal change of brain volume, disability and cognition in relapsing–remitting multiple sclerosis

R. Meijboom[1], M. Valdés Hernández[1], N. White[1], S. Wiseman[1], E. York[1], S. Colville[2], S. Chandran[2], P. Connick[2], A. Waldman[1]
[1]University of Edinburgh, Edinburgh Imaging, Centre for Clinical Brain Sciences, Edinburgh, UNITED KINGDOM, [2]University of Edinburgh, Anne Rowling Regenerative Neurology Clinic, Centre for Clinical Brain Sciences, Edinburgh, UNITED KINGDOM

Purpose/Introduction: Multiple sclerosis (MS) is a chronic neuroinflammatory disease of the central nervous system resulting in a range of deficits including mobility, visual and cognitive impairment. Disease course is relapsing and remitting (RRMS) in 85–90% of cases. MS aetiology is poorly understood. Obesity or high body mass index (BMI) has been suggested as a risk factor for developing MS, although current evidence for the effect of BMI on MS-related abnormalities, such as changes in brain grey (GM) and white matter (WM), and worsening of cognition and disability, is contradictory. Some studies have shown associations between BMI and the expanded disability status scale (EDSS) or volume changes in brain GM, but others report negative findings.[1, 2, 3, 4] Effects on cognition are underexplored, although one study reports an association between self-perceived cognitive change and high BMI. [5] As BMI is modifiable, its impact on disease severity in MS should be further elucidated. Here we investigate the associations between BMI and longitudinal change of disability, cognition and brain volume in RRMS patients.

Subjects and Methods: Twenty RRMS patients (mean age: 39.7 years, 6 males; mean disease duration 4.3 years) were recruited as part of FutureMS, a Scottish multi-centre longitudinal study in RRMS. Participants underwent T1w, T2w and FLAIR magnetic resonance (MR) imaging on the same 3T Siemens Verio scanner; and completed the EDSS and symbol digit modality test (SDMT), at baseline and 1-year follow-up. Cerebral and cerebellar GM and normal-appearing WM (NAWM) volumes were extracted using a combination of FSL5.01, Freesurfer6.0 and in-house software. Change over time was calculated for all measures. Pearson partial correlational analysis was performed for baseline BMI with change in cerebellar and cerebral GM volume, NAWM volume, EDSS and SDMT score; adjusted for age, gender, BMI change and disease duration (SPSS22). Results are uncorrected for multiple comparisons (SPSS22).

Results: Eleven patients had normal weight, five were overweight and four were obese according to BMI criteria. Baseline BMI correlated positively with cerebellar GM volume change, and negatively with EDSS score change, with and without adjustment (Table 1, Fig. 1). No significant correlations were observed between baseline BMI and change in SDMT, cerebral GM and NAWM volume.

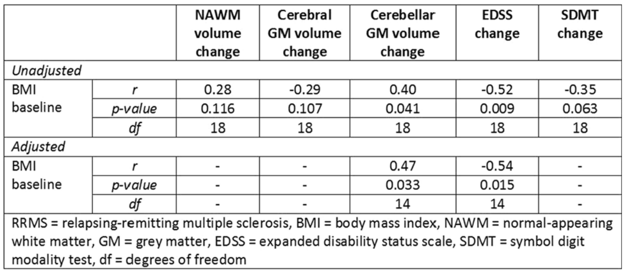

		NAWM volume change	Cerebral GM volume change	Cerebellar GM volume change	EDSS change	SDMT change
Unadjusted						
BMI baseline	*r*	0.28	-0.29	0.40	-0.52	-0.35
	p-value	0.116	0.107	0.041	0.009	0.063
	df	18	18	18	18	18
Adjusted						
BMI baseline	*r*	-	-	0.47	-0.54	-
	p-value	-	-	0.033	0.015	-
	df	-	-	14	14	-

RRMS = relapsing-remitting multiple sclerosis, BMI = body mass index, NAWM = normal-appearing white matter, GM = grey matter, EDSS = expanded disability status scale, SDMT = symbol digit modality test, df = degrees of freedom

Correlations between baseline BMI and changes (baseline - follow-up) in brain volume, disability and cognition in RRMS patients; with and without adjustment for age, gender, disease duration and BMI change.

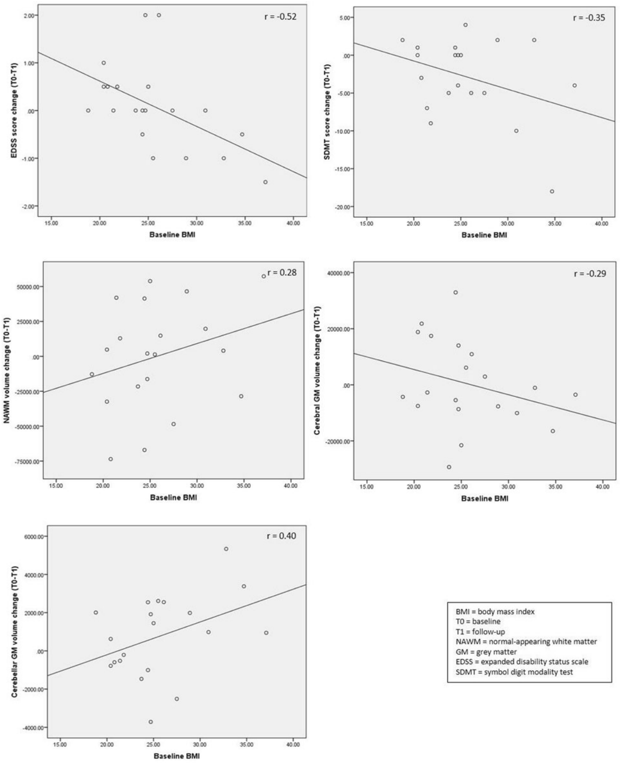

Unadjusted correlations between baseline body mass index and changes (baseline – follow-up) in brain volume, disability and cognition in relapsing-remitting multiple sclerosis patients.

Discussion/Conclusion: Higher baseline BMI in RRMS is associated with greater cerebellar GM volume loss and worsening of general disability. These preliminary results suggest that low BMI may be important for slower disease progression in RRMS. Our next efforts are directed at expanding the study of BMI to the wider FutureMS sample (N = 440) and also examining the effects of BMI on WM lesions and advanced MR measures of myelin integrity.

References:

[1]Zanzam 2019 Mult Scler Relat Disord.
[2]Coban 2015 Obes Res Clin Pract.
[3]Mowry 2018 Neurology.
[4]Graetz 2019 Mult Scler.
[5]Jelinek 2019 Eur J Neurol.

L04.14

Hypersense acceleration mantras: clinical applications what every resident must know

R. Vadapalli[1], A. S. Vadapalli[2], R. B. Annamraju[3], R. D. Mulukutla[4]
[1]Vijaya Diagnostics, Radiology, Hyderabad, INDIA, [2]Medway Maritime Hospital Windmill Road Gillingham Kent, Orthopaedic surgery, Hyderabad 500020, INDIA, [3]GE Healthcare, Digital innovations in affordable care, Bangalore, INDIA, [4]Udai Omni Hospitals, Spine surgery, Hyderabad, INDIA

Purpose/Introduction: To evaluate the role of Hyper Sense based acceleration based fast sequences in clinical Neuro, Spine and MSK practice

Subjects and Methods: To evaluate Hypersense based cube sequences we have examined 200 patients in the age group of 19–63 years with M:F ratio of 2;3 referred to our centre for various clinical indications for Neuro, MSK and Spine Imaging. The region-specific protocols have been supplemented with the hyper sense based 3D CUBE FLAIR and3D CUBE FLEX sequences after a Waiver from ERB with an additional time penalty of 4 min with the following sequence parameters:TR 6402 TE 138(ef) Ec:1, TI:1785 slice thickness:1 mm, Hyper SENSE acceleration 24 channel head and Spine coil and 16 channel knee coil with NEX of 1 and acquisition time of 2.42 min. The Clinical Impact of sequence in terms of diagnostic Aid, morphologic legibility, image quality, were rated by two independent expert Radiologists by Liekart's scale of 1 to 5. The problem specific sensitivity and specificity were calculated, the interobserver variability was recorded by Cohen's kappa statistics.

Results: 3D Hyper CUBE sequences provided high spatial resolution and speeded up the acquisitions for accurate detection of epileptogenic substrates with a sensitivity of 98 per cent and specificity of 89 per cent.in epilepsy imaging especially in refractory epilepsy with Liekart's scale rating of 4. 3D T1 Hyper sense sequences showed high sensitivity and specificity in dementia imaging with accurate detection of atrophy characteristics and volume analysis (9-0 per cent sensitivity 83 per cent specificity and Liekart scale of 4. 3D CUBE FLEX yielded excellent results for lumbosacral plexus with excellent image quality with Liekarts rating of 5. In MSK imaging the knee joint and hip joint and wrist, Ankle imaging showed a rating of 4 with excellent image quality. The interobserver variability was acceptable and is found to be between 0.9 and 0.9.z

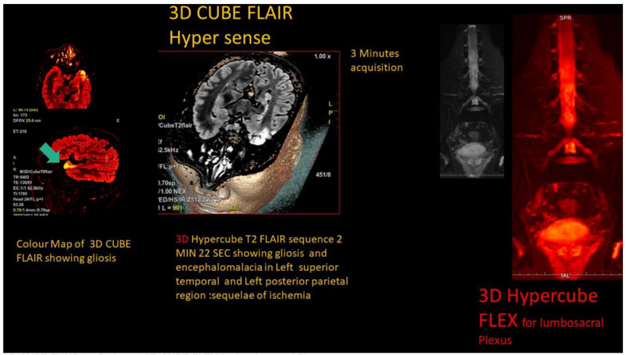

3D CUBE FLAIR for Brain and #D CUBE FLEX for Lumbosacral Plexus

Discussion/Conclusion: Ultrafast volume sequence in technically challenged anatomies with no SNR Penalties with the capability of MPR reconstruction and post-processing in other anatomical planes This novel acceleration technique of Hyper sense offers a high spatial resolution, Fast Imaging times and good image contrast for various anatomical regions acquiring 3D volume sequences using in Neuro, MSK and Spine and Brachial plexus imaging.

This novel acceleration technique of Hyper sense offers a high spatial resolution, Fast Imaging times and good image contrast for various anatomical regions acquiring 3D volume sequences using in Neuro, MSK and Spine and Brachial and Lumbosacral plexus imaging.

References:

1. Lustig M, Donoho D, Pauly JM. Sparse MRI: The Application of Compressed Sensing for Rapid MR Imaging. Magnetic Resonance in Medicine, 2007; 58:1182–1195. https://doi.org/10.1002/mrm.21391.

L04.15

Some MR-Elastography pitfalls at low and high frequency in the human brain

F. Andoh[1], M. Tardieu[1], C. Pellot-Barakat[2], X. Maître[1]
[1]IR4 M, CNRS, Univ. Paris-Sud, Université Paris-Saclay, Orsay, FRANCE, [2]Inserm, CEA, CNRS, Univ. Paris-Sud, Université Paris-Saclay, IMIV, Orsay, FRANCE

Purpose/Introduction: Brain MR-Elastography is usually performed in humans with 3 mm isotropic voxels at low mechanical excitation frequency, between 40 Hz and 60 Hz, to ease wave propagation deep inside the organ. Reported overall mean shear elasticity modulus expectedly increased from 2 kPa at 40 Hz to 2.5 kPa at 60 Hz [1] [2]. Yet, MRE quantitation is highly conditioned by data quality Q and sampling as 6 to 9 voxels per wavelength were found optimal in isotropic and homogeneous media to produce valid mechanical parameters [3]. Here, comparative *low* and *high* frequency whole brain MRE was investigated voxel-by-voxel to explicit the relationship between Q, data sampling, excitation frequency and some pitfalls of the technique.

Subjects and Methods: Shear waves were generated in the brain at 45 Hz and 113 Hz by pressure waves guided into the buccal cavity[4]. Displacement fields were acquired for the same volunteer in a 1.5 T Achieva system (Philips, Netherlands) with parameters reported in Table 1.

SequenceType	Excitation Frequency (Hz)	Encoding Frequency (Hz)	Encoding Gradient (mT·m-1)	FOV (mm3)	Voxels Size (mm3)	TE/TR (ms)	Sensibility (mrad·μm-1)	Time samples
Gradient Echo	45	140	21	216×140×172	2.70×2.70×2.70	583 / 9.2	12	4
Spin Echo	113	113	21	220×210×90	2.75×2.75×2.75	35/58	62	8

Table 1: Acquisition Parameters

Maps of shear dynamic and loss moduli, G_d and G_l, were extracted from the three motion-encoding directions by inversion of the Helmoltz equation of the rotational displacement field, **q**. Data quality maps, $Q = q/\Delta q$, were calculated according to [3]. T_1-weighted image was used as anatomical reference and was segmented with SPM12 (*UCL, United-Kingdom*) to infer masks of grey and white matters after removal of CSF, bone and background tissue. Correlation coefficients, $R_{45\ Hz}$ and $R_{113\ Hz}$, between Q and G_d, were calculated to quantify the influence of data quality.

Results: Q, G_d, and G_l maps are represented for a slice along the three directions on ***Fig. 1 and Fig. 2***. Mean G_d and G_l increase with the frequency excitation in the brain parenchyma : from $< Gd >_{45Hz} = 0.72 \pm 0.31$ kPa to $< Gd >_{113Hz} = 3.26 \pm 0.78$ kPa and from $< Gl >_{45Hz} = 0.55 \pm 0.25$ kPa to $< Gl >_{113Hz} = 1.98 \pm 0.56$ kPa without any significant mechanical difference between white and grey matters. Elsewhere, Q is rather homogenous at 45 Hz whereas, despite much higher values at the periphery of the cerebral hemispheres and cerebellum, Q falls deep inside the brain at 113 Hz. However, at 45 Hz, apart in the cerebellum where $Q > 100$, G_d and G_l appear highly correlated to Q ($R_{45Hz} = 0.70$), contrary to data at 113 Hz ($R_{113Hz} = 0.26$).

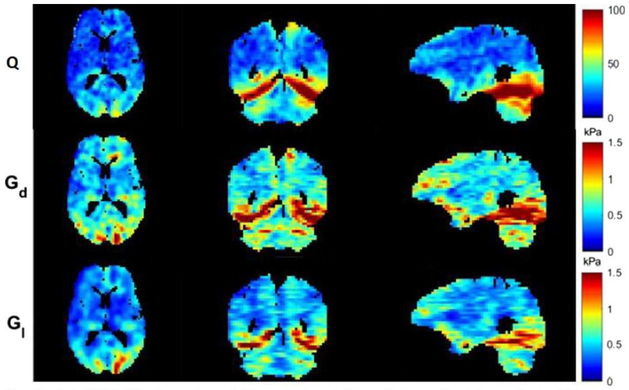

Figure 2.a: Brain MRE at 45 Hz: Q maps (top row), Gd maps (centre row), Gl maps (bottom row) in axial, coronal, and sagittal orientation. The colour scale is limited to exhibit the pattern of each parameter.

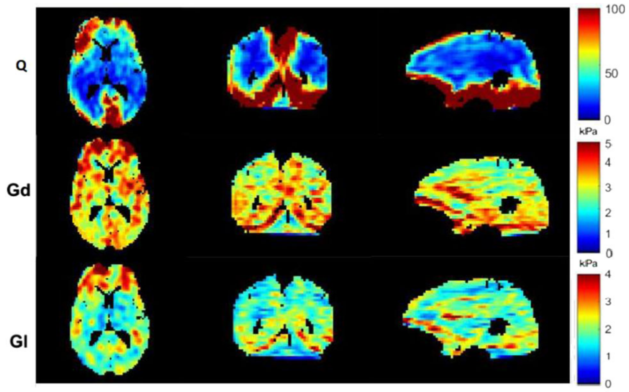

Figure 2.b: Brain MRE at 113 Hz: Q maps (top row); Gd maps (centre row); Gl maps (bottom row) in axial, coronal, and sagittal orientation. The colour scale is limited to exhibit the pattern of each parameter.

Discussion/Conclusion: Precision and accuracy of MRE data are obliterated at 45 Hz by poorer shear wave sampling $(\lambda/a)_{45\mathrm{Hz}} = 10$ and $(\lambda/a)_{113\mathrm{Hz}} = 6$. Thus, lower frequency data require higher *Q* value, which is partly achieved, exemplarily in the cerebellum here. Higher frequency data, despite larger *Q* inhomogeneity, present patterns that depart from *Q* and therefore brain viscoelasticity is effectively provided nearly everywhere with optimal precision and accuracy.

References:

[1] I. Sack et al., *PLoS ONE*, 2011.
[2] A. Arani et al., NeuroImage, 2015.
[3] J. Yue et al. Phys. Med. Biol. 2017.
[4] M. Tardieu, PhD thesis, Univ. Paris-Sud 2014.

L04.16

Cerebrospinal fluid and blood flow disturbances in the development of cognitive impairment in cerebral small vessel disease

L. Dobrynina[1], B. Akhmetzyanov[2], Z. Gadzhieva[1], **E. Kremneva**[3], L. Kalashnikova[1], M. Krotenkova[3]
[1]Research center of neurology, Neurology, Moscow, RUSSIAN FEDERATION, [2]Medical and Rehabilitation center, Radiology, Moscow, RUSSIAN FEDERATION, [3]Research center of neurology, Neuroradiology, Moscow, RUSSIAN FEDERATION

Purpose/Introduction: Sporadic small vessel disease, sSVD, is the main cause of vascular cognitive impairment (CI) and the leading cause of mixed dementia. The objective of our research was to assess the role of arterial, venous blood flow and CSF flow and their relationships in the development of CI in sSVD patients.

Subjects and Methods: 96 patients (64 female, mean age—60.6 ± 6.3 years) with cognitive complains and sSVD according to STRIVE criteria based on conventional 3T MRI were included into the study. Cognitive tests (MoCA, 10 words learning test, Trail Making Test B-A) and ADL scale were performed to assess cognitive domains and daily living independence. The phase-contrast MRI (PC-MRI, 3 T scanner) was used to measure blood flow in the internal carotid and vertebral arteries (the total arterial blood flow was taken into account) and internal jugular veins (level of C2-C3 vertebrae), in the straight and superior sagittal sinuses; CSF flow in aqueduct (Figs. 1–3). The indices of arterial pulsatility and intracranial compliance were calculated.

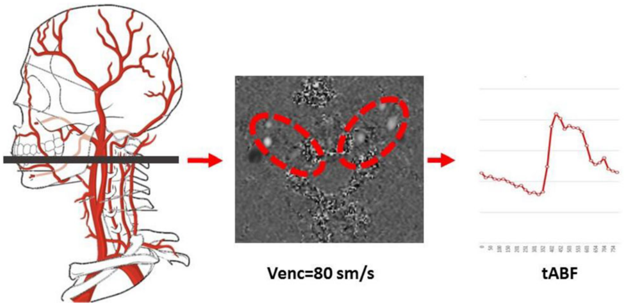

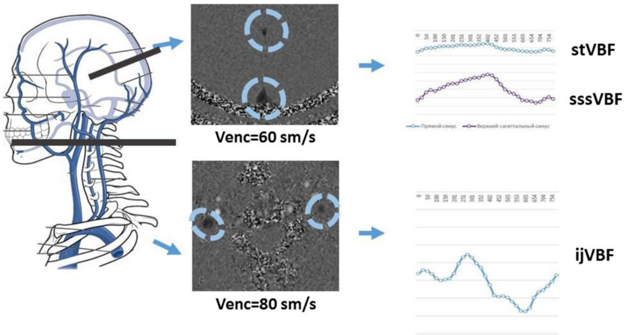

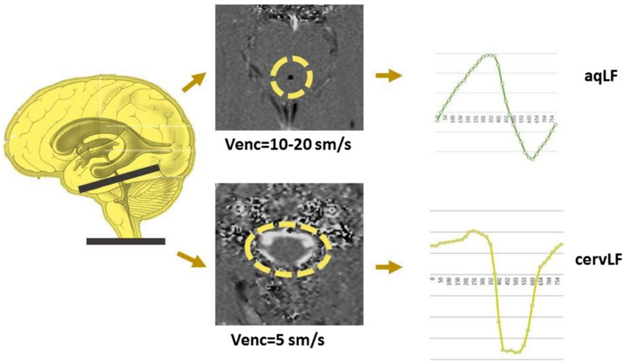

Results: Dementia and severe memory impairment were associated with an increase of arterial pulsatility index, the intracranial compliance index and the aqueduct CSF flow; severe impairment of executive function was additionally associated with a decrease in arterial blood flow, venous blood flow in the straight and superior sagittal sinuses. Parameters of blood flow and CSF flow were interrelated, the arterial pulsation index had an influence on all parameters.

Discussion/Conclusion: PC-MRI is simple and rapid way of performing non-invasive evaluation of vascular and CSF flow and their dynamic coupling in sSVD patients throughout disease progression. Features of changes in blood flow and CSF flow and their interconnections in patients with CI due to sSVD suggest the pathogenetic significance of impaired hydrodynamic processes in brain damage and development of CI in sSVD.

References:

1. Gorelick P.B., Scuter A., Black S.E. et al. Vascular contributions to cognitive impairment and dementia: a statement for healthcare professionals from the American Heart Association/American Stroke Association. Stroke 2011; 42: 2672–2713. https://doi.org/10.1161/str.0b013e3182299496.

2. Deramacourt V., Slade J.Y., Oakley A.E. et al. Staging and natural history of cerebrovascular pathology in dementia. Neurology 2012; 78: 1043–1050. https://doi.org/10.1212/wnl.0b013e31824e8e7f.

3. Wardlaw J.M., Smith E.E., Biessels G.J. et al. Neuroimaging standards for research into small vessel disease and its contribution to ageing and neurodegeneration. Lancet Neurol 2013; 12: 822–38. https://doi.org/10.1016/s1474-4422(13)70124-8.

4. Jolly T.A.D., Bateman G.A., Levi C.R. et al. Early detection of microstructural white matter changes associated with arterial pulsatility. Front Hum Neurosci. 2013. 7: 782. https://doi.org/10.3389/fnhum.2013.00782.

L04.17

Optimization of scanning conditions to detect trace concentrations of gadolinium with a heavy T2 FLAIR sequence

Y. Sato[1], N. Hayashi[2], T. Maruyama[3], K. Ujita[1], T. Suto[1], H. Watanabe[2], A. Ogura[2], Y. Tsushima[4]

[1]Gunma University Hospital, Department of Radiology, Maebashi, JAPAN, [2]Gunma Prefectural College of Health Sciences, Department of Radiological Technology, Maebashi, JAPAN, [3]Shinshu University Hospital, Department of Radiology, Matsumoto, JAPAN, [4]Gunma University Graduate School of Medicine, Department of Diagnostic Radiology and Nuclear Medicine, Maebashi, JAPAN

Purpose/Introduction: Contrast-enhanced MRI expands the range of signal intensities detected during examination and permits revealing several pathologic processes, including inflammation, infection, and malignancy, that would be undetectable with unenhanced MRI or other imaging modalities[1]. However, several studies have shown gadolinium deposition in the brain of patients administered gadolinium-based contrast agents[1, 2]. Imaging of low-concentration gadolinium is important to reveal the physiological mechanisms of gadolinium deposition. Previous studies have reported that a heavy T2 FLAIR sequence may be useful for the visualization of low concentrations of gadolinium[3]. However, optimization of the scanning conditions is insufficient for the detection of very small amounts of deposited gadolinium in the brain because these studies focused on the inner ear. Therefore, we conducted a phantom study to clarify the characteristics of the heavy T2 FLAIR sequence and optimization of TI and TE.

Subjects and Methods: We created a phantom using a plastic container filled with diluted gadobutrol (Gd-BTDO3A) and distilled water. The dilution was repeated to create 16 phantoms with concentrations ranging from 0.06 to 2000 μmol/L. In addition, three brain tissue phantoms with T1 and T2 values close to white matter, gray matter, and CSF were created. The heavy T2 FLAIR images were acquired changing the scanning conditions using a 1.5 T MRI scanner. TI was changed from 1500 to 2500 ms to clarify the null point of the CSF phantom. TE was changed in 100 ms increments from 200 to 1000 ms. TR was 8500 ms, slice thickness was 8 mm, FOV was 128 × 128 mm, and matrix size was 256 × 256. The acquired images were evaluated with the SNR of each gadolinium phantom center and the CNR between the gadolinium phantoms and CSF phantom.

Results: The signal intensity of the CSF phantom was null when TI was 1900 ms. In the heavy T2 FLAIR images acquired while changing the TE, differences in signal intensity of the gadolinium phantoms and CSF phantom were observed up to 4 μmol/L when the TE was 300 ms or longer. Moreover, the peak of the signal intensity shifted to the low concentration side when TE was prolonged. The CNR was at the maximum when the TE was 500 ms.

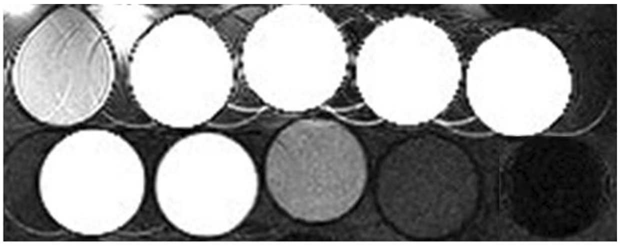

1040 μM	520 μM	260 μM	130 μM	65 μM
32.5 μM	16 μM	8 μM	4 μM	CSF

The heavy T2 FLAIR images of 9 gadolinium phantoms with concentrations ranging from 4 to 1040 μmol/L and CSF phantom when TE was set to 500 ms. The gadolinium phantoms were high signal intensity while the signal intensity of CSF phantom was null.

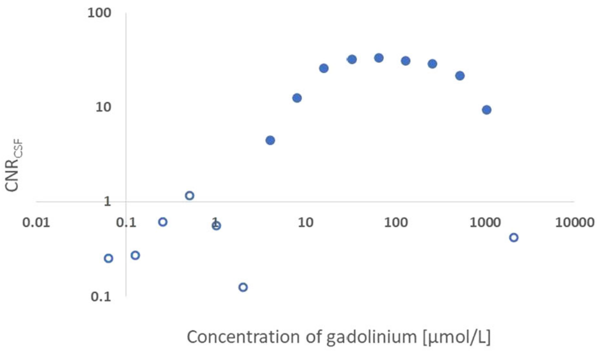

The CNR between the CSF phantom and the diluted gadolinium phantoms when TE was set to 500 ms. The CNR was greater than 1 when the concentration was 4 μmol/L or higher. It was possible to image up to 4 μmol/L using the heavy T2 FLAIR sequences.

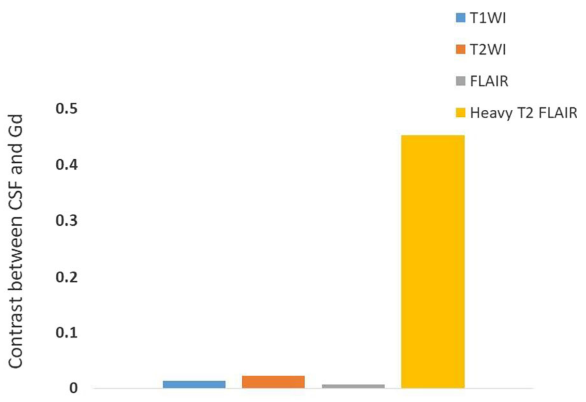

The contrast between the CSF phantom and the 4 μmol/L gadolinium phantoms. The heavy T2 FLAIR sequence when TE was set to 500 ms showed higher contrast than the conventional MRI.

Discussion/Conclusion: It was possible to image a low concentration of approximately 4 μmol/L using the heavy T2 FLAIR sequence. The CNR between the CSF phantom and the diluted gadolinium phantoms showed the highest value when TE was set to 500 ms. Imaging of low concentrations of gadolinium contributes to the elucidation of the physiological mechanism of gadolinium deposition. Furthermore, it may also contribute to the elucidation of the glyptic system that is considered to be involved in gadolinium deposition.

References:

1. McDonald RJ, et al. Radiology. 2015 Jun;275(3):772–82.
2. Kanda T, et al. Radiology. 2014 Mar;270(3):834–41.
3. Naganawa S, K et al. Magn Reson Med Sci. 2010;9(2):73–80.4.

L04.18

Brain activation evaluation and mental health correlations in patients with schizophrenia underwent a stem cells therapy

D. Ustyuzhanin[1], Y. Morozova[1], M. Shariya[1], A. Smulevich[2], V. Smirnov[1], S. Ternovoy[3]

[1]National Medical Research Center of Cardiology, Moscow, RUSSIAN FEDERATION, [2]Mental Health Research Center, Moscow, RUSSIAN FEDERATION, [3]Sechenov First Moscow State Medical University, Moscow, RUSSIAN FEDERATION

Purpose/Introduction: To evaluate the brain activation patterns using fMRI in patients with schizophrenia underwent a stem cells therapy, and to compare the activations zones with PANSS test.

Subjects and Methods: 15 patients (males, aged 30 ± 5 years) with schizophrenia were included in the study. Remission of schizophrenia with a predominance of asthenic disorders was confirmed by psychiatry examination. Patients received intravenous infusions of umbilical cord blood cells at the average dose of 250 × 106 viable cells per infusion (4 injections at 2 week intervals). Patients also received standard neuroleptics therapy in maintenance doses.

A functional MRI scans (3.0 T MRI scanner with standard phased array head coil) with continuous subtraction from 100 by 7 paradigm were performed in 2 points (before and in 3 months after treatment). SPM12 (the Functional Imaging Laboratory, University College, London) was used for data processing and analysis. Mental health clinical evaluation was performed by the scale of positive and negative symptoms of schizophrenia (PANSS) test.

Results: PANSS test showed significant improvement between before and after treatment points in following parameters: difficulty in abstract thinking ($p < 0.02$), somatic concern ($p < 0.05$), anxiety ($p < 0.01$), tension ($p < 0.01$), guilt feelings ($p < 0.01$), depression ($p < 0.001$), motor retardation ($p < 0.05$), poor attention ($p < 0.001$), disturbance of volition ($p < 0.01$), active social avoidance ($p < 0.01$). Before the treatment fMRI revealed a significant correlation of PANSS difficulty in abstract thinking parameter with brain activation in MNI -12, -52, 30 (left posterior cingulate gyrus) volume ($p_{\text{uncorected}} < 0.02$, cluster level).

After treatment we found a significant correlation of PANSS difficulty in abstract thinking parameter with 3 volumes: MNI 46, -38, 20 (right insula), $p_{\text{uncorected}} < 0.05$; MNI 0, 0, -6 (right sublobar white matter), $p_{\text{uncorected}} < 0.02$; MNI 52, 6, 8 (right precentral gyrus), $p_{\text{uncorected}} < 0.02$.

Discussion/Conclusion: Functional MRI revealed significant changes in brain activation patterns in patients with schizophrenia underwent a stem cells therapy with significant correlations with PANSS difficulty in abstract thinking parameter. This data is important for further evaluation of the pathophysiology of stem cell exposure in patients with schizophrenia.

References:

Castro MN, Villarreal MF, Bolotinsky N et al. Brain activation induced by psychological stress in patients with schizophrenia. Schizophr Res. 2015 Oct;168(1-2):313–21.
Moslem M, Olive J, Falk A. Stem cell models of schizophrenia, what have we learned and what is the potential? Schizophr Res. 2018 Dec 23. pii: S0920-9964(18)30719-9.
Liu Q, Du J, Fan J et al. Generation and Characterization of Induced Pluripotent Stem Cells from Mononuclear Cells in Schizophrenic Patients. Cell J. 2019 Jul;21(2):161–168.

L04.19

Vascular reactivity measured with high temporal resolution fMRI in hereditary and sporadic CAA

T. van Harten[1], S. Voigt[2], E. Koemans[2], S. van Rooden[1], M. van Buchem[1], J. Zwanenburg[3], M. Walderveen[1], M. Wermer[2], M. van Osch[1]

[1]Leiden University Medical Center, Radiology, Leiden, NETHERLANDS, [2]Leiden University Medical Center, Neurology, Leiden, NETHERLANDS, [3]University Medical Center Utrecht, Radiology, Utrecht, NETHERLANDS

Purpose/Introduction: Recent studies have shown that vascular reactivity measurements by functional Magnetic Resonance Imaging (fMRI) with a visual stimulus are a potential marker for hereditary (HCHWA-D) [1] and sporadic cerebral amyloid angiopathy (CAA).[2] To further sensitize and specify these reactivity measurements, ultra-high field MRI with a higher temporal resolution of 100 ms in combination with a shorter stimulus duration and a longer rest period may be used.

Subjects and Methods: To compare the new high temporal resolution protocol at 7T with the conventional method at 3T, three scans were made on the same day: 1) "3T_28 s": 3T MRI (17 slices, TE = 38 ms, 6 min) with a 28 s long stimulus and TR = 1500 ms; 2) "7T_28 s": 7T MRI (17 slices, TE = 22 ms, 6 min) with a 28 s long stimulus and TR = 1500 s; and 3) "7T_3 s": (1 slice, TE = 22 ms, 6 min) with a 3 s stimulus and TR = 100 ms. fMRI scans with the long stimulus timing are stimulated and processed according to the methodology as described previously. [1, 2] The short stimulus data were analysed similarly, but fitted with a double Gaussian instead of a trapezoid.(*1B-D* and *2B-F*). Bland–Altman plots were generated using Matlab. Scans were performed on patients with hereditary (n = 12;

mean age 49 yrs) and sporadic (n = 8; mean age 72 yrs) CAA and 2 healthy controls (only 7T with new protocol, 19 and 58 yrs).

Results: An activation map and fitted responses of a CAA patient are shown in *(1)*. Bland–Altman plots show good agreement of the obtained timing parameters between all three tested scans (*1E-J*), except for the TTP 7T_28 s vs 7T_3 s protocol(*1H*). Paired samples T-test results are shown in *Table 1*.

Preliminary results with the high temporal resolution scan show a marked difference in BOLD response between a healthy control and a sporadic, pre-symptomatic and symptomatic hereditary CAA patient, but not between controls *(2E-F)*. When comparing patients with controls, the TTB, TTP and amplitude were all different *(2G)*.

Discussion/Conclusion: The data shows that 3T and 7T fMRI scans with the same paradigm result in similar timing parameters, albeit a significantly higher amplitude. The high temporal resolution 7T scan in combination with a shorter stimulus duration (3 s vs 28 s) showed a similar TTB and amplitude, but a significantly lower TTP. Moreover, in patients showing a "flat-line" response with the 28 s stimulus, an HRF could be observed with the new 3 s protocol *(2A-B)*. This and the differences in TTP (*1H*), are potentially induced by the longer rest period. A limitation of our study is the small number of control subjects.

In conclusion, this new protocol may provide more sensitive estimations of parameters due to a more reliable fit, as well as provide additional information about the HRF especially in patients with severely disrupted vascular reactivity.

References:

1.Dumas, Ann of neurol, 2012.**72**(1):p.76–81.
2.van Opstal, The Lancet. Neurol, 2017.**16**(2):p.115–122.

L04.20

BOLD-fMRI cerebrovascular reactivity and resting-state fluctuations in Small Vessel Disease

J. Pinto[1], J. Moreira[1], T. Charrua[1], A. Fouto[1], L. Alves[2], S. Calado[2], P. Vilela[3], M. Viana Baptista[2], P. Figueiredo[1]
[1]ISR-Lisboa/LARSyS and Department of Bioengineering, Instituto Superior Técnico, Universidade de Lisboa, Lisbon, PORTUGAL, [2]Neurology Department, Hospital Egas Moniz, Centro Hospitalar de Lisboa Ocidental; CEDOC, Nova Medical School, New University of Lisbon, Lisbon, PORTUGAL, [3]Imaging Department, Hospital da Luz, Lisbon, PORTUGAL

Purpose/Introduction: Cerebral small vessel disease (SVD) is a major vascular contributor to stroke and dementia. BOLD-fMRI has been intensively explored to provide sensitive biomarkers of SVD, in particular through the measurement of cerebrovascular reactivity (CVR) in response to vasoactive stimuli or of spontaneous BOLD fluctuations during resting-state (rs-fMRI). While CVR is decreased [1], rs-fMRI fluctuations might be increased as a consequence of increased cardiac pulsatility [2]. Although the amplitude of CVR and rs-fMRI have been found to be correlated in healthy individuals [3, 4], this relation has not been studied in SVD patients. Here we aim to investigate the relationship between CVR and rs-fMRI in SVD patients.

Subjects and Methods: 17 SVD patients (50 ± 9 years old) were studied on a 3T Siemens scanner. BOLD-fMRI data were acquired (2D-GE-EPI, TR/TE = 2500/30 ms, 40 slices, 3.5 × 3.5 × 3.0 mm^3) during a breath-hold (BH) task (3 cycles of 15 s BH after inspiration, alternated with normal breathing following auditory cues, ~ 5 min) and during resting-state (~ 6.5 min). All data were analyzed using FSL, ANTs and R software. For CVR, after motion-correction and removal of low-frequency drifts, a general linear model (GLM) analysis was performed (regressors of interest: sine and cosine at task frequency and corresponding 1st harmonics), and both the amplitude and the time-to-peak (TTP) of the BH response were computed. For rs-fMRI, after motion-correction, regression of motion parameters, and removal of low-frequency drifts, the fractional amplitude of low frequency fluctuations (fALFF) was computed in the frequency band 0.01–0.10 Hz, as well as in the following frequency sub-bands: fALFF1 (0.01–0.023 Hz), fALFF2 (0.023–0.073 Hz) and fALFF3 (0.073–0.2 Hz). Pairwise Pearson correlation analysis was then performed between the CVR metrics amplitude and TTP and all fALFF metrics, averaged across gray matter (GM) and normal appearing white matter (NAWM).

Results: Statistically significant correlations ($p < 0.05$) were found between CVR-TTP in both GM and NAWM and fALFF metrics in NAWM, as depicted in Fig. 1. This correlation is determined mostly by the lowest frequencies (fALFF1, Fig. 1). No significant correlations were found between the CVR amplitude and fALFF metrics.

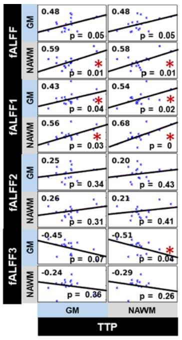

Fig.1: Pearson correlation between CVR-TTP and the fALFF metrics in SVD patients in both GM and NAWM tissues. Correlation coefficients are displayed on top left of each plot. Significant correlations are in indicated with *.

Discussion/Conclusion: We observed that the amplitude of low–frequency fluctuations in rs-fMRI across SVD patients is significantly correlated with the latency of their CVR response to a BH task. This relationship might be explained by the previously reported association of SVD with both rs-fMRI fluctuations and CVR latency. Further work is necessary to understand the physiological meaning of these relationships in SVD patients.

Acknowledgements: FCT grants PD/BD/135114/2017, PTDC/BBB-IMG/2137/2012, UID/EEA/50009/2019.

References:

[1] Thrippleton et al. Int J Stroke 13, 2018.
[2] Makedonov et al. PloS One 8, 2013.
[3] Jahanian et al. JCBFM 37, 2016.
[4] Liu et al. NeuroImage 146, 2017.

I17 Teaching Session

15:40–16:40 *Room 1: Willem Burger Zaal*

Diffusion Methods for Gadolinium-Free Imaging

I17.01

Basic Principles and Methods of Microstructural Diffusion as an Alternative to Gadolinium

A. Alberich-Bayarri
La Fe Polytechnics and University Hospital, Biomedical Imaging Research Group, Valencia, SPAIN

Learning Objectives: The goal of the lecture is to understand the basics of diffusion weighted images in MR and how diffusion can be analyzed with different signal models adapting to a variety of tissue microarchitecture characteristics.

Different curve fitting models including monoexponential, bi-exponential intra-voxel incoherent motions (IVIM), diffusion kurtosis imaging (DKI) and stretched exponential diffusion together with diffusion tensor imaging (DTI) techniques and their limitations will be discussed.

Body: Diffusion weighted images can be analyzed with a with a wide range of models in order to gather information acting as surrogate of the one we could obtain with the use of contrast media.

The influence of thte b-values in the stability of the resulting imaging biomarkers will be discussed.

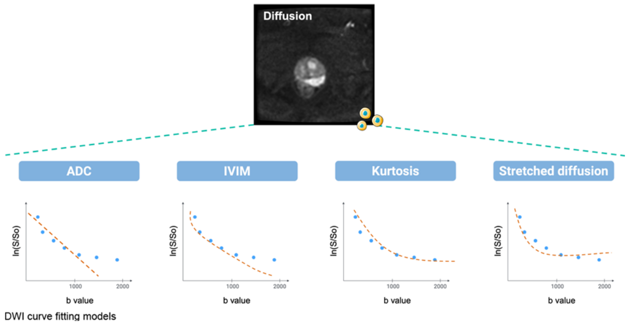

References:

1: Puig J, Blasco G, Schlaug G, Stinear CM, Daunis-I-Estadella P, Biarnes C, Figueras J, Serena J, Hernández-Pérez M, Alberich-Bayarri A, Castellanos M, Liebeskind DS, Demchuk AM, Menon BK, Thomalla G, Nael K, Wintermark M, Pedraza S. Diffusion tensor imaging as a prognostic biomarker for motor recovery and rehabilitation after stroke. Neuroradiology. 2017 Apr;59(4):343–351. https://doi.org/10.1007/s00234-017-1816-0. Epub 2017 Mar 14. Review. PubMed PMID: 28293701.

2: França M, Martí-Bonmatí L, Alberich-Bayarri Á, Oliveira P, Guimaraes S, Oliveira J, Amorim J, Gonzalez JS, Vizcaíno JR, Miranda HP. Evaluation of fibrosis and inflammation in diffuse liver diseases using intravoxel incoherent motion diffusion-weighted MR imaging. Abdom Radiol (NY). 2017 Feb;42(2):468–477. https://doi.org/10.1007/s00261-016-0899-0. PubMed PMID: 27638516.

3: Puig J, Sánchez-González J, Blasco G, Daunis-I-Estadella P, Federau C, Alberich-Bayarri Á, Biarnes C, Nael K, Essig M, Jain R, Wintermark M, Pedraza S. Intravoxel Incoherent Motion Metrics as Potential Biomarkers for Survival in Glioblastoma. PLoS One. 2016 Jul 7;11(7):e0158887. https://doi.org/10.1371/journal.pone.0158887. eCollection 2016. PubMed PMID: 27387822; PubMed Central PMCID: PMC4936699.

S14 Scientific Session

15:40–17:10 *Room 2 - Van Weelde Zaal*

Efficient MR Imaging

S14.02

Real-time sequence control for prospective motion correction in a dynamic, platform-independent MRI framework

D. C. Hoinkiss, C. Cordes, S. Konstandin, J. Huber, R. Wilke, M. Guenther
Fraunhofer MEVIS, MR Physics, Bremen, GERMANY

Purpose/Introduction: Dynamic adaption of the MR sequence during the imaging process is desired in advanced MR applications as used for interventions and prospective motion correction. This is typically based on platform-specific solutions that require a pre-defined execution order and code compilation prior to the scan. In contrast to other platform-independent approaches that require fixed sequence structures (e.g. [1–3]), we developed the dynamic sequence development framework gamma$^{\text{STAR}}$ (γ*) [4–6]. Here, the approach is extended to stream MR sequences in real time, enabling sequence changes during the scan, and demonstrated for the application of prospective motion correction.

Subjects and Methods: The real-time sequence stream buffers only a small number of pre-calculated hardware events while calculating subsequent events (Fig. 1 black). Between these calculation steps, the framework can connect to a websocket server to get possible parameter changes for the next buffer time (Fig. 1 red).

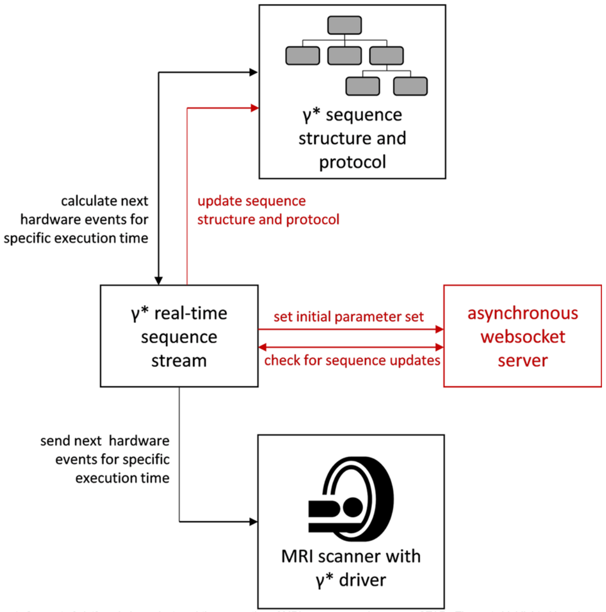

Figure 1. Concept of platform-independent, real-time execution of MRI sequences using gammaSTAR . The parts highlighted in red show the dynamic sequence changes that can be triggered by sending change requests to the asynchronous websocket server.

This concept is utilized to perform prospective motion correction using external image reconstruction (Gadgetron) and image registration (ITK) (Fig. 2). During the scan, the scanner sends the current raw data to an external computer where the subject motion is determined and the new slice position and orientation is transferred to the websocket server where it can be used by the gamma$^{\text{STAR}}$ sequence execution.

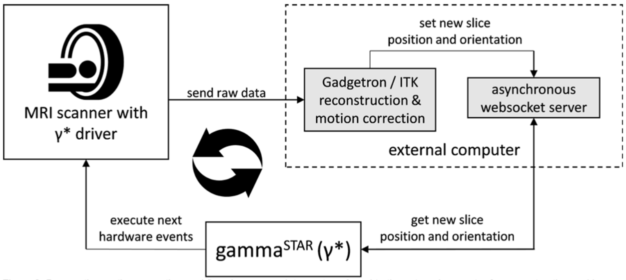

Figure 2. Prospective motion correction workflow: Image raw data are transferred to the external computer for reconstruction and image registration. The new slice information is sent to the websocket server to be used for subsequent hardware events.

For evaluation, a spin-echo EPI sequence was measured while performing image-based, prospective motion correction [7]. Sequence parameters of the sequence were: TR = 3000 ms/TE = 100 ms/12 slices/4 mm isotropic voxel size/100 repetitions/no head restraints. Measurements were performed with and without prospective motion correction at 3 T (MAGNETOM Skyra).

Results: Figure 3 shows the residual motion parameters and image overlays of the performed measurements. The typical long-term subject motion seen when measuring without head restraints (a) is reduced to a low extent when applying prospective motion correction (b).

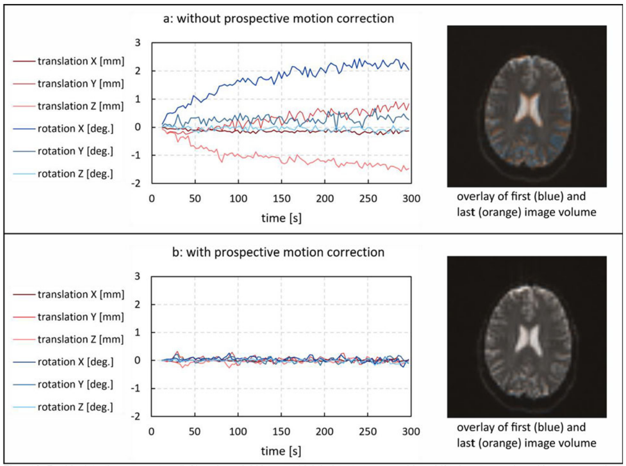

Figure 3. Residual motion parameters (left) and overlaid images (right) show a severe subject drift when measuring without prospective motion correction (a). This effect is reduced by enabling the prospective motion correction (b).

Discussion/Conclusion: We demonstrated an extension to the gamma$^{\text{STAR}}$ framework to allow real-time sequence changes during runtime and the application to prospective motion correction. This concept eliminates the need of synchronization steps between MR sequence and feedback device and could reduce the effort to transfer these otherwise sophisticated sequences to different scanners. The feedback device can be exchanged without changing the sequence behavior or code itself while allowing sequence changes ranging from simple parameter changes to timing and execution order changes.

Acknowledgements: This work was supported by the FhG Internal Programs (Grant No. Attract 142-600172).

References:

1. Magland et al. MRM 2016;75:257–65.
2. Layton et al. MRM 2017;77:1544–52.
3. Nielsen and Noll. MRM 2018;79:3128–34.
4. Archipovas et al. ISMRM 2017:1510.
5. Cordes et al. MRM (under review).
6. https://gamma-star.mevis.fraunhofer.de.
7. Thesen et al. MRM 2000;44:457.

S14.03

Efficient cardiac T_1 mapping using cardiac motion correction at 1.5 T

S. Lukanek[1], J. Schulz-Menger[2], T. Schäffter[1], C. Kolbitsch[1], **K. M. Becker**[1]
[1]Physikalisch-Technische Bundesanstalt (PTB), Braunschweig and Berlin, GERMANY, [2]Working Group on Cardiovascular Magnetic Resonance, Charité, Experimental and Clinical Research Center (ECRC) and Helios Klinikum Berlin Buch, Berlin, GERMANY

Purpose/Introduction: 2D Cardiac T_1 mapping is commonly acquired during a single breath hold (10–17 s). In addition, cardiac triggering is used to limit data acquisition to a small window (10–30% of the cardiac cycle) during the quiescent phase of the cardiac cycle[1]. Cardiac motion correction has been proposed for T_1 mapping to improve acquisition efficiency to 80% of the cardiac cycle[2, 3]. Nevertheless, this method uses a spoiled gradient-echo (sGRE) sequence on a 3T MR scanner, but most clinical cardiac examinations are performed at 1.5T using balanced steady-state free precession (bSSFP) due to the high SNR.

Here we compared a continuous image acquisition combined with cardiac motion correction[2] to achieve high-resolution (1.3 × 1.3 mm^2) T_1 mapping in 8 s at 1.5T using bSSFP and sGRE. T_1 times were evaluated in a T_1 phantom and in a healthy volunteer.

Subjects and Methods: Data was acquired in a commercial T_1 phantom and in a healthy volunteer (male, 25 years) at 1.5T (Siemens Healthineers). A continuous 2D golden-radial trajectory was used and multiple inversions were applied at fixed time intervals during 8 s (bSSFP acquisition: TR/TE = 3.2/1.6 ms, resolution = 1.3 × 1.3 × 8 mm^3, flip angle = 35°, sGRE in phantom: TR/TE = 4.5/2.05 ms, flip angle = 5°, resolution = 2.0 × 2.0 × 8 mm^3 and in vivo: TR/TE = 4.9/2.2 ms, flip angle = 5°, resolution = 1.3 × 1.3 × 8 mm^3 (Fig. 1). Cine images were reconstructed and cardiac motion fields (MF) were determined. For all cardiac phases and cycles, TI images were reconstructed from the same data using iterative SENSE. MF were used to transform all TI images to the same cardiac phase. T_1 maps were fitted pixel-wise. For sGRE, the signal equation is based on Look-Locker and for bSSFP a previously published model was used[4], extended for multiple inversions.

For reference, scans were carried out with 5(3)3 MOLLI (11 s, 1.4 × 1.9 × 7 mm^3). In the phantom, T_1 times were compared to a reference. Myocardial T_1 times (mean ± SD) were assessed in the septum.

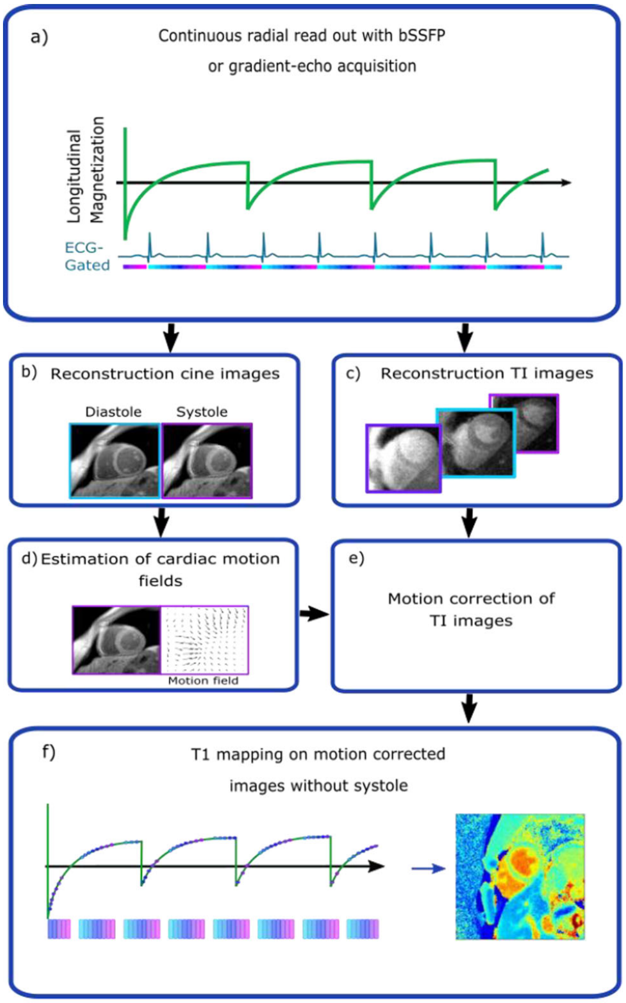

Figure 1. Cardiac motion compensated T1 mapping. a) Acquisition with continuous readout. b,d) Cine images were reconstructed, motion was estimated. c,e) TI images were reconstructed, motion corrected. f) T1 mapping on TI images with 80% of the data.

Results: Figure 2 shows that bSSFP and sGRE led to an accurate estimation of T_1 times with difference of -3.4 ± 6.1%, 4.1 ± 5.2% which were smaller than for MOLLI (6.6 ± 2.8%). Myocardial T_1 times were also comparable between bSSFP and sGRE (1149 ± 52.9 ms, 1142 ± 59.4 ms, respectively) and lower in MOLLI (1000 ± 47.3 ms). The sGRE T_1 map showed fewer artifacts and was more homogeneous than the bSSFP T_1 map, probably due to an acquisition which is less affected by field inhomogeneities, T_2 differences and magnetization transfer effects.

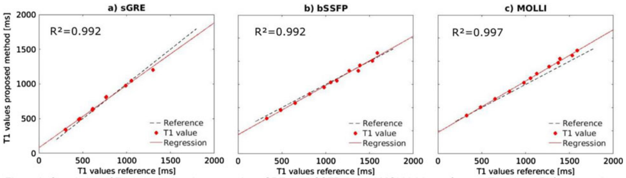

Figure 2. Correlation of T1 times in the phantom using sGRE (a), bSSFP (b) and MOLLI (c) to reference T1 values. Reference values were given by the manufacturer of the T1 phantom.

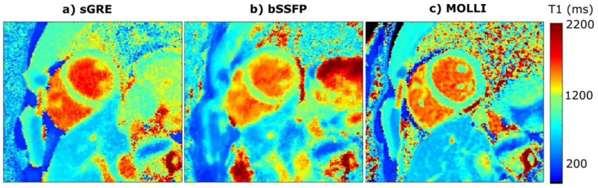

Figure 3. In vivo high-resolution T1 maps at 1.5 T using continuous acquisition with sGRE (a: 1.3x1.3x8mm³, 8s), bSSFP (b: 1.3x1.3x8mm³, 8s). MOLLI (c: 1.4x1.9x7mm³, 11s) for reference.

Discussion/Conclusion: In this study, feasibility for efficient native T1 mapping in 8 s with an in-plane resolution of 1.3 × 1.3 mm^2 at 1.5T was shown, using continuous data acquisition and cardiac motion correction.

References:

[1] Burt, JR, et al. *Radiographics*, 2014, *34*, 377–395.
[2] Becker, KM, et al. Proc. 27th Annual Meeting ISMRM 27, Canada, 2019;779 (in press).
[3] Becker, KM, et al. *MRM*, 2019, *81*, 1080–1091.
[4] Schmitt, P, et al. 2004, *MRM*, *51*, 661–667.

S14.04

3D Cartesian whole-heart CINE MRI exploiting patch-based spatial and temporal redundancies

T. Kuestner[1], A. Bustin[1], R. Neji[2], R. Botnar[1], C. Prieto[1]
[1]King's College London, London, UNITED KINGDOM, [2]MR Research Collaborations, Siemens Healthcare Limited, Frimley, UNITED KINGDOM

Purpose/Introduction: CINE MRI is the gold standard for the assessment of cardiac function. Conventionally, multi-slice 2D CINE is performed under multiple breath-holds to achieve left ventricular (LV) coverage. However, slice misalignments due to different breath-hold positions may lead to erroneous assessment of ventricular volume[1]. Moreover, due to anisotropic resolution multiple acquisitions need to be performed in several views, thereby increasing overall planning and scan time.

2D free-breathing with retrospective motion correction[2–4] or single breath-hold 2D real-time acquisitions[5, 6] have been proposed to minimize slice misalignments and improve patient comfort. Parallel Imaging and Compressed Sensing (CS)[7–10] have been used to enable single breath-hold 3D CINE. However, due to trade-off between spatial and temporal resolution all these methods only achieve anisotropic resolution. We have recently proposed a patch-based low-rank reconstruction (PROST)[11] that outperforms CS approaches by exploiting redundancies in 3D static images. Here we propose to extend this approach to further exploit redundancies in the temporal direction (called multi-bin (MB)-PROST), thus enabling 3D Cartesian whole-heart CINE, with high isotropic spatial and temporal resolution, in a single breath-hold scan.

Subjects and Methods: The proposed framework is depicted in Fig. 1. Data is acquired with an ECG-triggered 3D bSSFP sequence and a variable-density spiral-like Cartesian trajectory (VD-CASPR)[12] for each cardiac phase. An alternating tiny-golden and golden angle increment and outward-in trajectory between spiral-like arms are employed to minimize the influence of eddy currents. MB-PROST reconstructs the highly undersampled MR images by exploiting redundant information on a local (within a patch) and non-local (similar patches within a spatial neighborhood and amongst all cardiac phases) scale. MB-PROST alternates between two optimization problems: 1) an L2-norm regularized reconstruction using the denoised data from step 2 as a prior, and 2) an efficient low-rank patch-based denoising. The proposed 3D CINE was acquired on five healthy subjects at 1.5T with 1.9 mm^3 isotropic resolution, 16 cardiac phases (40–50 ms temp. res.) within a breath-hold of 26 ± 2 s (whole-heart, coronal)/21 ± 1 s (LV, short-axis).

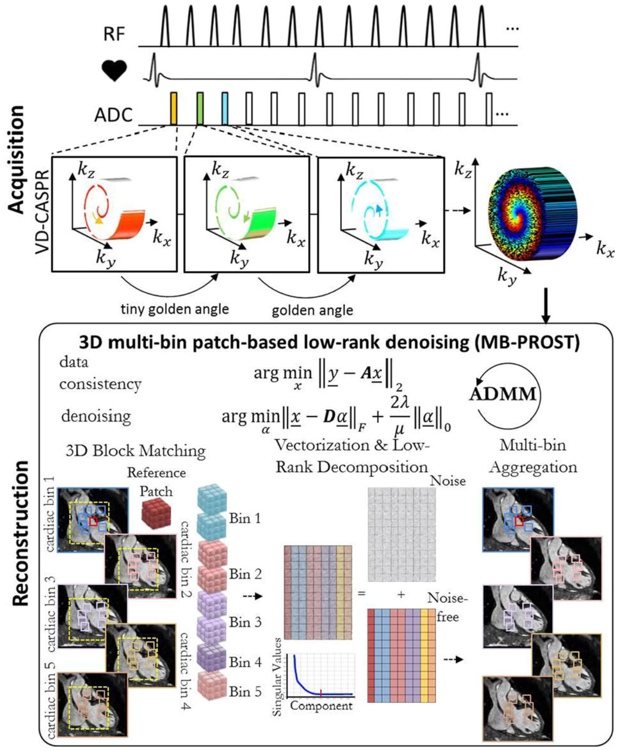

Fig. 1: Proposed isotropic 3D Cartesian CINE in a single breath-hold. A VD-CASPR sampling with tiny-golden and golden angle increment and out-inward trajectory enables high acceleration. MB-PROST exploits spatial-temporal redundancy.

Results: Whole-heart CINE images reformatted to short-axis of 4 subjects are shown in Fig. 2. Good quality is achieved with the proposed approach for all slices and cardiac phases. The proposed MB-PROST outperforms CS (Fig. 3).

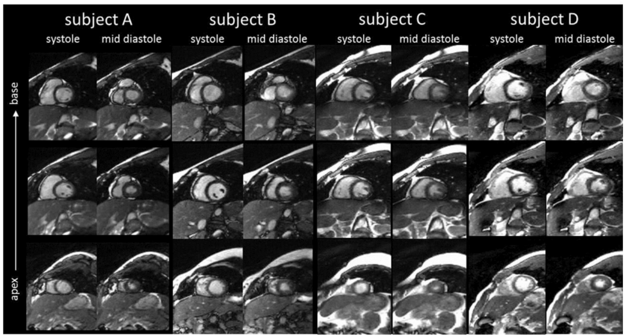

Fig. 2: Short axis 3D Cartesian CINE images of whole-heart acquisition from apex to base in systole and mid diastole. Images were reconstructed with MB-PROST.

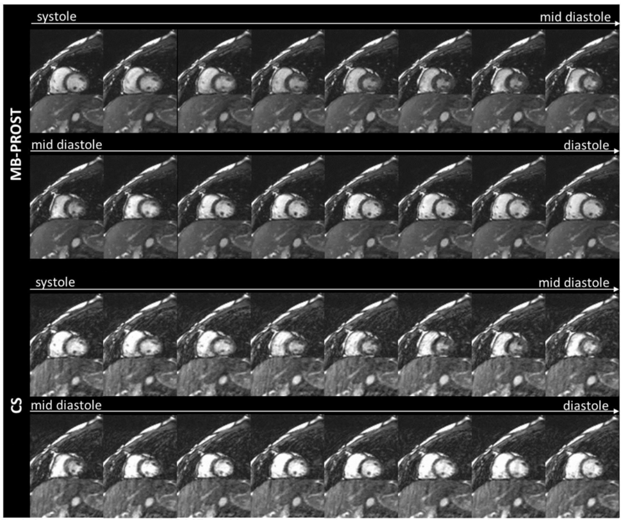

Fig. 3: Comparison of proposed MB-PROST and CS reconstruction (spatial wavelet and temporal total variation regularization) over all

Discussion/Conclusion: The proposed framework enables fast acquisition and good quality reconstruction of highly undersampled data enabling isotropic whole-heart/LV 3D Cartesian CINE in a single breath-hold.

References:

1. Jahnke Radiology 2006.
2. Schmidt JCMR 2013.
3. Hansen MRM 2012.
4. Usman MRM 2013.
5. Vincenti JACC 2014.
6. Xue JCMR 2013.
7. Kressler MRM 2007.
8. Wetzl MAGMA 2018.
9. Barkauskas JCMR2014.
10. Makowski JCMR2012.
11. Bustin MRM2019.
12. Prieto JMRI2015.

S14.05

Super-resolution T1 mapping with integrated motion compensation in a joint maximum likelihood framework

Q. Beirinckx[1], B. Jeurissen[1], M. Verhoye[2], A. J. den Dekker[1], J. Sijbers[1]
[1]University of Antwerp, Department of Physics, imec, Vision Lab, Antwerp, BELGIUM, [2]University of Antwerp, Department of Biomedical Sciences, Bio-Imaging Lab, Antwerp, BELGIUM

Purpose/Introduction: To date, 3D high resolution (HR) quantitative T1 mapping is not feasible in clinical practice due to prohibitively long acquisition times. Recent work has shown that super-resolution reconstruction (SRR), in which a 3D HR T1 map is directly estimated from a set of low through-plane resolution (LR) multi-slice (ms) T1-weighted (T1w) images with different slice orientations, can improve the trade-off between SNR, spatial resolution, and acquisition time[1]. In that work, however, inter-image motion compensation for SRR is performed in a preprocessing step in which the transformation parameters of each LR image are updated after image registration. As a result, potential registration errors might propagate in the T1 estimation as no feedback mechanism is in place. Moreover, due to missing subvoxel accuracy no HR information is readily available during preprocessing. In the current work, we explore the potential of an improved SRR T1 mapping method that aims at more accurate T1 maps by combining T1 and motion estimation in a joint Maximum Likelihood estimation (jMLE) framework.

Subjects and Methods: Fig. 1 shows our proposed SR-jMLE-T1 m forward model that combines a T1-weighting model and a multi-orientated SRR model with an explicit inter-image motion operator. We assume that the *N* LR T1w images are acquired with the inversion recovery (IR) sequence. By combining a set of LR T1w magnitude images, an HR $\boldsymbol{T_1}$ and $\boldsymbol{\rho}$ map can be estimated simultaneously with motion parameters $\boldsymbol{\theta}_n$, $n = 1 \ldots N$, using a jMLE that is implemented using a cyclic block-coordinate gradient descent method[4].

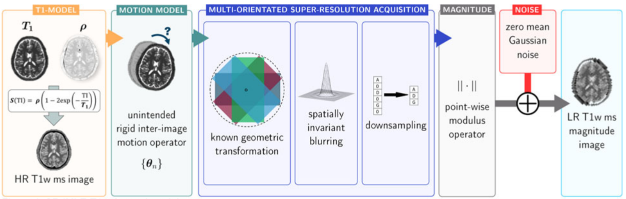

Figure 1. SR-jMLE-T1m forward model

To evaluate the SR-jMLE-T1 m method, a noise free $\boldsymbol{T_1}$ map (range 421–4327 ms) and $\boldsymbol{\rho}$ map (range 0–1) were simulated using normal brain data from Brainweb[3]. This [96 × 96 × 96] data set served as the ground truth (GT), from which a LR Gaussian distributed T1w data set was simulated. Acquisition settings are summarized in Table 1. Unintended motion was added using a Gaussian random walk model[2]. The LR set was processed with the SR-T1 method of reference[1], in which motion parameters were fixed after a rigid registration using a mean squared error metric, and compared with the proposed SR-jMLE-T1 m method.

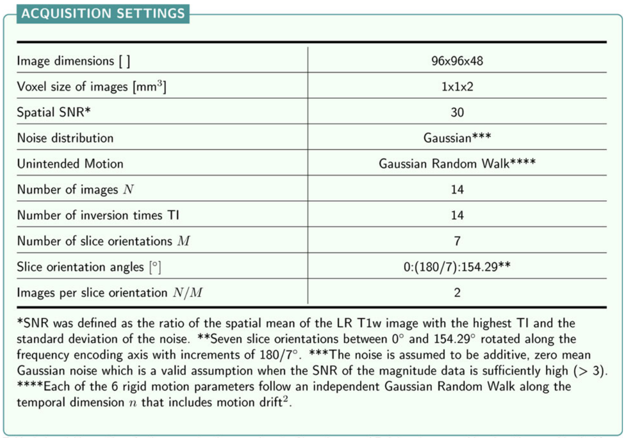

ACQUISITION SETTINGS

Image dimensions [ ]	96x96x48
Voxel size of images [mm^3]	1x1x2
Spatial SNR*	30
Noise distribution	Gaussian***
Unintended Motion	Gaussian Random Walk****
Number of images N	14
Number of inversion times TI	14
Number of slice orientations M	7
Slice orientation angles [°]	0:(180/7):154.29**
Images per slice orientation N/M	2

*SNR was defined as the ratio of the spatial mean of the LR T1w image with the highest TI and the standard deviation of the noise. **Seven slice orientations between 0° and 154.29° rotated along the frequency encoding axis with increments of 180/7°. ***The noise is assumed to be additive, zero mean Gaussian noise which is a valid assumption when the SNR of the magnitude data is sufficiently high (> 3). ****Each of the 6 rigid motion parameters follow an independent Gaussian Random Walk along the temporal dimension n that includes motion drift^2.

Table 1. Acquisition settings for the reconstruction experiments. Since the same LR data set was considered, settings are identical for both methods.

Results: From Fig. 1, it is clear that the SR-jMLE-T1 m method outperforms the previously reported SR-T1 method with pre-registration in terms of relative absolute difference (RAD), where the RAD value in voxel *j* is defined as $\mathrm{RAD}(j) = |\mathrm{T1}_{\mathrm{estimate}}(j) - \mathrm{T1}_{\mathrm{GT}}(j)| / \mathrm{T1}_{\mathrm{GT}}(j)$.

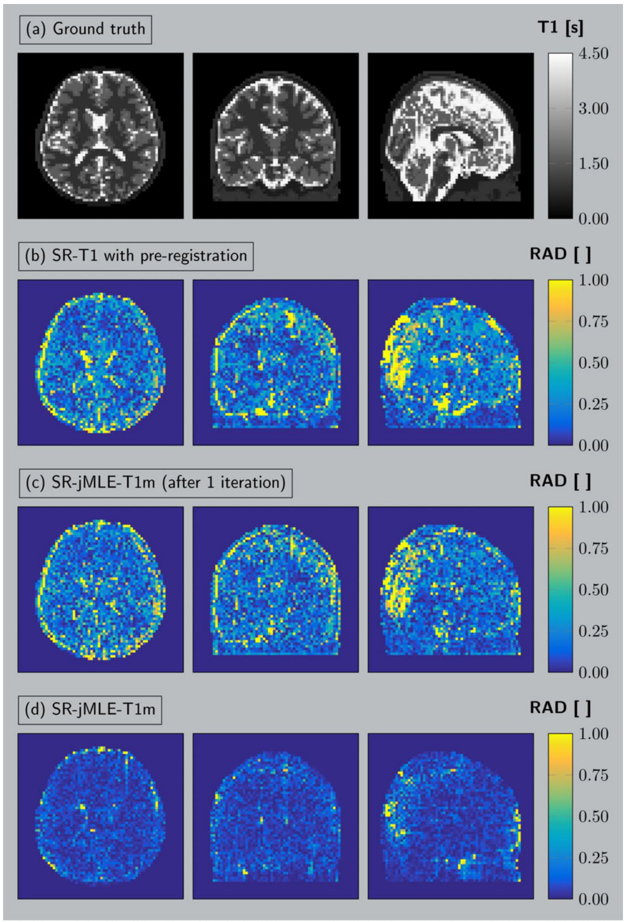

Figure 1: Axial, coronal, sagittal mid slices of (a) the noiseless GT T1 map, (b)-(d) RAD T1 maps of, respectively, SR-T1, and SR-jMLE-

Discussion/Conclusion: We showed the promising potential of a new SR-jMLE-T1 m method in which T1 mapping is combined with integrated motion compensation. These results encourage the authors to further develop the method and test it on clinical data.

References:

1. Van Steenkiste et al., *MRM*, 2017. 77(5):1818–1830
2. Ramos-Llordén et al., *IEEE TMI*, 2017. 36(2):433–446
3. Cocosco et al. *Online Interface to a 3D MRI Simulated Brain Database*
4. Beck et al., *SIAM J. Optim.*, 2013. 23(4):2037–2060

S14.06

Multi-contrast patch based super-resolution for diffusion weighted MRI of breast

R. Fenioux[1], M. Delbany[1], J. Felblinger[2], P.-A. Vuissoz[1], F. Odille[2]
[1]*IADI, INSERM U1254 and Université de Lorraine, Nancy, FRANCE,* [2]*IADI and CIC-IT, INSERM, CHRU de Nancy and Université de Lorraine, Nancy, FRANCE*

Purpose/Introduction: Diffusion-weighted imaging (DWI) is a promising technique for increasing the specificity of breast MRI. However, the detection of small size tumors is limited by its resolution, particularly in the through-plane direction. The use of a readout-segmented DW-EPI (rs-EPI) sequence followed by a super-resolution reconstruction (SRR) can improve the resolution without sacrificing SNR or scan time, to achieve isotropic high-resolution 3D images [1]. In this study, we propose a new SRR method by adapting a 3D patch-based SRR [2] for simultaneous reconstruction of multicontrast images (multiple b values). The method is applied to DWI scans of phantoms and healthy volunteers to improve the resolution from $1 \times 1 \times 3$ mm^3 to $1 \times 1 \times 1$ mm^3.

Subjects and Methods: The proposed SRR method is an adaptation of [2]. To regularize the SRR, it takes advantage of spatial redundancies in the data. For each voxel, similar 3D patches are extracted and grouped in a matrix. A singular value decomposition is used and the low singular values are zeroed to suppress the noise, resulting in a sparse matrix. The denoised patches are returned to their original positions.

An extension of this method for multicontrast images has been developed, where similar patches are extracted from all contrast images (Fig. 1). This approach requires an additional normalization step. The optimization problem is solved using an Augmented Lagrangian formulation.

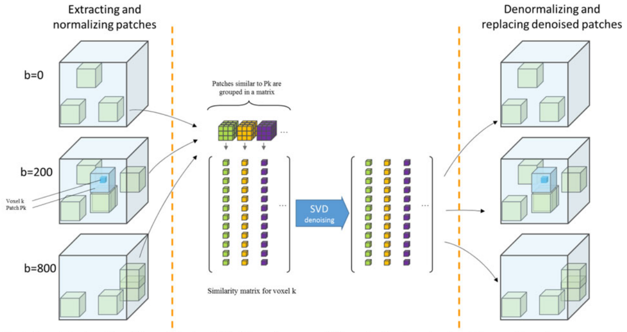

Fig. 1: Regularization step of the multicontrast Patch-based super-resolution using the three b values. The resulting volumes are used as priors for the super-resolution reconstruction using an augmented lagrangian formulation.

8 healthy women were scanned on a 3T PRISMA MR scanner (Siemens, Erlangen, Germany) with a breast coil array. Three low-resolution rs-EPI scans were performed (resolution = $1 \times 1 \times 3$ mm^3, b = 0, 200, and 800 s/mm^2) with an axial orientation and a 1 mm offset in the slice direction between each acquisition. One native high-resolution image is acquired for reference with the same parameters and scan time but a slice thickness of 1 mm (resolution = $1 \times 1 \times 1$ mm^3).

Results: The visual comparison shows the better quality of 3D Patch and multicontrast Patch compared to the native image (Fig. 2). The multicontrast patch method has a better SNR gain for non-zero b values and a smaller ADC bias than the Beltrami regularization (Table 1).

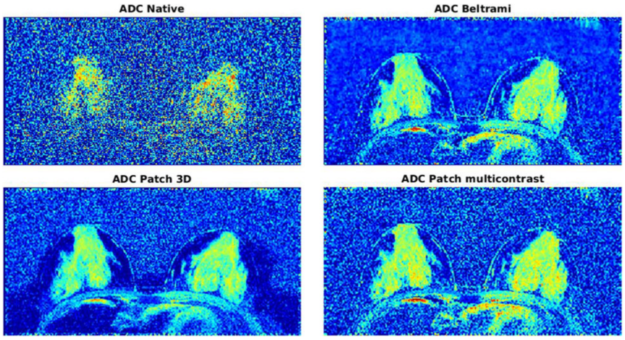

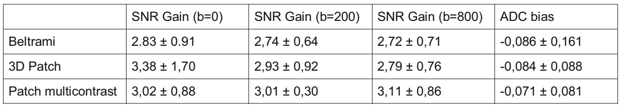

	SNR Gain (b=0)	SNR Gain (b=200)	SNR Gain (b=800)	ADC bias
Beltrami	2.83 ± 0.91	2,74 ± 0,64	2,72 ± 0,71	-0,086 ± 0,161
3D Patch	3,38 ± 1,70	2,93 ± 0,92	2,79 ± 0,76	-0,084 ± 0,088
Patch multicontrast	3,02 ± 0,88	3,01 ± 0,30	3,11 ± 0,86	-0,071 ± 0,081

Table 1: Performances of the Patch based methods compared to a Beltrami regularization. The multicontrast method provide a higher SNR gain for b=200 and 800 s.mm-2 and introduce a smaller bias in the ADC values.

Discussion/Conclusion: The two Patch-based super-resolution techniques were successfully applied to breast DW MRI. The multicontrast extension increases the SNR gain and could be used with higher b values. The increased quality at high resolution could facilitate the detection small structure such as tumors, or accelerate the scan using fewer Nex or multiband acceleration.

References:

[1] Delbany & al. (2018). One-millimeter isotropic breast diffusion-weighted imaging: Evaluation of a superresolution strategy in terms of signal-to-noise ratio, sharpness and apparent diffusion coefficient. MRM.

[2] Bustin & al. (2018). Isotropic Reconstruction of MR Images Using 3D Patch-Based Self-Similarity Learning. IEEE-TMI.

S14.07

Optimal design of a blended diffusion/relaxometry experiment

A. E. Buikema, A. J. den Dekker, J. Sijbers

imec-Vision Lab, Department of Physics, University of Antwerp, Antwerp, BELGIUM

Purpose/Introduction: Performing both diffusion (dMRI) and relaxometry MRI within a single clinical scan protocol is highly desirable as both modalities provide complementary information about the microstructure of brain tissues[1, 2]. Combining dMRI and relaxometry in a blended imaging protocol holds the potential to overcome limitations, e.g. in acquisition time or biomarker specificity. We propose a blended dMRI/relaxometry imaging protocol together with an optimal experiment design, based on the Cramér-Rao Lower Bound (CRLB), which allows increased precision of the model parameters of interest in a given acquisition time. To this end, we adopt the pulsed-gradient spin-echo sequence[3] and a diffusion time-dependent model[4, 5].

Subjects and Methods: The data is assumed to be Rician distributed, with underlying signal model as described in Fig. 1. To increase the precision with which the model parameters can be estimated, the diffusion weighted experiment design was optimized based on the CRLB. For each acquisition design, we added non-diffusion weighted signal with fixed TE = {50, 100, 150, 200}ms, with 5 realizations for each TE. The optimality criterion was chosen to be a weighted sum of the CRLBs of all model parameters, except S0, ψ and θ, where the CRLB of each parameter is weighted by the inverse square of the parameter value. This criterion was minimized with respect to 16 combinations of TE and Δ. We set limits of 50 ≤ TE ≤ 200 ms and 20 ≤ Δ ≤ 180 ms and started the optimization from the equidistant design described in Table 1.

For comparison, we simulated 500 realizations of Rician distributed single-voxel observations for both the equidistant and optimized design and for SNR = {25, 50, 75, 100}, where the SNR is defined based on the non-diffusion weighted signal at TE = 200 ms. The model parameters were estimated from the noisy data sets using the Maximum Likelihood estimator and the sample variances of the estimators were compared to the corresponding CRLBs.

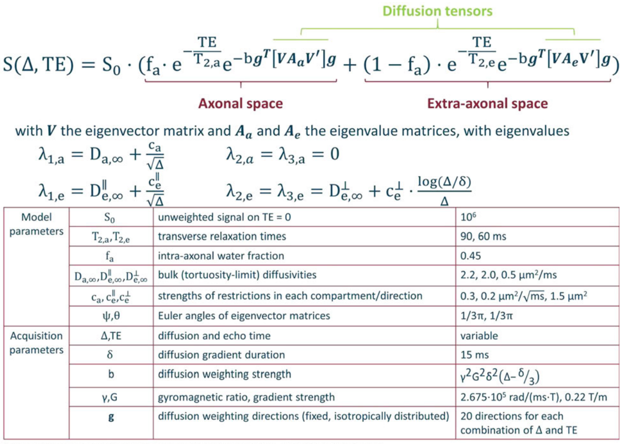

Diffusion tensors

$$S(\Delta, \mathrm{TE}) = S_0 \cdot (\underbrace{f_a \cdot e^{-\frac{\mathrm{TE}}{T_{2,a}}} e^{-b\boldsymbol{g}^T[\overline{\boldsymbol{V A_a V'}}]\boldsymbol{g}}}_{\text{Axonal space}} + \underbrace{(1-f_a) \cdot e^{-\frac{\mathrm{TE}}{T_{2,e}}} e^{-b\boldsymbol{g}^T[\overline{\boldsymbol{V A_e V'}}]\boldsymbol{g}}}_{\text{Extra-axonal space}})$$

with $\boldsymbol{V}$ the eigenvector matrix and $\boldsymbol{A_a}$ and $\boldsymbol{A_e}$ the eigenvalue matrices, with eigenvalues

$$\lambda_{1,a} = D_{a,\infty} + \frac{c_a}{\sqrt{\Delta}} \qquad \lambda_{2,a} = \lambda_{3,a} = 0$$

$$\lambda_{1,e} = D_{e,\infty}^{\parallel} + \frac{c_e^{\parallel}}{\sqrt{\Delta}} \qquad \lambda_{2,e} = \lambda_{3,e} = D_{e,\infty}^{\perp} + c_e^{\perp} \cdot \frac{\log(\Delta/\delta)}{\Delta}$$

Model parameters	S_0	unweighted signal on TE = 0	10^6
	$T_{2,a}, T_{2,e}$	transverse relaxation times	90, 60 ms
	f_a	intra-axonal water fraction	0.45
	$D_{a,\infty}, D_{e,\infty}^{\parallel}, D_{e,\infty}^{\perp}$	bulk (tortuosity-limit) diffusivities	2.2, 2.0, 0.5 μm²/ms
	$c_a, c_e^{\parallel}, c_e^{\perp}$	strengths of restrictions in each compartment/direction	0.3, 0.2 $\mu m^2/\sqrt{ms}$, 1.5 μm²
	ψ,θ	Euler angles of eigenvector matrices	1/3π, 1/3π
Acquisition parameters	Δ,TE	diffusion and echo time	variable
	δ	diffusion gradient duration	15 ms
	b	diffusion weighting strength	$\gamma^2 G^2 \delta^2 (\Delta - \delta/3)$
	γ,G	gyromagnetic ratio, gradient strength	$2.675 \cdot 10^5$ rad/(ms·T), 0.22 T/m
	$\boldsymbol{g}$	diffusion weighting directions (fixed, isotropically distributed)	20 directions for each combination of Δ and TE

Figure 1: Signal model, underlying parameter values and the acquisition parameters.

Results: Table 1 shows the acquisition framework for both the equidistant and optimized design.

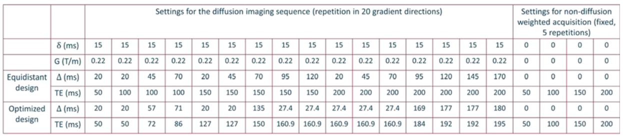

		Settings for the diffusion imaging sequence (repetition in 20 gradient directions)																Settings for non-diffusion weighted acquisition (fixed, 5 repetitions)			
	δ (ms)	15	15	15	15	15	15	15	15	15	15	15	15	15	15	15	15	0	0	0	0
	G (T/m)	0.22	0.22	0.22	0.22	0.22	0.22	0.22	0.22	0.22	0.22	0.22	0.22	0.22	0.22	0.22	0.22	0	0	0	0
Equidistant design	Δ (ms)	20	20	45	70	20	45	70	95	120	20	45	70	95	120	145	170	0	0	0	0
	TE (ms)	50	100	100	100	150	150	150	150	150	200	200	200	200	200	200	200	50	100	150	200
Optimized design	Δ (ms)	20	20	57	71	20	20	135	27.4	27.4	27.4	27.4	27.4	169	177	177	180	0	0	0	0
	TE (ms)	50	50	72	86	127	127	150	160.9	160.9	160.9	160.9	160.9	184	192	192	195	50	100	150	200

Table 1: Acquisition framework for the equidistant design versus the optimized design.

Figure 2 shows the weighted sum of CRLBs and sample variances for the equidistant and optimized design. Although the acquisition design is optimized based on SNR = 50, it is clear that the weighted sum of variances decreases for multiple SNR values compared to the equidistant design.

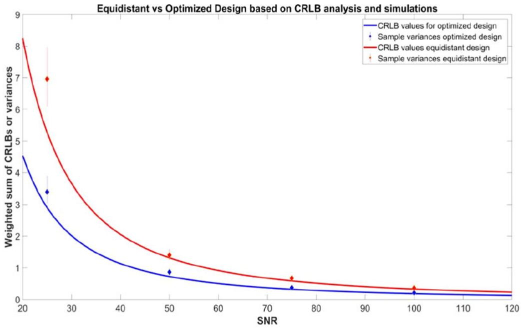

Figure 2: Weighted sum of CRLBs (lines) or sample variances (diamonds) including 95% confidence intervals for SNR equal to 25, 50, 75 and 100 for the equidistant design (in red) versus th optimized design (in blue).

Discussion/Conclusion: We proposed an optimized acquisition design for a blended dMRI/relaxometry protocol and compared it to an equidistant framework, based on a CRLB analysis and simulation experiments. The results show a gain in the precision of the estimates of the model parameters of interest in a given acquisition time, which contributes to the improvement of the trade-off between acquisition time and precision.

References:

1. Deoni, *Psychol Med.* **45**, 795–805 (2015).
2. Lamar, *Am J Geriatr Psychiatry* **22**, 111–21 (2014).
3. Stejskal, *JCP* **42**, 288–292 (1965).
4. Lee, *ISMRM* **26**, 0884 (2018).
5. Fieremans, *NI* **129**, 414–427 (2016).

S14.08

Flow effects in echo planar 4D flow MRI

H. Dillinger, J. Walheim, S. Kozerke
ETH Zurich, D-ITET, Zurich, SWITZERLAND

Purpose/Introduction: 4D Flow MRI is widely used in research [1]. Its clinical utility is, however, often limited by the long acquisition times. It is therefore desirable to shorten scan times. Recent work has revisited Echo Planar Imaging (EPI) for phase-contrast MRI and it has been concluded that EPI provides best image scores compared to other approaches [2]. Two-dimensional EPI phase-contrast imaging has been studied previously [3][4] and limitations in low flow regimes have been demonstrated. To this end, it is the objective of the present work to provide a computational analysis of flow-related artifacts in EPI phase-contrast imaging in multiple dimensions and for high blood flows.

Subjects and Methods: The simulation setup is outlined in Fig. 1. A computational fluid dynamic (CFD) simulation using the Reynolds Averaged Navier–Stokes approach (CFD-RANS) was performed on a U-bend geometry (50% stenosis) using OpenFOAMv1712. A parabolic inlet profile with a maximum velocity of 1 m/s, no-slip wall and zero-gradient boundary condition for the velocity at the outlet were applied. Inside the domain, particles were seeded on a 2D plane. For every particle, the equation given in Fig. 1b was solved using the velocity field and gradient waveforms as shown in Fig. 1c (considering gradient strength and slew rate limits of 30 mT/m and 195 T/m/s respectively). After each shot (Cartesian:1/EPI:5 lines), the initial conditions of the particles were reset to simulate newly arriving particles. A 0.1 × 0.1 m^2 FOV with a resolution of 1 × 1 mm^2 was assumed. Echo times (TE) were 2.1 ms and 4.3 ms for Cartesian and EPI respectively.

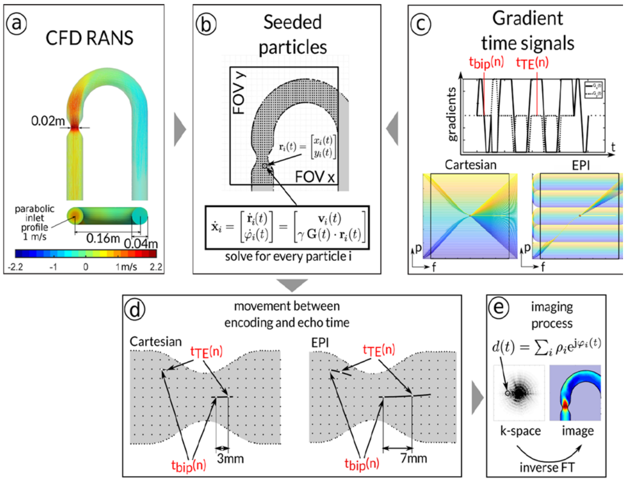

Figure 1: State vector equation is solved using velocity field and gradient signals as inputs. Due to movement of particles during readout, misalignment occurs.

Results: Figure 2 shows the comparison of the CFD solution to Cartesian and EPI readout for the velocity magnitude |u| (values outside ROI masked). Figure 3 shows the velocity profiles for flow in frequency and phase encoding direction respectively along the centerline.

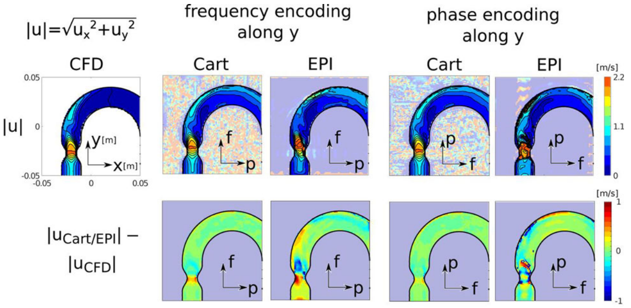

Figure 2: Velocity field magnitude and difference from ground truth (CFD) for different readout directions. For EPI readout, the resulting velocity image strongly depends on the readout direction.

In Fig. 3b, a shift of the peak velocity (PV) of 4 mm in y-direction and an underestimation of PV of 1.19% for the Cartesian readout is found. For EPI the velocity profile is deformed, the jet angle and its shape is altered. A shift of PV of 7 mm in y-direction and an overestimation of PV of 14.67% is found.

Velocity profiles in Fig. 3c show a shift of PV of 1.5 mm in y-direction and an underestimation of PV of 1.09% for Cartesian readout while for EPI velocity profile is deformed (shift of PV of 4.5 mm in y-direction and an overestimation of PV of 9.88%).

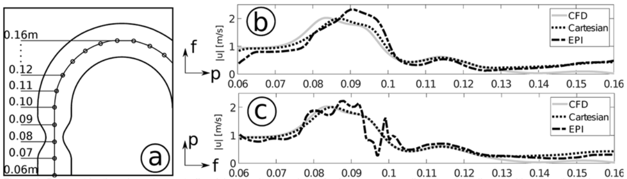

Figure 3: Parametrization along the centerline (a). Velocity magnitude for frequency encoding direction aligned with y direction (b) and x direction (b). The inflow effect is reduced for Cartesian readout for phase encoding direction aligned with y.

Discussion/Conclusion: Phase-contrast using EPI readouts shows artifacts for high flows with significant implications regarding the localisation of jet velocities and jet impingement. Accordingly, its application to 4D Flow MRI of high or stenotic flow is not recommended.

References:

[1] Dyverfeldt et al. (2015) JCMR, 17(1):1–19.
[2] Garg et al. (2018) JCMR, 47(1):272–281.
[3] Butts BS, Riederer S (1992) JMRI, 2(3):282–293.
[4] Nishimura et al. (1995) MRM, 33(4):549–556.

S14.09

T-Hex EPI: 3D Echo-planar imaging on a tilted hexagonal grid

M. Engel, L. Kasper, B. Wilm, B. Dietrich, L. Vionnet, K. Pruessmann
ETH Zürich, Institute for Biomedical Engineering, Zurich, SWITZERLAND

Purpose/Introduction: Rapid MR scanning of 3D volumes is aimed at in applications like fMRI with high temporal resolution[1]. 3D Fourier encoding lends itself to this task: it provides high SNR due to data acquisition from the entire volume, while being amenable to undersampling by optimal PI acceleration in all three dimensions.

Recently, a method has been proposed to acquire an arbitrary number of adjacent k-space planes on a tilted hexagonal grid (t-Hex) within one shot[2]. 3D k-space is covered extremely efficiently, exhibits a smooth T_2* weighting for a benign PSF and near-isotropic sampling in all indirect dimensions.

The technique has been shown on the basis of spiral readouts. In the present work, we demonstrate that this concept can be extended to echo-planar readouts, achieving isotropic brain imaging with 2 mm resolution in only 694 ms.

Subjects and Methods: T-Hex: The hexagonal grid (k-space cross section) is shown in Fig. 1.

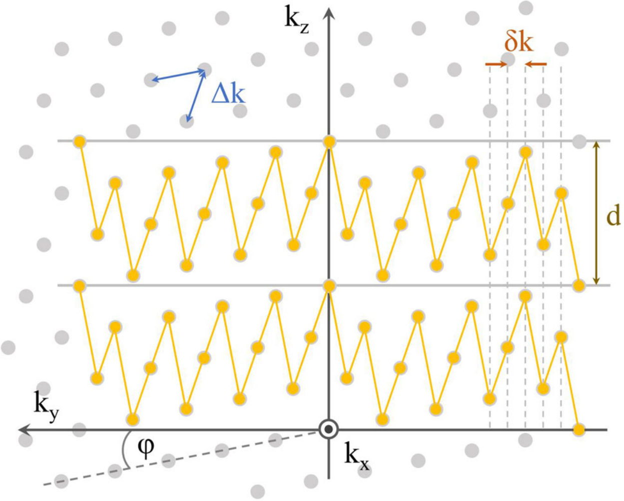

T-Hex grid: Each dot represents an FE line, the 2 yellow lines mark the paths taken by 2 subsequent shots. One band (d) includes 3 k-space planes and φ is chosen such that the sampling distance δk is constant and thus entails a smooth T2* weighting.

Evenly spaced progression in k_y direction and thus smooth T_2* weighting (Fig. 2 C) is achieved by tilting the grid by

$\varphi = \tan^{-1}[(P - 2)/(P \bullet \sqrt{3})]$,

where *P* is the number of k-space planes visited by each shot.

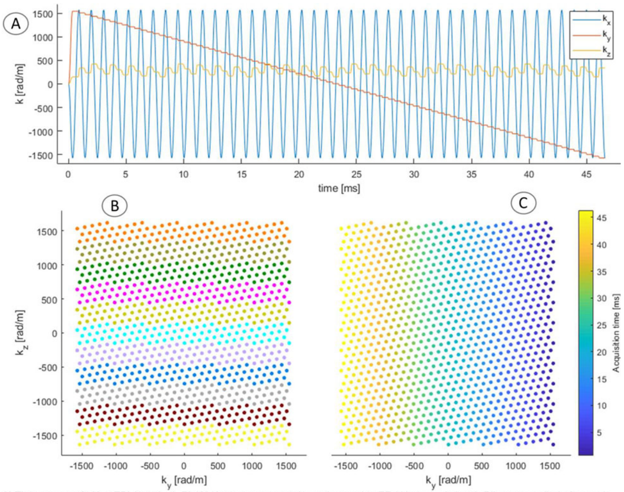

A) Time course of t-Hex EPI (1st shot). B) /C) K-space cross section orthogonal to FE (11 stacked shots). Blips are applied after each FE line. In C), colors encode acquisition time and thereby illustrate the smooth T2* weighting attained with t-Hex.

Hardware: Philips 7T Achieva system; 32 channel head array (Nova Medical); 16 ^{1}H NMR field probes and a dedicated MR acquisition system[3].

Sequence: GRE with T_2*-contrast, FOV = 24 × 24 × 12 cm^3, 2 mm^3 resolution, P = 3, 11 shots, T_{AQ} = 46.6 ms, TE = 27 ms, TR = 694 ms.

An iterative cg-SENSE image reconstruction[4] was performed, including MFI[5] for static off-resonance correction and based on pre-monitored trajectories[6]. Off-resonance and coil sensitivity maps were computed from a spin-warp pre-scan (6 echoes, TE 2–7 ms, 1.5 mm^3 resolution).

Results: See Fig. 3.

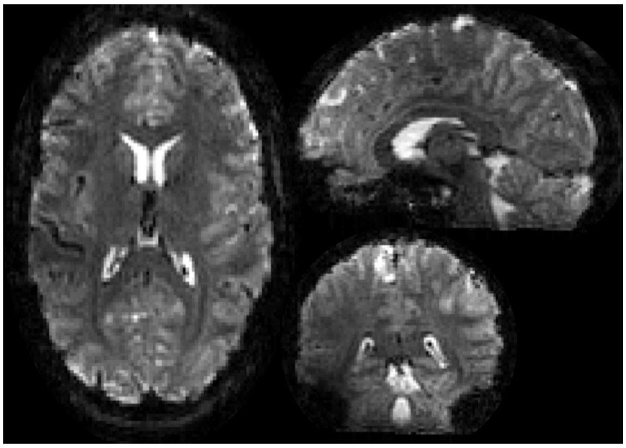

Central planes of resulting 3D whole-brain data, obtained in 694ms per frame. Compared to t-Hex spiral scans, t-Hex EPI offers greater robustness against off-resonance and thus sharper depiction of structures near the skull.

Discussion/Conclusion: The proposed acquisition scheme reconciles the speed benefit of tilted hexagonal sampling with EPI and thus with the best-understood and most widely used fMRI readout. The hexagonal grid in the PE plane achieves uniform (under-)sampling while its tilt ensures smooth T_2* weighting also for EPI. Compared to t-Hex spiral, the EPI variant comes at slight expense in terms of speed, which is offset by greater robustness against off-resonance.

Unlike for spiral imaging, where blipping up and down in k_z means an unwanted deceleration, EPI hardly suffers more from the t-Hex blips than it does anyway from its simultaneous in-plane phase-encoding blips, which makes t-Hex an inexpensive and worthwhile extension of conventional 3D EPI.

The present work follows up on the new t-Hex sampling scheme and applies it to the more conventional case of EPI. In a next step, it may be applied to multiband imaging. Here, t-Hex paves the way for uniform k-space sampling, which has not been possible so far in case of shifts smaller than FOV/2 between adjacent slices.

References:

1. Feinberg et al., PLoS ONE 2010.
2. Engel et al., Proc ISMRM 2018.
3. Dietrich et al., MRM 2016.
4. Pruessmann et al., MRM 2001.
5. Man et al., MRM 1997.
6. Barmet et al., Proc ISMRM 2010.

S15 Scientific Session

15:40–17:10 *Room 3 - Ruys & van Rijckevorsel Zaal*

Hardware & Safety

S15.02

MRI at 2.15 MHz in a low-cost Halbach-based scanner for pediatric neuroimaging

T. O'Reilly, W. Teeuwisse, K. Koolstra, A. Webb
Leiden University Medical Center, C.J. Gorter Center for High Field MRI, Leiden, NETHERLANDS

Purpose/Introduction: Halbach arrays are an attractive approach to building low-field MRI systems due to their relatively high magnetic field strength and very low stray fields. B_0 homogeneity of finite length Halbach arrays is, however, significantly reduced which has prevented the use of FFT-based image reconstructions in Halbach arrays with a sufficiently large bore size for human imaging[1]. In this work we set out to build a Halbach array-based magnet with a sufficiently large bore for imaging hydrocephalus in young children. The homogeneity of the Halbach array is optimised by varying the radius of the array along the length of the magnet.

Subjects and Methods: The Halbach array consists of 12 mm cube neodymium magnets placed in 23 layers spaced 22 mm apart, two rings of magnets were used to increase B_0 strength. Ring radii of 148 mm (50 magnets), to 221 mm (75 magnets) were simulated in CST Microwave studio (Darmstadt, Germany). The homogeneity over a 25 cm diameter spherical field of view was subsequently optimized by combining the fields of various layer radii using a genetic algorithm in Python. B_0 Shimming was performed by placing additional 3 mm cube neodymium magnets inside the bore. Gradients were constructed by winding 15 AWG copper wire on PMMA cylinders. A 15 cm diameter, 15 cm long solenoid was used as a transceiver coil.

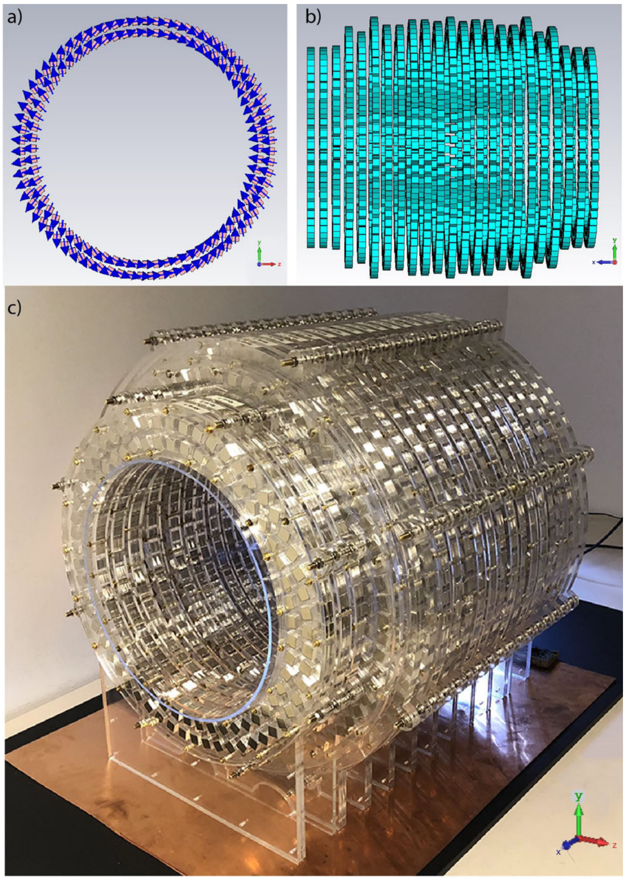

Figure 1. a) a single layer of the Halbach array with two rings of magnets. b) A side view of the optimised layout. c) An image of the constructed Halbach array.

2D Phantom images were acquired on a 3D printed 9 × 6 × 3.5 cm Shepp-Logan based phantom (see Fig. 3) using a spin echo sequence using no slice selection gradient with an in-plane resolution of 1×1 mm^2 with 8 signal averages and a total scan duration of 16 min.

Results: The optimised Halbach array had a field strength of 50.6mT and a homogeneity of 400 ppm over a 20 cm diameter spherical volume (DSV). The constructed magnet had a B_0 field strength of 50.4 mT and a homogeneity measured over a 20 cm DSV of 13000 ppm. After shimming the field strength increased to 50.5 mT and homogeneity measured over the same 20 cm DSV improved to 2500 ppm.

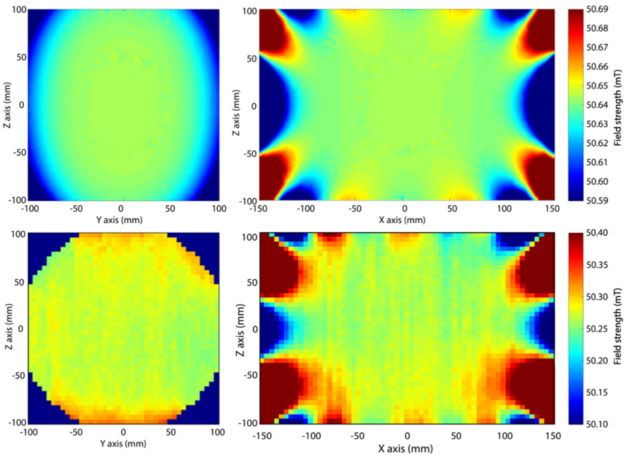

Figure 3 shows the reconstructed images.

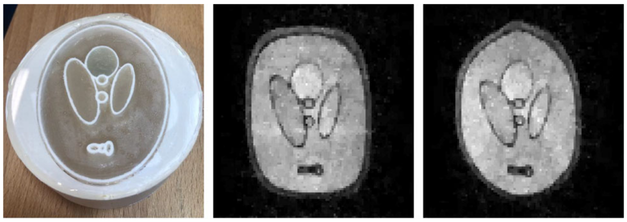

Figure 3. left) A 3D printed Shepp-Logan-based phantom. Center) Image acquired of the phantom with an in-plane resolution of 1.2x1.2 mm. Right) Image corrected for gradient non-linearities.

Discussion/Conclusion: Homogeneity of a finite-length Halbach array can be significantly improved by optimizing the radii of the layers that make up the array along its length. The homogeneity of the constructed magnet was lower than in simulations, which we mostly attribute to structural deformations of the individual layers in the Halbach array which can be improved in future designs. Shimming using small additional magnets provided a relatively easy approach for improving the homogeneity of the magnet. We were able to acquire 2D images in an acceptable time frame and future sequence optimization will reduce the acquisition time and gradient optimization will reduce gradient non-linearity artifacts. Component cost of the constructed magnet was 4000 euros, providing a basis for producing a low-cost MRI system in low-resource settings.

References:

[1] Cooley, C et al. MRM. 2015;73:872–883.

S15.03

Ultra-fast and intense magnetic fields for MRI and Peripheral Nervous System stimulation studies

D. Grau-Ruiz[1], L. Angelidakis[2], E. Pallas[2], J. P. Rigla[1], J. Alonso[2], A. Ríos[1], J. M. Benlloch[2]

[1]Tesoro Imaging SL, Valencia, SPAIN, [2]Spanish National Research Council (CSIC), Inst. for Instrum. for Molecular Imaging (i3 M), Valencia, SPAIN

Purpose/Introduction: Here we present the thermal and magnetic characterization of a planar, ultra-fast (10 µs) and intense (2.4 T/m) magnetic field gradient system [1] designed for a pre-clinical Magnetic Resonance Imaging (MRI) scanner we are building at i3 M [2]. Aside from imaging, our technology will be applied to Peripheral Nerve Stimulation studies when magnetic fields are switched in micro-second timescales, which can be used to benchmark existing models for physiological effects of electromagnetic fields in a regime thus far not accessible. Figure 1 shows data from the International Electrotechnical Commission directive 60601:22:33, which established requirements for the basic safety and essential performance of magnetic resonance equipment for medical diagnosis. The used models are known as Spatially Extended Nonlinear Node (SENN) models [3]. Green and red areas are being explored, however the rest of the territory is so far uncharted. Previous experiments hint at deviations from SENN models for rapidly varying magnetic fields [4]. Nevertheless, SENN continues being used, largely due to the overwhelming lack of experimental data other than in the green area.

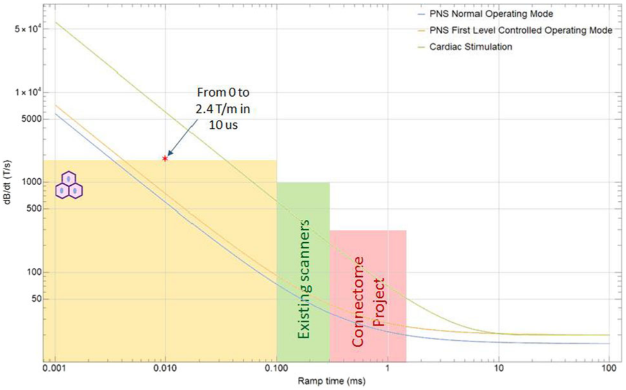

Figure 1. SENN theorical models used for Cardiac Stimulation (CS) thresholds, PNS thresholds and 80% of PNS thresholds

Subjects and Methods: Our gradient coils are manufactured out of OFHC Copper hollow tubes (4 × 3 mm^2, Ø2 mm). The coils are refrigerated by using a constant water flow provided by a HRS-090-AF-40 thermo cooler. A dielectric structure manufactured by sintering polyamide fixes the coil system mechanically. Figure 2 shows X-coil for a single axis fixed on the dielectric structure. Both a three-axis hall magnetometer and an impedance analyzer have been used to measure the magnetic field and resistance/inductance, respectively.

Figure 2. Manufactured X-coil using OFHC Copper hollow tube and fixing polyamide structure.

Results: The magnetic field profile (I = 1 A) for an X-axis gradient is shown in Fig. 3 (up), while the resistance and inductances values at different frequencies are shown in Fig. 3 (center). Vertical dotted red lines indicate the frequencies corresponding to rise-time pulses from 10 µs to 30 µs. All experimental measurements are in close agreement with simulations as well as the values obtained for the rest of the coils. Figure 3 (down) shows the water flow through the coils for different pressure values. Preliminary simulations show a temperature increase lower than 12.5 K in continuous operation at a current intensity of 500 A.

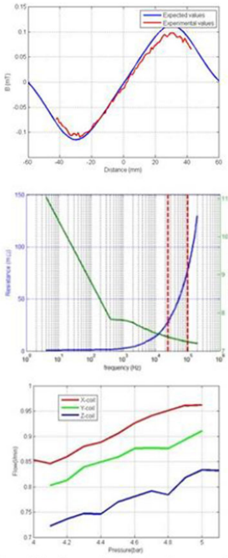

Figure 3. X-coil magnetic profile by using a current intensity of 1 A (up). X-coil set axis resistance and inductance experimental values in a frequency sweep (center). Coils hydraulic characterization (down)

Discussion/Conclusion: An ultra-fast and intense gradient system is presented. Electromagnetic and hydraulic measurements confirm the expected system behaviour. Our power supplies and gradient system open the door to a new regime of operation MRI and testing PNS stimulation thresholds under conditions where no other machine has previously reached.

References:

[1] D. Grau et al., *Patent Application* US P201830448 (2018)
[2] J.P. Rigla et al., arXiv:1808.05795 (2019).
[3] E.U. Saritas et al., *IEEE Trans Med Imaging* **32** (2013) 1600–1610.
[4] J.P. Reilly et al., *IEEE Trans BioMed Eng* **12** (1985) 1001–1011.

S15.04

2D echo-planar imaging with an ultrasonic resonant z-gradient

R. Metere[1], J. Schulz[1], D. Klomp[2], J. P. Marques[1], D. G. Norris[1]
[1]*Radboud University, Donders Institute, Nijmegen, NETHERLANDS,* [2]*University Medical Center Utrecht, Imaging and Cancer Division, Utrecht, NETHERLANDS*

Purpose/Introduction: The imaging performance in Magnetic Resonance Imaging (MRI) is largely determined by the performance of the gradients, which limit the spatio-temporal resolution.

Traditionally, the gradients have similar specifications in the three spatial directions.

However, it is technically feasible to manufacture a high-performance resonant gradient system in a single spatial direction[1].

This can be efficiently driven at high frequency (20 kHz) which is inaudible to the human ear[2].

The effect on imaging is a sin-modulation of the k-space trajectory similar to the wave-CAIPI scheme[3].

Here, we explore acquisition and reconstruction strategies based on 2D Echo-Planar Imaging (EPI) trajectories.

The sinusoidally-modulated EPI (sEPI) acquisitions (for different k-space trajectory parameters) are compared against similar blipped EPI (bEPI) acquisitions.

Subjects and Methods: Based on the gradient specifications (G = 45 mT/m, SR = 200 T/m/s) of a standard 3T system (Skyra, Siemens AG, Erlangen, Germany) and for a prototype resonant sinusoidal gradient coil for 3T systems (G = 45 mT/m, SR = 5655 T/m/s) (MR Coils, Zaltbommel, Netherlands), k-space trajectories were simulated using ab initio methods[4] of gradient moments based on ideal (trapezoidal or sinusoidal) shapes for the generated gradients.

The target resolution (2 mm iso.) and Field-Of-View (FOV) (256 × 256 mm) were kept constant.

bEPI trajectories with 1D-acceleration factor between 1 and 5 were compared against similarly undersampled sEPI trajectories.

For each trajectory, modified-Shepp-Logan phantom images (with 8 Ch receiver) were simulated and reconstructed using the BART[5] implementation of Parallel Imaging and Compressed Sensing (PICS).

Results: The trajectories, the reconstructed images and the difference with the fully sampled data is reported in

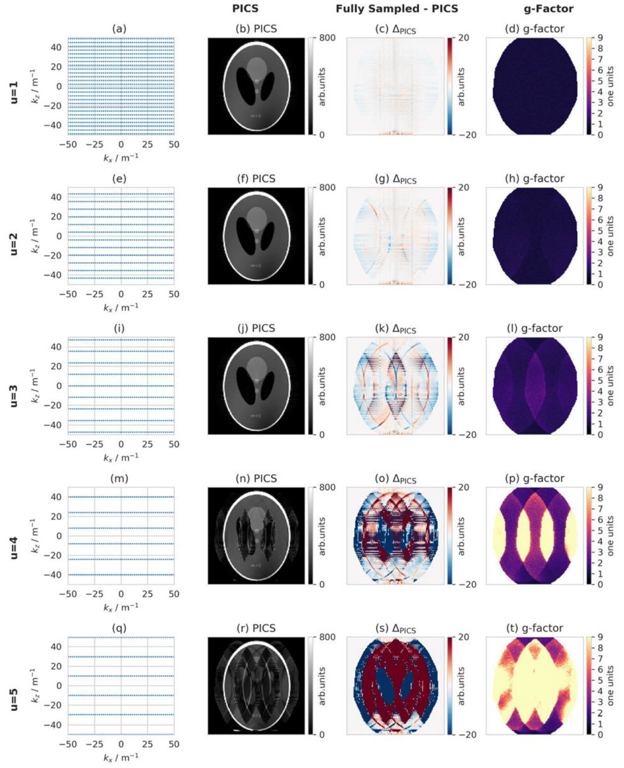

Fig.1: Overview of blipped EPI Acquisitions. The columns show: the k-space trajectory, the PICS reco, the difference between the PICS reco and the fully sampled image, the g-factor map. The rows shows bEPI for increasing acceleration factors k.

for bEPI and in

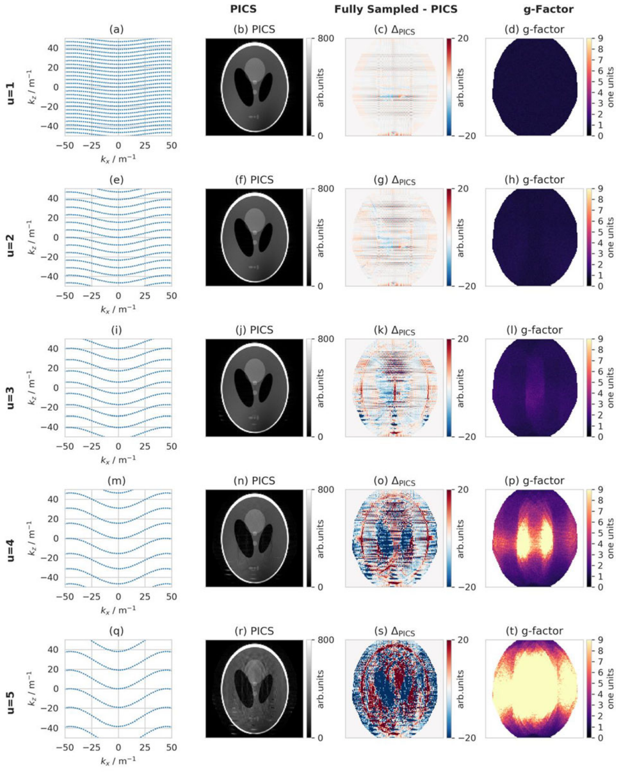

Fig.2: Overview of Sin-modulated EPI Acquisitions. The columns show: the k-space trajectory, the PICS reco, the difference between the PICS reco and the fully sampled image, the g-factor map. The rows shows sEPI for increasing acceleration factors u.

for sEPI. A summary of the predicted duration and the st.dev of the difference of the PICS reconstruction and the fully sampled reconstruction is presented in

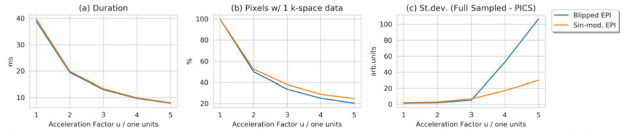

Fig.3: Parameters as a function of acceleration factor u. The considered parameters are the duration, the percent of pixels with at least 1 k-space point and the st.dev of the difference between the fully sampled and PICS recos.

Discussion/Conclusion: The results indicate that for higher acceleration factor the sin-modulation improved the PICS reconstruction accuracy and efficiency. While the coil sensitivity is used for PICS, the additional time required to obtain reference data is ignored for these calculations.

The duration differences between bEPI and sEPI are due to the fact that sEPI readout duration was adjusted for multiples of the sin-modulation wavelength.

Future work will include g-factor estimates and similar investigations using acquired data.

In conclusion, this work indicates that a ultrasonic (inaudible!) sinusoidal modulation can improve the reconstruction of 1D-accelerated acquisition schemes.

References:

1 Patent EP 3364205 A1 20180822.
2 Rossing +, Springer Handbook of Acoustics, 2014, Springer. http://www.springer.com/us/book/9781493907540.
3 https://doi.org/10.1002/mrm.25347.
4 Brown +, MRI: Physical Principles and Sequence Design, 2014, Wiley.
5 https://doi.org/10.5281/zenodo.1215477.z

S15.05

Novel passive decoupling approach for high resolution HTS RF coils based on the nonlinear electrical properties of superconductors

I. Saniour[1], G. Authelet[2], B. Baudouy[2], R.-M. Dubuisson[1], C. J. van der Beek[3], L. Darrasse[1], J. Briatico[4], J.-C. Ginefri[1], M. Poirier-Quinot[1]

[1]IR4 M, UMR8081, Université Paris-Sud/CNRS, Université Paris-Saclay, Orsay, FRANCE, [2]Irfu, CEA Paris-Saclay, Université Paris-Saclay, Gif-sur-Yvette, FRANCE, [3]Centre de Nanosciences et de Nanotechnologies, CNRS, Université Paris-Saclay, Palaiseau, FRANCE, [4]Unité Mixte de Physique, CNRS, Thales, Université Paris-Sud, Université Paris-Saclay, Palaiseau, FRANCE

Purpose/Introduction: In µ-MRI, RF high temperature superconducting (HTS) coils can significantly improve the sensitivity of the NMR signal detection[1]. However, conventional decoupling techniques are inefficient for HTS coils; hence, their use in receive-only mode is not possible. We present a decoupling method based on the nonlinear electrical properties of superconductors as a function of the transmitted RF power[2], allowing the material to pass from the superconducting to a dissipative state.

Subjects and Methods: A 12-mm diameter multi-turn HTS surface coil made of $YBa_2Cu_3O_7$ was used. It is cooled by a MR-compatible cryostat[3] integrated in a 1.5 T scanner (Achieva, Philips). A fine-tuning was achieved by controlling the coil's temperature[4]. The HTS coil was used in receive mode only and matched to an oscilloscope for setup 1 and to the MRI scanner for setup 2, using inductive coupling with a pick-up copper coil. The transmitted RF magnetic field (B_1^{trans}) was produced by a volume body coil. Setup 1 allowed the measurement of the induced voltage in the pick-up coil (V_{pickup}) as a function of the intensity of B_1^{trans} during the RF transmission step (B_1^{trans} was increased from 0.08 to 27µT). The pulse duration was calculated to keep the value of the NMR flip angle equal to 1. Measurements were performed with and without the HTS coil (pick-up coil only). The same RF transmission parameters were used in setup 2 for imaging a phantom[4].

Results: Figure 1a shows the field concentration factor CF, which is the ratio of B_1^{trans} over B_1^{pickup}, where the latter was calculated using V_{pickup}= df/dt = $jw_0B_1^{pickup}$ S, with S the surface of the pick-up coil. Without the HTS coil, CF ~ 10 is almost constant for all B_1^{trans} values. In the presence of the HTS coil, CF decreases as a function of B_1^{trans} from a value of about 68 to 10 at 0.05 µT and 5 µT, respectively. For B_1^{trans} higher than 5 µT, CF becomes identical to that without the HTS coil.

For lower values of B_1^{trans}, a deformation is observed in the MR images, whereas for B_1^{trans} = 1, 5 and 10 µT, the signal intensity is homogenous and mean signal-to-noise ratio (SNR) values are relatively high (Fig. 1b, c).

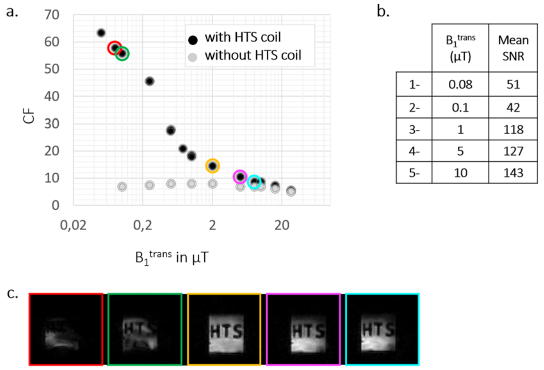

	B_1^{trans} (µT)	Mean SNR
1-	0.08	51
2-	0.1	42
3-	1	118
4-	5	127
5-	10	143

Figure 1. a) CF as a function of B1 transmitted by the body coil. b) Mean SNR as a function of the B1trans. c) (300 µm)3 resolution MR images acquired with TR/TE=21/8.5 ms, FOV=(25 mm)3 and a flip angle of 1 for different values of B1trans.

Discussion/Conclusion: During the RF transmission step, a modification of the superconductor's proprieties was observed by increasing B_1^{trans}. For B_1^{trans} larger than 5 µT, CF was constant *i.e.* the HTS coil was transparent to the B_1^{trans} field (dissipative state).

At 0.08 and 0.1 µT, MR images were deformed due to B_1 produced by the HTS coil during transmission step. The uniformity of the signal intensity and the SNR values presented in Fig. 1b, c for 1, 5 and 10 µT confirms that this decoupling method based on the nonlinear behavior of HTS material is effective and allows the use of HTS coil in receive mode only with standard acquisition sequences.

References:

1.Poirier-Quinot, MRM 2008, 2.Girard, RSI 2007, 3.Authelet, IOP Conf Ser:Mater Sci Eng 2017, 4.Saniour, ISMRM 2019

S15.06

Design, manufacture, and evaluation of a novel T_1 phantom for hand and wrist imaging

D. McHugh[1], R. Lamb[2], L. Trowell[2], A. Walker[2], M. Hall[3], G. Parker[1]

[1]The University of Manchester, Quantitative Biomedical Imaging Laboratory, Manchester, UNITED KINGDOM, [2]Leeds Test Objects Ltd., Boroughbridge, UNITED KINGDOM, [3]National Physical Laboratory, Teddington, UNITED KINGDOM

Purpose/Introduction: Quantitative MRI (qMRI) biomarkers require validation to become useful research tools or be adopted in clinical practice[1]. A number of recent publications have highlighted the role technique- and anatomy-specific phantoms play in this process, by providing a reference standard for evaluating qMRI measurement accuracy and precision[2–5]. Our interest is in T_1-weighted dynamic contrast-enhanced (DCE) MRI biomarkers for inflammatory joint disease (e.g. rheumatoid arthritis) in the hand and wrist, an area lacking readily-available specialised phantom provision. This work aims to address this unmet need by developing a novel T_1 phantom for hand and wrist imaging that will be made available for widespread adoption.

Subjects and Methods: *Design and manufacture*

Coil dimensions and typical scan resolution for hand and wrist DCE-MRI[6] were used to guide the size of the bulk phantom, and the size and spacing of the compartments, respectively (Fig. 1a). Six unique T_1 samples were obtained with $NiCl_2$-doped agarose gels, with the shortest and longest T_1 repeated at three positions (Fig. 1b), allowing assessment of B_1 inhomogeneity and correction methods. The phantom bulk contained degassed, deionised water.

Quantitative MRI

Scans (3T Philips Achieva) included T_1 and B_1 mapping, using variable flip angle (VFA) and actual flip angle imaging[7] (AFI), respectively (Fig. 1c). T_1 mapping was performed with and without correcting for B_1 using the AFI data. Compartment T_1 values were extracted from automatically-generated regions of interest. Test-retest data were acquired, running the protocol back-to-back on three separate days over one month.

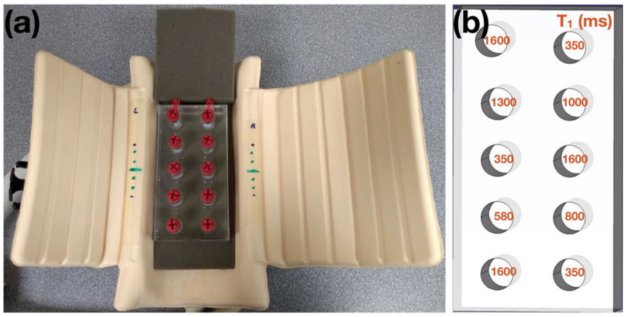

	T_1 mapping	B_1 mapping
Method	Variable flip angle	Actual flip angle imaging
Flip angle (°)	2, 6, 15	60
TR/TE (ms/ms)	4/1.2	[30,150]/2.7
Field of view (mm³)	180 x 135 x 60	180 x 135 x 60
Acquired voxel size (mm³)	1 x 1 x 2.5	2 x 2 x 3
Number of averages	6	2

Fig. 1. (a) Manufactured phantom in small extremity coil. (b) Arrangement of nominal T1 values, approximately covering the range observed in DCE-MRI; 350 ms and 1600 ms are repeated at the ends and centre. (c) Scan parameters for T1 and B1 mapping.

Results: Fig. 2 illustrates the utility of repeated T_1 samples in the phantom, highlighting B_1 inhomogeneity and the improvement in accuracy of the long T_1 samples when correcting for it. Figure 3 shows good scanner short-term T_1 repeatability, as demonstrated using the phantom, with mean coefficients of variation across the six scans of 2% and 0.8% without and with correcting for B_1, respectively.

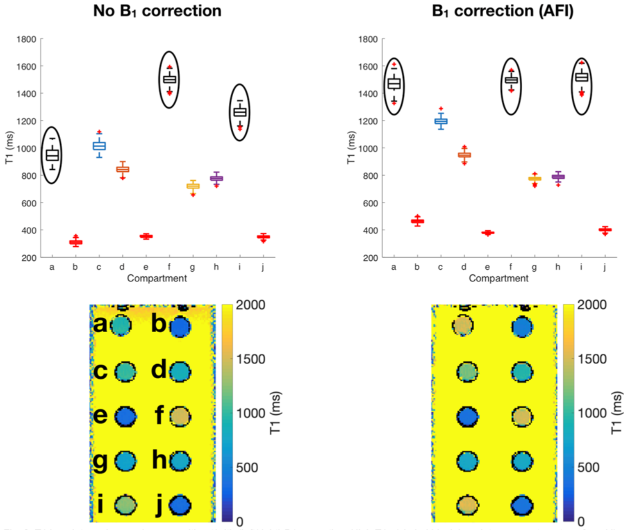

Fig. 2. T1 boxplots and example maps without/with (left/right) B1 correction. High T1s (circled black boxplots, compartments a, f, and i) show large variation depending on their spatial position; this variation is removed by correcting for B1.

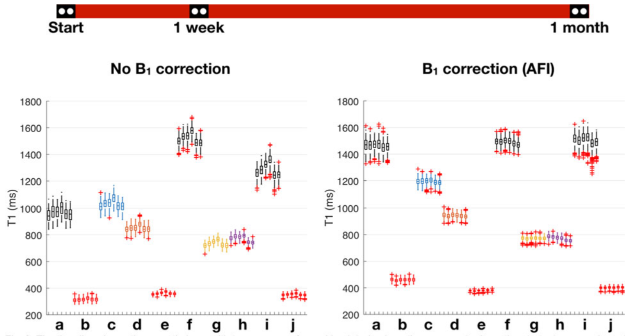

Fig. 3. The time line shows the scan timings, with two scans performed back-to-back on three separate days: the start, at one week, and one month. T1 boxplots for the three sets of test-retest scans, providing six measurements per compartment.

Discussion/Conclusion: qMRI phantoms should be anatomy-specific, and associated with particular acquisition protocols and analysis software[4]. This work has addressed these points in the context of hand and wrist DCE-MRI, by considering details of the coil, acquisition protocol, and anatomy of interest in the phantom design, and developing an automated analysis pipeline. With ongoing work aiming to refine the design, and incorporate metrology standards in manufacture, such a phantom is envisaged to aid longitudinal and multi-centre studies quantifying T_1 and derived biomarkers in the hand and wrist.

References:

[1]O'Connor et al., Nat Rev Clin Oncol 2017;14:169. [2]Sullivan et al., Radiology 2015;277:813. [3]Keenan et al., Magn Reson Med 2018;79:48. [4]Keenan et al., J Magn Reson Imaging 2019. [5]Captur et al., J Cardiovasc Magn Reson 2016;18:58. [6]Waterton et al., Eur Rad 2017;27:3662. [7]Yarnykh, Magn Reson Med 2007;57:192.

S15.07

A five channel transceive array with shielded coaxial loop coils for laryngeal imaging at 7T

I. Zivkovic, T. Ruytenberg, A. Webb
Leiden University Medical Center, Radiology Department, Leiden, NETHERLANDS

Purpose/Introduction: Imaging the larynx in high detail is critical for assessing laryngeal tumors and choosing a treatment plan. It is not easily performed due to extensive movement in the region and the lack of a commercially available coils. Dedicated custom-built receive coils at 3T have shown to be beneficial for image quality.[1, 2] In this work, we present a highly decoupled five channel transceive array at 7T consisting of shielded loop coils.[3] This way we are able to RF shim the larynx for improved TSE imaging.

Subjects and Methods: The transceive array was constructed of 5 shielded loop coils. The array is flexible due to the absence of lumped elements in the loops and was formed to fit the neck of a healthy volunteer. The shielded loop coils with a diameter of 10 cm were constructed from coaxial cable (Huber + Suhner 'K 02252 D-06', diameter 3.0 mm) and were capacitively matched.

For phantom experiments, a single coaxial loop and conventional loop were placed 1 cm above the rectangular phantoms to acquire sensitivity profiles. A 2D gradient-echo sequence was used with the following parameters: TR/TE = 11/4.9 ms, FA = 10^{o}, voxel size = 5 × 5 × 3.75 mm. A 3D gradient-echo sequence was used for heating, and also for performing the thermal measurements: TR/TE = 14/10 ms, FA = 10^{0}, scan duration = 15 min. The 5-channel transceive array was connected to a Philips 7T Multix system and phase RF shimming was performed.

In vivo scans were performed on a healthy volunteer after obtaining written informed consent. Scan parameters: 2D TSE, voxel size 0.7 × 0.7 × 1 mm^3, field of view 150 × 150 mm^2, TR/TE = 1000/7.4 ms, echo train length 15.

Results: Figure 1 shows sensitivity profiles and B_1^+ maps of the proposed transceive coil compared to the conventional elongated coil.

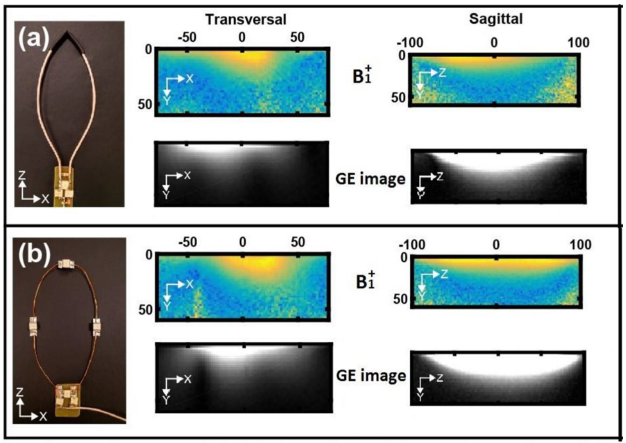

Figure 1. Comparison of the elongated coaxial (a) and elongated conventional coil (b). The power and sequence settings were identical for both coils. The B1+ and gradient echo images were performed.

Figure 2 shows thermal measurements of coaxial and conventional coil. The maximum heating of the coaxial coil was 4.1 °C and of conventional coil was 4.7 °C.

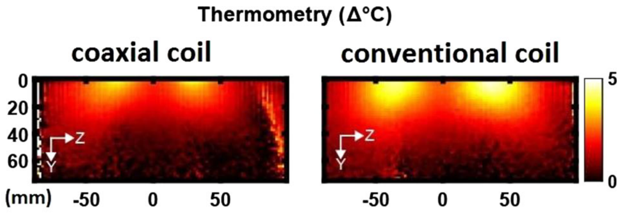

Figure 2. Thermal measurements of (left) coaxial and (right) conventional coil.

Figure 3 shows in-vivo larynx images with a breath-hold.

Figure 3 shows in vivo larynx images with a breath-hold.

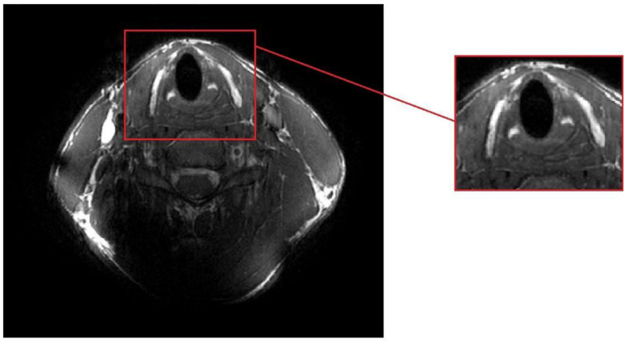

Figure 3. T1 TSE scan of the larynx with a breath-hold. Fine structure is visible in zoomed image.

Discussion/Conclusion: In this abstract transceive array was built for imaging the larynx at 7T, consisting of 5 shielded loops. The thermal measurements confirmed that the proposed coil has similar SAR characteristics as conventional coil and can be safely used as transceive element. We have set a first step in imaging this challenging anatomy in high detail, which becomes more difficult at higher field strengths due to motion induced magnetic susceptibility artefacts. We will be exploring more advanced imaging of the larynx in the future.

Acknowledgements: This work was made possible by NWO domain TTW under grant #13783 and European Research Council Advanced Grant (670629 NOMA MRI).

References:
1. Ruytenberg, T. et al. (2018). Frontiers in Oncology, 8, 216.
2. Van Egmond S. et al. (2019). Laryngoscope Investigative Otolaryngology, 4, 95–101.
3. Demaw D. QST. 1988;4:30–2.

S15.08

The influence of probes positioning for measuring RF-induced 3D-power deposition on a lead with E-field and temperature probes

F. Ketelsen[1], S. Scholz[1], W. Görtz[1], J. Kreutner[2], K. Kröninger[3], G. Schaefers[1]
[1]MR:comp GmbH, Gelsenkirchen, GERMANY, [2]MRI-STaR, Gelsenkirchen, GERMANY, [3]Technical University Dortmund, Dortmund, GERMANY

Purpose/Introduction: RF-induced heating of active implantable devices (AIMDs) is a well-known safety issue in MRI. Guidelines to determine the spatial power deposition are specified in [1]. This study examines the impact of the probe position and orientation on results of E-field and temperature measurements on a generic straight multi-electrode lead.

Subjects and Methods: Spatial power deposition was measured with an E_{rms} probe (SAR Probe, EX3DV4, SPEAG) and a fiber-optic temperature probe (TS5, OPTOCON). The test object (TO) was placed horizontally in a saline solution. Both probes were placed above and beside (lateral) the injected electrode at the smallest possible distance successively (Fig. 1).

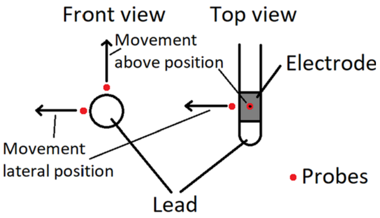

Fig. 1 shows the different probe positions and movement directions in top and front view.

Radial distance was increased up to 10 mm for the E_{rms} probe with increments of 0.2 mm. Additionally, the probe was rotated in 10° steps around its own axis per measurement.

Injected voltage for E-field measurement was maximized for best SNR under consideration of probe calibration.

For temperature measurement, voltage was increased further to get highest possible temperature gradient with given equipment. Injected voltage was applied for 30 s for each distance (increased with ascending steps up to 5 mm total distance). Due to linearity between voltage and electric field or temperature, the data was scaled accordingly for comparison.

Results: Results show a drop of E-field up to 26% when rotating the probe in lateral position around its principal axis (Fig. 2).

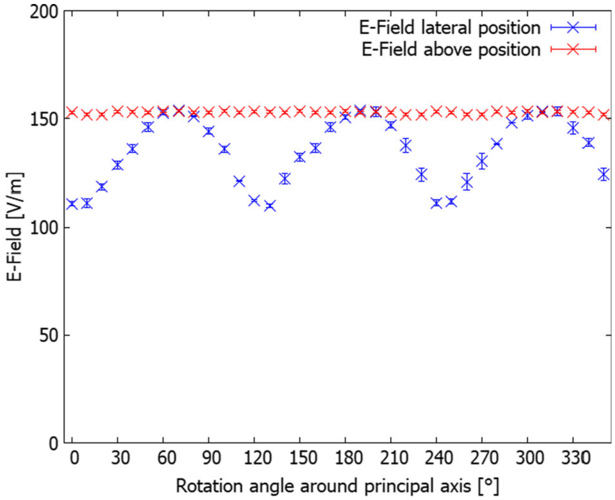

Fig. 2 shows the angle dependency of the E-Field value in both positions, lateral (blue) und above (red).

Furthermore, the decay constant, describing the exponential E-field decrease in radial distance, is up to 13% smaller for e.g. 10° versus above TO. The rotation influences neither the E-field nor exponential function above TO.

The temperature is consistent for both sides of the TO. Above TO, a delayed increase in temperature can be observed for larger distances. To compare above orientation from the E_{rms} probe with the lateral position temperature values, the temperature gradient, which is obtained through a linear regression of 10 s, is converted into E-Field. Results show that the spatial power deposition is radially symmetric, considering that the sensitive element of the E_{rms} probe was further away from the electrode than temperature sensor (Fig. 3).

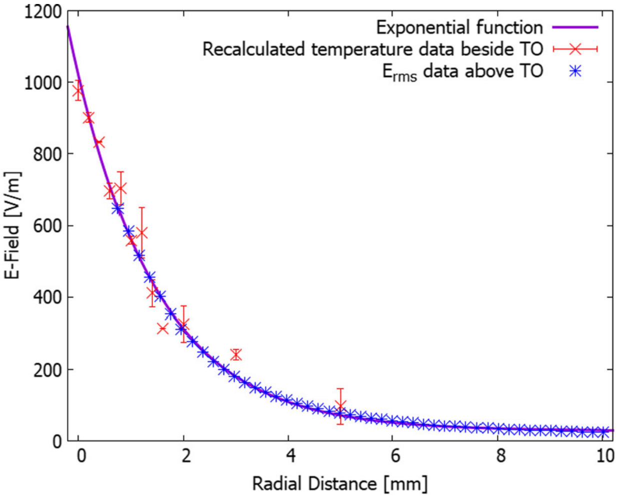

Fig. 3 shows that the recalculated temperature values (red) and the Erms values (blue) can be described with the same exponential function (violet), obtained by a fit based on Erms data.

Discussion/Conclusion: The influence of probe position for measuring spatial power deposition for both methods is shown. At lateral position, E_{rms} probe provides no reproducible results due to the strong angle dependency. This can lead to a drastic underestimation of the safety hazard.

The opposite is true for the temperature probe. By convection, the results are distorted at a greater distance above TO. This leads to an overestimation of power deposition.

The validity of the radial symmetry of the spatial power deposition was shown and is a necessity for the applicability of both probe types.

References:
ISO/TS 10947 Assessment of the safety of magnetic resonance imaging for patients with an active implantable device, 2018

S15.09

Global head SAR assessment of MRI-induced temperature change

J. Blackwell[1], G. Oluniran[1], M. Krasny[1], B. Tuohy[2], **N. Colgan**[1]
[1]National University of Ireland Galway, Physics, Galway, IRELAND,
[2]Galway University Hospital, Galway, IRELAND

Purpose/Introduction: Underestimation of SAR (Specific Absorption Rate) in MRI poses potential risks to patients and in particular individuals with compromised thermoregulation (1–2). EU standards imposes a head SAR limit of 3.2 W/kg as SAR effects are negligible at up to 3 W/kg (3). We developed a phantom and protocol where heating due the RF pulse is measured and verified against scanner displayed SAR.

Subjects and Methods: The spherical 3-Litre phantom comprised of agar (60 g/L), NaCl (10 g/L) and CuSO4 (1 g/L) dissolved in distilled hot water. T1 properties of the phantom were determined at room temperature using a STIR sequence. The phantom was manufactured to achieve thermal equilibrium. A baseline image is acquired using a 2D fast gradient echo. SAR loading is generated with a clinical 3D FLAIR sequence followed by a repeat 2D fast gradient echo. Our phantom is nonperfused, and the period of heating is relatively short. Thus, physiological and conduction effects are ignored(4). Temperature maps were generated using Proton Resonance Frequency Shift (PRF) thermometry(5). Global SAR was estimated by averaging temperature changes over the whole phantom and compared to the scanner's SAR display. The procedure was repeated for five independent scanners.

Results: WE process each scanner using a FLAIR sequence to generate the RF depositon. The results are in Table 1

scanner model	sScanner SAR readout [W/Kg]/	Calculate SAR [W/Kg]	Percentage error %
GE 1.5T Signa Explorer	0.42	0.41	2.3
Siemens 1.5T Symphony	1.88	1.90	1
Philips 3T Achieva	1.52	1.52	
GE 1.5T Signa Explorer	0.55	0.55	1
Siemens 1.5T Magnetom Sola	1.50	1.49	1.2

SAR measurements from individual scanners

Discussion/Conclusion: We have found that our SAR estimates are in good agreement with the MRI scanner displayed data. We have developed a phantom that can independently verify MRI SAR

References:
(1) Shellock FG. Radiofrequency energy-induced heating during MR procedures: a review. J Magn Reson Imaging. 2000;12(1):30–6.
(2) Crook N et al., A review of the safety implications of magnetic resonance imaging at field strengths of 3 Tesla and above. Radiography. 2009;15(4):351
(3) https://www.accessdata.fda.gov/scripts/cdrh/cfdocs/cfres/res.cfm?id = 140518
(4) Wang, Z., Lin, J., Vaughan, J. and Collins, C. (2008). Consideration of physiological response in numerical models of temperature during MRI of the human head. *Journal of Magnetic Resonance Imaging*, 28(5), pp.1303–1308.
(5) Rieke, V. and Butts Pauly, K. (2008). MR thermometry. *Journal of Magnetic Resonance Imaging*, 27(2), pp.376–390.

S16 Scientific Session

15:40–17:10 *Room 4 - Plate & Van der Vorm Zaal*

Animal Models: Brain & Others

S16.02

Analysis of resting state connectivity with graph theory reveals network changes in a rat model of absence epilepsy

L. Wachsmuth[1], K. Kemper[1], F. Albers[1], H. Lambers[1], M. Datunashvili[2], A. Lüttjohann[2], S. Kreitz[3], T. Budde[2], C. Faber[1]
[1]*University of Muenster, Clinical Radiology TRIC, Muenster, GERMANY,* [2]*University of Muenster, Physiology I, Muenster, GERMANY,* [3]*University of Erlangen, Erlangen, GERMANY*

Purpose/Introduction: Genetic Absence Epilepsy Rats from Strasbourg (GAERS) represent an established animal model for childhood absence epilepsy[1]. Absences show characteristic spike and wave discharges (SWD) in electrophysiological or optical recordings. In adult GAERS prevalence of absence seizures is 100%. Absences occur up to several hundred times per day, characterized as periods of behavioral immobility. Increased anxiety and learning impairments have been reported[2]. The objective of this study was to apply graph theory analysis to resting state fMRI data to reveal potential changes in neuronal networks between GAERS and nonepileptic control rats (NEC).

Subjects and Methods: Adult female GAERS (n = 16) and NEC (n = 12) were intracranially injected with the chemical calcium sensor OGB-1 into M1 under isoflurane (Iso). A 200 µm optic fiber was implanted for SWD monitoring during fMRI. Ventilated, paralyzed rats were transferred to a 9.4T MRI. Anesthesia was switched to Narcolept (15 µg/kg fentanyl and 1.5 mg/kg droperidol i.p., every 20 min). BOLD fMRI was performed (GE-EPI, TR 1 s, TE 18 ms, resolution 0.32 × 0.35 mm^2, slice thickness 1.2 mm, 30 min) under Narcolept in the pre-seizure state, during seizure state and lastly 20 min after going back to 1.5% Iso which suppresses SWDs. Here, only Iso data were considered. Preprocessed data (SPM realign and reslice) were analyzed with MagnAn (BioCom, Uttenreuth). Brain regions were defined according to an anatomical template. Cross-correlation matrices of regional time courses were averaged and thresholded to reveal the 10 strongest connections per brain region. Networks were created with Gephi (open source) and communities[3] and betweenness centrality[4], indicating how many shortest paths pass through a node, were calculated.

Results: Two major changes in community affiliations become apparent in network graphs of NEC and GAERS: First, cortical regions, yellow in NEC, split into two communities, yellow and violet in GAERS, indicating a segregation into neo- and paleocortex. Second, the community comprising regions of the limbic system (green) integrate more nodes in GAERS, indicating higher connectivity between these regions.

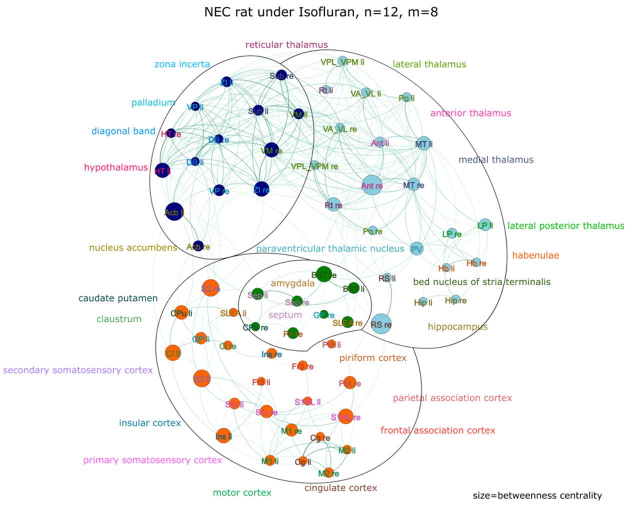

Force based network graphs of NEC rat under Iso. Nodes represent brain regions, edges indicate connections. Node size codes betweenness centrality. Black contours and node color isolate the different communities.

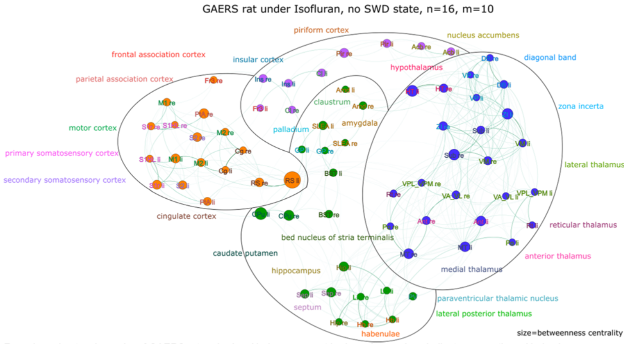

Force based network graphs of GAERS rat under Iso. Nodes represent brain regions, edges indicate connections. Node size codes betweenness centrality. The black contours and node color isolate the different communities.

Connectivity strength is overall lower in GAERS when compared to NEC except for hippocampus. Stronger connections between thalamus and hippocampus may balance lower connections to neocortex. Interhemispheric differences in betweenness centrality indicate that laterality of brain networks may also be affected by absence seizures.

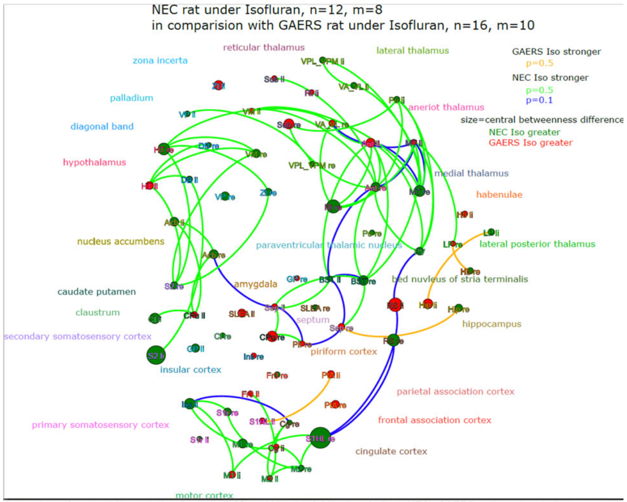

Comparison of connectivity strengths: Green (p<0.05) and blue (p< 0.01) edges indicate NEC >GAERS, yellow edges indicate NEC< GAERS. Node size codes difference in betweenness centrality, green: NEC > GAERS, red: GAERS > NEC.

Discussion/Conclusion: Graph theoretical analysis identified differences in resting state connectivity in cortex and limbic system, involved in anxiety, memory and learning processes[5].

References:

1. Depaulis A, J Neurosci Methods (2016);260:159–74.
2. Marks WN, Eur J Neurosci (2016);43(1):25–40.
3. Blonde l, J Stat Mech (2008) P10008.
4. Brandes U, J Math Sociol (2001) 25:163–77.
5. Vann SD, Nat Rev Neurosci (2009) 10(11):792–802.

S16.03

Brain state and CSF production define glymphatic washout in the rat brain

M. Segeroth[1], L. Wachsmuth[1], A. Heß[2], F. Albers[1], C. Faber[1]
[1]WWU Muenster, Translational Research Imaging Center, Muenster, GERMANY, [2]BioCom GbR, Uttenreuth, GERMANY

Purpose/Introduction: The Glymphatic System has been identified as a brain-wide paravascular pathway for waste clearance[1, 2]. Cerebrospinal fluid (CSF) elutes soluble proteins and waste, but whether CSF travels by bulk flow through parenchyma, or distributes along arteries and exchanges with interstitium by diffusion is still investigated. Clearance intensifies during sleep and several studies report an impact of depth and type of anesthesia, brain state, and CSF formation. We applied different MRI-techniques to systematically study glymphatic clearance in rat under three different anesthetic regimens and in various brain regions.

Subjects and Methods: MRI at 9.4T was performed under Isoflurane (ISO) (n = 8); Medetomidine (MED) (n = 7) or ISO + MED (n = 8). Gadovist (21 mM, 50 min continuous infusion of 1.6 µl/min) was administered via a modified venous catheter, implanted into the cisterna magna. At least 40 T1weighted (T1w) 3D-FLASH scans were acquired during 6 h and registered on a modified Waxholm Space Atlas (79 Regions). Additional experiments were performed with intubated animals (ISO n = 6, MED n = 6, ISO + MED n = 7; 53 breaths/min). We acquired apparent diffusion coefficient (ADC) maps in brain parenchyma and aqueduct, T2weighted (T2w) images to assess size of subarachnoidal space, and time of flight (TOF) angiograms. In some animals (n = 11) brain state was simultaneously monitored by optical recordings with the genetically-encoded Ca-indicator GCaMP.

Results: Optical calcium recordings revealed slow wave sleep-like brain state under ISO and ISO + MED. Awake like brain state was observed under MED. Glymphatic activity, indicated by signal changes in T1w scans, tends to higher signal amplitudes and areas under curve under MED and ISO + MED compared to ISO and faster distribution towards the olfactory bulb(OB) resulting in a better CSF intrusion into brain parenchyma under MED. This is achieved by bigger subarachnoidal spaces in T2w scans with higher ADC values in aqueduct confirming higher CSF formation under MED and ISO + MED than under ISO. Significantly smaller arteries in TOF scans under these anesthetic regimens may lead to an increase of paravascular space. ADC in cortex was lowest under MED followed by ISO + MED as compared to ISO. The decay rates were faster under MED compared to ISO + MED in neocortex and OB. Cell swelling due to higher neural activity under MED may hinder diffusion in brain parenchyma in the awake state.

Discussion/Conclusion: Our data support the notion that the interstitium is cleared via fast dispersion along cerebral arteries and diffusion of CSF. The size of the arteries in combination with the rate of CSF formation determines CSF intrusion, but the interstitial clearance correlates with brain state. Increased CSF production and brain state must therefore be taken into account, to explain enhanced glymphatic clearance during sleep.

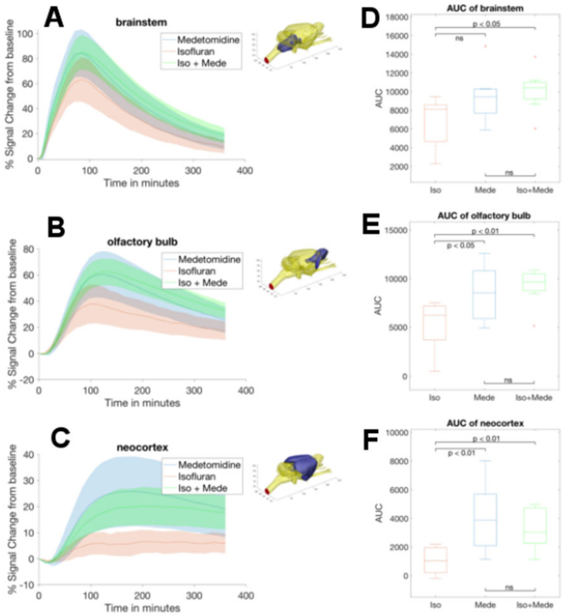

Contrast enhanced MRI after Gadovist administration into cisterna magna. Time-Signal curves (A-C) reveal signal increase under MEDE (blue), ISO (red) and ISO+MEDE (green) (mean ± confidence interval). (D-F) represents the area under the curve (AUC).

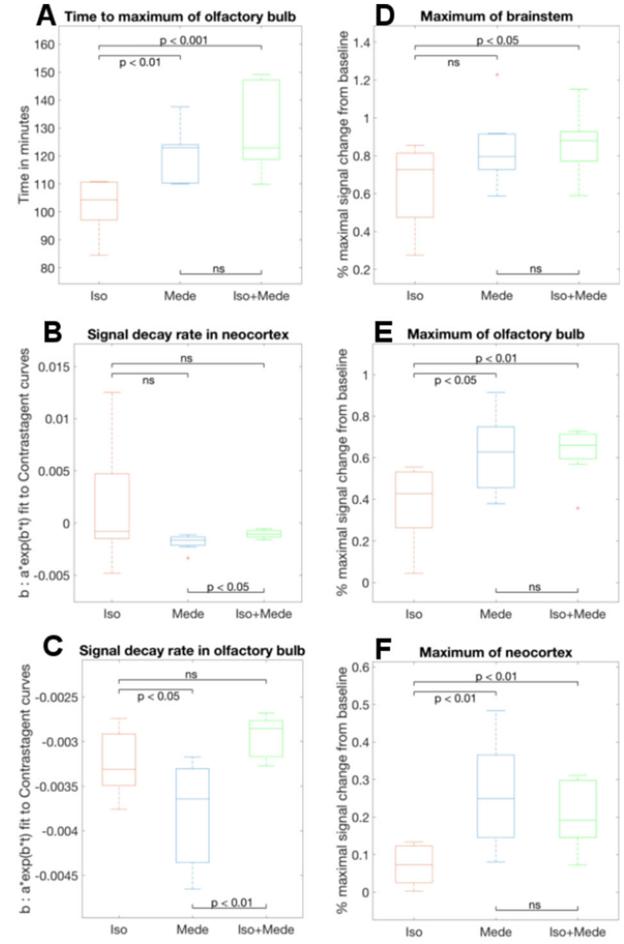

(A) time to peak in olfactory bulb (B,C) signal decay rates after reaching the maximum (D-F) Maximum signal change from baseline tending to higher signal enhancement under MEDE and ISO+MEDE compared to ISO.

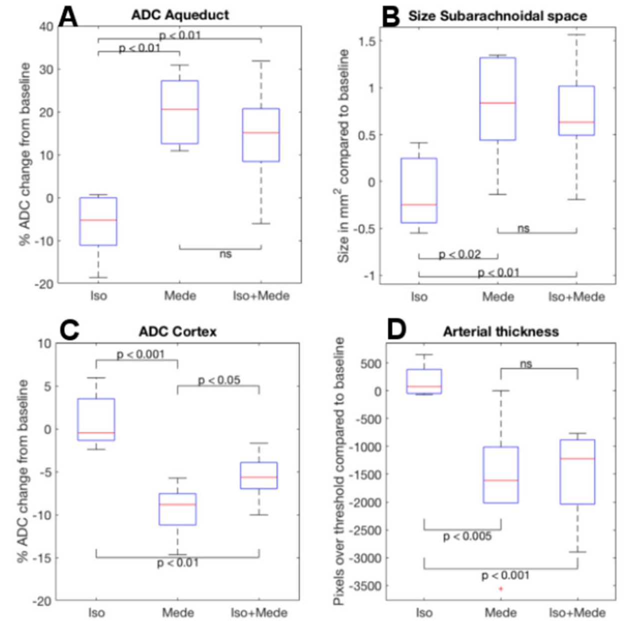

(A) ADC reduction in the aqueduct, indicating higher diffusion under MEDE and ISO+MEDE compared to ISO (B) increase in the size of the subarachnoidal space (C) ADC reduction in a cortical ROI (D) thickness of the arteries.

References:

1 Iliff et al. Sci Transl Med. 2012.
2 Abbott et al. Acta Neuropathol. 2018.

S16.04

Brain activity in an animal model of paclitaxel- induced neuropathic pain

J. T. Costa-Pereira[1], R. Oliveira[1], **I. Guadilla**[2], M. J. Guillén[2], I. Tavares[1], P. López-Larrubia[2]
[1]Faculty of Medicine of University of Porto, Department of Biomedicine, Experimental Biology unit, Porto, PORTUGAL, [2]CSIC-UAM, Instituto de Investigaciones Biomédicas "Alberto Sols", Madrid, SPAIN

Purpose/Introduction: Paclitaxel (PTX) is widely used for cancer treatment but also causes numerous deleterious effects. Chemotherapy-induced neuropathy (CIN) is one of the most common complications and neuropathic pain arises frequently as drawback [1]. The mechanisms underlying pain during CIN are starting to be uncovered namely the alterations at the peripheral nervous system [2]. However, the effects of cytostatic at the central nervous system remain poorly understood. This experimental work aimed to evaluate the effects of PTX on neuronal activation in brain areas involved in pain modulation using functional magnetic resonance imaging (fMRI) approaches.

Subjects and Methods: Wistar rats were intraperitoneally injected in 4 alternate days with PTX (2 mg/ml), 4% dimethyl sulfoxide (DMSO)(vehicle) or saline. Imaging studies were performed at 0 (T0), 28 (T28) and 56 days (T56) after CIN induction in a 7T MRI system. Rats were anaesthetized with isoflurane (1–1.5%, 1L/min O_2). Before scanning, mechanical nociceptive stimulation was applied to the hindpaw.

Diffusion images were acquired in 3 directions with 9b values (0–1800 s/mm^2) and TR/TE = 3000/31 ms, 4-s EPI readouts, Δ/δ = 20/4 ms, 0.164 mm^2/pixel, slice-thickness 1.5 mm, axial orientation. Magnetization transfer (MT) images were acquired with TR/TE = 2500/10 ms and MT train: 50 pulses, 5.5μT, 5 ms, offset 1500 Hz. Images were computed with homemade program software to yield parametric maps, and ROIs were manually selected.

Rats were sacrificed at T56 with a focused high-power microwave (5000 W). ^{1}H HR-MAS spectra of dissected brain regions were acquired in a 11.7T with a CPMG sequence and processed with LCModel.

Results: PTX treatment induced a significantly decrease of MT ratio (MTR) percentage at T28 compared with T0 in PAG and hypothalamus (Fig. 1). A significant increase of apparent diffusion coefficient (ADC) values was observed in periaqueductal gray (PAG) at T28 and T56 in PTX group compared with vehicle group. However, the thalamus and hypothalamus showed a decrease of ADC values over time (Fig. 2). A higher statistic difference on Fast Diffusion Coefficient (FDC) values in hypothalamus and thalamus was observed at T56 between saline and PTX groups. The PAG showed a Slow Diffusion Phase (SDP) significantly higher in PTX group at T56 compared with T0. In hypothalamus, a significant decrease of SDP was detected in PTX group at T56 compared with saline group and paclitaxel treatment at T28 (Fig. 3). Some detected metabolites in thalamus and hypothalamus, namely taurine, changed throughout of three experimental groups.

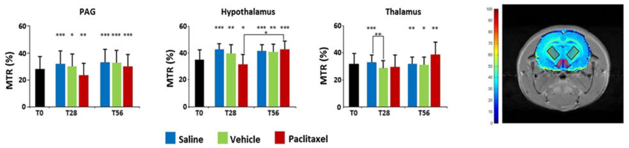

Figure 1. Magnetization Transference (MT) evaluation represented as percentage. The values corresponded to different regions (PAG, hypothalamus and thalamus) in the three different time point: T0 (baseline, no treatment), T28 (28 days after CIN induction) and T56 (56 days after CIN induction). Areas in representative MT map show the hypothalamus (red) and thalamus (black).

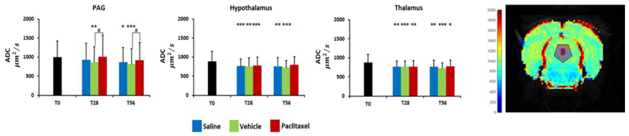

Figure 2. Apparent Diffusion Coefficient (ADC) values obtained from DWI studies in PAG, hypothalamus and thalamus. T0 corresponds with the values of all the studies before the different treatments: saline (blue), vehicle (green), and paclitaxel (red). Representative ADC map shows PAG (shaded).

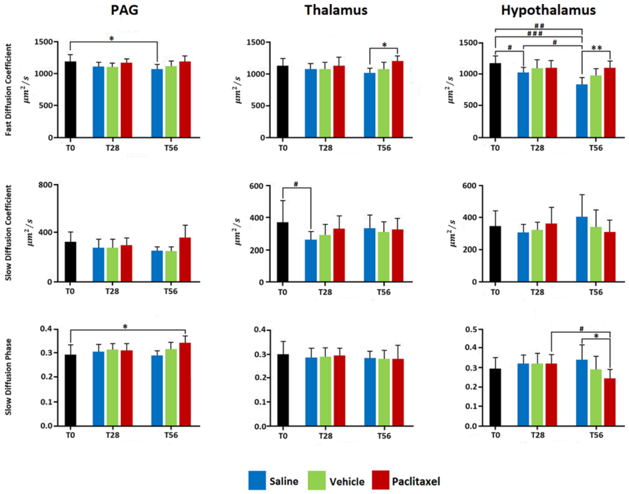

Figure 3. Functional Diffusion by a biexponential fitting of the signal in PAG, thalamus and hypothalamus. Three parameters are represented: Fast Diffusion Coefficient (FDC, up), Slow Diffusion Coefficient (SDC, center) and Slow Diffusion Phase (SDP, down).

Discussion/Conclusion: Our results point to changes in PAG, a key area involved in pain modulation, during PTX-induced CIN. A new finding of this study is the changes in the activity of the hypothalamus, which is crucial homeostatic center.

References:

[1] Polomano, et al. Pain 2001;94(3):293–304.
[2] Sisignano, et al. Nat Rev Neurol 2014;10(12):694–707.

S16.05

Graph-theoretical network analysis in an absence epilepsy rat model using rs-fMRI data

K. Kemper[1], L. Wachsmuth[1], F. Albers[1], H. Lambers[1], D. Thomas[1], M. Datunashvili[2], A. Lüttjohann[2], T. Budde[2], C. Faber[1]
[1]Westfälische Wilhelms-Universität Münster, Institute for Clinical Radiology Translational Research Imaging Center (TRIC), Münster, GERMANY, [2]Westfälische Wilhelms-Universität Münster, Department of physiology I, Münster, GERMANY

Purpose/Introduction: Absence seizures are non-convulsive, brief periods of impaired consciousness which are accompanied by large-amplitude synchronized spike-and-wave discharges (SWDs). We acquired brain-wide resting state fMRI data from SWD free periods and SWD periods in Genetic Absence Epilepsy Rats from Strasbourg (GAERS). Networks were calculated using graph theory to analyse differences between the pre-SWD and SWD state to detect targets for future optogenetic intervention in the functional networks.

Subjects and Methods: FMRI with simultaneous fibre-based fluorescence monitoring of SWDs[1] was performed in n = 10 ventilated and relaxed GAERS at 9.4 T under Fentanyl/Droperidol anaesthesia (60 µl/120 µl, every 20 min) using a GE-EPI (TR 1 s, TE 18 ms, resolution 0.32 × 0.35 mm^2, 1.2 mm slices, 9 slices, 30 min scan time). FMRI was acquired prior to and after SWDs onset (after 116 ± 27 min). In SWD state, SWDs were detected during 40–80% of the time. Data were pre-processed (realign (SPM), smooth, filter, mask, global residual (MagnAn package, BioCom, Germany)) and registered to brain regions according to the Paxinos and Watson rat brain atlas. Networks were created out of cross correlation matrices (averaged and thresholded to on average 10 connections per brain region). Communities[2] and the network parameter betweenness centrality[3], indicating how many shortest connections pass through a node, were calculated (Gephi). Significantly different connections between pre-SWD and SWD state were assessed using a T-Test between the respective correlation matrices.

Results: The thalamus was strongly connected in both networks (Figs. 1 and 2). The average degree of thalamic nodes was 13 ± 6 in pre-SWD state compared to 9 ± 4 in non-thalamic regions.

Compared to pre-SWD state, during SWD state more intrathalamic connections were observed (degree 16 ± 4), suggesting increased internal processing, which may result in a lower accessibility for external influences[5] (fig. 3).

The retrosplenial cortex (RS) seemed to function as a connection between a thalamic group (green) and a cortical group (orange) because of the high betwenness centrality (Fig. 2). This region has been related to neurodegenerative diseases[6].

Another region of interest is the bed nucleus of stria terminalis (BST) which has a high increase in betwenness centrality and in connections (Fig. 3), a region that has been related with anxiety or stress[7] respectively.

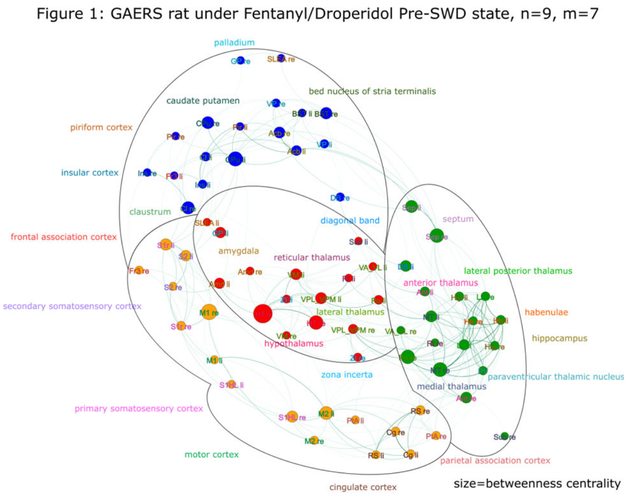
Figure 1: GAERS rat under Fentanyl/Droperidol Pre-SWD state, n=9, m=7

size=betweenness centrality

Force based network arrangement of GAERS in pre-SWD state. Nodes represent brain regions; the size indicates the betweenness centrality. The edge colour represents the weight. Communities are shown in one colour and marked with black lines.

Figure 2: GAERS rat under Fentanyl/Droperidol during SWD state, n=14, m=8

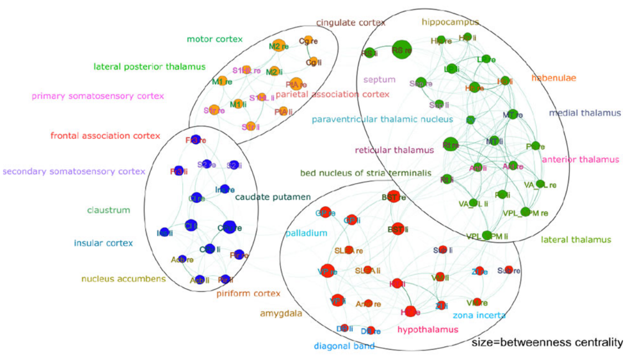

Force based network arrangement of GAERS in SWD state. Nodes represent brain regions; the size indicates the betweenness centrality. The edge colour represents the weight. Communities are shown in one colour and marked with black lines.

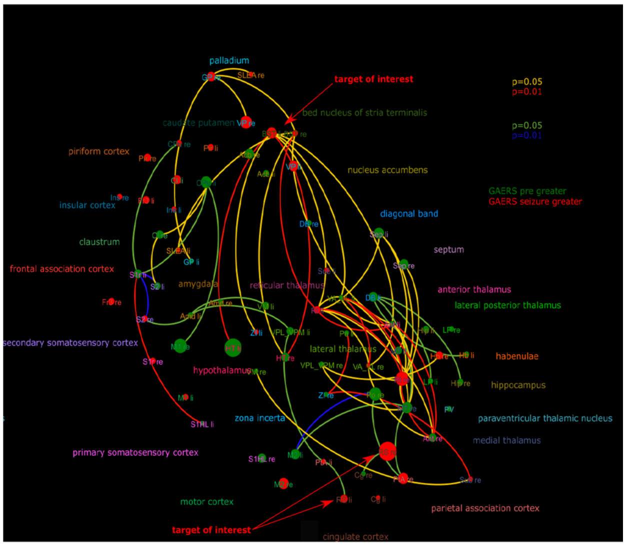

On the network arrangement of pre-SWD, the differences between pre-SWD and SWD state are highlighted. Edge colours indicate range of p-value of the T-Test. Nodes colour and size show difference in betweenness centrality.

Discussion/Conclusion: Graph theoretical analysis revealed new brain regions such as RS or BST affected by seizure onset. These regions will be targeted in further electrophysiological examinations.

References:

[1] Albers F, MIB (2018) 20(2):171–182.
[2] Blondel V, J Stat Mech (2008) (10), P1000.
[3] Brandes U, J Math Sociol (2001) 25:163–77.
[4] Kleinberg J, JACM (1999) 46(5):604–632.
[5] Lüttjohann A, Front Physiol (2015) 6:16.
[6] Vann SD, Nat Rev Neurosci (2009) 10(11):792–802.
[7] Somerville L, Biol Psychiatry (2010) 68(5):416–424.

S16.06

Oscillatory pattern of response in MRSI-based Glioblastoma therapy follow-up: an immune system biomarker?

L. Villamañan[1], P. Calero[1], S. Wu[1], N. Arias-Ramos[1], S. Ortega-Martorell[2], M. Pumarola[3], M. M. Julià-Sapé[4], C. Arús[1], **A. P. Candiota**[4]

[1]Department of Biochemistry and Molecular Biology, Biosciences Faculty, Universitat Autònoma de Barcelona, Cerdanyola del Vallès, SPAIN, [2]Department of Applied Mathematics, Liverpool John Moore University, Liverpool, UNITED KINGDOM, [3]Department of Animal Medicine and Animal Surgery, Veterinary Faculty, Universitat Autònoma de Barcelona, Cerdanyola del Vallès, SPAIN, [4]Centro de Investigación Biomédica en Red, Department of Biochemistry and Molecular Biology, Biosciences Faculty, Universitat Autònoma de Barcelona, Cerdanyola del Vallès, SPAIN

Purpose/Introduction: Glioblastoma (GB) is the most common primary malignant brain tumour with poor prognosis even after aggressive therapy (Temozolomide, TMZ, plus radiotherapy). When using volumetric MRSI coupled to a pattern recognition approach in a longitudinal GL261 GB preclinical study, an oscillatory pattern of response to TMZ was detected with 6–7 days periodicity [1], which we hypothesize relates to the immune system cycle participation in response as described by others [2]. The purpose of the present study was to evaluate response to another schema of TMZ administration and to characterize the cellular populations contributing to the MRSI response pattern upon TMZ therapy.

Subjects and Methods: GL261 GB tumours were induced in C57BL/6j mice ($n = 15$) and TMZ administered every 6 days at 60 mg/kg ($n = 12$) as in [3], while $n = 3$ were controls. High-resolution T2w MRI and consecutive 14 ms TE MRSI with 3–4 grids were acquired every 2 days [1]. A semi-supervised NMF methodology was applied for calculating nosologic maps [4] and the tumour responding index (TRI) [1]. Mice were euthanized by cervical dislocation. Immunostainings for CD3 (T cells) and Iba-1 (microglia/macrophages) characterization were performed in 6 additional mice from [1] and analyzed with NDPView and Image J.

Results: TRI oscillations (6.0 ± 1.3 days, Fig. 1) were confirmed in mice treated with the every-6-days TMZ administration ($n = 3$), in agreement with 6.3 ± 1.3 days reported in [1].

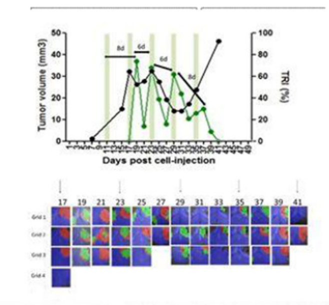

Color-coding of nosological images: Blue, normal brain; Red, non-responding tumour; Green, responding tumour.

Top: Tumour volume (black line), and percentage of responding pixels (TRI, green line) for case C1264. Green columns indicate TMZ administration day. Bottom: nosological images superimposed to the T2w-MRI. Arrows indicate TMZ administration da

Significant differences ($p < 0.05$) were found for CD3 (4.8 ± 2.9 vs 3.3 ± 2.5 positive cells/field) and Iba-1 (21.9 ± 11.4 vs 16.8 ± 9.7% of immunopositive areas), respectively between the responding and non-responding areas predicted by the NMF, Figs. 2 and 3. Responding zones achieved up to 42% Iba-1 immunopositivity, in contrast with a minimum of 1.4% in control/unresponsive.

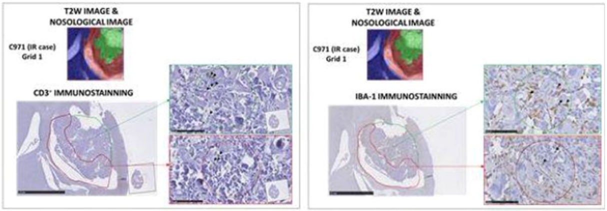

Example of CD3 (left) and Iba-1 immunostaining (right) in different analysed fields of case C971 (TMZ-treated) originating from green (responsive) and red (unresponsive) zones. Arrows point to positive cells.

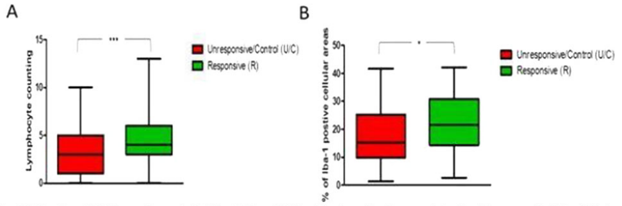

Boxplot showing: A) CD3+ positive cells/field (n=147) and B) % of Iba-1 positive immunostained cellular areas /field (n=148), in red and green areas of MRSI grids of treated and control cases.

Discussion/Conclusion: The 6-day TMZ administration schedule caused the TRI to oscillate at a frequency (ca. 6 days) agreeing with the mouse immune system cycle [5], accordingly, MRSI spectral changes could be reflecting immune system presence/activation/action against GL261 tumours. Immunohistochemistry showed higher number of T-lymphocytes and microglia/macrophages in zones classified by NMF as "responding". Since macrophages can represent up to 30% within GB tumour mass [6], they could be partially contributing to spectral pattern changes. Indeed, the participation of the immune system in TMZ therapeutic effects has been described [2]. Results suggest that in this model, the MRSI response pattern could act as an immune system biomarker.

References:

1. Arias-Ramos N et al. Metabolites (2017) 7: pii:E20.
2. Kim TG et al. Clin Vaccine Immunol (2010) 17:143–53.
3. Ferrer-Font L et al. Pharmaceuticals (Basel) (2017) 10: pii:E24
4. Delgado-Goñi T et al. NMR Biomed (2016) 29:732–43.
5. Karman J et al. J Immunol (2004) 173:2353–61.
6. Glass R and Synowitz M. Acta Neuropathol (2014) 128:347–62.

S16.07

Characterization of long-term cerebral alterations in a mouse model of in utero high dose irradiation using anatomical and diffusion MRI

L. Mouton[1, 2], O. Etienne[3], D. A. Barrière[4], E. Pérès[5], F. Boumezbeur[4], F. Boussin[6], D. Le Bihan[4]
[1]*CEA/NeuroSpin, Gif sur Yvette, FRANCE,* [2]*CEA/NeuroSpin/Frédéric Joliot Institutes, Gif sur Yvette, FRANCE,* [3]*Stem Cells and Radiation, CEA, INSERM, Université Paris Sud, Université de Paris, LRP, UMR Genetic Stability, Fontenay-aux-Roses, FRANCE,* [4]*CEA/NeuroSpin/Frédéric Joliot Institute, Gif sur Yvette, FRANCE,* [5]*Normandie Univ, UNICAEN, CEA, CNRS, ISTCT/CERVOxy group, UMR6030 GIP CYCERON, Cean, FRANCE,* [6]*Stem Cells and Radiation, CEA, INSERM, Université Paris Sud, Université de Paris, LRP, UMR Genetic Stability, Fontenay-aux-Roses, FRANCE*

Purpose/Introduction: *In utero* exposure to ionizing radiation can lead to long-term cerebral alterations in adulthood [1]. Magnetic Resonance Imaging (MRI) has demonstrated its ability to non-invasively assess radio-induced structural and microstructural brain damage [2–4]. This study aims at developing and validating new tools to characterize those cerebral alterations using anatomical and diffusion MRI.

Subjects and Methods: Pregnant C57BL/6 N mice were irradiated on the 14.5th gestational day (E14.5) with a dose of 1 Gy from a ^{137}Cs source with a medical irradiator. At 3 months-old, irradiated ($N_{IRR} = 13$) and non-irradiated ($N_{Sham} = 21$) male offsprings were imaged using an 11.7 T MR scanner. The MRI protocol consisted in the acquisition of: (i) a whole-brain 3D T_2*-weighted anatomical images and (ii) a diffusion MRI (20 b-values: 0–3000 s/mm^2 along 6 directions). Figure 1 illustrates our ROIs-based semi-automatic pipeline analysis performed on: (i) anatomical images and (ii) diffusion parametric maps (MD, Kurtosis, FA, S-index [4–5]) to evaluate respectively volumetric and microstructural changes.

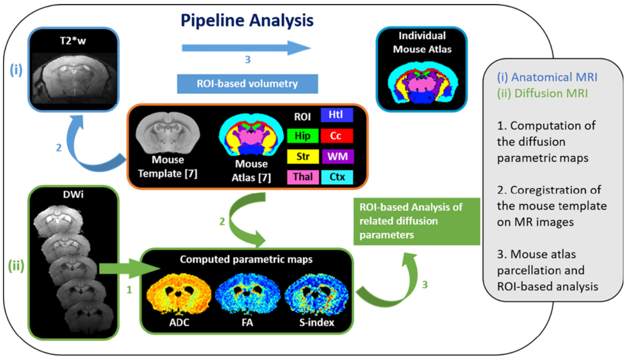

Figure 1: Major steps of anatomical (top, blue) and diffusion weighted images (bottom, green) analysis by using an in-house atlas of the mouse brain (middle, orange).

Statistical significance between irradiated and sham cohorts were assessed using a Student's t-test. A radio-sensitivity map was also computed based on the relative amplitude of the atrophies for the considered brain parcellation.

Results: As shown in Fig. 2, global brain atrophy (– 10%, $p < 0.005$) was observed in irradiated cohort. Except in the cerebellum, all the ROIs presented atrophies ranging from 5 to 25% with the largest ones observed in the corpus callosum, cortex and olfactory bulbs.

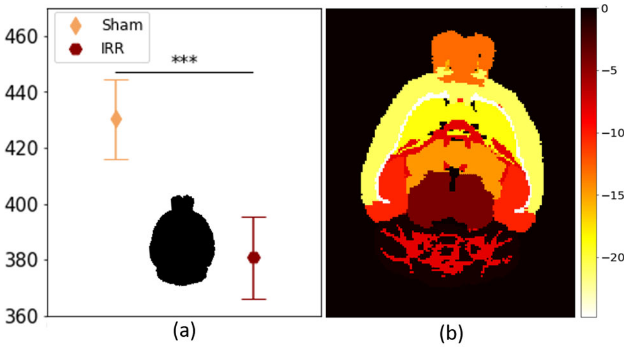

Figure 2: a) The whole brain volume Sham (430 ± 14 mm^3) and IRR (381 ± 15 mm^3) mice (mean ± std). b) Radio-sensitivity map (%) of the mice exposed to 1Gy *in utero* compared to Sham mice. Student's t-test was computed between Sham and exposed to 1Gy *in utero* mice : *** p<0.005.

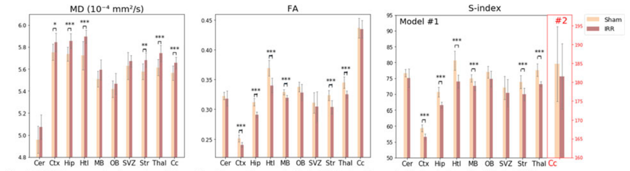

Figure3: Diffusion parameters by region of interest for Sham and exposed mice to 1Gy *in utero* (mean ± std). Cerebellum (Cer), Cortex (Ctx), Hippocampus (Hip), Hypothalamus (Htl), MidBrain (MB), Olfactory Bulb (OB), Subventricular zone (SVZ), Striatum (Str), Thalamus (Thal) and Corpus Callosum (Cc). Student's t-test was computed between Sham and exposed to 1Gy *in utero* mice : *** $p<0.001$; ** $p<0.05$. Left : Mean Diffusivity, Middle : Fraction Anisotropy, Right : S-index calculated with model #1 in grey matter (isotropic) areas and model #2 in Cc (anisotropic)

In parallel, significant differences in diffusion parameters were observed: increased MD combined to decreased FA and S-index values in irradiated mice compared to sham mice (Fig. 3).

Discussion/Conclusion: These results are similar to Verreet's work demonstrated that in utero (E14.5) exposure to substantial ionizing radiations (1 Gy) induced neurogenesis impairment leading to both a microcephaly and reduced cellular or axonal density at the adult stage [1]. Our semi-automatic analysis pipeline allowed the precise and robust estimation of widespread volumetric and microstructural alterations, consistent with the diverse cognitive and behaviour deficits (decreased activity, deficit in spatial learning and memory) observed by Verreet et al. [1, 6]. As in our previous study [3], S-index is the most sensitive diffusion metric to detect radiation-induced brain damages. In conclusion, this study paves the way for MRI investigations of cerebral dysplasia in children following therapeutic irradiation.

References:

[1] Verreet T et al., Front Behav Neurosci 2016; [2] Gazdzinski L et al., Int J Radiat Oncol Biol 2012; [3] Pérès E et al., Int J Radiat Oncol Biol Phys 2018; [4] Iima M, Le Bihan D. Radiology. 2016; [5] Gupta M et al., NMR Biomed 2013; [6] Verreet T et al. J Neurodev Disord 2015; [7] Barrière DA et al. (in submission).

S16.09

MRI-CEST imaging of tumor metabolism and acidosis for characterizing murine tumor aggressiveness

A. Anemone[1], M. Capozza[1], C. Dhakan[2], B. Rani[1], S. Zullino[1], F. Arena[1], E. Terreno[1], D. Longo[2], S. Aime[1]

[1]University of Torino, Dept of Molecular Biotechnologies and Health Sciences, Turin, ITALY, [2]National Research Council of Italy (CNR), Institute of Biostructures and Bioimaging (IBB), Turin, ITALY

Purpose/Introduction: Cancer metabolism is routinely assessed by the quantification of the FDG uptake by PET imaging, despite radiation exposure issues and reduced spatial resolution that limits heterogeneity assessment. The aim of this study was to exploit radiation-free MRI-CEST (Chemical Exchange Saturation Transfer) methods for investigating different aspect of tumour metabolism, including dysregulated glucose uptake following the injection of natural D-glucose[1] or of 3-O-Methyl-D-glucose [2] and tumor acidosis following iopamidol administration [3] in two murine models exhibiting distinct metabolic rate.

Subjects and Methods: 4T1 (mouse mammary carcinoma) and PC3 (human prostate cancer) cells were subcutaneously implanted in both flanks of female BALB/c and male Athymic Nude-Foxn1^{nu} mice, respectively. CEST MRI protocol was performed on a Bruker 7T MRI scanner. Each mouse underwent i.v. injection of glucose (dose 5 g/kg) or of 3OMG (dose 3 g/kg) followed by Iopamidol injection (dose 4gI/Kg) 30 min later. Z-spectra before and after contrast media injections were acquired and CEST contrast was calculated between POST and PRE images. Contrast enhanced maps were calculated for glucose or 3OMG and tumor pHe maps for iopamidol. 2 days after the MRI acquisition mice were kept fasted overnight and injected with ^{18}F-FDG for PET imaging. GLUT1 and NHE1 expression were quantified by Western Blot.

Results: The two tumour models showed a marked different FDG uptake: significantly higher uptake in 4T1 tumours than in PC3 tumours (SUV: 0.62 and 0.32; %ID/cc: 3.23 and 1.15 for 4T1 and PC3 respectively, $P < 0.0001$, Figs. 1d, 3 and 2e, f). Similarly, CEST analysis revealed that the PC3 prostate tumour model displayed a lower glucose contrast in comparison to the 4T1 breast tumour model ($\Delta ST\ \% = 3.0$ and 2.5 for 4T1 and PC3, respectively) and a significantly lower 3OMG uptake ($\Delta ST\ \%$ 2.0 and 1.5 for 4T1 and PC3, respectively, $P = 0.03$, Figs. 1a, b and 2b, g). Consistently with the higher glucose uptake, 4T1 tumour model presented a more acidic extracellular pH than the PC3 model, reflecting an increased tumour acidosis (mean pHe 6.7 and 6.8 for 4T1 and PC3, $P = 0.02$, Figs. 1c and 2c, d, h, i). Western blot analysis showed an increased expression of GLUT1 in 4T1 cell line compared to PC3, reflecting the higher glucose metabolism and tumor acidosis for the 4T1 breast tumor model (Fig. 1f) displayed in vivo.

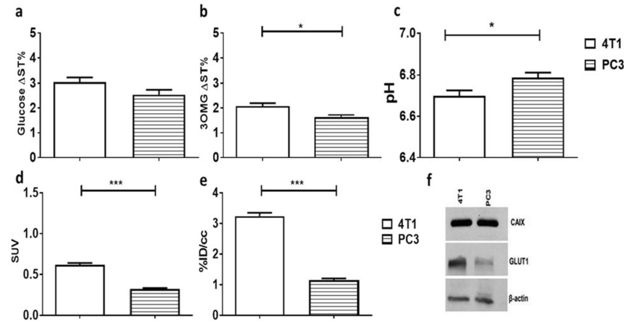

Figure 1: Average values calculated for each tumor model of (a), Glucose ΔST% (b), 3OMG ΔST% (c), tumor pHe (d), 18F-FDG PET uptake as SUV and as %ID/cc (e.f). Western blot analysis in 4T1 and PC3 cell lines (f).

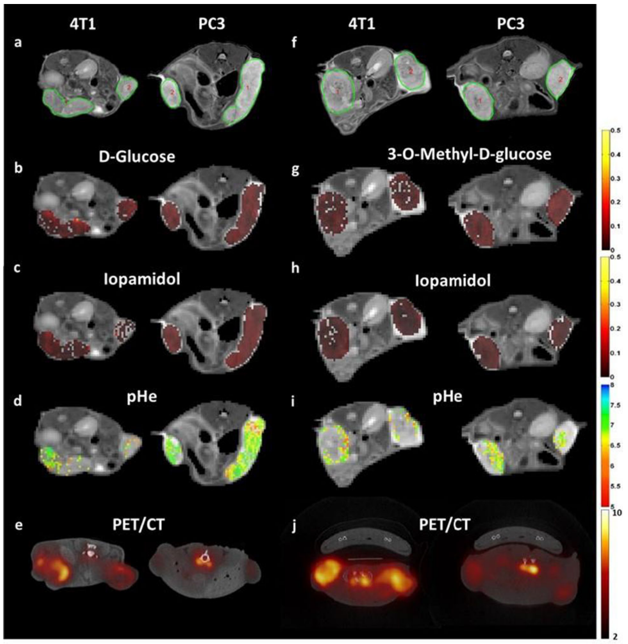

Figure 2: Representative T2w images (a,f), GlucoCEST map after D-glucose (b) or 3OMG injection (g), CEST contrast (c,h) and pH maps (d,i) and fused FDG-PET/CT images for 4T1 and PC3 tumor bearing mice.

Discussion/Conclusion: These findings highlight a good characterization of different aspects of tumour metabolism by exploiting complimentary MRI-CEST approaches in comparison to PET imaging.Tthe metabolic MRI-CEST profiling of tumours can be considered a new radiation-free approach to distinguish differences in cancer aggressiveness and heterogeneity.

References:

[1] van Zijl PC, et al. Proc Natl Acad Sci U S A. 2007, 4359.
[2] Navon G, et al. Magn Res Med 2018 79, 1061.
[3] Longo DL, et al.; Cancer Research 2016, 76, 6463.

L05 Lightning Talks

15:40–16:40 *The Stage*

MRI Applications Outside of the Brain

L05.01

Comprehensive characterization of experimental aortic valve stenosis by multiparametric MRI

U. Flögel[1], C. Quast[2], C. Jacoby[1], F. Bönner[2], I. Gyamfi-Poku[2], K. Piayda[2], R. Erkens[2], M. Kelm[2]
[1]Heinrich Heine University, Experimental Cardiovascular Imaging, Düsseldorf, GERMANY, [2]Heinrich Heine University, Department of Cardiology, Düsseldorf, GERMANY

Purpose/Introduction: Aortic valve stenosis (AS) is one of the most frequent valve diseases in the elderly with relevant prognostic impact. Because sufficient experimental models were lacking, we recently refined an experimental model of gradable experimental AS closely mimicking disease progression in humans[1]. Here, we aimed at developing a comprehensive MRI approach for simultaneous assessment of changes in valvular, myocardial as well as aortic morphology and function in this murine AS model.

Subjects and Methods: Experimental AS was induced in male 12-week-old wildtype mice (C57Bl/6) by wire injury[1] and subjected to high resolution MRI at 9.4T 4 weeks after surgery. Cine loops (16 frames, $58.5 \times 58.5\ \mu m^2$) were recorded at 9.4T using a 25 mm ^{1}H quadrature resonator and an ECG- and respiratory-gated segmented FISP sequence (TE = 1.23 ms). Aortic flow profiles were obtained from velocity maps acquired at the atrio-ventricular level using an ECG- and respiration-triggered slice-selective 2D FLASH sequence with a four-point Hadamard scheme for flow velocity encoding (12 frames). Cardiac tissue characterization was carried out by T1 and T2 mapping as described previously[2]

Results: As expected, in mice subjected to wire injury we observed an impaired valve opening and a more triangular orifice as compared to controls (n = 9 each). Besides detection of the restricted orifice area, long axis slices revealed an altered shape and thickening of the valve as consequence of the remodelling processes induced by the surgical procedure (Fig. 1).

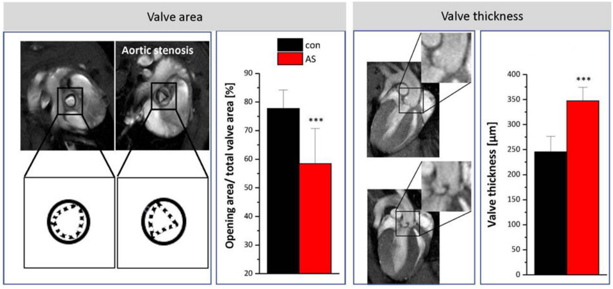

Figure 1: Valvular structure and function

While control mice showed a bell-shaped flow profile in early systole, aortic valve stenosis resulted not only in significantly enhanced peak flow velocity, but also in a fragmented pattern of the flow profile with isolated spikes of accelerated velocities across the valvular area and also areas with negative flow peaks (Fig. 2).

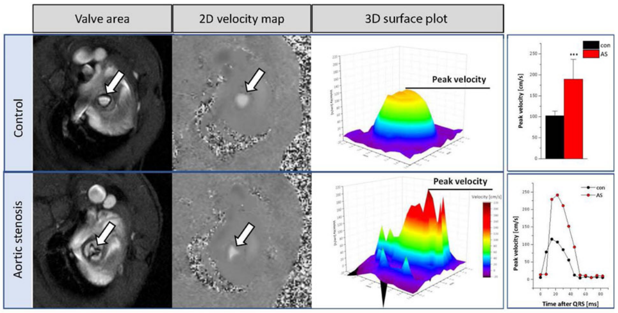

Figure 2: Aortic flow profiles

As a consequence of the long-term occuring turbulent flow patterns, transversal strain of the aortic root was significantly enhanced, which was also associated with an increase in aortic wall thickness at the level of the aortic valve (Fig. 3).

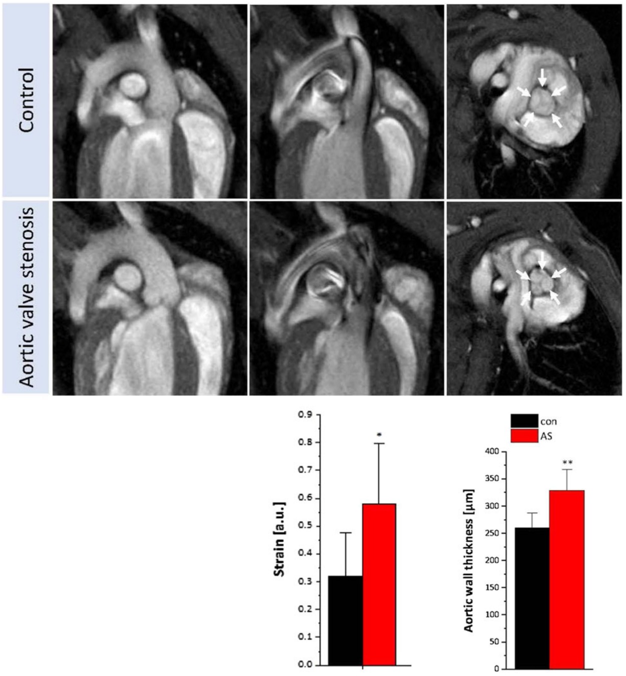

Figure 3: Aortic wall strain and morphology

Of note, global cardiac function in terms of EF and cardiac output was unaffected in AS mice. However, diastolic wall thickness was slightly but significantly bigger comparable to a mild hypertrophy of the left ventricular wall. Finally, cardiac tissue characterization by T1 and T2 mapping suprisingly revealed reduced values for both parameters in AS, which clearly argues against development of myocardial edema at this time.

Discussion/Conclusion: In a murine model of AS, MRI is capable to reliably display transvalvular aortic flow profiles with concomitant quantification of structural and functional changes in aortic valve, left ventricle, and ascending aorta.

References:

1. Niepmann et al. Clin Res Cardiol. 2019 in press.
2. Haberkorn SM et al. Circ Cardiovasc Imaging 2017;10(8). pii: e006025.

L05.02

Long-term stability of native MOLLI 5 s(3 s)3 s T1 mapping in young healthy subjects

T. Dresselaers[1], S. Tilborghs[2], M. Versluis[3], G. Claessen[4], K. Goetschalckx[4], P. De Bruin[3], R. Willems[4], F. Maes[2], J. Bogaert[1]
[1]KU Leuven, Department of Imaging and Pathology, Radiology, Leuven, BELGIUM, [2]KU Leuven, Department of Electrical Engineering, ESAT/PSI, Leuven, BELGIUM, [3]Philips, Health Systems, Eindhoven, NETHERLANDS, [4]KU Leuven, Department of Cardiovascular Sciences, Leuven, BELGIUM

Purpose/Introduction: In cardiac MR myocardial T1 values of an individual are typically compared to a normal range based on a group of healthy subjects (scanner/sequence-specific). This normal range will to some extend include physiological and tissue differences between healthy subjects. Therefore, when longitudinal data is available it may be relevant to compare results not only to the normal range but also between time points. This may be feasible as myocardial T1 mapping using different MOLLI sequences has been shown to be very reproducible [1] although several sources of bias are known (e.g. off-resonance). Recently, it was reported that native T1 derived from a 3(3)3(3)5 sequence is a robust marker for long-term follow-up [2]. To further validate this finding more studies are required, though (sequences, B0, etc.).

In this study we assess the inter- and intra-subject T1 variability from long-term follow-up (~ 1.5 years) data in 29 young athletes. We assume that no physiological/tissue changes occur during this period (no contrast enhancement was observed).

Subjects and Methods: Data was included from native T1mapping acquired on a 1.5T Achieva (Philips) using a MOLLI 5 s(3 s)3 s in mid, base and long axis orientation as part of a CMR study in young athletes (15–20 years; 16 M/13F)[3]. T1 maps were calculated offline after motion correction [4]. On each slice endo- and epicardial contours were drawn and T1 distributions (histograms) derived (5 ms bins; range 650–1750 ms; Fiji, http://imagej.nih.go/ij)). Next these histograms were pooled over all slices for each subject per time point.

Results: When including all subjects inter- and intra-subject variability at both time points were similar (inter at t1: 20.0 ± 3.7 ms, t2: 18.7 ± 3.6 ms and intra: 17.1 ± 3.3 ms; Fig. 1). After a basic quality control (QC) 7/29 subjects were excluded as either time point did not meet the requirements (excl. criteria: regional var. > 70 ms/poor BH/arrhythmia or triggering errors). For the remaining 22 subjects the intra-subject (12.3 ± 2.6 ms) was lower than the inter-subject variability (t1: 17.9 ± 3.2 ms, t2: 15.8 ± 3.0 ms). This is also reflected in a high intra-subject degree of overlap of the full myocard T1 histograms (Figs. 2 and 3).

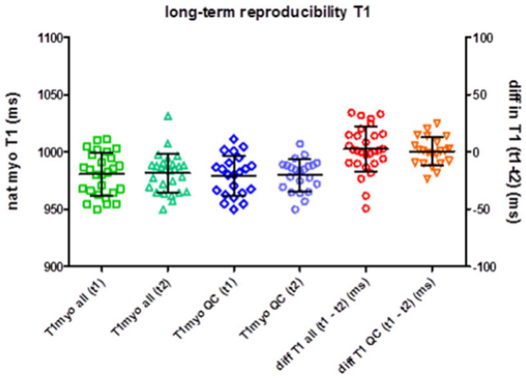

Fig.1: Variability in myocardial T1 (full myocard from mid/base/4CH images pooled) between subjets at time point 1 or 2 (left axis) and the intra-subject variability (right axis) with and without quality control (QC).

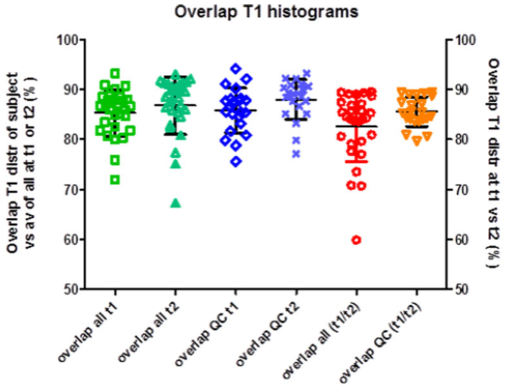

Fig.2: Overlap of the distribution in T1 values from the myocardium (mid/base/4CH data pooled) for a subject vs the average histogram across all subjects at that time point (left axis) or vs the next time point for that subject (right axis) .

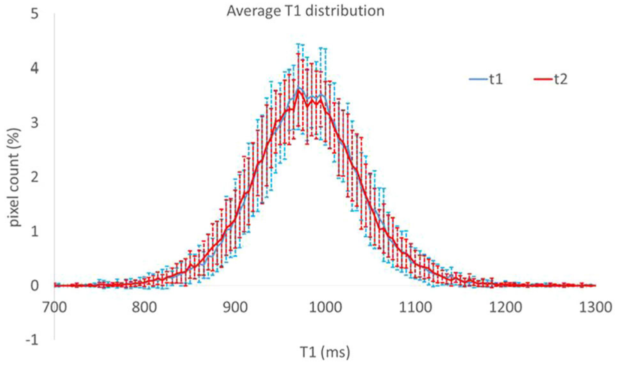

Fig.3: Overage T1 distribution (5ms bins) for all subjects (that met the QC restrictions) at both time points (error bars indicate variation across subjects). Note the vey high degree of overlap between both time points.

Discussion/Conclusion: Our study has limitations as we cannot exclude that subtle pathology or structural adaptations to the training have developed (no contrast enhancement was observed). In addition, our quality control resulted in 25% of data being excluded in these healthy volunteers.

We conclude that the intra-subject variability is lower than the inter-subject variability if certain quality demands are applied and that under these conditions MOLLI 5 s(3 s)3 s T1 mapping allows for long term reproducible measurements.

References:

[1] Shao et al. Magn Reson Med. 2017, 78(5):1746.
[2] Aus dem Siepen F et al. Open Heart 2018, 24;5(1):e000717.
[3] Claessen G et al. Eur Heart JCI 2019(9):1062.
[4] Tilborghs S et al. Med Image Anal. 2019, 52:212.

L05.03

Characterisation of circumferential strains from in vivo MR images: insight into a possible diagnostic measure for plaque vulnerability

R. D. Johnston[1], A. J. Stone[1], M. Bourke[2], P. Madhavan[2], Z. Martin[2], C. Kerskens[3], C. Lally[1]
[1]Trinity College Dublin, Trinity Centre for Bioengineering and Department of Mechanical and Manufacturing Engineering, Dublin, IRELAND, [2]St James Hospital, Vascular and Endovascular Surgery, Dublin, IRELAND, [3]Trinity College Dublin, Trinity College Institute for Neuroscience, Dublin, IRELAND

Purpose/Introduction: Atherosclerotic plaque rupture is one of the leading causes of stroke as plaque development can go unnoticed until a clinical event occurs [1]. Percent stenosis, a measure based on luminal narrowing is an insufficient metric for diagnosing plaque rupture, as plaque rupture can occur below the critical threshold of 50% stenosis [2]. Biomechanical models, generated from clinical imaging, have the potential to predict failure of atherosclerotic plaques and improve the risk assessment of plaque rupture. Using US elastography techniques [3], strain alone has been suggested as a possible rupture metric. Therefore, the aim of this study is to determine the strain magnitude in carotid vessels in vivo using MR imaging and ascertain if it may be a good clinical indicator of potential plaque rupture

Subjects and Methods: T2 weighted MRI scans were obtained from patients under evaluation for a carotid endarterectomy procedure and healthy volunteers. For vessel wall imaging, a 3T Philips Achieva whole body MRI scanner combined with an 8-channel dedicated bilateral carotid artery coil was used. ECG and cardiac triggering were used to synchronize the acquisition of images to both diastolic and systolic phases.

Curves were delineated from images of the vessel wall (see Fig. 1) for healthy and diseased datasets. Circumference measurements were calculated for the vessel at both phases to obtain strain measurements

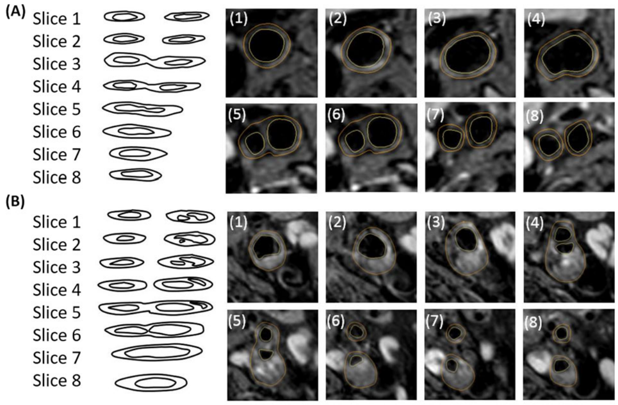

Figure 1: Curve extraction of (A) healthy and (B) diseased arterial wall from T2 weighted images, showing delineation of the

Results: Consistent values for circumferential strain and apparent elastic modulus were observed in healthy datasets, where strains ranged from 8 to 12%, see Fig. 2A. In patients, more variation in the strain ranges was clearly observed in each dataset, see Fig. 2B. This is due to the variable morphology and mechanical properties of the plaque in each dataset. Higher strains were observed at locations proximal and distal to plaque accumulation, while lower strains and higher stiffnesses were observed where the plaque had inwardly remodelled to occlude the lumen diameter, see Fig. 3D–F. It is noteworthy that dataset 3 showed the highest strains at these locations and a larger strain gradient across the plaque, see Fig. 3F. This could be an indicator of increased vulnerability to rupture in this plaque

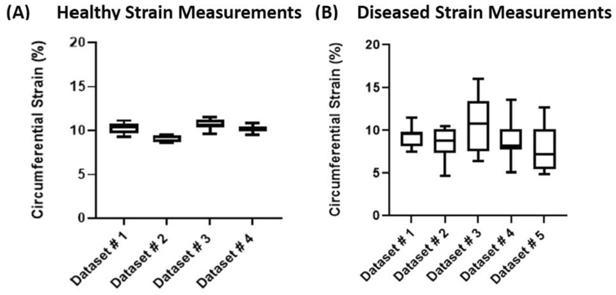

Figure 2: (A) Calculated circumferential strains for healthy volunteers (N=4). (B) Calculated circumferential strains for diseased volunteers (N=5). Box plots represent 1st and 3rd quartiles

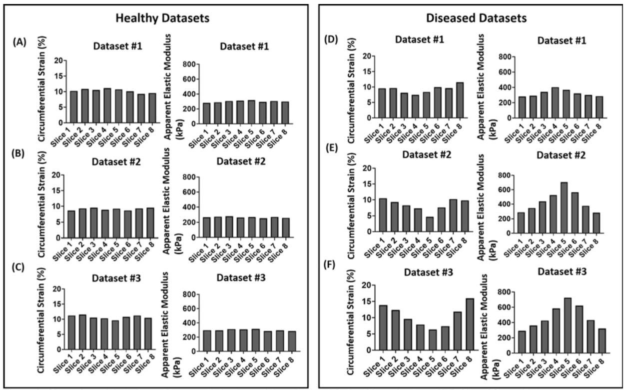

Figure 3: Circumferential strains and apparent elastic modulus observed for healthy volunteers (A,B,C) and for patients undergoing endarterectomy (D,E,F) for each slice acquired.

Discussion/Conclusion: Circumferential strains in carotid arteries in vivo are highly variable where atherosclerotic plaques are present. High strains observed at locations proximal and distal to plaque accumalations could indicate increased vulnerability. From our results, this would suggest that the vessel in dataset 3 would be at highest risk of rupture. Future work will test further datasets to validate the robustness of this strain measure to identify plaque vulnerability.

References:

[1] Mozaffarian et al., Circulation, 133(4): e38–360, 2016.
[2] Mughal et al., Expert Rev Cardiovasc Ther, 9(10):1315–1330, 2012.
[3] Huang, C. et al. Ultrasound in Med. & Biol., 42(2), 365–377, 2016.

L05.04

Joint evaluation of geometric vessel wall and hemodynamic parameters from multi-modal MR images

L. Kaufhold[1], A. Harloff[2], M. Huellebrand[1], C. Strecker[2], J. Zimmermann[3], A. J. Krafft[4], J. Hennig[4], A. Hennemuth[5]
[1]Fraunhofer MEVIS, Bremen, GERMANY, [2]University of Freiburg, Department of Neurology Medical Center, University of Freiburg, Faculty of Medicine, Freiburg, GERMANY, [3]Technical University of Munich, Department of Computer Science, Munich, GERMANY, [4]University of Freiburg, Department of Radiology, Medical Physics, Medical Center, University of Freiburg, Faculty of Medicine, Freiburg, GERMANY, [5]Charité-Universitätsmedizin Berlin, Berlin, GERMANY

Purpose/Introduction: Magnetic resonance tomography is a powerful tool for the assessment of blood vessels as it can capture high-resolution information about structure as well as hemodynamics. Both may play a role in the development of atherosclerotic plaques, which is a major cause for stroke. However, jointly evaluating complementary vessel wall measurements from different modalities, examinations and patients requires a scheme for reliably finding corresponding measurements.

Subjects and Methods: MRI data for one patient and eleven healthy volunteers was acquired on a 3T scanner (Prisma, Siemens) comprising PC-MRI and 3D T1-weighted sequences with spatial resolutions of $0.75 \times 0.75 \times 0.75\ \mathrm{mm}^3$ and $0.6 \times 0.6 \times 0.6\ \mathrm{mm}^3$ respectively and covered the common, internal and external carotid arteries (CCA, ICA and ECA) around the bifurcation.

The quantitative image analysis is performed in 8 reference cross-sections that are placed along the centerline and are defined with respect to flow diverter, which can be independently detected in all images.Wall shear stress and wall thickness are quantified from PC-MRI and T1-weighted MRI contrast images respectively in each cross-section and pooled into 12 sectors by computing the mean values within the sectors.

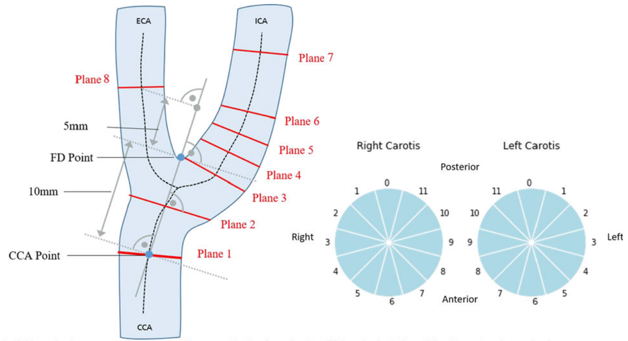

Definition of reference cross-sections with respect to the flow diverter (FD) and orientation of the 12 sectors for evaluation..

We perform segmentations of the vessel needed for the estimation of the wall shear stress in the PC-MRA using a watershed algorithm. The wall segmentation is obtained by using a cross-section wise optimal path approach. Errors of the segmentation are corrected manually.

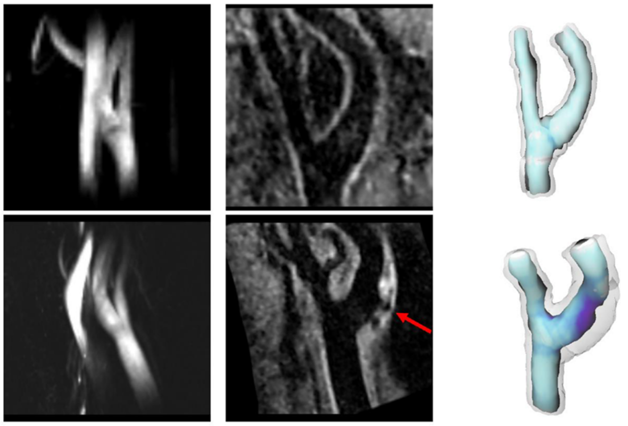

Coronal slice from PC-MRA (left), curved MPR of T1-weighted MR image (middle) and color-coded segmentation of the lumen and wall obtained in the T1-weighted MR image (right) from healthy test person (top row) and patient with plaque (bottom row).

Results: Resulting values of all volunteers were averaged in order to create a baseline values that can be compared to the patient. The patient shows higher wall thicknesses as well as more variable WSS values around the bifurcation.

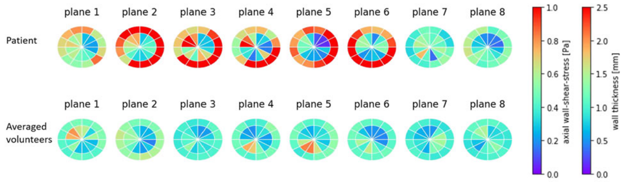

Wall thickness (outer ring) and axial WSS (inner ring) measured in 12 sectors of 8 reference planes Top: Averaged across all volunteers. Bottom left: Patient suffering from atherosclerosis.

Discussion/Conclusion: In the application to the joint evaluation of WSS and wall thickness from PC-MRI and T1-weighted MRI images, we were able to quantitatively and visually inspect correlations between vessel wall thickness and wall shear stress.

References:

[1] L. Kaufhold, A. Harloff, C. Schumann, A. J. Krafft, J. Hennig, and A. Hennemuth. Image-based assessment of uncertainty in quantification of carotid lumen. In Medical Imaging 2018: Image Processing, volume 10574, page 105742 J. International Society for Optics and Photonics, 2018.

[2] J. Zimmermann, D. Demedts, H. Mirzaee, P. Ewert, H. Stern, C. Meierhofer, B. Menze, and A. Hennemuth. Wall shear stress estimation in the aorta: Impact of wall motion, spatiotemporal resolution, and phase noise. Journal of Magnetic Resonance Imaging, 48(3):718–728, 2018.

[3] George W Petty, Robert D Brown Jr, Jack P Whisnant, JoRean D Sicks, W Michael O'Fallon, and David O Wiebers. Ischemic stroke subtypes: a population-based study of incidence and risk factors. Stroke, 30(12):2513–2516, 1999.

L05.05

Assessment of strain and hemodynamic forces in the mouse heart using retrospectively gated CINE imaging

D. T. Dekkers[1], **B. F. Coolen**[1], M. R. Daal[1], C. P. Blanken[2], D. Hautemann[3], R. C. Wüst[1], G. J. Strijkers[1]
[1]Amsterdam UMC, Biomedical Engineering and Physics, Amsterdam, NETHERLANDS, [2]Amsterdam UMC, Radiology, Amsterdam, NETHERLANDS, [3]Medis medical imaging systems BV, Leiden, NETHERLANDS

Purpose/Introduction: The current classification for heart failure is based on ejection fraction and does not consider more subtle alterations in heart function. As such, new parameters are warranted to assess myocardial function. Global longitudinal strain (GLS) and hemodynamic forces, which follow from the motion of the left ventricular (LV) tissue and from the exchange of momentum across the mitral and aortic orifices, may help to reveal suboptimal cardiac function[1]. The **aim** was to study whether recently developed image feature tracking algorithms can be used to determine GLS and hemodynamic forces in the mouse heart.

Subjects and Methods: Cardiac function in 3 isoflurane-anesthetized mice was assessed by cardiac MRI, using a 7.0 Tesla MR Solutions small animal scanner equipped with a 38-mm-diameter mouse volume coil. To obtain a cardiac cine over the complete cardiac cycle, a single longitudinal-axis slice was acquired using a high frame rate retrospectively gated cardiac sequence[2] with the following sequence parameters: TR/TE = 7/2.35 ms, flip angle = 15°, FOV = 30 × 30 mm^2, matrix size = 192 × 192, slice thickness = 1 mm, number of k-space repetitions = 400, total time = 13 min. Off-line reconstruction was performed in MATLAB. Imaging data were binned into 25, 40 or 60 frames (to study optimal frame rate) per cardiac cycle. All images were analyzed using the Qstrain plugin in the MEDIS suite MR software. For comparison, we also acquired CINE MRI data of 2 human subjects. GLS was determined using 2-, 3-, and 4-chamber views (and combinations thereof; Fig. 1). Hemodynamic forces were obtained in the 3-chamber view, as the model requires the mitral and aortic valve diameters. Values are mean ± std.

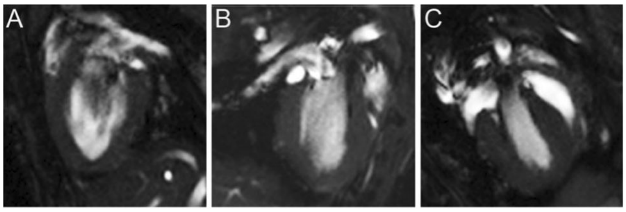

Examples of long-axis mouse hearts (A:2-; B:3-; C:4-chamber views) used for this study.

Results: Average GLS was 29.7 ± 0.1%, and 32.2 ± 3.3% in the human and mouse cines respectively (combined planes). The relative error was larger in the single-plane analysis compared to using two planes (12 ± 8 and 6 ± 4%, $p = 0.001$), suggesting that at least two planes are needed for accurate GLS determination. Next, we determined the optimal frame rate. Higher frame rates come at the cost of reduced SNR, hampering accurate feature tracking. The relative error at 60 frames (compared to 25) was 14 ± 14% and the reduction in SNR resulted in some problems with feature tracking. Hemodynamic force analysis resulted in atypical curves in mice (compared to human data) due to artifacts resulting from rapid blood flow and papillary muscle motion.

Discussion/Conclusion: Initial results are promising, but further optimization of image quality and feature tracking is required for the assessment of hemodynamic forces in mice. When successful these tools can be used to study early changes in cardiac function in mice with heart failure.

References:

[1] Lapinskas et al. (2019). JACC Cardiovasc Imaging 12:377.

[2] Motaal et al. (2013). NMR Biomed 26:451.

L05.06

Comparison of myocardial T1-Mapping using real-time MRI and MOLLI at 1.5 Tesla

A. Müller-Lutz[1], C. Schleich[1], J. Wiedkamp[1], J. Stabinska[1], F. Pillekamp[2], H.-J. Wittsack[1], D. Klee[3]
[1]University Dusseldorf, Medical Faculty, Department of Diagnostic and Interventional Radiology, D-40225 Düsseldorf, GERMANY, [2]University Children's Hospital, Heinrich-Heine University Düsseldorf, Department of General Pediatrics, Neonatology and Pediatric Cardiology, D-40225 Düsseldorf, GERMANY, [3]University Dusseldorf, Medical Faculty, Department of Diagnostic and Interventional Radiology, D-40225 Dusseldorf, GERMANY

Purpose/Introduction: To compare myocardial T1-mapping with real-time MRI[1] and the modified look-locker sequence MOLLI[2].

Subjects and Methods: The study was approved by local ethics committee. 20 volunteers (with written informed consent) without any history of cardiac diseases were examined at a 1.5 Tesla MRI.

Acquisition parameters of the MOLLI sequence were: FOV = 380 × 380 mm^2, resolution = 1.5 × 1.5 × 8 mm^3, TE/TR = 1.10 ms/305.02 ms, FA = 35°, TA = 13.0 s. 8 images were acquired in order to fit a T1 map.

For real-time-MRI, a radial undersampled inversion recovery FLASH sequence with the following parameters was used: FOV = 380 × 380 mm^2, resolution 1.2 × 1.2 × 8 mm^3, TR = 2.63 ms, TE = 1.76 ms, flip angle = 6°, TA = 4.3 s. Image reconstruction with the NLINV algorithm was performed. 101 images were acquired and inline processed revealing a T1 map.

T1 values were evaluated for basal, equatorial and apical AHA heart segments (accordingly to the American Heart Association heart model[3]) and the complete basal, equatorial and apical myocardium.

Bland–Altman analysis was performed to compare T1 values measured with both sequences.

Results: Data of 6 patients were excluded due to perturbation of the ECG signal or motion artefacts. Further analysis was performed in the remaining 14 volunteers.

T1-values obtained with the real-time and MOLLI-sequences were not significant different in the apical slice (real-time: T1 = (1014.97 ± 30.37) ms, MOLLI: T1 = (1000.98 ± 27.09) ms). In contrast in the equatorial and basal slices significant higher T1-values were obtained with real-time MRI (basal: real-time: T1 = (1052.03 ± 40.78)ms, MOLLI: T1 = (1000.44 ± 19.30)ms, p-value: 0.02; equatorial: real-time: T1 = (1014 ± 21.42)ms, MOLLI: T1 = (1001.79 ± 30.17)ms, p-value < 0.01).

Table 1 summarizes the obtained T1-values for the AHA heart segments of the basal, equatorial and apical slice. In nine of sixteen segments, T1-values were significantly higher with real-time MRI compared to MOLLI.

Segment	mean T1 (real-time) [ms]	std T1 (real-time) [ms]	mean T1(MOLLI) [ms]	std T1(MOLLI) [ms]	Segment	mean T1 (real-time) [ms]	std T1 (real-time) [ms]	mean T1(MOLLI) [ms]	std T1(MOLLI) [ms]
1	1091.95	63.71	985.18	23.99	9	1061.78	31.09	1020.44	41.67
2	1059.41	31.57	1010.99	26.55	10	1027.25	32.66	1003.32	30.58
3	1073.46	33.06	1006.05	22.27	11	980.26	32.53	985.70	24.21
4	1052.99	57.92	1019.48	41.29	12	965.40	22.62	999.46	32.75
5	989.65	62.38	989.79	26.58	13	991.39	36.79	997.46	36.55
6	1019.43	51.69	984.60	25.37	14	1026.79	43.94	1009.25	45.10
7	994.96	24.55	987.17	54.12	15	1037.07	34.58	991.82	41.78
8	1041.93	29.64	1005.40	42.85	16	1007.78	24.72	1009.73	27.73

Tab 1. Overview of T1-values (real-time and MOLLI) over all volunteers.

Bland–Altman analysis revealed a mean difference of T1-values with the real-time and MOLLI sequence of (26.00 ± 52.59)ms (see Fig. 1).

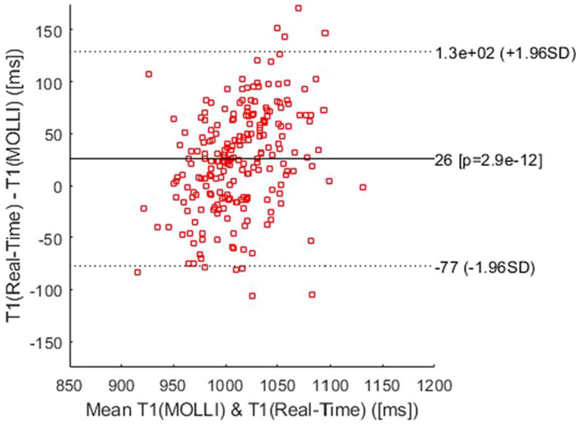

Fig. 1: Bland-Altman plot for T1 values obtained in 16 segments of 14 volunteers. The mean difference of T1-values obtained by the real-time MRI sequence and MOLLI was 26 ms.

Discussion/Conclusion: Slightly higher T1-values were measured with real-time MRI compared to MOLLI. Future studies are necessary to evaluate the diagnostic potential T1-mapping with real-time MRI.

References:

[1] Wang X et al. High-resolution myocardial T1 mapping using single-shot inversion recovery fast low-angle shot MRI with radial undersampling and iterative reconstruction. Br J Radio. 2016; 89(1068):20160255

[2] Messroghli DR et al. Modified Look-Locker inversion recovery (MOLLI) for high-resolution T1 mapping of the heart. Magn Reson Med. 2004; 238(3):1004–1012

[3] Cerqueira MD et al. Standardized myocardial segmentation and nomenclature for tomographic imaging of the heart. A statement for healthcare professionals from the Cardiac Imaging Committee of the Council on Clinical Cardiology of the American Heart Association. Int J Cardiovasc Imaging. 2002; 18(1):539–42.

L05.07

Simple semi-automatic quantification of haematomyocardial barrier permeability for polyacetate complexes of Gd in ischaemic and inflammatory myocardial damage

W.-Y. Ussov[1], A. Y. Fisenko[2], M. I. Bakhmetyeva[3], O. V. Mochuia[1], N. V. Savello[4], O. I. Belichenko[5]

[1]Tomsk Medical Research Center/Institute of Cardiology, MRI Res. Lab, Tomsk, RUSSIAN FEDERATION, [2]Siberian State Medical University, Internal Medicine, Tomsk, RUSSIAN FEDERATION, [3]M.V.Lomonosov Moscow State university, Mechanics and mathematical faculty, Moscow, RUSSIAN FEDERATION, [4]R-Pharm Co., Saint, Petersburg, RUSSIAN FEDERATION, [5]Russian National State University of fitness, sport, youth and tourism, Research Institute of Sport Medicine, Moscow, RUSSIAN FEDERATION

Purpose/Introduction: We developed and applied for quantification of microvascular permeability in damaged myocardium a model—based approach employing the dynamic acquisition of magnetic resonance imaging of paramagnetic contrast diffusion to damaged myocardium and kinetic Gjedde-Rutlend-Patlak (GRP) analysis of blood clearance of the contrast concomitantly with it's rise in the damaged tissue, in ishemic or inflammatory tissue [1].

Subjects and Methods: The model is based on the passive gradient-driven diffusion, unidirectional for first minutes after injection of the contrast, used as Gjedd-Rutland-Patlka technique. If the C_{myoc}—depicts the concentration of the paramagnetic in the blood, and the C_{blood}–means the blood level of the contrast agent, whwreas the $k_{blood\text{-}myocardium}$—is the index of diffusion of the contrast from blood to myocardium, then assuming thediffusion unidirectional for first minutes post injection we can plot the ratio $\{(\int C_{blood}(t)dt)/C_{blood}\}$—as abscissa X, and $\{C_{myoc}/C_{blood}\}$—as ordinata Y, $k_{blood\text{-}myocardium}$ can be obtained then from such linear plot as it's slope. We substituted the concentrations themselves with the values of intensities of scans of the heart.

CE-MRI of the heart was carried out using dynamic scannig, after slow bolus injection of 0.1 mM per 1 kg of BW. The groups of patients comprised 21 persons with acute myocardial infarction and also nine persons with firstly revealed myocarditis. Uptake kinetics to the myocardium was imaged using fast T1-w protocols with fat supression for up to 12 min after bolus injection and then processed using RadiAnt software (Medixant, Poznan, Polska), and also original software for dynamic data analysis written using MATLAB 6.1 (SCILAB also), with output of GRP plots and calculation of $k_{blood\text{-}myocardium}$ values.

Results: The physiological sence of the $k_{blood\text{-}myocardium}$ means this value depicts the clearance of paramagnetic to myocardium, per minute, per unit of myocardial volume. The value of the $k_{blood\text{-}myocardium}$ diffusion koefficient was, respectively, as high as 3.09 ± 1.32 (2.36–11.9) ml/min/100 g of tissue, in myocardial infarction although treated successfully with thrombolysis and stenting (n = 21) and 1.78 ± 0.67 (0.50–2.42) ml/min/100 g of tissue— —in inflammatory myocarditis damage of myocardium (n = 9); In normal controls $k_{blood\text{-}myocardium}$ was close to zero values and namely as low as 0.09 ± 0.06 (< 0.2) (ml/min/100 g of tissue)—Table 1.

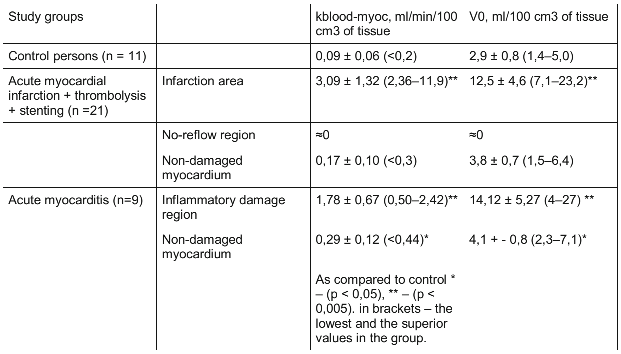

Study groups		kblood-myoc, ml/min/100 cm3 of tissue	V0, ml/100 cm3 of tissue
Control persons (n = 11)		0,09 ± 0,06 (<0,2)	2,9 ± 0,8 (1,4–5,0)
Acute myocardial infarction + thrombolysis + stenting (n =21)	Infarction area	3,09 ± 1,32 (2,36–11,9)**	12,5 ± 4,6 (7,1–23,2)**
	No-reflow region	≈0	≈0
	Non-damaged myocardium	0,17 ± 0,10 (<0,3)	3,8 ± 0,7 (1,5–6,4)
Acute myocarditis (n=9)	Inflammatory damage region	1,78 ± 0,67 (0,50–2,42)**	14,12 ± 5,27 (4–27) **
	Non-damaged myocardium	0,29 ± 0,12 (<0,44)*	4,1 + - 0,8 (2,3–7,1)*
		As compared to control * – (p < 0,05), ** – (p < 0,005). in brackets – the lowest and the superior values in the group.	

Diffusion velocity coefficient Kblood-myocardium and specivic myocardial tissue blood volume V0 (as ml/100 cm3 of tissue), calculated from Gjedde-Rutland-Patlak plots

Use of this protocol provided highly significant separation of ishemic and iflammatory conditions.

Discussion/Conclusion: The model-based indexes of diffusion of paramagnetic to the infarction are significantly different from the inflammation, and deliver additional object-based characteristics of the vascular permeability of the damaged haematomyocardial barrier.

References:

1. Peters AM. Graphical analysis of dynamic data: the Patlak-Rutland plot. Nucl Med Commun. 1994;15(9): 669–72

L05.08

Learning curves in radiological reporting of Whole-body MRI in plasma cell disease: a retrospective study

A. Stecco, **D. Negroni**, A. Cassarà, S. Berardo, E. Soligo, A. Trisoglio
A.O.U. Maggiore Hospital, UPO University, Novara, ITALY

Purpose/Introduction: To analyze inter-observer agreement and the learning curves of three residents undergoing training in the use of whole-body magnetic resonance diffusion-weighted imaging with background body signal suppression (WB-MRI with DWIBS) in patients with plasma cell disease.

Subjects and Methods: Three readers in-training with different levels of experience examined the anonymized and randomized Whole-Body MRI images of 52 patients with a diagnosis of plasma cell disease recorded between January 2015 and February 2017 and analyzed their morphological (T1w, T2w with and without fat suppression) and functional sequences. Reports of an expert radiologist were considered the standard of reference. Images were analyzed in two sessions, during which each reader was timed. Readers reported the number of segments with lesions and staged the disease using the Durie-Salmon PLUS staging system. Weighted Cohen's κ and Z-test were used to compare the trainers' reports with those of the expert-radiologist, and learning curves were drawn up to show changes between the two sessions.

Results: Weighted Cohen's κ of number of lesioned segments increased from 0.536 ± 0.123 to 0.831 ± 0.129 (Prob > Z under 0.005), thus approaching the goal of $\kappa > 0.8$. Trainers reached the level of experienced-radiologist in terms of time by the 33rd patient. Agreement concerning the Durie Salmon PLUS increased from 0.536 ± 0.123 to 0.831 ± 0.129 (Prob > Z under 0.005).

Discussion/Conclusion: The findings of this study demonstrate that Whole-Body MRI with DWIBS can be learned in about 80 reports and leads to a high level of interobserver concordance when using the Durie-Salmon PLUS staging system.

References:

Stecco A, Buemi F, Iannessi A, Carriero A, Gallamini A, Stecco A, et al. Current concepts in tumor imaging with whole- body MRI with diffusion imaging (WB-MRI-DWI) in multiple myeloma and lymphoma. Leuk Lymphoma [Internet]. 2018;1–11. Available from: https://doi.org/10.1080/10428194.2018.1434881

Rajkumar SV, Dimopoulos MA, Palumbo A, Blade J, Merlini G, Mateos MV, et al. International Myeloma Working Group updated criteria for the diagnosis of multiple myeloma. Lancet Oncol [Internet]. 2014;15(12):e538–48. Available from: http://dx.doi.org/10.1016/S1470-2045(14)70442-5

Durie BGM. The role of anatomic and functional staging in myeloma: Description of Durie/Salmon plus staging system. Eur J Cancer. 2006;42(11):1539–43.

Kwee TC, Luijten PR. Diffusion-weighted whole-body imaging with background body signal suppression (DWIBS): features and potential applications in oncology. Eur Radiol. 2008;18:1937–52.

L05.09

WITHDRAWN

L05.10

Change in T2' measurements in the rabbit placenta during gestation

R. Draveny[1], C. Bertholdt[2], M. Dap[2], C. Schaaf[3], O. Morel[2], M. Beaumont[3]
[1]*Université de Lorraine, Inserm, IADI, Nancy, France, Siemens Healtcare SAS, Saint-Denis, FRANCE,* [2]*Université de Lorraine, Inserm, IADI, Nancy, FRANCE,* [3]*Université de Lorraine, Inserm, IADI, Nancy, France, CHRU-Nancy, Inserm, Université de Lorraine, CIC Innovation Technologique, Nancy, FRANCE*

Purpose/Introduction: Pre-eclampsia and Intra-Uterine Growth Restriction are two major pregnancy complications related to chronic utero-placental hypoperfusion [1]. In order to overcome 2D ultrasound limits for the detection of these pathologies, the obstetrical community investigates the potential of MRI, which is compatible with pregnancy [2]. It is well known that T2* values were significantly lower in pathological cases [3]. However, T2* changes may originate either from a change in the intrinsic T2 value (as it is observed during pregnancy [4]) or from a change in T2' value which is reflecting local field inhomogeneities (due to impaired placental perfusion and/or oxygenation). The aim of the present study was to discriminate these two effects by looking at the T2 and T2' values during physiological pregnancy in the rabbit using quantitative MRI.

Subjects and Methods: MRI acquisitions were performed on normal pregnant rabbits at two gestational age (GA = 21/28 days out of 30 days), on a 3T MR scanner (MAGNETOM Prisma$^{\mathrm{fit}}$, Siemens Healthcare, Erlangen, Germany), using a transmit/receive knee coil. Raw images to generate T2 maps were acquired using a 2D multi-echo spin-echo sequence (spatial resolution = 0.8*0.8*2 mm^3, 7 TE ranging from 14.3 to 100.1 ms, TR = 2130 ms). Raw images to generate T2* maps were acquired using a 2D multi-echo gradient-echo sequence (spatial resolution = 0.6*0.6*2 mm^3, FA = 60°, 9 TE ranging from 2.78 to 26.3 ms, TR = 291 ms). Non-rigid image registration using Residual Complexity similarity measure [5] was applied between T2 images set and T2* images set. T2 and T2* maps were obtained by a pixel-wise fitting with Levenberg–Marquardt method, and the model used was a mono-exponential decay for both. Then, T2' map was generated using the following relation: $1/T2^* = 1/T2 + 1/T2'$.

T2, T2* and T2′ mean and standard deviation values were computed from ROIs using manual delineation of the placenta on a single-slice for 5 fetuses per GA from different rabbits.

Results: Relaxation time maps are displayed on Fig. 1, at two different GA. The global results presented on Fig. 2 showed that T2, T2* and T2′ are all decreasing with GA.

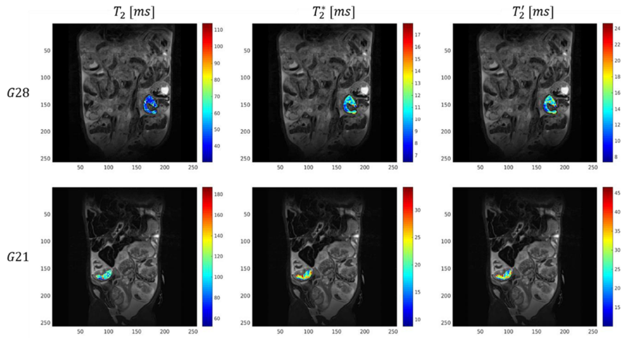

Figure 1: T2/T2*/T2' maps for a ROI covering one placenta of the rabbit, at G28 and G21.

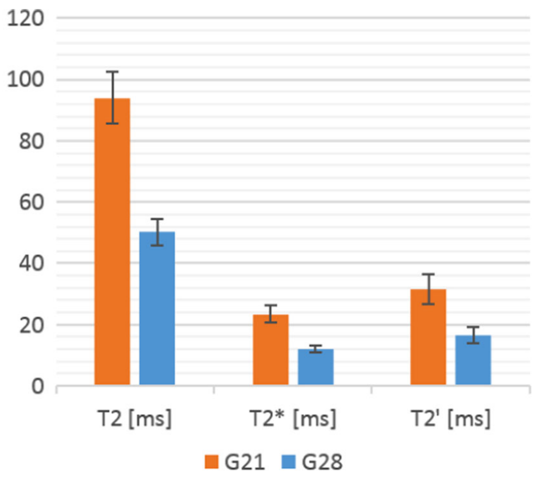

Figure 2: Evolution of mean relaxation times T2/T2*/T2' on the ROI covering the placenta with gestational age. n=5 fetuses.

Discussion/Conclusion: In this preliminary study, we have shown that the decrease in T2* value with GA is due to a decrease in both T2 and T2′ values. Indeed, as expected, both structural and oxygenation changes occur during pregnancy. Therefore, looking at T2 and T2′ rather than just T2* can help to discriminate placental oxygenation modification from placenta structural evolution.

To further investigate the T2′ added value to characterize placental function, future analysis will be conducted to compare T2′ values measured during gas challenge and between normal and pathological pregnancies paired for the GA.

References:

[1] M. Kovo and al. Thr Research, 2013.
[2] B.M. Mervak and al. JMRI, 2019.
[3] M. Sinding and al. UOG, 2016.
[4] C. Wright and al. Placenta, 2011.
[5] A. Myorenko and X. Song. IEEE, 2010.

L05.11

T-staging of prostate cancer: prevalence and predictive value of frequently used signs of posterolateral extraprostatic extension on prostate MRI

F. Pesapane[1, 2], C. Standaert[3], P. Devisschere[3], G. Villeirs[3]
[1]Università degli Studi di Milano, Postgraduation School in Radiodiagnostic, Milan, ITALY, [2]-, -, -, ITALY, [3]Ghent University Hospital, Ghent, Belgium., Department of Radiology and Nuclear Medicine, Gent, BELGIUM

Purpose/Introduction: In prostate cancer (PCa), the extraprostatic extension (EPE) is associated with a greater risk of positive surgical margins, further decreasing the chance of long-term control and a worse prognosis (1). However, staging with MRI is challenging, and meta-analyses showed a wide range of sensitivity and specificity values (2, 3). One of the reason is that criteria used for detecting EPE are very variable in the literature (2, 3, 4). Therefore, we performed a retrospective study with the aim of identifying practical MRI staging criteria for EPE, based on the evolutionary concept of PCa growth from truly intraprostatic to truly extraprostatic, in accordance with established histopathologic criteria.

Subjects and Methods: The presence of EPE in index lesions visible on prebiopsy mpMRI (consisting of T2w images, DWI and DCE on a 3 T-system) of biopsy-proven PCa patients was retrospectively blindly assessed by two radiologists with 8- and 17-years of experience on the basis of 8 selected criteria IMAGE01. Histopathology from radical prostatectomy was used as a standard of reference. The prevalences and positive predictive values (PPV) of all criteria were calculated for each reader separately and averaged for the two readers together. Cohen' *K* and means of percentage were used to assess the agreement.

Results: In the selected 51 patients (mean age: 63 years; range: 55–77 years; mean PSA: 17.2 ng/mL; range: 1.4–935.5 ng/mL), tumor-capsule contact was the most prevalent sign (prevalence 51, 0%–62, 7%, average 56, 9%), but with the lowest PPV (average 51.9%), although increasing with broader capsular contact (56.5% if ≥ 10 mm; 87.5% if ≥ 20 mm; 100% if ≥ 25 mm). “Early signs” of EPE such as bulging, capsular disruption and unsharp prostatic margin showed a prevalence of 11.8%–18.6% on average, with 74.5%–86.3% of agreement; the average PPVs range was 69.0%–75.0%. “Late signs” of EPE such as irregular prostatic contour, periprostatic fat infiltration, rectoprostatic angle obliteration and periprostatic mass showed a prevalence of 2.9%–8.8% on average, with 86.3%–94.1% of agreement; the average PPV’s ranged between 85.7% and 100%.

Discussion/Conclusion: The goal of a staging MRI should be either to rule out EPE (when the PCa does not abut the prostatic capsule), or to predict the likelihood of EPE on a scale from low (early signs) to high (late signs). MRI staging criteria for the identification of EPE of PCa can be based on the evolutionary concept of cancer growth from truly intraprostatic to truly extraprostatic. Early signs show high prevalences but low PPV, while late signs show lower prevalences but higher PPV. MRI-staging following this evolutionary concept can standardize morphologic staging and decrease the existing multireader variability.

References:

1 Epstein Urology 56(2) (2000) 283–8
2 de Rooij Eur Urol 70(2) (2016) 233–45.
3 Engelbrecht Eur Radiol 12(9) (2002) 2294–302.
4 Soylu Diagn Interv Radiol 18(4) (2012) 365–73.

L05.12

Volume-dependent comparative analysis of positron emission tomography and diffusion-weighted magnetic resonance imaging parameters in non-small cell lung cancer tissue

S. Lucic[1], I. Djan[1], D. Kuhelj[2], K. Koprivsek[1], B. Zaric[1],
M. A. Lucic[1]
[1]University of Novi Sad, Medical Faculty, Novi Sad, SERBIA,
[2]University of Ljubljana, Medical Faculty, Ljubljana, SLOVENIA

Purpose/Introduction: The aim of the study was to explore possible correlation and interconnection between the values of apparent diffusion coefficient (ADC_{mean}), obtained by diffusion weighted magnetic resonance imaging (DWI), and standardized uptake value (SUV_{max}), obtained by ^{18}F-FDG PET/CT in the lung non-small cell lung cancer (NSCLC) tissue, and in regard to the tumour volume.

Subjects and Methods: Fifty-four newly diagnosed patients with verified lung NSCLC (17 squamous cell and 37 adenocarcinoma) underwent chest MRI examination on 3T MRI unit, that included respiratory triggered DWI (3 diffusion-encoding gradient directions, with 2 b values (0 and 1000 s/mm^2), TR 5000 ms/TE 80 ms, slice thickness 4 mm, inter-slice gap 0.8 mm) measurements, followed by ^{18}F-FDG PET/CT examination within the maximally 24–48 h interval. A region-of-interest (ROI), covering the exactly same area of the tumour in each single patient was determined, and maximal standard uptake values (SUV_{max}) and mean ADC values (ADC_{mean}) were analyzed and measured by one independent radiologists and nuclear medicine specialists, and numerical data sets from both diagnostic modalities were obtained. Maximal NSCLC volume (V_{max}) was calculated and determined, and patients were grouped into group 1 ($V_{max} < 10$ cm^3; n = 31), group 2 (10 cm^{3}max < 20 cm^3; n = 14), and group 3 ($V_{max} > 20$ cm^3; n = 9). Data sets were statistically analyzed by use of two-tailed Pearson's correlation coefficient (r), and Spearman's rank correlation coefficient (ρ), with the level of confidence determined at $p < 0.05$.

Results: Though on the border level, in the whole group of patients, regardless of V_{max} significant correlation between SUV_{max} and ADC_{mean} values (r = 0.327; $p = 0.055$ and $\rho = 0.201$; $p = 0.248$) has not been found. In group 1 ($V_{max} < 10$ cm^3), significant correlation between both SUV_{max} and ADC_{mean} values was encountered (r = 0.539; $p = 0.031$ and $\rho = 0.535$; $p = 0.033$). In group 2 and 3, correlation between two observed biomarkers was not significant (group 2: r = −0.202; $p = 0.601$ and $\rho = -0.200$; $p = 0.606$; group 3: r = 0.339; $p = 0.373$ and $\rho = 0.100$; $p = 0.798$), yet SUV_{max} values solely demonstrated significant correlation with V_{max} in group 2 (r = 0.749; $p = 0.020$).

Discussion/Conclusion: Mutual interconnection between SUV_{max} and ADC_{mean} varies depending on tumour volume, indicating ^{18}F-FDG PET/CT and DWI as complementary diagnostic modalities, providing not uniform and/or exactly the same, but rather differently acquired and based information in both assessment of lung NSCLC metabolism and cancer tissue cellularity, successively. Indicated two tumourous hallmarks are most probable causes of correlation absence in more voluminous NSCLC's with more heterogeneous internal structure, affirming SUV_{max} and ADC_{mean} as possible biomarkers for internal tumourous tissue bioarchitectonics complementary scrutinizing.

References:

Nomori H et al. Comparing DWI and PET for pulmonary nodules measuring from 1 to 3 cm in size. Surg Today. 2015;45(12):1535–41.

L05.13

MRI assessment of steatosis in pancreas, liver and skeletal muscle in patients with obesity, overweight and normal BMI in correlation with the metabolic syndrome criteria and central obesity

B. Brzeska[1], J. Pieńkowska[1], O. Kozak[2], M. Kaszubowski[3],
E. Szurowska[1]
[1]Medical University of Gdansk, II Department of Radiology, Gdansk, POLAND, [2]Medical University of Gdansk, I Department of Radiology, Gdansk, POLAND, [3]Gdansk University of Technology, Department of Economic Sciences, Gdansk, POLAND

Purpose/Introduction: Obesity, defined as a body mass index (BMI) exceeding 30 kg/m^2, is a serious health problem, which can be called epidemics on a global scale and is one of the most important causes of death that can be prevented.

The aim of the study was to assess ectopic fat accumulation in pancreas, liver and skeletal muscles in patients with obesity, overweight and normal BMI in correlation with the metabolic syndrome (MetS).

Subjects and Methods: The study included 267 patients aged from 18 to 83. Abdominal MRI exams were performed on 1.5 T Siemens Magnetom Aera MR system. Ectopic fat accumulation in pancreas, liver and skeletal muscles was evaluated in MRI using fat-water separated Dixon imaging technique. To measure pancreatic fat and water signal three regions of interest (ROIs) were placed in the head, body and tail of pancreas. Liver fat was assessed by using ROIs which were as large as possible with a homogeneous signal avoiding large vessels and enlarged bile ducts. Two additional round ROIs were drawn on bilateral paraspinal muscles at the lumbar vertebra 3 level. Metabolic syndrome was defined according to the criteria modified by National Cholesterol Education Program Adult Treatment Panel III Guidelines. Central obesity was defined using gender and ethnic-specific values for waist circumference.

Results: There was a statistically significant correlation between the degree of steatosis of the assessed organs and BMI value as well as waist circumference ratio, that determined the degree of central obesity. Based on the waist circumference values analysis, it was found that fat accumulation occurs most rapidly in muscles, then in pancreas and at the end in liver.

Also higher pancreas steatosis depending on the number of fulfilled metabolic syndrome criteria was demonstrated, ranging from an average of 7.84% in patients who met one criterion to 13% in a patient meeting all five criteria. In the remaining patients in whom no components of metabolic syndrome were observed, the average steatosis of pancreas was 5.42%.

Discussion/Conclusion: Assessment of ectopic fat accumulation within pancreas with the simultaneous assessment of waist circumference can play a significant role and may have important clinical implications. By monitoring these two elements, metabolic risk may be predicted, and therefore, early prevention or possible therapeutic intervention may be applied.

References:

1. OECD. OECD obesity update. 2017. http://www.oecd.org/health/obesity-update.htm.
2. World Health Organization. Obesity and overweight 2017 http://www.who.int.
3. Sakai NS, Taylor SA, Chouhan MD. Obesity, metabolic disease and the pancreas—quantitative imaging of pancreatic fat. *Br J Radiol* 2018; 91: 20180267.

L05.14

Pseudodiffusion and Perfusion Fraction Parameters of Intravoxel Incoherent Motion Can Both Augment Our Understanding of HBV-induced Hepatic Fibrosis and Help Non-invasive Staging

M. Gulbay
Ankara Numune Education and Research Hospital, Radiology, Ankara, TURKEY

Purpose/Introduction: Intravoxel incoherent motion (IVIM) parameters pseudo-diffusion coefficient (D*) and perfusion fraction (*f*) were found constantly decreasing with progressing fibrosis in previous studies (1). Nevertheless, D* is proportional with capillarity (2) and neoangiogenesis is a key for progressing fibrosis in chronic viral hepatitis (3). Thus, a constant decrease of D* is not expected hypothetically. We assessed D* and *f* value and histologic amount of angiogenesis to evaluate their relationship and their way to change in progressing fibrosis as well as their capability to differentiate patients with different fibrosis severity.

Subjects and Methods: Respiratory triggered single shot spin echo-EPI using 12-*b* values (0, 10, 20, 30, 40, 50, 80, 100, 200, 400, 800, 1000) was performed *before* the biopsy procedure in 37 chronic HBV patients that liver biopsy indicated. D* and *f* maps were generated using all *b*-values and a 10 mm ROI to calculate mean D* and *f* value was placed to the biopsy site in three consecutive slices. Both routine H&E staining to evaluate Ishak stages and CD34 immunostaining to calculate microvessel density (MVD), a parameter quantifying angiogenesis, were performed to all 37 biopsy specimens.

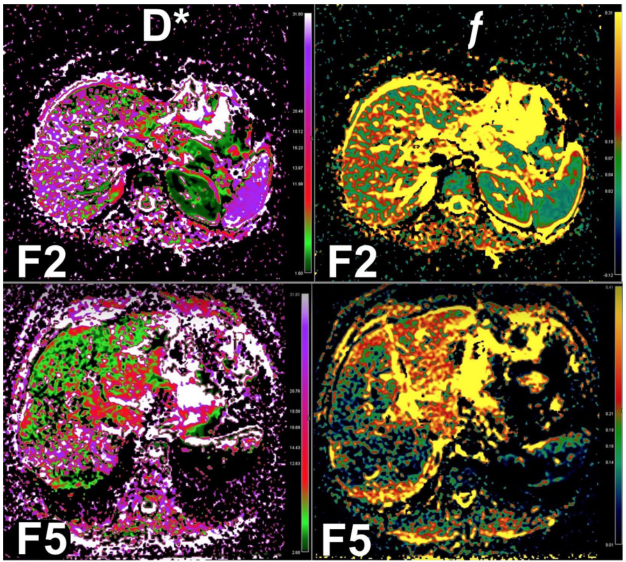

D* and f maps of patients with Stage F2 and F5 hepatic fibrosis

Results: MVD and D* had a similar pattern across the Ishak stages that the parameters reached a peak at Stage 4 while parameter *f* reached its peak at Stage 2 then decreased with progressing fibrosis.

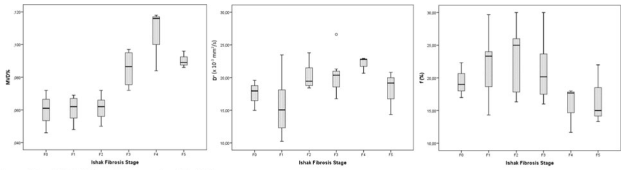

Box plots of MVF, D* and f across the Ishak Stages

There was a significant correlation between MVD and D* ($r = 0.415$, $p = 0.015$), although no correlation found between *f* and D* ($p = 0.992$) or *f* and MVD ($p = 0.119$). Patient grouped as No or Mild (F0–1), Moderate (F2–3) and Marked (F4–5) fibrosis and there was a significant difference of D* ($p = 0.001$) and *f* ($p = 0.046$) in these fibrosis severity groups. Post hoc Tukey HSD test also pointed to significant differences.

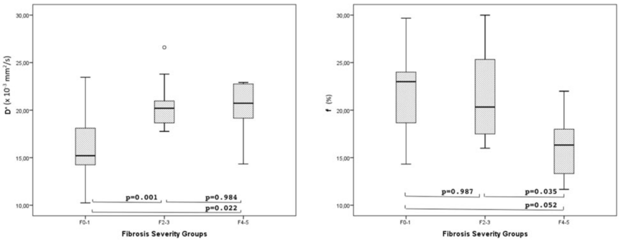

Box plots of D* and f across the Fibrosis Severity Groups with post hoc Tukey HSD results

Discussion/Conclusion: D* was found as a radiologic marker for MVD. These two parameters continued to increase until severe fibrosis emerged and then both were found decreased. D* also was found successful to differentiate the fibrosis groups. Parameter *f* was found significantly decreased only between F2–3 and F4–5 groups. This finding shown that hepatic perfusion was well maintained until fibrosis reached severe stages. D* and MVD were pointed and increasing microvascularity, though *f* was not accompanied this increment. We thought that this finding was supporting that the angiogenesis occurring in the progressing stages of fibrosis was for creating portosystemic shunts rather than related to inflammation.

References:

1. Zhang B, Liang L, Dong Y, et al. Intravoxel Incoherent Motion MR Imaging for Staging of Hepatic Fibrosis. PLoS ONE 2016; 11(1): e0147789
2. Le Bihan D, Breton E, Lallemand D, et al. Separation of diffusion and perfusion in intravoxel incoherent motion MR imaging. Radiology 1988; 168(2):497–505
3. Elpek GO. Angiogenesis and liver fibrosis. World J Hepatol 2015; 7(3): 377–391

L05.15

Pressure measurement in the stomach using MRI and microbubble-based contrast agents

E. Abdurakman[1], M. Bencsik[2], C. Hoad[3], S. McGowan[2], G. Cave[2], D. Fairhurst[2], G. Major[4], P. Gowland[3], R. Bowtell[3]
[1]City, University of London, Division of Midwifery and Radiography, London, UNITED KINGDOM, [2]Nottingham Trent University, School of Science & Technology, Nottingham, UNITED KINGDOM, [3]University of Nottingham, Sir Peter Mansfield Imaging Centre, Nottingham, UNITED KINGDOM, [4]Nottingham University Hospitals NHS Trust and University of Nottingham, National Institute for Health Research (NIHR) Biomedical Research Centre, Nottingham, UNITED KINGDOM

Purpose/Introduction: In a previous in vitro study (1), we have demonstrated that alginate spheres loaded with gas-filled microbubbles can be used as an MRI pressure probe, exhibited a sensitivity of up to 40% signal changes per bar at the field strength of 3T. In the current work, we carried out further in vivo investigations on healthy volunteers to demonstrate the capability of this microbubble-based contrast agent to sense spatially varying pressure changes in the human stomach.

Subjects and Methods: Gas-filled microbubbles were prepared with phospholipids (DPPC and DSPE-PEG2000) as a membrane material encapsulating a perfluorocarbon gas (C_3F_8) (2). These bubbles were then mixed with sodium alginate gel and added dropwise into a saturated aqueous solution of calcium lactate, forming soft-solid alginate spheres with entrapped microbubbles. A locust bean gum solution was used to further immobilise these buoyant spheres.

Then, volunteers were asked to ingest approximately 500 ml meal consisted of a mix of alginate spheres and locust bean gum with a volume ratio of 1:1, before the MRI scan of the stomach was carried out. MRI acquisition was triggered by respiratory gating and an image post processing was performed by using a cross-correlation analysis, where the software was written on MATLAB to allow a region of interest (ROI) tracking from frame to frame on interpolated images. The images were analysed by selecting two square-shaped ROIs (Fig. 1), one from the meal, where pixel intensity changes due to the pressure are expected, and another one from a small section of the liver, where pixel intensity deviations are expected to be much lower.

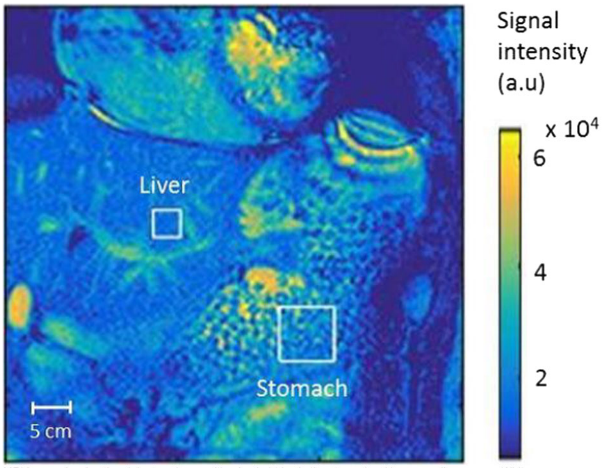

MRI image showing the alginate spheres with microbubbles in the stomach, with surrounding organs. White squares represent the ROI selections for signal intensity analysis in the meal and the liver.

Results: The peristaltic movement within the stomach is seen to alter the overall signal intensity of the microbubble contrast agent meal. The signal intensity change exhibited in the meal within the antrum region is between 5 to 10% (Fig. 2).

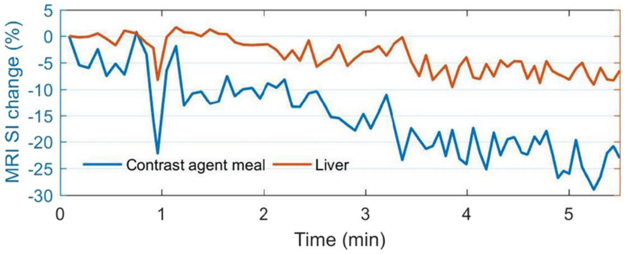

MRI Signal intensity changes within the ROIs in the meal of alginate spheres with microbubbles and the liver. Signal intensity change in the meal is between 5 to 10%,

Discussion/Conclusion: These microbubble-loaded alginate spheres have shown great potential as biocompatible MR contrast agents measuring localised pressure changes in the human stomach. With further improvement, this exciting work will open up an alternative and less invasive route to achieve a better understanding of the clinical condition such as functional dyspepsia. In comparison to the current existing techniques, manometry and bariatric, this method also provides a shorter examination time.

References:

1. Abdurakman E, Bencsik M, Cave G, Fairhurst D, Hoad C, Gowland P, et al. Alginate Spheres with Microbubbles as MRI Contrast Agents for Gastric Pressure Measurement. ESMRMB 2016 Congress; 29th September–1st October 2016; Vol. 29. Springer; 2016.
2. Bencsik M, Al-Rwaili A, Morris R, Fairhurst DJ, Mundell V, Cave G, et al. Quantitation of MRI Sensitivity to quasi-monodisperse microbubble contrast agents for spatially resolved manometry. Magnetic Resonance in Medicine. 2013 NOV 2013;70(5):1409–18.

L05.16

Non-invasive Assessment of Splanchnic Flow in Patients Suspected of Mesenteric Ischaemia using MRI 4D Flow: Pilot Study

P. Hall Barrientos[1], K. Knight[2], D. Black[3], A. Vesey[4], G. Roditi[3]
[1]NHS Glasgow, Glasgow, UNITED KINGDOM, [2]NHS Glasgow, Academic Unit of Surgery, Glasgow, UNITED KINGDOM, [3]NHS Glasgow, Radiology, Glasgow, UNITED KINGDOM, [4]NHS Lanarkshire, Vascular Surgery, Glasgow, UNITED KINGDOM

Purpose/Introduction: The most common cause of chronic mesenteric ischaemia is atherosclerosis which results in limitation of blood flow to the gastrointestinal tract. This usually manifests as abdominal pain provoked by eating with accompanying weight loss. Although atherosclerosis is a common problem, true mesenteric angina is relatively rare due to the presence of 3 main arteries supplying the gastro-intestinal tract. Patients with abdominal pain and a diagnosis of atherosclerotic disease are increasingly being referred for imaging to rule out mesenteric vascular insufficiency.

This study aimed to evaluate a 4D flow work-in-progress package as a potential tool for the analysis of blood flow within the mesenteric vessels beyond the limitations of 2D single-slice based acquisitions.

Subjects and Methods: The mesenteric vessels of seven people were scanned, 5 patients and 6 healthy volunteers. A baseline MRI was acquired after 6 h of fasting followed by a post-meal MRI obtained 50 min after ingestion of 220 ml EnsurePlus. Two 4D flow datasets were acquired, one focused over the superior mesenteric artery and the other over the portal vein. Standard 2D PC-MRI slices were acquired along the aorta (supra-coeliac, renal and infra-renal), portal vein (PV), splenic vessel (SV), superior mesenteric artery/vein (SMA/SMV).

Studies were performed on a 3 T Siemens Prisma with a body array coil and ECG gating. The sequences used were as follows: 4D flow: TR/TE 45.92/3.19 ms, spatial resolution 1.8 × 1.8 × 1.8 cm, $\alpha = 7°$, venc = 150–200 and 30–50 cm/s, ~ 20 cardiac phases and TA ~ 8 min. 2D: TR 51.9 ms, TE 5.1 ms, spatial resolution 0.8 × 0.8 × 5 mm, $\alpha = 20°$, venc 150 and 50 cm/s, ~ 30 cardiac phases and TA 9 s. 4D flow datasets were analysed using a WIP package and 2D datasets were analysed using Argus by Siemens. Paired two-tailed Student p-values were calculated to detect the differences between 2D and 4D peak velocities and net flow, and pre- and post-meal net flow in the PV.

Results: In the volunteer cohort there was a marked increase in blood flow post-meal within the PV ($p = 0.009$). This was not seen in the patient cohort ($p = 0.078$). When 2D and 4D net flow measurements, in both aorta and PV, were compared it was found that 4D technique over estimated ($p = 0.02$, mean bias 2.13 ± 11.7 mL/s).

Discussion/Conclusion: The 4D flow software has enabled measurement of flow parameters within the mesenteric vessels. The software has also enabled 3D visualisation of blood flow thin PV, SMV and SV, which could enhance the current diagnostic assessment methods. 2D flow acquisition of the smaller vessels such as the SV and IMV was challenging and time-consuming. This study has given the ground work for a larger cohort study to be undertaken.

References:

1. Roldan-Alzate et al., *J Mag Reson Imaging*, 42(4) 1009–1017, 2015.
2. Stankovic et al., *Radiology*, 262(3):862–873, 2012.
3. Lycklama A Nijeholt et al., *J Hepatol*, 26(2):298–304, 1997.

L05.17

Effects of arterial input function selection on kinetic parameters of dynamic contrast-enhanced MRI of uterine fibroids

T. Sainio[1], J. Saunavaara[1], G. Komar[2], K. Joronen[3], A. Perheentupa[3], R. Blanco Sequeiros[2]

[1]*Turku University Hospital, Department of Medical Physics, Turku, FINLAND,* [2]*Turku University Hospital, Department of Radiology, Turku, FINLAND,* [3]*Turku University Hospital, Department of Obstetrics and Gynecology, Turku, FINLAND*

Purpose/Introduction: Kinetic parameters derived from dynamic contrast-enhanced magnetic resonance imaging (DCE-MRI) data have been shown to predict poor immediate treatment result of MR-guided high-intensity focused ultrasound (HIFU) therapy of uterine fibroids. However, there are currently several co-existing methods in selecting the arterial input function (AIF) which can limit the comparability of the results [1, 2]. This study analyzes the impact of AIF selection on kinetic parameters of uterine fibroids derived from commonly selected AIF source vessels compared to a population-based AIF model.

Subjects and Methods: Twenty-five patients with 30 uterine fibroids underwent DCE-MRI as a part of routine clinical screening protocol. Kinetic parameters (K^{trans}, k_{ep}, v_e, and v_p) were determined using extended Tofts model with 3 different AIFs: internal iliac artery (IIA), external iliac artery (EIA) and population-based AIF model. Average value for each kinetic parameter was calculated from three regions of interest (ROI) for each uterine fibroid. The effect of AIF selection on kinetic parameters was evaluated by comparing means of kinetic parameters and with the number of implausible v_e values (> 100%) between different AIF selections.

Results: Mean values of K^{trans} and v_e were significantly higher with population-based AIF compared to IIA and EIA based AIF selections, and mean value of v_e was significantly higher with EIA based AIF compared to IIA based AIF selection. Population-based AIF more often led to implausible v_e values, and IIA based AIF less often when comparing to other AIF selections. Mean value of k_{ep} was significantly lower with population-based AIF compared to IIA and EIA based AIF selections, and mean value of k_{ep} was significantly lower with EIA based AIF compared to IIA based AIF selection.

Discussion/Conclusion: The AIF selection has a significant impact on kinetic parameters of uterine fibroids, which limits the comparability of the parameters derived from different AIF sources. The IIA appears to be the best choice for AIF determination because it showed the least number of implausible v_e values.

References:

[1] Y.-S. Kim, H. K. Lim, J.-H. Kim, H. Rhim, B. K. Park, B. Keserci, M. O. Köhler, D.-S. Bae, B.-G. Kim, J.-W. Lee, T.-J. Kim, S. Sokka, J. H. Lee, Dynamic contrast-enhanced magnetic resonance imaging predicts immediate therapeutic response of magnetic resonance-guided high-intensity focused ultrasound ablation of symptomatic uterine fibroids., Investigative radiology 46 (10) (2011) 639–647.

[2] C. Wei, X. Fang, C. bin Wang, Y. Chen, X. Xu, J. ning Dong, The predictive value of quantitative DCE metrics for immediate therapeutic response of high-intensity focused ultrasound ablation (HIFU) of symptomatic uterine fibroids, Abdominal Radiology (2017) 1–7.

L05.18

Liver function evaluation in hilar cholangiocarcinoma patients with Gd-EOB-GTPA contrast enhanced MRI with Tc99 m-mebrofenin hepatobiliary scintigraphy as a gold standard: a pilot study

M. Shorikov, O. Sergeeva, D. Frantsev, M. Lapteva, A. Kashkadaeva, S. Averinova, B. Dolgushin

N.N. Blokhin RCRC, Radiology, Moscow, RUSSIAN FEDERATION

Purpose/Introduction: Comparison of Gd-EOB-GTPA contrast enhanced MRI liver function evaluation with "gold standard" hepatobiliary scintigraphy

Such work was rarely performed before on a small groups of patients [1, 2].

Subjects and Methods: Fifteen hilar cholangiocarinoma patients (male/female = 5/8, age range 29–70 years) after previous biliary decompression underwent 19 pairwise Gd-EOB-DTPA contrast-enhanced MRI and Tc99 m-mebrofenin hepatobiliary scintigraphy studies at 1- to 3-day intervals.

In the same 30–50 pixel ROIs, MRI signal was measured on precontrast, 10, 20, 30 and 40 min phases in II-III, IV, V-VIII, VI-VII liver segments and then reevaluated as a percentage of the signal on a precontrast phase. Volumes of these segments were also measured, total liver and right and left liver lobes functions were measured as area under mean of MRI signal intensity curve on 10–40th min multiplyed by volume. Persentages of the right and left liver lobe function to total liver function were calculated.

On Tc99 m-mebrofenin hepatobiliary scintigraphy total liver function and right and left lobes functions were similarly calculated as areas under curve.

Mann–Whitney criteria, log-linear regression were used for statistical analisys.

Results: Percentages of right and left lobe liver functions calculated with two methods were highly correlated ($R^2 = 0.9$, $p < 0.001$) and showed no signigicant difference when compared with Mann-Whiney criteria ($p > 0.5$).

Speed of Tc99 m-mebrofenin evacuation from the liver and its lobes was also possible to predict with log-linear regression ($R^2 = 0.9$, $p < 0.001$) of MRI signal intensities on 10–40th min

Discussion/Conclusion: Gd-EOB-GTPA contrast enhanced MRI liver function evaluation shows good correlation with hepatobiliary scintigraphy in a pilot study; further extended investigation is required to determine whether it can substitute the "gold standard".

References:

1. Rassam F., Zhang T., Cieslak K.P., Lavini C., Stoker J., Bennink R.J., van Gulik T.M., van Vliet L.J., Runge J.H., Vos F.M. Comparison between dynamic gadoxetate-enhanced MRI and 99mTc-mebrofenin hepatobiliary scintigraphy with SPECT for quantitative assessment of liver function. European Radiology, 2019, https://doi.org/10.1007/s00330-019-06029-7.
2. Geisel D., Ludemann L., Froling V., Malinowski M., Stockmann M., Baron A., Gebauer B., Seehofer D., Prasad V., Denecke T. Imaging-based evaluation of liver function: comparison of 99mTc-mebrofenin hepatobiliary scintigraphy and Gd-EOB-DTPA-enhanced MRI. Eur Radiol, 2015. 25(5): 1384–91, https://doi.org/10.1007/s00330-014-3536-8.

L05.19

Application of an UTE-based short-T2-signal-fraction mapping in patients with congenital myopathies

E. Caldas de Almeida Araujo[1], A. Vignaud[2], G. Guillot[3], B. Marty[1], P.-Y. Baudin[4], T. Stojkovic[5], L. Servais[6], B. Eymard[5], P. G. Carlier[1]
[1]*Institute of Myology, Neuromuscular Investigation Center, Paris, FRANCE,* [2]*UNIRS & University Of Paris-Saclay, CEA/DRF/JOLIOT/NeuroSpin, Gif-Sur-Yvette, FRANCE,* [3]*University Of Paris-Saclay, IR4 M UMR8081, CNRS, Orsay, FRANCE,* [4]*Consultants for Research in Imaging and Spectroscopy, Tournai, BELGIUM,* [5]*Institute of Myology, Neuromuscular Reference Center, Paris, FRANCE,* [6]*I-Motion, Paris, FRANCE*

Purpose/Introduction: Quantification of interstitial fibrosis is essential to grasp the whole picture of skeletal muscle (SkM) involvement in disease. There is no validated imaging alternative to biopsy, an invasive procedure which is far from systematically representative of the whole muscle. It was proposed that the short-T2 signal observed in UTE could reflect the amount of extra cellular matrix[1], suggesting UTE as a good candidate to fulfil this task. In this work, we looked for alterations of the short-T2-signal fraction in the SkM of patients with congenital myopathies (CM).

Subjects and Methods: Experiments were performed on a 3T system (SIEMENS, PRISMA, Erlangen, DE) using the vendor's 15-channel knee transceiver coil. Fat-fraction (FF), T2*, and short-T2-fraction (sT2f) maps (spatial res. 1×1 mm^2) were extracted from UTE data acquired in the calf of 16 controls (Age: 30 ± 8) and 10 CM patients(Age: 45 ± 21) using the method described in (1). Regions of interest (ROIs) were traced in the Soleus, Gastrocnemius Lat. and Med., which presented no visible aponeurosis. The average and standard deviation, of FF, T2* and sT2f were calculated for each ROI. Both quantities were compared between the two groups using one-way ANOVA. A global sT2f (gsT2f) was also calculated per subject, as the mean sT2f weighted by the ROIs' sizes.

Results: Fasciae and aponeurosis were systematically highlighted in the sT2f maps. FF, FF heterogeneity and T2* heterogeneity were increased in CM patients ($p < 0.001$). No differences were observed for sT2f and T2*. T2* presented mild negative correlations with FF ($r = -0.24$, $p < 0.001$) and FF heterogeneity ($r = -0.33$, $p < 0.001$). T2* heterogeneity correlated with FF ($r = 0.70$, $p < 0.001$) and FF heterogeneity ($r = 0.58$, $p < 0.001$). sT2f presented mild negative correlations with FF ($r = -0.50$, $p < 0.001$) and FF heterogeneity ($r = -0.33$, $p < 0.001$). In patients, a negative correlation was observed between gsT2f and age ($r = -0.54$, $p < 0.05$).

Discussion/Conclusion: The increased T2* heterogeneity results from differences of T2* between muscle and fat. The negative correlation between T2* and FF heterogeneity probably reflects increased magnetic susceptibility gradients in more heterogeneous tissues. Fibrosis has been previously reported in CM patients[2], however in this study sT2f was not altered in these patients. Moreover, the gsT2f decreased with age, while the amount of ECM is expected to increase.

Although a high sT2f was systematically observed in fasciae, in SkM It may as well arise from macromolecular pools in the contractile apparatus. So, while fatty replacement seems to lead to a decrease of sT2f, the replacement of myofibers by ECM might not be systematically reflected by an increase of sT2f.

References:

1. Araujo ECA et al. *Magn Reson Med*. 2017;78(3):997–1008.
2. Cassandrini D et al. *Ital J Pediatr*. 2017;43(1):1–16.

L05.20

Comparison of perfusion parameters in psoriasis arthritis patients before and after therapy

A. Müller-Lutz, C. Schleich, M. Tsoneva, J. Stabinska, H.-J. Wittsack
University Dusseldorf, Medical Faculty, Department of Diagnostic and Interventional Radiology, D-40225 Düsseldorf, GERMANY

Purpose/Introduction: To investigate perfusion parameters in metacarpophalangeal (MCP), distal interphalangeal (DIP) and proximal interphalangeal (PIP) joints in order to access therapeutic success in psoriasis arthritis (PsA) patients after anti-TNF therapy.

Subjects and Methods: The study was approved by local ethics committee. Written and informed consent was obtained from all patients before initiation.

Perfusion parameters were determined by dynamic contrast enhanced MRI (DCE) to 12 PsA patients (mean age: 59 years, age range: 42 – 74 years) at baseline and 6 months after initiating of anti-TNF therapy. Thereby, anti-TNF therapy was applied after failure of synthetic disease-modifying antirheumatic durc (csDMARD), methotrexate (MTX) and monotherapy. Imaging was performed on a 3T MRI scanner (MAGNETOM Skyra, Siemens Healthcare).

DCE war performed by a 3D gradient echo sequence using following parameters: TE/TR = 1.9 ms/5.8 ms, acquisition time = 6:07 min:s, number of dynamic scans = 110, flip angle = 8°, field of view = 140 mm, slice thickness = 3 mm.

To calculate quantitative perfusion parameters, two additional T1 sequences were applied using the dual flip-anlge approach[1].

The following perfusion parameters were determined to detect possible differences between baseline and 6 months after initiation of anti-TNF therapy: The quantitative parameters K_{Trans} and K_{ep} as well as the semi-quantitative parameters IAUC, Initial Slope and Peak.

Results: Considering the most affected regions of MCP, DIP or PIP, the best therapeutic success was observed in PIP joints. Here, all investigated parameters showed a significant difference between baseline and after 6 months of therapy (Tables 1, 2).

Parameter	DIP baseline	DIP therapy	PIP baseline	PIP therapy	MCP baseline	MCP therapy
KTrans [ml/ g/ min]	0,160 ± 0,097	0,062 ± 0,031	0,125 ± 0,087	0,050 ± 0,029	0,180 ± 0,165	0,145 ± 0,179
KEp [1/min]	0,323 ± 0,148	0,176 ± 0,140	0,438 ± 0,502	0,090 ± 0,095	0,305 ±0,135	0,198 ± 0,182
Initial Slope [mmol/l/s]	0,007 ± 0,005	0,003 ±0,002	0,005 ± 0,003	0,002 ± 0,002	0,008 ± 0,007	0,005 ± 0,007
IAUC[mmol/l x s]	8,588 ± 6,329	3,443 ± 2,061	6,993 ± 4,379	2,922 ± 1,537	9,214 ± 8,140	6,771 ± 7,980
Peak [mmol/l]	0,380 ± 0,480	0,153 ± 0,059	0,345 ± 0,214	0,144 ± 0,060	0,391 ± 0,298	0,328 ± 0,297

Quantitative and semi-quantitative perfusion parameter in the most affected regions at baseline and six months after anti-TNF therapy.

	DIP	PIP	MCP
p-value KTrans	0.013	0.025	0.345
p-value KEp	0.036	0.046	0.035
p-value Initial Slope	0.013	0.032	0.174
p-value IAUC	0.009	0.018	0.271
p-value PEAK	0.124	0.012	0.100

Table 2. P-values of the most affected regions for the parameters KTrans, KEp, Initial Slope, IAUC and Peak observed at baseline and after 6 months anti-TNF therapy.

Discussion/Conclusion: Perfusion imaging is able to detect differences in the most affected PsA regions before and after therapy with anti-TNF. Therefore, anti-TNF therapy is a possible therapeutic method in patients, where therapy with csDMARD, methotrexate and monotherapy failed.

References:

[1] Müller-Lutz et al. Comparison of quantitative and semiquantitative dynamic contrast-enhanced MRI with respect to correlation to delayed gadolinium-enhanced MRI of the cartilage in patients with early rheumatoid arthritis. J Comput Assist Tomogr (2015: 39(1):64–9.

L05.21

Sub-regional quantification of tissue-specific hydration state in patellar tendinopathy with 3D ultrashort echo time MRI

S. J. Breda[1], D. H. Poot[1], D. Papp[1], G. P. Krestin[1], R. J. de Vos[2], E. Oei[1]

[1]Erasmus University Medical Center, Radiology & Nuclear Medicine, Rotterdam, NETHERLANDS, [2]Erasmus University Medical Center, Orthopedics, Rotterdam, NETHERLANDS

Purpose/Introduction: Patellar tendinopathy is a painful activity-related injury of the patellar tendon, frequently occurring in jumping athletes such as basketball and volleyball players [1]. Regional differences in tendon morphology and composition of the extracellular matrix in patellar tendinopathy account for alterations of patellar tendon hydration state [2]. MRI is frequently used for imaging the patellar tendon and to monitor treatment response, but is limited by the fast free induction decay of collagen in tendon. Ultra-short echo time (UTE) MRI enables voxel-wise quantification of signal from tissues with short T2* [3]. Quantitative analysis of these images is typically performed using relative large regions of interest covering the entire tendon [4, 5]. However, this may compromise precision to detect subtle changes over time, due to the heterogeneity of the patellar tendon and the uneven distribution of the pathological changes. [6] We aimed to calculate T2* biomarkers with a novel image-analysis approach using different anatomical sub-regions of the patellar tendon.

Subjects and Methods: MRI was performed on the symptomatic knee of 7 jumping athletes affected with patellar tendinopathy using a 3.0T system and a 16 channel flexible surface coil. Four 3D UTE Cone acquisitions with in total 16 echoes were acquired in the axial plane. After image registration, T2* maps were generated using mono- and bi-exponential fitting methods. Masks delineating the outer margins of the patellar tendon were drawn on 10 consecutive slices covering the proximal patellar tendon. Tissue-specific analysis was performed by sub-selecting voxels based on the percentage short T2* of the bi-exponential model using thresholds (0–30% for extracellular matrix, 30–60% for intermediate voxels and 60–100% for collagen) to calculate median T2* values per subject. For each tissue, mean T2* and mean percentage short T2* was calculated over all subjects. RMSD between scans on subsequent days was calculated in one patient to assess repeatability.

Results: Mean (SD) age of the participants was 21.6 (3.1) years. Mean (SD) mono-exponential T2* was 2.7 ms (1.5) for collagen and 11.5 ms (6.7) for extracellular matrix. Visual inspection of the sub-selected voxels showed clear discrimination between the different tissues. RMSD of mono-exponential T2* ranged from 1.11 to 2.42 ms in one subject.

Discussion/Conclusion: The patellar tendon is a heterogeneous tissue, where collagen is represented by ultrashort T2* and extracellular matrix mostly by long T2* components. Sub-regional tissue-specific T2* biomarkers can be distinguished by semi-automatic voxel selection methods using bi-exponential fitting parameters and this provides a promising tool to detect changes in tendon hydration state with enhanced precision.

References:

[1]. Zwerver et al., 2011.
[2]. Parkinson et al., 2010.
[3]. Chang, et al., 2015.
[4]. Chang et al., 2015.
[5]. Kijowski et al., 2017.
[6]. Khan et al., 1999.

L05.22

Can disease progression be predicted in forearm muscle of Duchenne muscular dystrophy patients using quantitative fat-water NMRI?

H. Reyngoudt[1], P.-Y. Baudin[2], J. Le Louër[1], G. Honnet[3], L. Servais[4], B. Marty[1], P. G. Carlier[1]

[1]Institute of Myology, AIM-CEA, NMR Laboratory, Neuromuscular Investigation Center, Paris, FRANCE, [2]Consultants for Research in Imaging and Spectroscopy, Tournai, BELGIUM, [3]Genethon, Evry, FRANCE, [4]Trousseau Pediatric Hospital AP-HP, I-Motion, Paris, FRANCE

Purpose/Introduction: Several studies in Duchenne muscular dystrophy (DMD) have shown trajectories of both functional and qNMRI outcome measures[1−4]. Here, we present longitudinal qNMRI data in forearm for up to seven years in the AFM Genethon-sponsored DMD natural history study. We wanted to investigate how well disease progression, using muscle fat fraction (FF), could be predicted using a sigmoidal model.

Subjects and Methods: A 3-point 3D gradient echo ($TE_1/TE_2/TE_3$ = 2.7/3.95/5.15 ms; TR = 10 ms; flip angle = 3°) for fat-water separation was obtained on a clinical 3T Siemens Prisma scanner at 1-year intervals in anterior forearm muscles. Thirty-five DMD boys (12.6 ± 3.3 years) were included of which 29 subjectshad at least two NMR scans. A 2-parameter sigmoidal model was fitted on each individual FF trajectory with the following constraints: FF at age = 0 years is smaller than 1%; slopes > 0; asymptote at 90% FF. First, we investigated the whole data set, regardless of the number of visits per subject, when using only the 1st time point for fitting. Then, in 8 of 35 subjects who all had 5 consecutive yearly NMR exams, trajectories were fitted in four different ways: using 1, 2, 3 and 4 time points. The difference between the actual measured FF and the fitted FF value on subsequent time points was calculated.

Results: Using only the first time pointin the overall data set, an average error on the actual measured FF of 3.7% (n = 26), 5.4% (n = 22), 5.0% (n = 16), 7.5% (n = 9), 8.4% (n = 7) and 10.1% (n = 5) were observed for the 2nd, 3rd, 4th, 5th, 6th and 7th time point, respectively (Fig. 1).

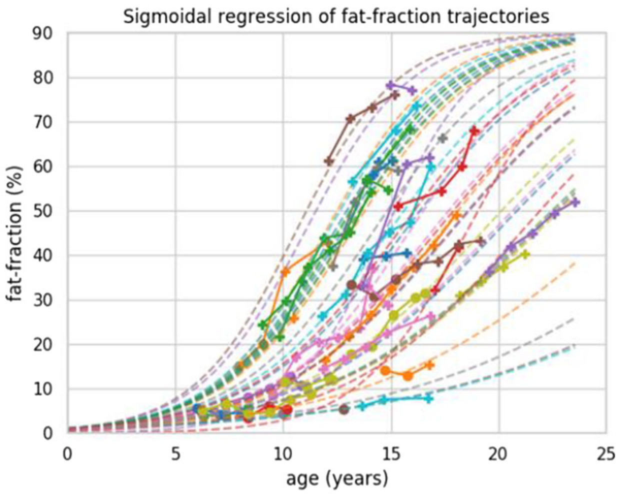

Fig. 1: Regression of fat fraction at multiple visits in forearm of DMD patients.

In the sub-cohort of the 8 patients with 5 consecutive time points, using just the first time point led to an average error of 4.0%, 5.7%, 5.9% and 8.4% for the 2nd, 3rd, 4th and 5th time point, respectively (Fig. 2).

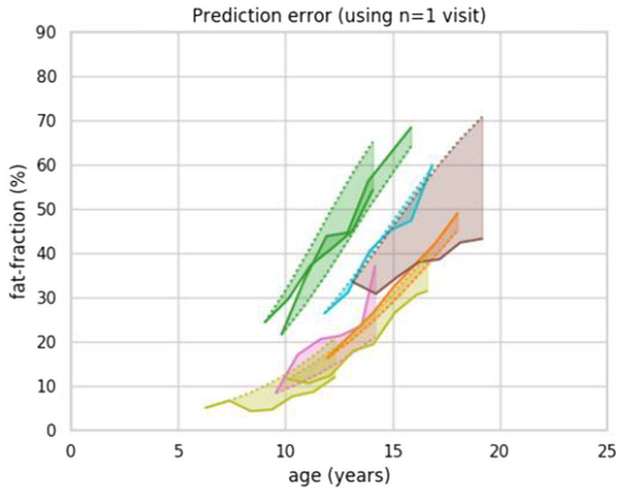

Fig. 2: Prediction error between predicted and actual FF value when using only the first visit to fit the data.

Using the first two time points, an error of 4.3%, 8.4% and 11.0% were observed for the 3rd, 4th and 5th time point, respectively. Using the three time points, an error of 4.9% and 7.0% were observed for the 4th and 5th time point, respectively. Finally, using the four first time points, an error of 3.8% was obtained for the 5th time point (Fig. 3).

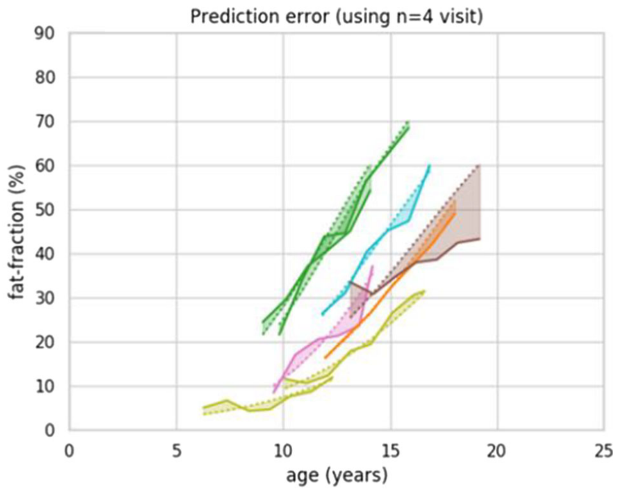

Fig. 3: Prediction error between predicted and actual FF value when using the first four visits to fit the data.

Discussion/Conclusion: These data indicate that, at least when using a 3rd and 4th time point in the sigmoidal fitting, the error on the FF values for subsequent time points decreases. In this subset, adding a 2nd time point did not decrease the difference with the actual measured FF values, due to some trajectories deviating strongly from the imposed sigmoid. Further investigations on the models used are necessary to assess whether FF trajectories can actually be used to predict disease progression, including a confrontation with functional and clinical data.

References:

[1] Mercuri et al., Neuromuscular Disord. 2016;26(9):576–83.
[2] Hamuro et al., CPT Pharmacometrics Syst. Pharmacol. 2017;6(9):596–603.
[3] Hogrel et al., Neurology 2016;86(11):1022–30.
[4] Ricotti et al. PLoS One 2016;11(9):e0162542.

L05.23

MRI of wrist bone marrow: isotropic mapping of fat fraction, water and fat T1 and T2* relaxation times

L. Marage[1], J. Lasbleiz[1], M. Lederlin[2], G. Gambarota[1], H. Saint-Jalmes[1]

[1]Univ Rennes, Inserm, LTSI – UMR 1099, Rennes, FRANCE, [2]CHU Rennes, Rennes, FRANCE

Purpose/Introduction: To provide a fast, voxel-by-voxel quantification of MRI biomarkers in wrist bone marrow. Five biomarkers, namely the fat fraction as well as the T1 and T2* relaxation times for both water and fat (FF, $T1_W$, $T1_F$, $T2^*_W$ and $T2^*_F$) were measured. These parametric maps of bone marrow biomarkers could be of interest in investigations of pathologies such as osteoarthritis [1].

Subjects and Methods: MRI data of 5 healthy volunteers were acquired at 1.5 T with a wrist dedicated coil. The MR sequence was a 4-echoes bone-marrow-optimized VIBE-Dixon with TR/TE (8.2/1.06, 2.4, 4.4, 6.8 ms) for a 1.2 mm^3 isotropic voxel. This MR sequence was repeated with 5° and 15° flip angle, for a 2min48sec total scan time.

Data were analyzed with a voxel-by-voxel adaptation of a previous published method [2] thanks to the high SNR provided by the wrist coil. Isotropic maps of FF, $T1_{W, F}$ and $T2^*_{W, F}$ were obtained by fitting the data to the signal equation. In addition, a quantification based on a region-of-interest (ROI) approach was also done on a 88 voxel-area ROI located in radius bone marrow near the joint.

Results: Figure 1 shows an example in coronal view of an MR image of the wrist. The corresponding FF, T1 $_{W,\ F}$ and T2* $_{W,\ F}$ parametric maps are also displayed.

The ROI located in the radius, as illustrated in the native image of Fig. 1, is replicated over all volunteers to calculate the average and standard deviation for each biomarker as shown in Table 1.

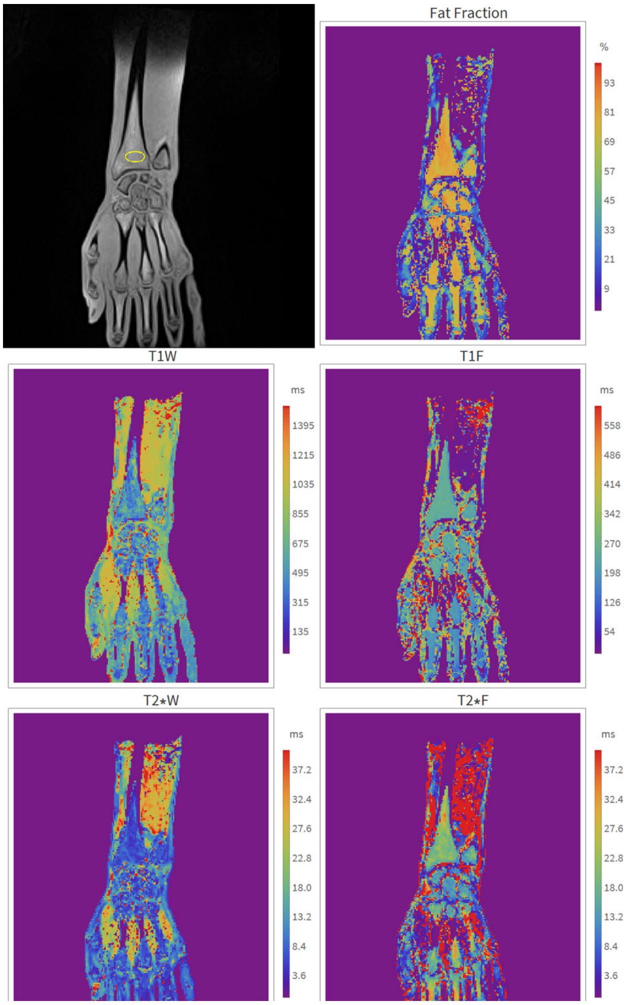

Fat Fraction (%)	81 ± 2
T1W (ms)	446 ± 74
T1F (ms)	269 ± 8
T2*W (ms)	4.6 ± 0.4
T2*F (ms)	22 ± 3

Table 1 Volunteers average ± standard deviation of the Fat Fraction, the T1 of water and fat, the T2* of the water and fat in the radius head.

Discussion/Conclusion: We developed an MRI data acquisition protocol, performed in less than 3 min, which provides five isotropic parametric maps with a 1.2 mm^3 isotropic resolution.

The voxel-by-voxel biomarker mapping is validated by the ROI analysis in radius, shown in Table 1. The bone marrow is well discernable in the different mappings. Since the parameters have been optimized for the bone marrow, the maps look noisy in other tissues like muscle.

The isotropic mapping developed in the current study could help in early joints disorders diagnosis and preferentially in osteoarthritis. Furthermore, this method may be easily adapted for other joints where similar kind of pathologies occur [3].

References:

[1] McQueen FM. *Annals of the Rheumatic Diseases*. 2007;66(12):1549–1552. https://doi.org/10.1136/ard.2007.082875.

[2] Le Ster C et al. *Journal of Magnetic Resonance Imaging*. 2016;44(3):549–555. https://doi.org/10.1002/jmri.25205.

[3] Li G et al. *Arthritis Research & Therapy*. 2013;15(6):223. https://doi.org/10.1186/ar4405.

L05.24

Intravoxel incoherent motion (IVIM) MRI in wrist bone marrow using the multishot readout-segmented (RESOLVE) echo planar imaging sequence

L. Marage[1], J. Lasbleiz[1], M. Lederlin[2], H. Saint-Jalmes[1], G. Gambarota[1]

[1]Univ Rennes, Inserm, LTSI, UMR 1099, Rennes, FRANCE, [2]CHU Rennes, Rennes, FRANCE

Purpose/Introduction: To measure the intravoxel incoherent motion (IVIM) diffusion and perfusion parameters (D, D* and f) in wrist bone marrow. To this aim, the multi-shot readout-segmented (RESOLVE) echo-planar diffusion sequence was employed, in order to obtain MR images with an improved spatial resolution and reduced distortions -when compared to single-shot echo-planar imaging.

Subjects and Methods: MRI experiments were performed on five healthy volunteers at 1.5 T (Aera Siemens) using a wrist coil. IVIM data were acquired with the RESOLVE sequence and the following parameters: TR/TE = 2400/58 ms, FOV = 377 × 377 mm^2, matrix = 188 × 188, 10 slices of 4 mm, iPAT = 3. Seven b-values (0, 50, 100, 150, 400, 800, 1000 s/mm^2) were acquired [1]. The SPAIR (Spectral Attenuated Inversion Recovery) fat suppression module was employed. The acquisition time was 4min41sec.

A region-of-interest (ROI) of a 24-voxel-area was drawn in the head of the radius and the IVIM signal decay was analyzed. The IVIM parameters D, D* and f were quantified by fitting the signal decay to the bi-exponential IVIM model equation.

Figure 1. Coronal RESOLVE MR image of the wrist (b-value = 50 s/mm²).

Results: MR images acquired with the RESOLVE sequence were characterized by minimal distortions and a good spatial resolution, which allowed for a clear visualization of the wrist joint structures. Figure 1 shows an example of a coronal MR image of the wrist, acquired with a b-value of 50 s/mm^2. The ROI used for the IVIM data analysis is also shown. Figure 2 illustrates two IVIM signal decays, one from a volunteer with a high value of f (8%) and another from a volunteer with a low value of f (4%). In the Table, the value of D, D* and f averaged over the five volunteers are shown.

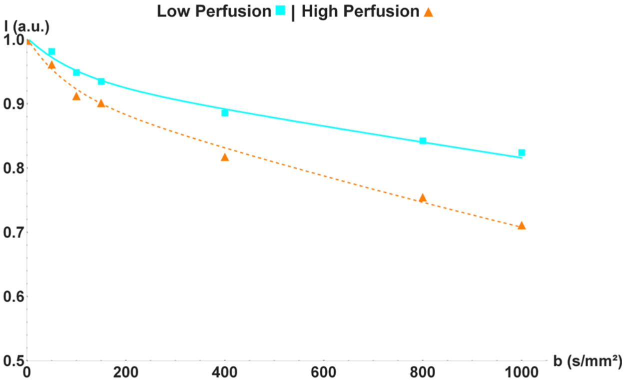

Figure 2. Example of two IVIM decay curves (one in a volunteer with a perfusion fraction f = 8%, the other in a volunteer with f = 4%).

f (%)	6 ± 2
D (× 10-3 mm²/s)	0.24 ± 0.08
D*(× 10-3 mm²/s)	9 ± 3

Table. Values of the f, D and D* in the radius bone marrow, averaged over five volunteers.

Discussion/Conclusion: In the current study, we have demonstrated the feasibility of measuring IVIM diffusion and perfusion parameters (D, D* and f) in radius bone marrow. Previous studies of diffusion MRI in wrist have focused only on measurements of the diffusion coefficient D [2, 3]. The values of D and D* (and to a minor extent, f) measured in the current study are smaller than those observed in other tissues. This is probably related to the tissue structure/composition of the head of the radius, which is rich in trabecular bone. This anatomical region is of particular interest for investigations of osteoporotic processes. The IVIM parameters, as assessed in the current study, could be useful as potential biomarkers of disease progression and response to therapy.

References:

[1] Lasbleiz et al. J Magn Reson Imaging. 2019;49(3):768–776.
[2] Li X et al. Magnetic Resonance Imaging. 2014;32(4):350–353.
[3] Barendregt AM et al., Eur Radiol. 2017;27(11):4889–4899.

L05.25

Angular dependence of UTE signal of cortical bone: a pilot study of assessing structure of collagen matrix using MRI

K. Masuyama[1], M. Tang[2], M. Todoh[3], T. Yamamoto[2]
[1]Teine Keijinkai Hospital, Sapporo, JAPAN, [2]Faculty of Health Sciences, Hokkaido University, Sapporo, JAPAN, [3]Faculty of Engineering, Hokkaido University, Sapporo, JAPAN

Purpose/Introduction: Collagen fibers form a matrix in the cortical bone and the properties of the bone matrix, i.e. orientation and density of collagen fibers mainly determine bone strength that predicts a risk of bone fracture. The current methods to measure bone mineral density often fail to predict risks of bone fracture, and a non-invasive method to assess the collagen matrix is expected to be developed. Focusing on the susceptibility anisotropy of collagen molecule, we investigated how MR signal of cortical bone varies by changing the angle between the bone axis and B_0 and demonstrated a new possibility to assess the structure of collagen matrix.

Subjects and Methods: A bovine femur bone was fixed on the center of a rotating plate and this plate was placed at the center of a 1.5-T MRI. The bone axis was set parallel to B_0. The cortical bone was imaged by UTE pulse sequence (TE = 70 µs). This imaging was repeated by rotating the plate every 30°. The signal at the rotating center (81 mm^2) on each image was measured. This experiment was applied to two bone samples (4-month old and 2-year old) and a water phantom with the same shape as the bone samples. The simplified relationship of MR signal (S) of cortical bone and R_2^* is written by $lnS/TE = lnS_0/TE - R_2^* = lnS_0/TE - (R_2 + \gamma/2\pi \bullet \Delta B)$,
where S_0 is the proton density, γ is the gyromagnetic ratio and ΔB is the local magnetic distortion in a voxel (0.8 mm^3). The values of lnS/TE at all angles were plotted to observe angular dependence of R_2^*. The maximal amplitude of R_2^* changes (ΔR_2^*) were obtained from each plot.

Results: The lnS/TE value for both bones showed 180°-periodic angular dependence in that ΔR_2^* is quite larger (4-month old bone: 2.1 kHz, 2-year old bone: 0.9 kHz) than that of the water phantom (0.2 kHz) (Fig. 1).

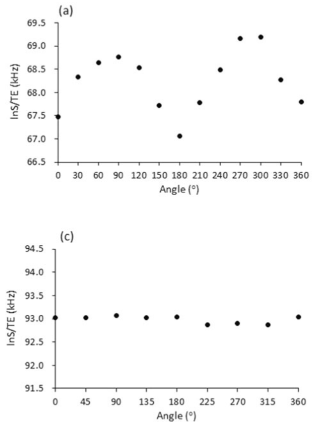

Discussion/Conclusion: The results of the angular dependence lead that ΔB was highest/lowest when the bone axis aligned perpendicular/parallel to B_0. Because collagen fibers tend to align to the bone axis, this ΔB property reflects the anisotropic susceptibility collagen: susceptibility difference along long and short axes.[1] Evidence that the values of ΔR_2^* of bones were much larger than that of water phantom suggests the small influence of shape anisotropy on the results of bones. The ΔR_2^* decreased from 4-month to 2-year old bone. This tendency may reflect the structural changes of bone; collagen fibers in younger bone aggregate partially and tend to order having inter-collagen spaces with minerals the amount of which increases with maturity[2] (Fig. 2). The aggregated collagens produce larger ΔB than the distributed ones.

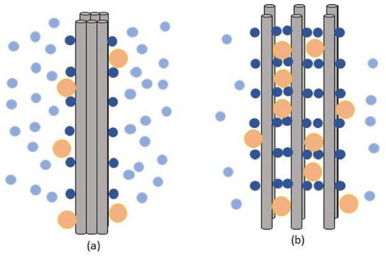

Fig.2 The pictures of bone structure in immature (a) and mature bone (b). The gray cylinders represent collagen fibers. The yellow circles represent mineral substance. The light and dark blue circles represent non-bound and bound water, severally.

Our results indicate that the structure of collagen matrix in cortical bone would be assessed by MRI.

References:

1. Wei H, et al. Investigating magnetic susceptibility of human knee joint at 7 Tesla. Magn Reson Med 2017;78:1933–1943.
2. Bonucci E. The mineralization of bone and its analogies with other hard tissues. Adv Top Cryst Growth 2013:145–184.

L05.26

Prospective multiparametric MR monitoring of changes in hyaline cartilage of the knee joint after implantation of biological collagen type I matrix implants

A. Sprlakova-Pukova[1], **J. Tintera**[2], M. Repko[3], P. Valis[3]
[1]The University Hospital Brno, Department of Radiology and Nuclear Medicine, Brno, CZECH REPUBLIC, [2]IKEM, ZRIR, Prague, CZECH REPUBLIC, [3]The University Hospital Brno, Department of Orthopedics, Brno, CZECH REPUBLIC

Purpose/Introduction: The aim of this study is to present preliminary results of assessment of cartilage quality and to determine the surgical effects of two types of surgery using dGEMRIC [1, 2]: microfracture and implantation of Cares_S.

Subjects and Methods: A prospective cohort of 37 patients with cartilage defect have undergone the surgery either by microfracture (13 patients) or by implantation of biological collagen type I matrix implants (15 patients). MRI examination including dGEMRIC was performed before treatment and 6, 12 and 18 months after surgery.

T1 value and dGEMRIC index (dGi) from three ROIs were extracted: a) non weight -bearing zone (reference zone), b) the defect and c) the cartilage nearby. dGi was calculate as

dGi = $(R1_{post} - R1_{pre}).C = (1/T1_{post} - 1/T1_{pre}).C$, where scale factor C = 10 000.

Results: The values of T1 after Gd contrast agent application (T1Gd) in non- weight bearing zone (ROI a) before surgery were 370–540 ms; 6 month after surgery were T1Gd values between 300 and 460 ms; 12 month after surgery were T1Gd values 270–520 ms; 18 month after surgery T1Gd values were between 230 and 460 ms.

The baselineT1Gd values in the defect zone (ROI b) were between 328 and 550 ms; 6 month after surgery were T1Gd values between 250 and 530 ms; 12 month after surgery were T1Gd values between 200 and 570 ms; 18 month after surgery were T1Gd values between 240 and 575 ms.

The values in the cartilage nearby the defect (ROI c) were in the baseline examination between T1Gd 340–600 ms; 6 month after surgery were T1Gd values between 260 and 550 ms; 12 month after surgery were T1Gd values between 220 and 560 ms; 18 month after surgery were T1Gd values between 230 and 460 ms.

Table 1 shows median dGi in all ROIs and examinations.

	before surgery	6 months after	12 months after	18 months after
ROI a)	4.5	7.6	10.4	10.6
ROI b)	8.3	9.9	13.5	13.1
ROI c)	1.5	4.5	6.3	6.9

Median dGi in all ROIs

Discussion/Conclusion: The general decrease of GAG content in all three ROIs was detected. Surprisingly, the least significant changes of GAG content were seen in the area close to defects.

However, there is a positive tendency to adjust the decrease of GAG content in all three investigating areas. dGEMRIC is feasible method to evaluate the quality of cartilage.

The study was supported by Ministry of Health of the Czech Republic, grant nr. 16-30833A.

References:

1. Bashir A, Gray ML, Boutin RD, et al. 1997. Glycosaminoglycan in articular cartilage: in vivo assessment with delayed Gd(DTPA)(2-)-enhanced MR imaging. Radiology 205:551–558.
2. Burstein D, Velyvis J, Scott KT, et al. 2001. Protocol issues for delayed Gd(DTPA)(2)-enhanced MRI (dGEMRIC) for clinical evaluation of articular cartilage. Magn Reson Med 45:36–41.

L05.27
WITHDRAWN

L05.28
Polyunsaturated fatty acids (PUFA) depletion is associated with high serotonin turnover in human whole breast tumour

S. M. Cheung[1], E. Husain[2], Y. Masannat[3], K. Wahle[4], S. D. Heys[3], J. He[1]

[1]University of Aberdeen, Aberdeen, UNITED KINGDOM, [2]Aberdeen Royal Infirmary, Pathology Department, Aberdeen, UNITED KINGDOM, [3]Aberdeen Royal Infirmary, Breast Unit, Aberdeen, UNITED KINGDOM, [4]University of Strathclyde, Strathclyde Institute of Pharmacy and Biological Sciences, Glasgow, UNITED KINGDOM

Purpose/Introduction: Breast cancer is the most common cause of cancer-related death among women (1), with research focus increasingly shifted to disease prevention and personalised medicine (2). During tumour initiation, the conversion from polyunsaturated fatty acids (PUFA) to inflammatory agent of eicosanoids is increased (3), stimulating tumour necrosis factor-α (TNFα) and macrophages to sustain an inflammatory tumour microenvironment (4). Elevated inflammation is associated with increased serotonin turnover linked to poor 10-year survival rate (5). Earlier evidence showed PUFA deficiency increased serotonin turnover, however it was evaluated in animal brain models (6). Specialist double quantum filtered (DQF) magnetic resonance spectroscopy (MRS) allows accurate detection of PUFA, while overlapping water and lipid signals are suppressed (7). We hypothesised that there is an association between PUFA from whole breast tumours and serotonin expression.

Subjects and Methods: Thirty female patients (aged 39–78 years, 12 serotonin ≤ H-score 100 and 18 serotonin > H-score 100) with invasive ductal carcinoma undergoing breast surgery were enrolled (Table 1). Freshly excised breast tumours were scanned on a 3T whole body clinical MRI scanner (Achieva TX, Philips Healthcare, Best, Netherlands) using a 32-channel receiver coil for high sensitivity detection. PUFA spectrum was acquired from a single voxel covering the whole tumour using DQF MRS method (7), with TR/TE of 1.25 s/130 ms, spectral editing frequency at 2.8 ppm. A reference spectrum was acquired from the same voxel with the same TR/TE as PUFA spectrum. The PUFA (5.3 ppm) in DQF MRS spectrum was referenced to methyl fat (0.9 ppm) in the reference. All spectra were quantified using AMARES algorithm (8) in the jMRUI software (v5.0., TRANSACT, Leuven, Belgium) (9). Serotonin and Ki-67 expression were assessed histologically.

Parameters	All (n=30)	Serotonin (≤100) (n=12)	Serotonin (>100) (n=18)	*p*-value
Age	61.1 ± 11.5	57.6 ± 11.7	63.4 ± 11.0	0.1819
Body Mass Index (BMI)	30.4 ± 6.4	30.3 ± 5.7	30.5 ± 7.2	0.9288
Tumour Size (cm)	2.5 ± 0.8	2.6 ± 0.7	2.4 ± 0.8	0.4428
Serotonin (0-300)	107 ± 62	47 ± 22	147 ± 46	NA
Tumour Type				
Invasive Ductal Carcinoma, No Special Type (IDC, NST)	30	12	18	-
Grade				
II	15	5	10	
III	15	7	8	-
Human Epidermal growth factor Receptor 2 (HER2+)	6	2	4	-
Triple-Negative Breast Cancer (TNBC)	7	5	2	-

Results: There was a significant difference in PUFA ($t = 2.1970$, $p = 0.0442$) between low serotonin (1.45 ± 0.81%) and high serotonin (0.90 ± 0.42%) breast tumours (Fig. 1). There was no significant difference in Ki-67 expression ($z = 1.820$, $p = 0.0687$) between low serotonin (median of 21.7%, IQR: 12.3–39.7%) and high serotonin (median of 14.5%, IQR: 7.8–18.7%) breast tumours. PUFA was negatively correlated with serotonin expression ($r = -0.3616$, $p = 0.0496$), but not with Ki-67 expression (Fig. 2).

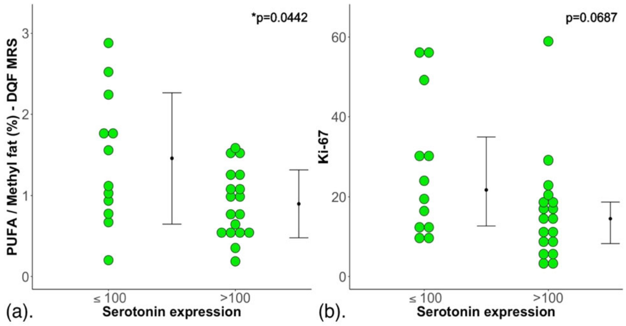

Figure 1.The group difference in (a) polyunsaturated fatty acids (PUFA) and (b) Ki-67 are shown in dot plots. Statistically significant p values are marked by '*'. There was significant difference in PUFA between low and high serotonin breast tumour

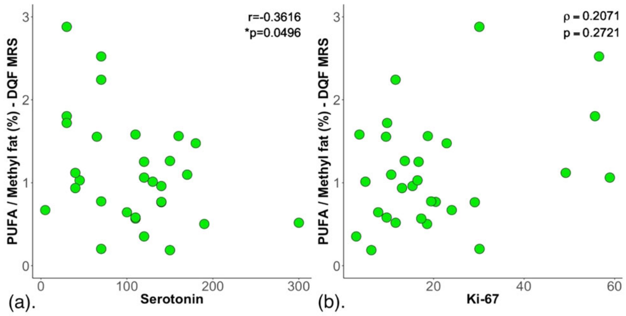

Figure 2. Polyunsaturated fatty acids (PUFA) was correlated against (a) serotonin expression and (b) Ki-67 expression within the entire cohort. A significant negative correlation was observed between PUFA and serotonin expression.

Discussion/Conclusion: Our results showed that there was a significant reduction in PUFA in high serotonin breast tumour. PUFA in human breast cancer is associated with serotonin mediated through the inflammation process, and may not be related to the cell division arising from proliferative activities.

References:

1. ONS. London: 2017.
2. Breast Cancer Now. London: 2019.
3. Basu. *Lip Tech* (2016).
4. Herr. *Front Cardiovasc Med* (2017).
5. Leoncikas. *Sci Rep* (2016).
6. McNamara. *Pr L EFA* (2010).
7. He. *MRM* (2007).
8. Vanhamme. *JMR* (1997).
9. Naressi. *Comp Biol Med* (2001).

L05.29

Intracellular Water Lifetime as a Tumour Biomarker for diagnosis and therapy outcome by FFC-Relaxometry in breast cancer

R. Maria Rosaria, S. Baroni, S. Rapisarda, S. Aime,
S. Geninatti Crich
University of Turin, Turin, ITALY

Purpose/Introduction: The diagnostic power of Magnetic Resonance Imaging in tumour phenotyping could be improved observing the marked decrease of T_1 in biological tissues at low magnetic field strength. It is well known that the T_1 of a given tissue changes as a function of the applied magnetic field strength. In particular, the lower is the magnetic field the higher is the differences among tissues. Known as "T_1-dispersion", this phenomenon is a marker of disease and it is invisible to conventional, fixed-field MRI scanners. The Fast Field-Cycling (FFC)-NMR is the only practicable way of measuring it. An overall increase of water content together with an impairment in water exchange across membranes have fundamental role in this behaviour. The measurement of the intracellular water lifetime (τ_{in}) in vitro and in vivo may bring relevant information on the ongoing metabolism of the tumour cell, as report on the pathological status, grade and therapeutic outcome.

Subjects and Methods: The measurement of τ_{in} was performed in vitro and in vivo on murine adenocarcinoma cell line (4t1). Different doses of doxorubicin have been tested before the T_1 measurement. The data were analysed using two-site exchange (2SX) model (Fig. 1) in which the Bloch equations are modified to describe two-compartments (intra and extracellular) in which water exchange modulates the observed relaxation behaviour.

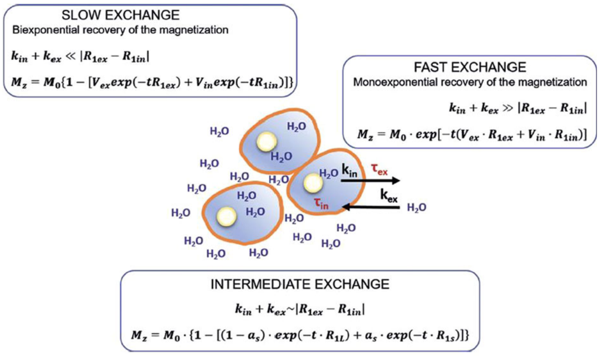

The water exchange and the magnetisation (MZ) value in relationship with the intra and the extra space.The MZ is dependent on the "relaxation" term,|R1in- R1ex|,and an"exchange"term|kin + kex|,(Kin/ex= 1/tin/ex), defined as the NMR "shutter-speed".

Results: The most striking result from the fitting procedure is that the in vitro and in vivo decrease of τ_{in} (Fig. 2)due to the slower tumour metabolism caused by doxorubicin, not observed in resistant cell line.

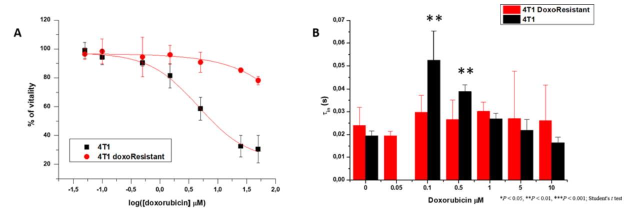

A) Vitality test on 4t1 and 4t1 doxo resistant treated for 24h with different concentration of drug; B) τin determination after doxorubicin treatment for 24h

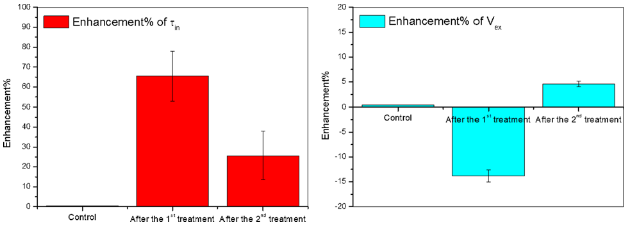

Discussion/Conclusion: Recently [1, 2], we showed that the τ_{in} represents a hallmark of tumour tissue cells status that can be easily monitored by measuring T_1 at different and relatively low magnetic field strengths. A fast exchange through cell membranes indicates a high metabolic rate and thus a high activity of the tumor cells. Thus it is possible to measure the high metabolic pressure by an enhance water exchange with the exterior of the cell. Therefore, τ_{in} can be considered an important tumour biomarker directly depending on the rate of cell proliferation, cell migration and in responding to external stimuli as hypoxia or extracellular acidosis. Currently, tumour responses to therapy are monitored primarily by imaging evaluating essentially the decrease of tumor size. This approach, however, lacks sensitivity and can only give a delayed indication of a positive response to treatment. In this study, we propose the use of FFC-NMR to provide relevant information about response to treatment by monitoring changes of water exchange rates through cell membranes that are directly dependent on the metabolism alterations caused by the chemo- or radio-therapy.

References:

[1] MR Ruggiero, et al. *Angew Chem Int Ed Engl*, **2018**.
[2] MR Ruggiero, et al., *Molecular physics* **2018**.

L05.30

Optimal phased-array signal combination for polyunsaturated fatty acids measurement in breast cancer using multiple quantum coherence MR spectroscopy At 3T

V. Mallikourti[1], S. M. Cheung[1], T. Gagliardi[2], Y. Masannat[3],
S. Heys[3], J. He[1]
[1]University of Aberdeen, Aberdeen Biomedical Imaging Centre, Aberdeen, UNITED KINGDOM, [2]Department of Clinical Radiology, Aberdeen Royal Infirmary, Aberdeen, UNITED KINGDOM, [3]Breast Unit, Aberdeen Royal Infirmary, Aberdeen, UNITED KINGDOM

Purpose/Introduction: Polyunsaturated fatty acid (PUFA), a key marker in breast cancer [1], can be non-invasively quantified using multiple quantum coherence (MQC) magnetic resonance spectroscopy (MRS), at the expense of losing half of the signal [2]. Effective combination of MRS signal from phased-array coils has been proposed to increase the signal to noise ratio (SNR) [3]. Investigations so far focused on conventional brain MRS with different spectral appearance and biochemical environment compared to MQC MRS in breast. We therefore set out to identify the optimal signal combination algorithm for PUFA spectra in breast tumours using MQC MRS.

Subjects and Methods: 17 whole breast tumours, freshly excised from patients (age range 42–78 years), 15 healthy female volunteers (age range 61–76 years) and 5 patients (age range 59–69 years) were scanned on a clinical 3T MRI scanner (Philips Healthcare, Netherlands). A 32- and a 16-channel receiver coil were used for excised tumours and participants in vivo respectively. Single voxel PUFA spectra and reference unsuppressed water spectra were acquired.

The investigated signal combination algorithms were adaptively optimised combination (AOC) [5], noise decorrelation combination [6], Whitened Singular Value Decomposition [7], S/N^2 [8], S/N [9], and Signal Weighting [10]. Comparisons were performed using the SNR improvement of PUFA reference to Equal Weighting. The SNR improvement from the optimal algorithm was correlated against PUFA content, water/fat ratio and voxel volume.

Results: AOC gave the highest SNR improvement in excised breast tumours (median, 39.5%; interquartile range: 35.5–53.2%), volunteers (82.4 ± 37.4%), and patients (63.0 ± 28.2%) (Table 1, Fig. 1). There was no significant correlations between SNR improvement from AOC and PUFA content (rho = 0.256, p = 0.320), voxel volume (rho = 0.125, p = 0.632) or water/fat ratio (rho = 0.353, p = 0.165) in tumours (Fig. 2). Using AOC in patients, the SNR increases by 18.5 ± 10.9% or equivalently, acquisition time is 1.5 times faster compared to non-noise decorrelated algorithms.

	Ex vivo experiments			In vivo experiments				
	Breast tumour specimens (N = 17)			Healthy volunteers (N = 15, 30 voxels)			Patients (N = 5)	
Methods	SNR	SNR improvement %	p-value	SNR	SNR improvement %	p-value	SNR	SNR improvement %
Equal	12.5 (6.9 – 18.4)	-	-	37.0 ± 21.6	-	-	10.4 ± 6.8	-
Signal	14.2 (8.3 – 24.7)	24.8 (16.6 – 34.8)	< 0.001	49.1 ± 33.1	29.5 ± 19.5	< 0.001	13.3 ±7.7	29.8 ± 14.4
S/N	14.4 (8.3 – 25.6)	27.2 (17.7 – 38.3)	< 0.001	50.6 ± 33.3	34.2 ± 18.4	< 0.001	13.8 ± 8.2	34.4 ± 14.4
S/N2	14.4 (8.3 – 26.0)	27.8 (17.9 – 40.8)	0.001	51.5 ± 33.3	37.4 ± 17.8	< 0.001	14.1 ± 8.7	37.0 ± 14.9
WSVD	23.0 (13.1 – 32.2)	41.4 (26.1 – 53.6)	0.074	66.5 ± 39.6	81.3 ± 42.3	0.312	9.0 ± 8.5	8.8 ± 69.5
nd-comb	16.7 (9.5 – 27.1)	37.7 (33.8 – 49.8)	0.039	64.9 ± 40.6	79.2 ± 36.1	< 0.001	16.9 ± 11.3	60.3 ± 26.3
AOC	16.3 (9.6 – 27.3)	39.5 (35.5 – 53.2)	-	65.9 ± 41.1	82.4 ± 37.4	-	17.2 ± 11.7	63.0 ± 28.2

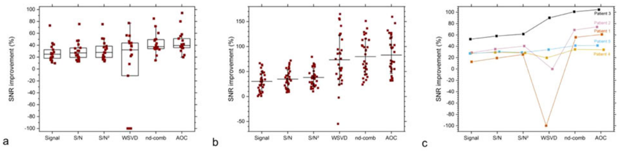

SNR improvement for (a) excised breast tumours, (b) healthy volunteers, and (c) patients. The box plot shows the median and interquartile range while the error bar shows the mean and standard deviation of SNR improvement from each algorithm.

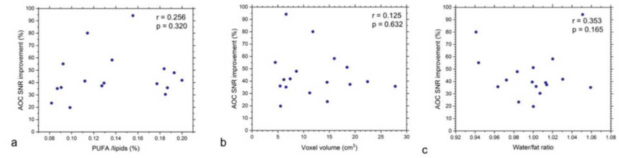

Spearman's rank tests between SNR improvement and experimental parameters in excised breast tumours. The SNR improvement derived from AOC was correlated against (a) PUFA content, (b) voxel volume, and (c) water/fat ratio in excised breast tumours.

Discussion/Conclusion: AOC outperformed the rest combination algorithms and was independent from experimental conditions demonstrating its utility on MQC MRS in breast cancer. Therefore, AOC is the most suitable algorithm to improve SNR or accelerate the acquisition of PUFA in a clinical setting, where noises are often correlated across channels.

References:

1. Schmitz, et al., MRM **54**(1), 43–50 (2005).
2. He, et al., MRM **58**(6), 1079–1085 (2007).
3. Roemer, et al., MRM **16**(2), 192–225 (1990).
4. He, et al., JMR **106**(3), 203–211(1995).
5. Fang, et al., MRM **75**(6), 2235–2244 (2016).
6. Martini, et al., NMR in Biomedicine **23**(1), 66–73 (2010).
7. Rodgers & Robson, MRM**63**(4), 881–891 (2010).
8. Hall, et al., NeuroImage **86**, 35–42 (2014).
9. Dong & Peterson, MRI **25**(8), 1148–1154 (2007).
10. Natt, MRM **53**(1), 3–8(2005).